# Development of Resistive Plate Chambers for muon detection system of the CBM Experiment at FAIR


*By*

**MITALI MONDAL**

**PHYS04201504013**

**Variable Energy Cyclotron Centre, Kolkata**


*A thesis submitted to*

*The Board of Studies in Physical Sciences*

*In partial fulfillment of requirements*

*for the Degree of*

**DOCTOR OF PHILOSOPHY**

*of*

**HOMI BHABHA NATIONAL INSTITUTE**

**May, 2022**

# STATEMENT BY AUTHOR



Mitali Mondal

# DECLARATION

I, hereby declare that the investigation presented in the thesis has been carried out by me. The work is original and has not been submitted earlier as a whole or in part for a degree / diploma at this or any other Institution / University.

Mitali Mondal

# List of Publications arising from the thesis

## Journal

1. "Performance of a prototype bakelite RPC at GIF++ using self-triggered electronics for the CBM Experiment at FAIR",
   Mitali Mondal et al., **Nucl. Inst. and Meth. A, 1025, 166042 (2022).**

2. "Development and characterization of 6-gap bakelite Multi-gap Resistive Plate Chamber"
   Rajesh Ganai, Mitali Mondal et. al., **JINST 13, P07022 (2018).**

## Proceedings of conferences

1. "Performance of a Low Resistive Bakelite RPC using PADI Electronics"
   Mitali Mondal et. al., **Springer Proc. Phys. 261, 1119-1123 (2021)**.

2. "Timing Studies of Bakelite Multi-gap Resistive Plate Chamber"
   Rajesh Ganai, Mitali Mondal et.al., **Nucl. Inst. and Meth. A 936, 505-506 (2019)**.

3. "Characterization of Prototype Oil-free Bakelite RPC for High Rate Experiments"
   Mitali Mondal et.al., **Proc. DAE Symp. Nucl. Phys. 61, 946–947 (2016)**

4. "Performance Studies of Bakelite Multi-gap Resistive Plate Chamber with Cosmic Rays"
   Rajesh Ganai, Mitali Mondal et. al., **JINST 14, C06010 (2019)**.

5. "Testing of a Resistive Plate Chamber using NINO-ASIC based Front End Electronics"
   Mitali Mondal et. al., **Proc. DAE Symp. Nucl. Phys. 62, 1024–1025 (2017)**.

6. "Development of 6-gap Bakelite Multigap Resistive Plate Chamber"
   R. Ganai, Mitali Mondal et. al., **Springer Proc. Phys. 203, 129 (2016)**.

7. "Feasibility Study of Using RPCs in CBM Muon Chamber"
   E. Nandy, Mitali Mondal et. al., **DAE Symp. Nucl. Phys. 61, 1024 (2016)**.

Mitali Mondal

***Dedicated to my family and friends,***

# ACKNOWLEDGEMENTS

I would like to express my deepest gratitude to my Ph.D. supervisor, Prof. Subhasis Chattopadhyay, whose enormous knowledge of science combined with his endless enthusiasm for research has tremendously helped me in completing this thesis. His constant guidance throughout all these years in every aspect of my Ph.D. career was extremely helpful. I would like to express my profound and heartfelt gratitude to Dr. Rajesh Ganai, my senior in the lab who has helped me learn each and every little thing about research, from the basic principle of RPC to setting up an experiment in the lab. This journey would have been much more difficult without his guidance. I sincerely acknowledge Mr. Jogender Saini who supported me a lot during my experiments at the VECC. Without his help, it wouldn't be possible for me to learn so many things about electronic instruments. I thank Dr. Zubayer Ahmmed for his collaboration, support, and encouragement. I convey my deepest gratitude to Mr. Rama Narayana Singharaju, Mr. Partha Bhaskar, Mr. Vinod Negi, and Mr. Shuaib Ahmmed for their generous help while I encountered any difficulties in electronics even on the non-working days. I sincerely thank Dr. Anand Kumar Dubey for all his help and support throughout these years. I thank the members of my thesis committee and referees for their constructive suggestions. I am grateful to Dr. Paramita Mukherjee, and Dr. Gopal Mukherjee for their teachings, valuable suggestions, and encouragement. A special thank goes to Dr. Tilak Ghosh for his student-friendly behavior. I am utterly grateful to him for helping us out in solving any issues regarding our stay at VECC. A special note of thanks goes to Dr. Saikat Biswas whose valuable suggestions have enriched my understanding of RPCs. I also thank Dr. Sarmishtha Bhattacharya, Dr. Gayathri N. Banerjee, and Dr. Parnika Das for their well wishes. I am grateful to all my lab colleagues: Ganesh da, Tushar da, Sukumar Da, Jayanta Ji, Khokon Da, Sanat Da, Tirthankar Da, Nabarun da, Bhaskar da, Santu da, Amit da, and Kamal da for their help during detector fabrication, electronics assembly, and tests. I also like to thank VECC grid colleagues, mainly Prasun da, Abhishek, and Ashique, for their help during computer and software-related issues. Warm affection and gratitude are extended towards my friends and juniors: Shreyasi, Sanchari, Sumit, Soumen, Santanu, Mahfuzur, Sridhar, Sinjini, Abhishek, Om, Tanay, Debabrata, Shuvo, Gitesh; and seniors: Deb Sankar da, Souvik da, Ajit da, Somnath da, Debojit da, Subikash da, Ekata di, Balaram da, Aminul da who have provided me a friendly environment and supported me all these years. I would also like to extend my thanks to my friends: Ananya and Sushmita who have been a constant positive presence in my life from my childhood days. Words are inadequate to express my love and gratitude for the way my friends: Shabir, Apar, Debabrata, and Vivek have taken care of me for months like a family in one of the difficult times of my life. I am grateful to my father, Mr. Sunil Kumar Mondal and my sister, Dr. Chaitali Mondal for motivating me in pursuing higher studies. I especially thank my brother-in-law, Dr. Ankurava Sinha to convince me to come to appear for the interview at VECC and also to support me morally through all the years of my Ph.D. life. Finally, I want to thank my mother, Mrs. Karuna Mondal for loving me unconditionally and supporting me in every step of my life. I express my gratitude again to all to whom I owe so much.

Mitali Mondal

# Contents

# Homi Bhabha National Institute

## Synopsis of PhD Thesis

**1. Name of the Student: Mitali Mondal**

**2. Name of the Constituent Institution: Variable Enerrgy Cyclotron Centre, Kolkata**

**3. Enrolment No. : PHYS04201504013**

**4. Title of the Thesis: Development of Resistive Plate Chambers for muon detection system of the CBM Experiment at FAIR**

**5. Board of Studies: Physical Sciences**

## SYNOPSIS

(Limited to 10 pages in double spacing)

The universe is made of molecules and atoms, where protons and neutrons are constituents of nucleus in an atom. These hadronic phases of matter, i.e, protons, neutrons consist of quarks and gluons. The strong force binds the quarks and gluons inside a hadron under normal nuclear density and temperature. Hence, free quarks or gluons don't exist in nature. However, at a very high temperature and/or baryo-chemical potential, quarks and gluons behave like free particles covering the entire volume of the nuclear matter. This phenomenon is referred to as asymptotic freedom [1] where the strong interaction weakens with decreasing distances and increasing temperature. The state of deconfinement of quarks and gluons is known as the Quark-Gluon Plasma (QGP). As predicted by the fundamental theory of strong interactions, Quantum ChromoDynamics (QCD), the transition between the hadronic matter to QGP is supposed to be a smooth crossover in the regime of very high temperature $\sim$ 160 MeV and of vanishing net-baryon densities [2]. In the regime of moderate temperature ($\sim$ 50 MeV) and very high net baryon densities, the transition is predicted to be a first order phase transition. These two types of transitions converge at the critical point. The accelerator based facilities, the Large Hadron Collider at CERN in Switzerland and the Relativistic Heavy Ion Collider at BNL in the United States, are able to create the hot and dense QGP state at extremely high temperatures in the heavy-ion collisions [3]. The universe is believed to be filled with this soup of Quark-Gluon Plasma for a few millionths of a second after the Big Bang. At the SPS at CERN and at the SIS100 accelerator of the upcoming Facility for Anti-Proton and Ion Research (FAIR) centre, nuclear matter to be strongly compressed. The matter density of 6-12$\times\rho_0$ ($\rho_0 \simeq 0.17$ fm$^{-3}$ is the normal nuclear matter density) can be achieved in the center of the reaction zone in these facilities [4]. The core of the neutron star may comprise of such a high density. So, valuable information can be obtained through the study of the QCD phase diagrams to that of the early universe, the core of neutron stars, collapse of massive neutron stars, collisions between neutron stars etc. Also, nucleus accounts for 99.9 percent of the mass of an atom. Therefore, protons and neutrons are responsible for the mass of the visible universe. But, the total masses of dynamic quarks of a proton and a neutron is almost 100 times smaller than the mass of a proton and a neutron. It is predicted that the heavy-ion collision experiments will also be able to explain the origin of hadron masses.

The Compressed Baryonic Matter (CBM) experiment is a future fixed-target heavy-ion experiment at FAIR at GSI, Darmstadt, Germany. It will explore the QCD phase diagram at low temperatures and high net baryon densities by colliding proton beams and heavy-ions beams to a fixed target in the energy range of $E_{lab}$ = 2-11 AGeV (in the SIS100 setup). The SIS accelerator will provide high intensity beams of protons and a wide range of ions. The research at the CBM experiment is focused on the systemetic study of rare and penetrating probes such as low mass vector mesons ($\rho$, $\omega$, $\phi$), charmonium (J/$\varphi$, open charm) etc [5]. Low mass vector measons and charmonium will be detected by their leptonic decay channels and open charm via hadronic decay channel. At FAIR energies, the production cross-sections of these probes are very small. An interaction rate of 10 MHz in CBM will only allow the detection of rare diagnostics probes with high statistics. A free-streaming data-readout and electronics will be installed to deal with the high interaction rate. Also, fast, radiation-hard detectors with high rate capabilities high rate capable are necessary to handle the huge particle densities produced in the collisions. The detector system in CBM will have the provision for measuring both the electron-positron decay channel as well as the di-muon decay channel, although they will be operated in different time periods. The different detector configurations which will be used in the di-muon configuration of CBM are: Micro-vertex Detector (MVD) and Silicon Tracking System

(STS) situated in the gap of a 1 T superconducting magnet, then Muon Chamber (MuCh), Transition Radiation Detector (TRD), Multi-Gap Resistive Plate Chamber (MRPC) for the time-of-flight measurements (TOF) and Projectile Spectator Detector (PSD) for collision centrality determination. In the di-electron configuration, MuCh will be replaced by a Ring Imaging Cherenkov Detector (RICH) [6].

A Muon Chamber (MuCh) system is being developed in India to detect the di-muon pairs originating from the rare diagnostic probes. This detector system will perform particle tracking in a broad momentum range. MuCh consists of segmented hadron absorbers and detector triplet stations in between each set of absorbers. The rate of particles on the detector surface per unit area decreases radially and downstream. For the $1^{st}$ and $2^{nd}$ MuCh stations, Gas Electron Multiplier (GEM) chambers will be used. Resistive Plate Chambers (RPCs) have been proposed as a technology option for the $3^{rd}$ and $4^{th}$ stations of MuCh. Simulation results indicate the hit rates on the 3 rd and 4 th stations of MuCh reach a maximum of 13 kHz/cm$^2$ and 4.7 kHz/cm$^2$ respectively for minimum-bias Au-Au collisions at a beam energy of 10 AGeV [7]. The RPCs in CBM, therefore, should be capable of handling these high rates for muon detection with high efficiency ($\sim$ 90 %). Several cosmic ray experiments [8, 9], neutrino experiments [10, 11] and accelerator based experiments [12, 13, 14] have incorporated RPCs for charged particle detection.

Resistive Plate Chamber (RPC) is a type of gaseous detectors invented in 1981 by R. Santanico and R. Cardarelli [15]. It utilised a constant and uniform electric field produced between two electrode plates separated by a gas gap. The electrode plates of RPC are made of materials with high volume resistivity, $\sim 10^9$ - $10^{12}$ $\Omega$ cm, usually made of high pressure laminate phenolic resin (bakelite) or glass. A thin conductive layer of paint upon the electrode plates are used for uniform application of high voltages. Small polycarbonate spacers of higher volume resistivity than that of the electrodes are used for maintaining the uniform gas gap. A gas mixture consisting of Ar, isobutane, R134a is used in RPC. A charged particle or any radiation passing through the detector causes ionization inside the gap due to the interaction with the gas and produce electron-ion pairs. These electrons are primary electrons which cause further ionization due to their acceleration in the electric field and initiate an avalanche of charge carriers. The applied electric field inside the gas gap gets distorted due to the avalanche and in turn, it effects their own movement, also further multiplication. This is known as space-charge effect [16]. Due to the movement of electrons and ions inside the gas gap, electrical signals are induced on the readout elements, which are capacitively coupled to the gap. The conductive coating on the electrodes become transparent to the induced signal due to their high surface resistivity. The readout is mounted on the surface of the electrode plates separated by an insulating material, mylar. The high-resistivity of the electrode plates made of bakelite or glass limits the discharge to a small area, allowing for high rate applications. The simple structure and low cost of material makes RPC a feasible choice for large area applications. RPCs may be operated in two modes, avalanche mode and streamer mode. The mode of operation is decided by the gas gain of the detector. The gas gain depends on the applied electric field as well as the gas mixture inside the detector. In avalanche mode, the detector operates in the limited-proportional region and the gas gain is much lower than $10^8$, the Raether limit. The development of secondary avalanches can be prevented due to the low gas-gain and only the simple multiplication of charge carriers takes place. An electron quenching gas $SF_6$ is used in the avalanche mode. When gas gain increases further, beyond the limit $10^8$, the photons generated during the recombination, excitation and de-excitation of electrons start contributing to the avalanche development. A conductive channel between the two electrode plates forms through which the discharges occur. This leads to the creation of weak sparks. A large current pulse induced by the streamers rules out the pre-amplication part of the signal, thus simplifying the readout electronics. The average charge produced in a streamer mode RPC is $\sim 100$ pC, while the value for avalanche mode RPC is typically $\sim 1$ pC. Thus sophisticated front-end electronics is necessary to process the small signal in avalanche mode of RPCs. The voltage drop ($V_d$) across the electrodes which limits the rate capability of a RPC is determined by the Ohmic model,

$$V_d = \Phi \, \rho \, t \, \langle Q \rangle \tag{1}$$

A reduction of the three detector parameters, i.e., the bulk resistivity of the electrode material ($\rho$), the total thickness of both the electrodes ($t$) and the average charge produced in the gas for each incident particle($\langle$ Q$\rangle$), can help in minimising $V_d$, thus increasing the rate capability of RPC under heavy particle flux ($\Phi$) [20]. RPCs come in various shapes, and also according to the number of gas-gaps between two electrode plates, RPCs are categorised as single-gap RPC, double-gap RPC or Multi-gap RPC (MRPC). To prevent the avalanche growth and their transition into streamers, the inclusion of resistive plates to divide the gas-gap became a best possible solution. Movement of charges in any of the gas-gaps induces signal on the metallic readout plate. Also, MRPC has very good time resolution (sub-100 ps) [21] due to the smaller fluctuation of primary ionisation position over a very narrow range inside smaller gas-gap.

This thesis aims at the development of a RPC detector proposed to be used at the $3^{rd}$ and $4^{th}$

stations of CBM-MuCh. As a part of the R&D programme, the following subjects were addressed for the aforementioned goal,

A) characterisation of different types of RPCs, i.e., single gap RPC and Multi-gap RPC with cosmic muons using conventional NIM electronics and sophisticated front-end electronics (FEE),

B) studying a low-resistive prototype RPC with different kinds of FEE, C) characterisation of a low resistive prototype RPC with high momentum muon beam in presence of high rate gamma background,

D) a detailed study about the crosstalk in RPC with different PCB and gas mixture ratios,

E) Testing of real-size RPCs for the $3^{rd}$ station of CBM-MuCh with CBM specific electronics.

A) A single-gap oil-free bakelite RPC (30 cm $\times$ 30 cm $\times$ 0.3 cm) [17] with a gas-gap of 0.2 cm was fabricated at VECC. The volume resistivity of bakelite electrodes was $\sim 9 \times 10^{11}$ $\Omega$cm and they were procured from an Indian bakelite company. The RPC was tested using an avalanche mode gas mixture ratio of R134a : Iso-butane : $SF_6$ :: 94.1 : 5.2 : 0.7 in a cosmic ray test bench at VECC using standard NIM based electronics for signal processing [18]. Copper strips of width 2.3 cm was used as the readout of the signals. The detector was able to detect cosmic muons with $\sim$ 90% efficiency at 12500 V with a noise rate of $< 1$ Hz/cm$^2$. We have operated the detector with various thresholds and the noise rate in RPC increases with voltage and decreasing threshold as per our expectation. Then, a FEE board made of NINO chip was used for testing the RPC prototype with cosmic rays. NINO is a 8-channel amplifier-discriminator chip and was first developed by CERN for the ALICE-TOF [19]. The detector was tested with different gas mixture ratios of avalanche mode and the efficiency went up to $\sim$ 88 % at 11000 V with a NINO threshold setting of 2.5 mV.

A 6-gap oil-free bakelite MRPC of outer electrode dimension 15 cm $\times$ 15 cm $\times$ 0.3 cm and inner electrode dimension 14 cm $\times$ 14 cm $\times$ 0.050 cm with each gas-gap thickness of 0.025 cm was fabricated at VECC. The MRPC was studied using the conventional NIM based electronics and with a gas mixture of R134a : Iso-butane :: 85 : 15 and achieved $>$ 85 % efficiency at 15800 V with a threshold of 20 mV and a noise rate $\sim$ 1.3 Hz/cm$^2$. The best time resolution achieved was 160 ps at 15800 V [25] using a Philip Scientific TDC module.

B) In parallel, we have systematically studied a few samples of low resistivity bakelite plates procured from Indian as well as International market. A bakelite sample procured fron an Italian company appeared to be promising. A sample RPC prototype has been made in VECC and characterised. But the linseed oil coating made in-house on the inner surface of the bakelite got accumulated and caused sparks. The current increased dramatically and the prototype couldn't recover from this situation. After this study on different bakelite samples, we procured a prototype single gap, double-layered linseed oil coated bakelite RPC ($\sim$ 30 cm $\times$ 30 cm $\times$ 0.2 cm) with a gas-gap thickness of $\sim$ 0.2 cm from an Italian Company, General Technica. The pick-up strips of 2.3 cm strip-width and 2.5 cm strip-pitch were fabricated at VECC. The volume resistivity of the bakelite sample was $\sim 4 \times 10^{10}$ $\Omega$-cm which was lower than that of the Indian bakelite sample. The prototype was tested extensively with cosmic rays using different electronics. The efficiency of the prototype RPC was measured to be $> 93$ % at 10600 V with a NINO threshold of 2.5 mV and a dark rate of 0.5 Hz/cm$^2$ with a gas mixture ratio of R134a : $iC_4H_{10}$ : $SF_6$ :: 94.2 : 4.7 : 1.1. The time resolution of RPC was found to be $\sim$ 1.2 ns at 10600 V. The TOF system at the CBM experiment is using a PreAmplifier-DIscriminator board (PADI) [22] as a self-triggered electronics for their glass MRPC detectors. We have tried characterising the RPC prototype with PADI electronics also. The efficiency plateau in this case started at 10500 V and the efficiency reached $> 93$ % in the plateau region with a dark rate of 1.1 Hz/cm$^2$ [23]. Both NINO and PADI have been developed for timing applications, time resolution of these electronics are $\sim$ 30 to 50 ps. In CBM MuCh, we need electronics having time resolution $\sim$ ns only. The GEM chambers in the $1^{st}$ and $2^{nd}$ stations of CBM-MuCh will be readout by a self-triggered front-end electronics board called STS/MuCh-XYTER [24]. The use of a common chip in the entire CBM-MuCh avoids the non-uniformity and complexity involved in using different readout systems. This, however adds a challenge to the operation of RPCs, as these will have to be operated at low gain in order to match the available dynamic range (100 fC) of the ASIC. Since MuCh-XYTER is a charge sensitive preamplifier (CSP) based electronics, we have first operated the prototype RPC with commercial CSP 142IH and conventional NIM electronics after CSP. The results were promising. The operating voltage of the detector drops down to 9900 V with a measured efficiency of 95 % with the same gas mixture ratio, R134a : $iC_4H_{10}$ : $SF_6$ :: 94.2 : 4.7 : 1.1. The charge of an average signal was measured from the CSP using MANAS [26] electronics, it can go up to 260 fC.

C) The prototype RPC was then tested in the Gamma Irradiation Facility (GIF++) beam test at CERN, Geneva, Switzerland. At GIF++, high momentum muon beam (100 GeV/c) from the H4 beamline in the SPS is being provided in the presence of an intense $^{137}$Cs source with an activity of 13.9 TBq. The prototype was operated in avalanche mode with a gas mixture of R134a: $iC_4H_{10}$ : $SF_6$ :: 95.2% : 4.5% : 0.3% coupled with a self-triggered MuCh-XYTER electronics at GIF++. In a self-triggered system, all the hit messages are stored, which crosses the set threshold. Detector performances in terms of time correlation, time resolution, muon detection efficiency, hit rate have been studied. The analysis was carried out using the time-stamps of the hits. The prototype showed a

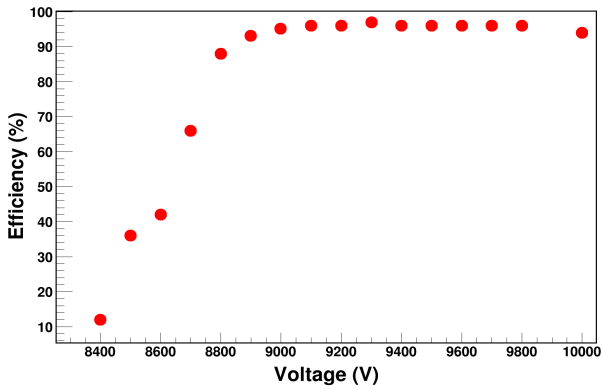


(a) Muon detection efficiency with high voltage when exposed to the muon beam alone at GIF++.

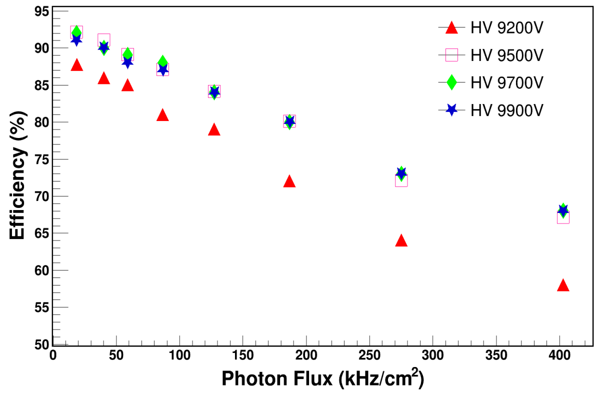


(b) Muon detection efficiency as a function of the photon flux for a range of high voltages at GIF++.

muon detection efficiency of $\sim$ 96 % with 50 fC of MuCh-XYTER photon background and the efficiency plateau started from 9000 V shown in the Fig.(a). The detector could detect muons with > 80 % efficiency in the presence of a high photon background shown in the Fig.(b). GIF++ results indicated relatively bigger ($\sim$ 3.8 strips) cluster size. Big clusters could be the result from two sources, i.e., large avalanche size or crosstalk between readout strips.

D) We have performed detailed study on the crosstalk phenomenon in RPC at VECC. We have systematically studied various PCB material consists of pads and strips with different gas mixture ratios.

E) Large size trapezoidal shaped RPCs will be used for the last two stations of the MuCh system in the CBM experiment. Real size modules for the $3^{rd}$ station, which have bases of 100.26 mm and 509.8 mm, and a height of 1161.3 mm, have been tested at VECC. The volume resistivity of the bakelite plates used here was $\sim 3 \times 10^9$ - $1 \times 10^{10}$ $\Omega$ cm and each plate thickness was 1.2 mm. The systemetic studies of the modules were done coupling with MuCh-XYTER electronics. One real size RPC module detected cosmic muons with $\sim$ 90 % efficiency at 9000 V with a gas mixture of R134a: $iC_4H_{10}$ : $SF_6$ :: 95.2% : 4.5% : 0.3% at VECC.

In summary, we have started our R&D in developing RPC for the $3^{rd}$ and $4^{th}$ stations CBM-MuCh using indigenous high resistive bakelite material. Then, we have worked with RPC made of Italian bakelite plates which have lower bulk resistivity compared to Indian bakelite samples. We have tested and characterised the detector with cosmic rays and in high irradiation photon background at GIF++, CERN, Switzerland using a self-triggered FEE MuCh-XYTER. Then real-size trapezoidal RPCs for CBM using low resistive bakelite RPC materials have been characterised with MuCh-XYTER electronics using cosmic rays.

# References


[1] D. Gross, *Asymptotic freedom and QCD: A historical perspective* , *Nucl. Phys. B. Proc. Suppl.* **135** (2004) 193.

[2] J. Bartke, *Introduction to Relativistic Heavy Ion Physics* , *World Scientific Singapore* (2008).

[3] Peter Senger and Norbert Herrmann, *Cosmic Matter in the Laboratory: The CBM Experiment at FAIR*, *Nuclear Physics News*, Vol. 28, No. 2 (2018).

[4] I. C. Arsene et al., *Dynamical phase trajectories for relativistic nuclear collisions* , *Phys. Rev. C* **75** (2007), 034902 .

[5] C. Höhne (for the CBM Collaboration), *The CBM experiment at FAIR exploring the QCD phase diagram at high net baryon sensities* ., *Int. J. Mod. Phys. E* **16** (2007) 2419.

[6] T. Balog, *Overview of the CBM detector system*, *J. Phys.: Conf. Ser.* **503** (2014) 012019.

[7] E. Nandy, *Simulation with MuCh geometry and test beam set up, 28th CBM collaboration meeting, Tübingen, 26-30 September,* (2016).

[8] G. A. Agnetta, et al., *Use of RPC in EAS physics with the COVER-PLASTEX experiment*, *Nucl. Instrum. Meth. Phys. Res. A* **381** (1996) 64.

[9] L. Lopes et al., *Resistive Plate Chambers for the Pierre Auger array upgrade*, *JINST* **9** (2014) (C10023).

[10] F. P. An et al., *The detector system of the Daya Bay Reactor Neutrino Experiment*, *Nucl. Instrum. Meth. A* **811** (2016) 133.

[11] A. Kumar et al., *RPC detector characteristics and performance for INO-ICAL experiment*, *JINST* **11** (2016) (C03034).

[12] Y. Haddad et al., *High Rate Resistive Plate Chamber for LHC detector upgrades*, *Nucl. Instrum. Meth. A* **718** (2013) 424.

[13] D. Piccolo et al., *The RPC-based IFR system at BaBar experiment: preliminary results*, *Nucl. Instrum. Meth. A* **477** (2002) 435.

[14] M. Yamaga et al., *RPC systems for BELLE detector at KEKB*, *Nucl. Instrum. Meth.* **456** (2000) 109.

[15] R. Santanico and R. Cardarelli, *Development of Resistive Plate Chambers*, *Nucl. Instrum. Meth.* **187** (1981) 377.

[16] C. Lippmann, *Space charge effects and induced signals in resistive plate chambers*, *Nucl. Instrum. Meth. Phys. Res. A* **508** (2003) 19.

[17] R. Ganai et al., *Study of Performance of Bakelite Resistive Plate Chamber (RPC)*, *Springer Proceedings in Physics.* **174** (2016) 547.

[18] M. Mondal et al., *Characterization of Prototype Oil-free Bakelite RPC for High Rate Experiments)*, *$61^st$ DAE-BRNS Symp. on Nucl. Phys.* (2016) 547.

[19] F. Anghinolfi et al., *NINO: An ultra-fast and low-power front-end amplifier/discriminator ASIC designed for the multigap resistive plate chamber*, *Nucl. Instrum. Meth. A* **533** (2004) 183.

[20] G. Aielli et al., *Improving the RPC rate capability*, *JINST* **11** (2016) P07014.

[21] I. Deppner and N. Herrmann on behalf of the CBM collaboration., *The CBM Time-of-Flight system*, *JINST* **14** (2019) C09020.

[22] H. Flemming and H. Deppe, *The GSI event-driven TDC with 4 channels GET4*, *IEEE NSS,Orlando, FL* (2009) 1082.

[23] M. Mondal et al., *Performance of a Low-Resistive Bakelite RPC Using PADI Electronics*, *Springer Proc. Phys.* **261** (2021) 1119.

[24] K. Kasinski et al., *STS-XYTER, a high count-rate self-triggering silicon strip detector readout IC for high resolution time and energy measurements*, *IEEE Nucl. Sci. Symp. Med. Imag. Conf. Rec. (NSS/MIC)* (2014) 1.

[25] R. Ganai et al., *Development and characterization of 6-gap bakelite Multi-gap Resistive Plate Chamber*, *JINST* **13** (2018) P07022.

[26] R. N. Singaraju et al., *Test setup for the readout electronics of ALICE-PMD*, *DAE symp. Nucle. Phys.*, (1999) 428-429.

## Publications in Referred Journals and Conference Proceedings:

1. Rajesh Ganai, **Mitali Mondal**, Shaifali Meheta, Zubayer Ahammed and Subhasis Chattopadhyay, *Development and characterization of 6-gap bakelite Multi-gap Resistive Plate Chamber*, Journal of Instrumentation **13**, (2018) P07022.

2. **Mitali Mondal**, Tanay Dey, Subhasis Chattopadhyay, Jogender Saini, Zubayer Ahammed, *Performance of a prototype bakelite RPC at GIF++ using self-triggered electronics for the CBM Experiment at FAIR*, Communicated at Nucl. Inst. Meth. Phys. Res. A.

3. **Mitali Mondal**, Rajesh Ganai, Zubayer Ahammed and Subhasis Chattopadhyay, *Characterization of Prototype Oil-free Bakelite RPC for High Rate Experiments*, Proc. DAE Symp. Nucl. Phys. **61**, (2016) 946-947.

4. **Mitali Mondal**, Rajesh Ganai, Chandan Barai, Jogender Saini, Zubayer Ahammed and Subhasis Chattopadhyay, *Testing of a Resistive Plate Chamber using NINO-ASIC based Front End Electronics*, Proc. DAE Symp. Nucl. Phys. **62**, (2017) 1024-1025.

5. **Mitali Mondal**, Jogender Saini, Zubayer Ahammed and Subhasis Chattopadhyay, *Performance of a Low Resistive Bakelite RPC using PADI Electronics*, Springer Proc. Phys. **261**, (2021) 1119-1123.

6. Rajesh Ganai, **Mitali Mondal**, Zubayer Ahammed and Subhasis Chattopadhyay, *Development of 6-gap Bakelite Multigap Resistive Plate Chamber*, Springer Proc. Phys. **203**, (2016) 129.

7. Rajesh Ganai, **Mitali Mondal**, Zubayer Ahammed and Subhasis Chattopadhyay, *Timing Studies of Bakelite Multi-gap Resistive Plate Chamber*, Nucl. Inst. Meth. Phys. Res. A. **936**, (2019) 505-506.

8. Rajesh Ganai, **Mitali Mondal**, Mehul Kumar Shiroya, Zubayer Ahammed and Subhasis Chattopadhyay, *Performance Studies of Bakelite Multi-gap Resistive Plate Chamber with Cosmic Rays*, Journal of Instrumentation **14**, (2019) C06010.

9. Ekata Nandy, **Mitali Mondal**, Rajesh Ganai, Zubayer Ahammed, and Subhasis Chattopadhyay, *Feasibility Study of Using RPCs in CBM Muon Chamber*, DAE-BRNS Symp. Nucl. Phys. **61**. (2016) 1024.

**Signature of Student:** Mitali Mondal

**Date:** 27/07/2021

The Doctoral Committee recommends submission of Ph. D. thesis by Mitali Mondal.

## Doctoral Committee:

| S. No. | Name | Designation | Signature | Date |
|---|---|---|---|---|
| 1. | Dr. Paramita Mukherjee | Chairman | P. Mukherjee | 27/7/21 |
| 2. | Dr. Subhasis Chattopadhyay | Guide/Convener | [illegible] | 27/7/21 |
| 3. | Dr. Gopal Mukherjee | Member 1 | Gopal Mukherjee | 27/07/21 |
| 4. | Dr. Tilak Ghosh | Member 2 | T. Ghosh | 27/7/21 |
| 3. | Dr. Saikat Biswas | Member 3 | Saikat Biswas | 27/7/21 |

# Chapter 1

# Introduction to the physics of high energy heavy-ion collisions

## 1.1 Introduction

### 1.1.1 The Standard Model of Particle Physics

The Standard Model (SM) [1,2] of particle physics is the best understanding at present to describe the elementary particles in nature and the interactions among them. Developed in the early 1970, SM classifies almost all of the fundamental particles and describes three among the four fundamental forces in nature, named the strong, electromagnetic and weak force. The fourth force, gravity, can not be explained by SM. The gravitational force is weakest among four fundamental forces in the microscopic level and becomes dominant in the astronomical scale. Einstein's general theory of relativity governs the gravitational force and attempts to combine it with SM are ongoing. The particles covered under the SM are summarised in Fig. 1.1. They are classified into two types, fermions with half-integer spin and bosons with integer spin. There are further subdivision of fermions into quarks and leptons. Also, bosons are subdivided into gauge bosons with spin 1 and scalar bosons with spin 0. Quarks can have six different flavours, up (u), down (d), strange (s), charm (c), beauty (b) and top (t). There are six leptons in nature, electrically charged electron (e), muon ($\mu$), taon ($\tau$) and their chargeless neutrino partners, electron-neutrino ($\nu_e$), muon-neutrino ($\nu_\mu$) and taon-neutrino ($\nu_\tau$) respectively. The fermions form a family of three generations according to similar properties in nature. Each generation consists of two quarks, one

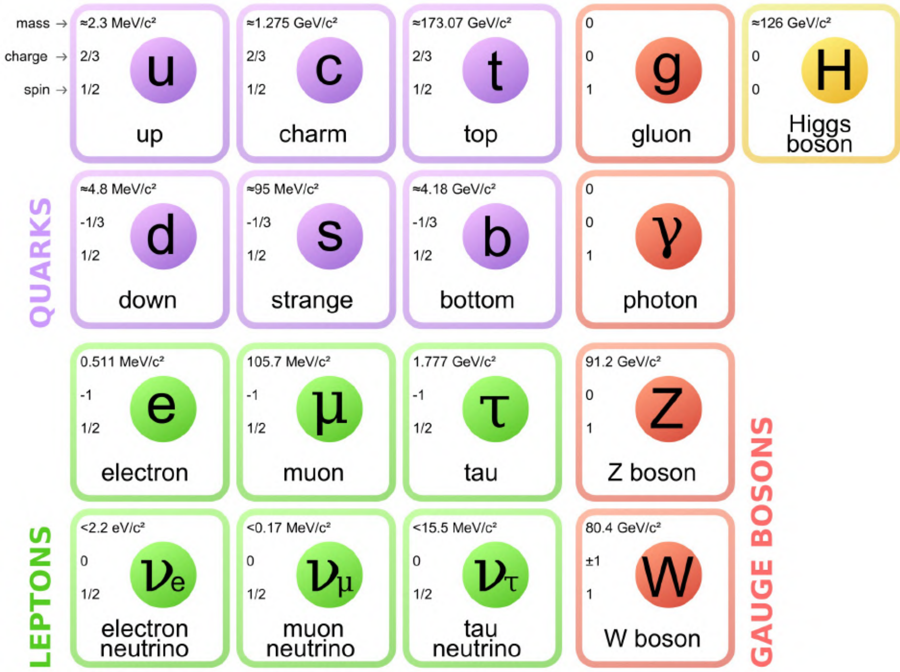


Figure 1.1: Schematic depiction of elementary particles in the Standard model. [3].

charged lepton and its corresponding neutrino. The first generation quarks u and d construct all the ordinary matter around us, which along with the second generation s quark are known as light quarks. The charm quark from the second generation alongwith the beauty and the top quarks which from the third generation are the heavier versions of the first generation quarks, known as heavy quarks. Heavy quarks are unstable in nature. For each of the quarks and leptons, there exists an anti-particle with same mass and spin, but different quantum numbers.

The fundamental interactions take place between fermions, which are matter particles themselves via the exchange of gauge bosons. These gauge bosons are also known as mediators. SM is based on a local Quantum Field Theory (QFT) where the three fundamental interactions, electromagnetic, weak and strong, are described by different gauge groups and different mediators.

**Weak Interaction:** The mediators of the weak interaction are massive $W_{\pm}$ and $Z_0$ bosons. Due to the massive carriers, the range of this interaction is very small, $10^{-18}$ m, smaller than the size of a nucleus. Weak interaction is described with the gauge symmetry group SU(2) [4] and is the only interaction capable of changing quarks flavour. All fermions interact via this interaction. The weak interaction is divided into charged current and neutral current mediated by W boson and Z boson respectively. The charged current can convert a heavier fermion to a lighter one while the neutral current is involved in the scattering process.

**Electromagnetic Interaction:** All electrically charged particles interact through electromagnetic interaction and it is described by the Quantum Electro-Dynamics (QED). The mediator of this interaction is photon, a chargeless and massless boson. Due to the zero rest mass of photon, the electromagnetic interaction has an infinite range. As there is a single gauge boson and single quantum number, electromagnetic charge Q, the electromagnetic interaction is defined by a U(1) symmetry group.

**Strong Interaction:** The strong interaction is described by Quantum Chromodynamics (QCD). This interaction is associated with the SU(3) symmetry group with colour charge [**?**]. The mediator of this interaction is massless gauge boson called gluon. Quarks have colour charge, so they interact via gluons. The strong interaction acts only at small distances, on the order of $10^{-15}$ m and dominates over all the other interactions.

During the 1960s, Sheldon Lee Glashow, Abdus Salam, and Steven Weinberg independently proposed a theory which unified the electromagnetic interaction and the weak interaction, known as the Electro-Weak theory. The theory is explained by the unified gauge group, SU(2) $\times$ U(1). The spontaneous electro-weak symmetry breaking through the Brout-Englert-Higgs mechanism gives rise to the masses of weak-gauge bosons and a scalar particle called "Higgs Boson". Peter Higgs in 1964 predicted that fundamental particles (except neutrinos) get their masses during the interactions with the Higgs boson [5]. The Higgs Boson was discovered in 2012 by the LHC experiments CMS and ATLAS at CERN [6–8], which led to the winning of the Nobel prize in Physics 2013 by François Englert and Peter W. Higgs. The Higgs doesn't have any effect on the electromagnetic field leading to the zero rest mass of photon and the symmetry group U(1) is unbroken due to this [9].

### 1.1.2 Quantum Chromodynamics

QCD [10] is a non-Abelian gauge theory which explains the strong interactions between quarks and gluons [11]. It obeys the rules of gauge symmetry group SU(3). QCD is analogous to the theory of electromagnetic interaction, Quantum Electrodynamics (QED) [12] which is mediated by photons. Each quark can have three color charge states, red (r), green (g), blue(b). The color charge in QCD is analogous to the electric charge in QED. Although color charge is a vector quantity unlike the electric charge which is scalar quantity. The mediator of strong interaction, gluons also carry a color and anti-color charge. Therefore gluons can self-interact. As photon does not possess any electric charge, it doesn't interact with itself. This is an essential difference between QCD and QED. There are eight types of gluons in QCD. The self-interaction of gluons is a consequence of the non-Abelian nature of color symmetry. It can also describe the way to form a colour neutral state. A quark and anti-quark can form a color-neutral state, known as meson. Also, a color neutral state, baryon is formed by three quarks with three different color states. Exotic hadrons like tetra-quark are also color neutral states. The potential difference between two quarks separated by a distance r is represented in QCD as [13],

$$V_s(r) = -\frac{4\alpha_s}{3r} + kr \tag{1.1}$$

where $\alpha_s$ is the coupling constant for strong interaction and k is a spring constant with a magnitude $\sim$ 1 GeV/fm. The second term of the above equation dominates at large distances (> 1 fm), thus the potential energy increases linearly as quarks go further apart. If enough energy can be provided to pull apart quarks, it would be enough to form new color neutral particles such as $q\overline{q}$ out of QCD vaccum. Hence, free quarks do not exist in nature. This is known as "quark confinement". They exist inside the color neutral bound states of hadrons, like protons, neutrons, baryons, mesons. At short distances (r < 1 fm), the potential energy between quarks is dominated by the first term in the equation. At short distances, the coupling constant ($\alpha_s$) of the strong interaction depends on the momentum transfer ($Q^2$) between quarks and also on the distance between them. A large value of $Q^2$ correlates with high energy and small distance between quarks. At r $\rightarrow$ 0 (large $Q^2$), the interaction between quarks vanishes and they behave as free particles. This phenomenon is known as "Asymptotic Freedom". It allows the perturbative calculation of QCD.

### 1.1.3 QCD Phase Diagram

The different states of the QCD matter can be depicted in a diagram, called phase diagram, between temperature vs baryo-chemical potential ($\mu_B$), defined as the derivative of entropy with respect to the net baryon number in thermodynamical region, shown in Fig. 1.2. The energy

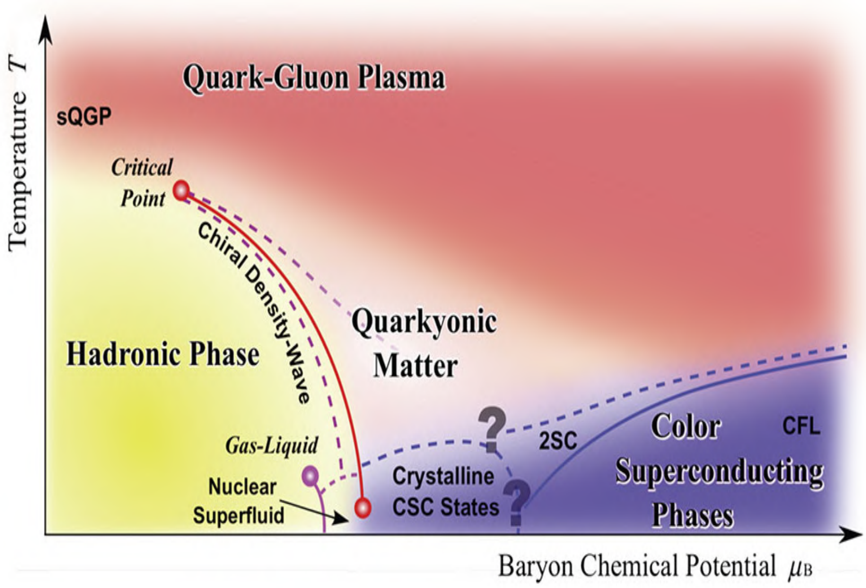


Figure 1.2: Phase diagram (temperature, Baryo-chemical potential ($\mu_B$)) of QCD matter, ranging from the regular nuclear matter to the Quark-Gluon Plasma [14].

required to include one baryon to the system is interpreted as $\mu_B$ and it is connected to the baryon density as $\mu_B = (\mathrm{n_q} - \mathrm{n_{\overline{q}}})/3$, where $\mathrm{n_q}$ and $\mathrm{n_{\overline{q}}}$ are the quark and anti-quark number densities, respectively. The phase diagram is mainly divided into two regions, one is hadron gas and another is Quark Gluon Plasma. The region at low T and low $\mu_B$ in the phase diagram consists of ordinary nuclear matter where the quarks and gluons are bound inside the colour neutral hadrons. At T = $\mu_B$ = 0, the vacuum exists. At high energy densities, the property of Asymptotic freedom represents a deconfined state of quarks and gluons in the medium, which is defined as the Quark Gluon Plasma (QGP). QGP state can be formed by increasing the temperature and/or increasing the $\mu_B$ (net baryon density). A smooth crossover phase transition from the hadronic phase to the QGP phase at a very high temperature (T $\sim$ 160 MeV) and vanishing $\mu_B$ is predicted by the Lattice QCD [15]. In the beginning of the universe, a hot and dense soup of QGP phase existed after a few microseconds of the Big Bang. At high $\mu_B$ and moderate T, a first order phase transition from hadronic gas to QGP state is predicted [16]. The core of a neutron star is expected to have this kind of QGP due to the gravitational collapse. These two kinds of phase transitions from hadronic to partonic matter converge at a critical point in the phase diagram. At the critical point, physical parameters are expected to be strongly fluctuating. A new exotic phase called Quarkyonic matter [17] is assumed to be present beyond the first order phase transition which has properties of both high density baryonic matter and deconfined quark matter. A triple point would form for these three phases, hadronic matter, quarkyonic matter and QGP [18]. At low temperature and extremely high $\mu_B$, quarks form Cooper pairs that condensate analogous to the electrons in a metal due to superconductivity. This phase is named as color superconducting phase (CSC) [19, 20] due to the local colour symmetry breaking and analogy to the superconductivity in metal. The colour superconducting phase is experimentally inaccessible at the present case scenario in the laboratory. At high $\mu_B$, the diquark state comprise phases of different quantum number structures where color degree of freedom couples strongly with flavor degree of freedom in Colour Flavour Locked (CFL) phase.

There is another phase transition that is directed in the conventional nuclear phase. At low temperature and $\mu_B$, matter is confined to hadrons. Hadrons consist of nucleons which are bound inside the atomic nuclei. The ground state of matter is in the liquid phase at T = 0. As the temperature increases, nuclear binding forces are incapable to bind the nucleons inside the nucleus. At this stage, a phase transition of matter from the liquid to the gas phase takes place.

The chiral phase transition [21] is another kind of phase transition which is supposed to occur in the QCD phase diagram. The QCD Lagrangian is symmetric in the limit of vanishing quark masses, which is defined as the chiral symmetry. A massless quark can be right-handed (spin in the direction of motion) or left-handed (spin in the opposite of the direction of motion). In Quantum Field Theory, the chirality or handedness of a quark is Lorentz invariant since a massless quark travels at the speed of the light [22]. Chiral symmetry is spontaneously broken in nature due to the finite quark mass confined inside the hadrons. At high temperature and/or at high net baryon density, due to the deconfinement of quarks, their masses become nearly zero. Hence, the spontaneously broken chiral symmetry is predicted to be restored in the QGP phase. Also, the chiral phase transition and the deconfined phase transition may not be necessarily equivalent. The mass of a hadron composed of light quarks is a matter of intense investigations in the nuclear physics research. A hadron is much heavier than the sum of masses of its constituent quarks. The study of chiral phase transition at extreme conditions of nuclear matter might reveal the mystery of the origin of hadron masses.

The exploration of the QCD phase diagram under extreme conditions can provide valuable information regarding the early stage of universe, the interior of neutron star and the origin of hadron masses via the chiral symmetry restoration.

### 1.1.4 Experimental Investigation of QCD Phase Diagram

Relativistic heavy-ion collision experiments provide us the unique opportunity to investigate the certain regions of the QCD phase diagram and to study the QCD matter at extreme conditions. In heavy-ion collisions, the matter at extreme conditions, i.e, strongly compressed and heated, gives rise to the formation of a fireball with a volume of a few tenth of $fm^3$ and lifetime in the order of fm/c only. The energy density of the system should be sufficiently high to reach a thermal equilibrated QGP phase. The system expands and cools down due to the high internal pressure. Quarks and gluons start to get confined inside hadrons at critical temperature $T_C$. The process is defined as hadronisation. During hadronisation, inelastic collisions between the hadrons occur until the chemical freeze-out commences. Particle production stops at this point, thus the particle yield and ratios change only due to decays after the chemical freeze-out. The thermal freeze-out sets in after the system cools down further and elastic scattering stops, kinematics is fixed, i.e, particle momenta doesn't change any further. Fig. 1.3 depicts the evolution of heavy-ion collision. Two different kinds of heavy-ion collision experiments probe different regions of the phase diagram, one is collider experiments and another is fixed-target experiments. In the collider experiments, two heavy-ion beams are accelerated and then brought to collision. In the fixed-target experiment, heavy-ion beam is accelerated and collided to a static object. The main difference between these two kind of experiments is that a large value of centre of mass energy ($\sqrt{s_{NN}}$) is achievable in collider experiments than that in the fixed-target experiments. The lumionisity of collision is higher in a fixed target experiment than that in a collider one. The first nucleus-nucleus collision experiment to explore the properties of QCD matter started at BEVALAC at the Lawrence Berkeley National Laboratory (LBNL) in Berkeley, USA with the Bevatron [24] and at the Joint Institute for Nuclear Research (JINR) with Nuclotron in Dubna in 1970s and early 1980s at fixed target

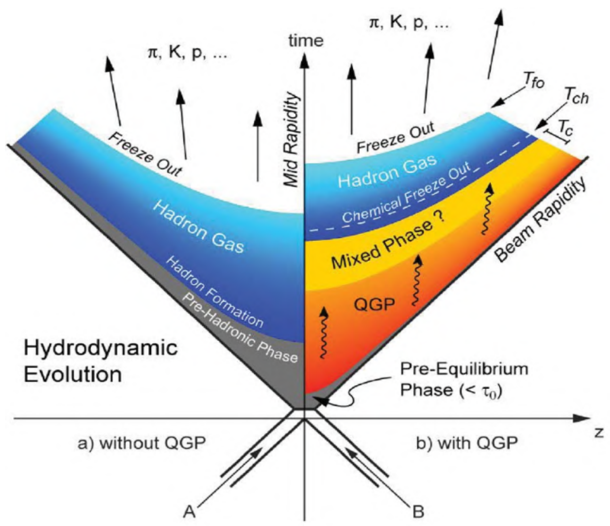


Figure 1.3: The evolution of the fireball produced in a relativistic heavy-ion collision is shown schematically in the light cone picture. The pre-equilibrium partonic phase, thermalized quark-gluon plasma, hadronization and its subsequent freeze out are the phases which unfold as the time progresses [23].

energies ranging up to 2 GeV per nucleon (AGeV). Shortly thereafter, a fixed target experiment up to energies of 2 AGeV has been carried out at Schwerionen-Synchrotron (SIS18) accelerator at GSI Helmholtz Centre for Heavy-Ion Research in Darmstadt, Germany. Although, the energies in these experiments were insufficient to reach the deconfinement region of the QCD phase diagram, they have studied in detail the production of pions and strange particles, and discovered the collective flow of nucleons. By the early 1990s, the experiments are continued at the Alternating Gradient Synchrotron (AGS) at Brookhaven National Laboratory (BNL), where Au-Au nuclei collided with energies between 2 AGeV and 11 AGeV, and at the CERN Super Proton Synchrotron (SPS), where Pb-Pb nuclei with energies between 10 AGeV to 160 AGeV were collided with a fixed target. Enhancement of the yield of strangeness and the suppression of charmonium were the first signatures of QGP phase transition. The first collider experiment for heavy-ion collision was the Relativistic Heavy-Ion Collider (RHIC) at BNL which investigated the collisions of gold nuclei at the top center of mass energy of $\sqrt{s_{NN}}$ = 200 GeV. Much higher centre of mass energy (TeV range) has been achieved at Large Hardon Collider (LHC) at CERN (Pb-Pb collisions : $\sqrt{s_{NN}}$ = 2.76 TeV in 2010-2011 and $\sqrt{s_{NN}}$ = 5.02 TeV in 2015 and in 2018, Xe-Xe collisions : $\sqrt{s_{NN}}$ = 5.44 TeV in 2017). With increasing energy, signatures of the formation of the QGP phase were observed at very high temperature and low $\mu_B$. The collision trajectory as calculated by a 3-fluid

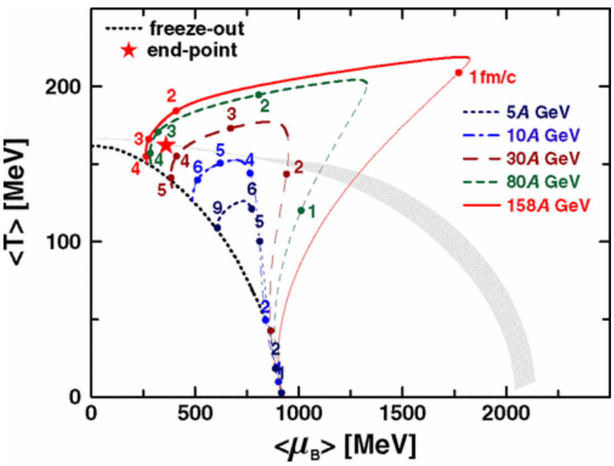


Figure 1.4: The dynamical trajectories for central Pb+Pb collisions in the plane of T versus $\mu_B$ for incident energies from 5 AGeV to 158 AGeV calculated with a 3-fluid hydrodynamics model. Different areas in the phase diagram are covered by the trajectories at different energies. Bold parts of the trajectory lines indicate thermalized baryon-rich nuclear system at equilibrium, while the thin lines represent the pre-equilibrium phase of the collision. The phase transition boundary from the hadronic phase to the QGP is represented by the light-grey shaded area. Dotted line is the experimental freeze-out curve. The critical end-point predicted by the lattice QCD calculations is denoted by the star symbol. The numbers written next to the trajectories correspond to time steps in fm/c in the centre of mass frame of the colliding nuclei. The system at very high energies enters regions of extremely high $\mu_B$ very rapidly, but also reaches the freeze-out at relatively low $\mu_B$ in very short time. On the other hand, at lower energies, the system remains longer in the QGP phase and freezes out at larger $\mu_B$ [25].

hydrodymanics model [25] on the T-$\mu_B$ plane is illustrated in Fig. 1.4 for central collisions of two Pb nuclei at incident energies ranging from 5 AGeV to 158 AGeV. It is not possible to create a fireball at high net baryon densities during collision at RHIC and LHC energies since the nuclei become transparent and the colliding nuclei only deposit partial energy before leaving the interaction zone. Also, the system hadronize at very short duration at higher energies, while a QGP phase for a longer duration is expected at lower energies. At low CERN-SPS or FAIR energies, the net-baryon density ($\rho_B$) at freeze-out attains the maximum value according to a theoretical calculation of particle yields estimated in heavy-ion collisions. The calculations indicate, that total energies between $\sqrt{s_{NN}}$ = 6 AGeV and 10 AGeV which corresponds to beam energies between 30 AGeV and 40 AGeV for fixed target experiments are best-suited for creating the maximum net-baryon density in the laboratory [9]. Therefore, heavy-ion collisions at moderate beam energies are feasible to search for the important milestones in the QCD phase diagram at high net baryon densities, like, the critical end point, the predicted first order phase transition and chiral phase transition. Several existing and planned experiments are focused on operating at moderate beam energies to explore the high $\mu_B$ region of the QCD phase diagram : the "Beam Energy Scan (BES)" programme at STAR and PHENIX collaborations at RHIC [26] and NA61/SPINE experiment at SPS [27], HADES at SIS18 [28], the heavy-ion collider experiment Multi-Purpose Detector (MPD) at Nuclotron-based Ion Collider fAcility (NICA) at JINR [29] and the fixed-target experiment Baryonic Matter at Nuclotron (BM@N) at NICA-Nuclotron at JINR [29]. Apart from beam energy, interaction rate and beam luminosity play a major role in the investigation of QCD matter at high $\mu_B$ which limits the above-mentioned experiments. Bulk observables can be mea-

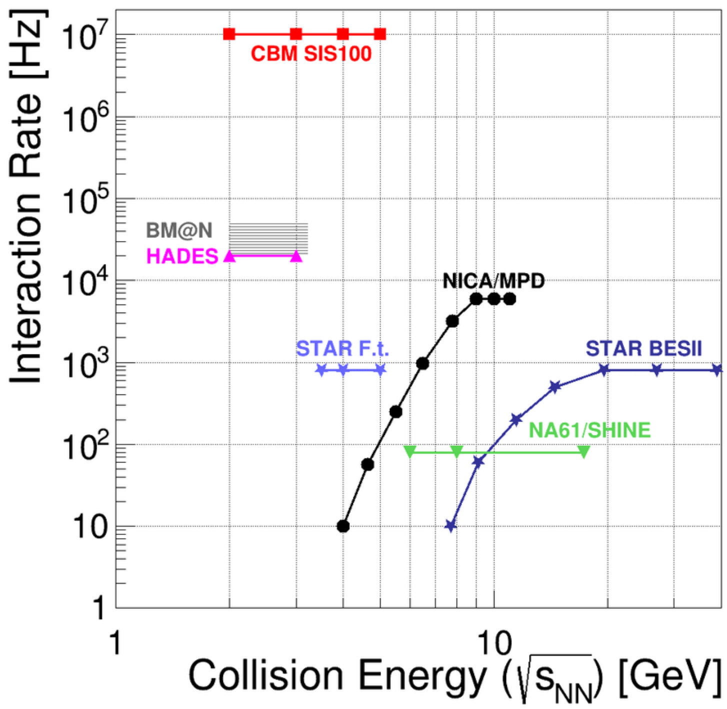


Figure 1.5: Interaction rates as a function of the center-of-mass energy achieved by existing and planned heavy-ion experiments dedicated to the exploration of the phase diagram of strongly interacting matter at high net baryon densities [30–33]. The fixed-target operation of STAR is denoted by "STAR F.t.". Some conceptual stages high-rate experiments are also proposed at JPARC [34] and at SPS [35].

sured in these experiments, but rare probes which carry the information of early phases of fireball evolution like the particles $\phi$ , hyperons ($\Omega$, $\Xi$ ,$\Sigma$, $\Lambda$), $J/\psi$, D have mostly not been measured yet at lower energies. Fig. 1.5 shows the interaction rate for existing and future heavy-ion collision experiments. The Compressed Baryonic Matter (CBM) experiment at the future Facility for Anti-proton and Ion Research (FAIR) will study systematically the bulk observables as well as rare diagnostic probes with high statistics at high interaction rate (upto 10 MHz). Instead of a single observable, the nature of QGP and the phase transitions at high baryon densities could be revealed by a combination of multiple observables. A set of physics observables in the of relativistic heavy-ion collisions at high baryon density and moderate temperature have been discussed below.

### Collective Flow

The directional distribution of particles, their energies and momenta are referred as the "collective flow". Pressure gradient inside the early fireball causes the collective flow of hadrons. Thus it becomes sensitive to equation of State (EOS) of nuclear matter at high nuclear density. The collective flow is measured via the Fourier expansion of the azimuthal distribution of final state hadrons, and proportional to $(1 + \mathrm{v1} \cos \phi + \mathrm{v2} \cos 2\phi + \ldots)$, where the Fourier coefficients v1 and v2 are interpreted as directed (in-plane) flow and elliptic flow respectively and $\phi$ is the azimuthal angle relative to the reaction plane. The initial pressure of the system is reflected by the strength of the elliptic flow which is defined as a function of transverse momentum for different particle species [36]. According to RHIC data, it has been observed that the elliptic flow co-efficient shows a scaling behaviour with the number of constituent quarks of hadrons irrespective of the quark flavours, not with the hadron masses thereby reflects a partonic collectivity. The scaling however breaks at LHC energy. The CBM experiment will test this scaling in the low energy region. Directed flow gets strongly influenced by the softest region in the EOS when the density becomes less sensitive to the change in pressure. The disappearance of directed flow is predicted to be a signature of the first order phase transition at high net baryon density [37–39].

### Multi-strange hyperons

Multi-strange hyperons ($\Lambda$, $\Xi$ and $\Omega$) i.e. baryons which consist of more than one strange quark are important observables of the excited medium created in relativistic heavy-ion collisions. The reaction products which contain $s$ and $\bar{s}$ quarks must be created during the collision since the participant nucleons in a heavy-ion reaction do not carry any strangeness. Multi-strange hyperons at the top SPS energies appear to be produced in chemical equilibrium. During hadronization, multi-particle collisions drives the equilibration near the phase boundary in the high particle density regime [40,41]. It has been interpreted as a strong indication for a phase transition from a partonic phase to the hadronic final state. In Au+Au collisions at 6 AGeV energy in AGS, only about 300 $\Xi^-$ hyperons have been measured which is statistically very poor [42]. The measured yield of $\Xi^-$ hyperons in Ar + KCl collisions at SIS18 energies ($\sqrt{s_{NN}} = 2.61$ GeV) from the HADES experiment exceeds by about a factor of 20 from the statistical model prediction. This is an indication that $\Xi^-$ is far off chemical equilibrium [43]. Thus a different chemical freeze-out condition is possible to exist for strange hyperons at sub-threshold energies compared to that of bulk hadrons. Due to the lack of data of $\Xi^-$ yields at SIS-100 energies, this finding cannot be attributed to a specific phenomenon. Also, no statistically relevant experimental data exists on the sub-threshold production of $\Omega$ and anti-$\Omega$ baryons exist below $\sqrt{s_{NN}} = 8.9$ GeV [44]. A systematic high-precision measurement of multi-strange hyperons in relativistic heavy-ion collisions at SIS100 energies would shed more light on the the impact of deconfinement and chiral symmetry restoration in QCD matter at high net-baryon densities [45]. According to the transport model calculations, which do not feature a partonic phase, strangeness exchange reactions involving kaons and lambdas are the main sources of the production of muti-strange hyperons [46, 47]. In elementary collisions, at lower energies close to or even below the production threshold, these sequential collisions are more prevalent. Therefore, the yield of multi-strange hyperons is associated to the fireball density and hence, sensitive to high density EOS. Therefore, for the exploration of high density nuclear matter EOS, a systematic study of multi-strange (anti-) hyperons production for different nuclei-nuclei collisions and different beam energies will be carried out at CBM experiment at FAIR.

### Vector Mesons

In-medium properties of hadrons i.e., mass, width or in general the hadron spectral function get modified as an effect of the chiral symmetry restoration in the QGP phase [48]. The information regarding the modified hadron properties in the medium can be accessed by the dileptonic decay channels of short-lived vector mesons ($\rho$, $\omega$, $\phi \rightarrow e^+ + e^-$ and $\rho$, $\omega$, $\phi \rightarrow \mu^+ + \mu^-$). Dileptons are very important probes for heavy-ion collision due to their distinctive feature of being emitted throughout the evolution of the fireball. Since leptons interact only electromagnetically with the particles in the collision medium, undistorted information about all phases of the fireball evolution can be provided by them. Among all of the vector mesons, $\rho_0$ mesons have shortest lifetime. Therefore, the probability of decaying into dileptons in the medium for $\rho_0$ mesons is higher, while $\omega$ and $\phi$ mesons are more likely to decay outside after penetrating the fireball at moderate momenta. The mass distribution of the vector meson at the instant of decay can be determined by the invariant-mass spectra of the lepton pairs. It is quite a challenge to extract the pure dilepton invariant-mass spectra from the vector mesons due to their small multiplicities and branching ratios to dilepton pairs, and the large physical background. The average temperature of the dense fireball can be measured from the slope of the invariant mass distribution of dileptons between 1 and 2.5 GeV/$c^2$ [49]. It will also indicate the onset of deconfinement and the location of the critical endpoint. The disentanglement of the early partonic phase from the late hadronic phase is also possible from the measurement of the flow of dileptons as function of their invariant mass [50, 51]. No di-lepton data from heavy-ion collision is available in the beam energy range between 2 AGeV and 40 AGeV [52]. Therefore, the CBM experiment will measure the invariant-mass spectra of dileptons emitted from the dense phase of the fireball at FAIR energies which is of great importance for heavy-ion physics.

#### Open and Hidden Charm

Particles containing charm quarks act as a probe for the entire process of fireball evolution due to their production at the very first stage of reaction [53]. c$\bar{c}$ pairs are formed by the hard processes at the CBM energies in the heavy-ion collisions due to the large mass of charm quarks and then hadronize into D mesons (a bound state of a light quark and a heavy c quark denoted as open charm ), charmed baryons (baryons made of at least one charm quark), or charmonium (a bound state of c$\bar{c}$ ) depending upon their interaction with the medium. As c$\bar{c}$ pairs are produced back-to-back, their probability to hadronize in open charm mesons is greater than in charmonia. Depending upon the state of the medium, i.e, partonic/hadronic medium, the charm quarks/open charm hadrons exchange momenta with the medium during the fireball evolution. Therefore, few important diagnostic probes of the early stage of collision are momentum distributions, correlations, and elliptic flow of open charm hadrons. Due to Debye screening, gluons produced in the partonic phase will screen c and $\bar{c}$ quark. Therefore, the suppression of charmonium production has been predicted as a signature of QGP formation [54]. At NA50 experiment with Pb+Pb collision, the ground state of charmonium or known as hidden charm, J/$\psi$ suppression has been first observed at

158 AGeV [55]. Then, the effect was also observed in RHIC [56] and LHC [57] experiments. There is no experimental data available at beam energies below 158 AGeV on open and hidden charm production in heavy-ion collisions. Therefore, the CBM experiment has a unique opportunity to fill this gap and study the charm production at production threshold, $J/\psi$ suppression with high statistics.

### Event by Event Fluctuations

Event-by-event fluctuations of conserved quantities such as electrical charge, baryon number, strangeness, particle yields, ratios, or kinematic properties serve to probe the existence of the state of partonic matter in early stage of the fireball if we omit the contribution from statistical fluctuations and volume fluctuations [58]. Since the fluctuations in a thermal system are related to various susceptibilities [59], it can provide insight into the properties of matter created in high-energy nuclear collisions and possible phase transitions. According to the Lattice QCD, higher moments of the distributions are very sensitive to the phase transitions and to the proximity of the critical end point [52]. No data of the higher-order moments of the event-by-event distributions at SIS100 energies are available until now. For the first time in history, in order to search for the QCD critical point and the first order phase transition at the high net-baryon density region, the CBM experiment will perform a high-precision study of higher-order fluctuations at SIS-100 beam energies [52].

### Hypernuclei and strange objects

The hyperons ($\Lambda$, $\Sigma$, $\Xi$, $\Omega$) produced in high energy heavy-ion collisions get captured by the nuclei in addition to protons and neutrons and then the nuclei is termed as hypernuclei. The information about the hyperon-nucleon and hyperon-hyperon interactions will be provided by the discovery of (double-)$\Lambda$ hypernuclei and determination of their lifetimes. The understanding of the high density EOS and neutron star core depends on these interactions. Theoretical models predict that the yield will be maximum at the CBM energies for the single and double hypernuclei, strange dibaryons and heavy multi-strange short-lived objects (composite states with multiple units of strangeness) which are generated via coalescence in heavy-ion collisions. Available beam energies at CBM give rise to an unique possibility to address some fundamental scientific questions like the existence of strange matter in the form of heavy multi-strange objects, the extent to which the chart of nuclei can be extended towards the third (strange) dimension by producing single and double hypernuclei [60].

# Chapter 2

# The Compressed Baryonic Matter (CBM) Experiment

Among the four scientific pillars of the future accelerator Facility for Anti-proton and Ion Research' (FAIR), Compressed Baryonic Matter (CBM) experiment is a dedicated fixed target heavy-ion experiment with the goal to explore the QCD phase diagram in the region of moderate temperatures but very high net-baryon densities, realized in nature at the core of the neutron stars [61]. In laboratory, densities compared to that at the core of neutron star can be produced for a time span of about 5–10 fm/c in heavy-ion collisions at FAIR energies. The experimental observables, specially the rare probes which are to be measured at CBM, have very low production cross-section. Therefore, the CBM experiment is designed to measure these observables precisely with high statistics at an unprecedented collision rates upto 10 MHz. The experimental challenge of CBM experiment is to combine a large-acceptance fast detector system and a free streaming read-out electronics with high-intensity beams provided by the FAIR accelerators. The required interaction rate can be achieved by adjusting the target thickness property.

## 2.1 The Future Facility for Antiproton and Ion Research (FAIR)

FAIR is an international accelerator facility under construction at the existing site of the GSI Helmholtz Centre for Heavy Ion Research in Darmstadt, Germany for fundamental physics research [62]. It will provide unique research opportunities in the fields of nuclear & hadron physics, atomic & nuclear astrophysics, materials research, plasma physics and radiation biophysics [63]. The layout of the FAIR facility is illustrated in Fig.2.1. The facility consists of a double ring syn-

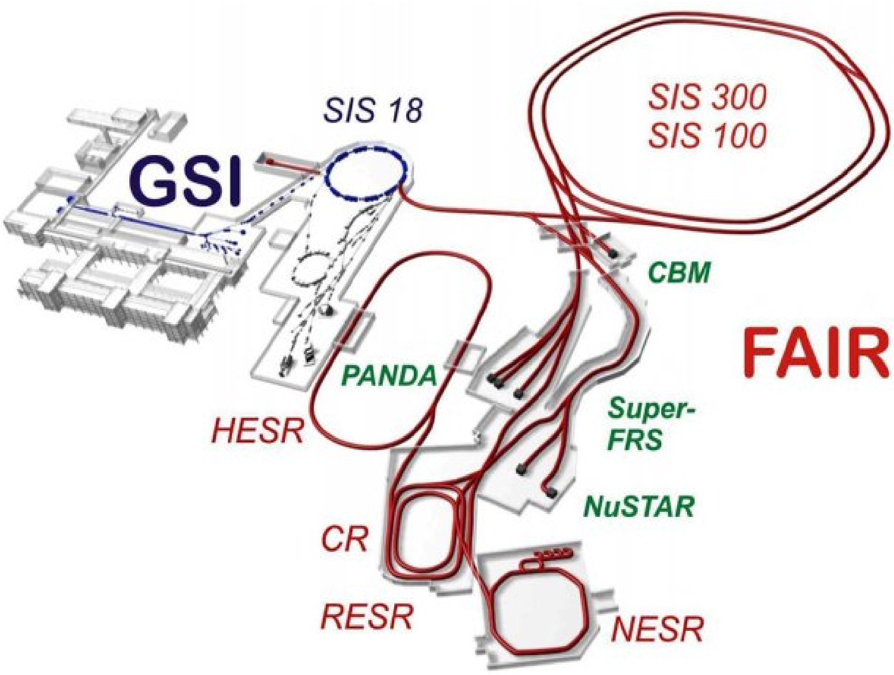


Figure 2.1: Layout of the existing (SIS18) and planned Facility for Antiproton and Ion Research (FAIR), the superconducting synchrotrons SIS100 and SIS300, the collector ring CR, the accumulator ring RESR, the new experimental storage ring NESR, the super fragment separator Super-FRS, the antiproton production target, and the high energy storage ring HESR. New accelerator and storage rings are highlighted in red, experimental sites are indicated with green letters [64].

chrotron facility SIS100/300 with five times the circumference of the existing facility SIS18, rings for accumulation, cooling and storage of primary and secondary beams, and dedicated detector setups. The injectors for the new facility will be the upgraded existing GSI accelerators UNILAC (Universal Linear Accelerator) and SIS18. The Magnetic rigidities of the future SIS100 and SIS300 synchrotrons are 100 Tm and 300 Tm, respectively. In the present version of constructions even thousands tunnel will be built for both SIS100 and SIS300, only SIS100 accelerator will be built for the modularized start version (MSV) of the project. The four scientific pillars of the FAIR research programme are: APPA (Atomic, Plasma Physics and Applications), CBM (Compressed Baryonic Matter experiment), PANDA (anti-Proton ANnihilation at DArmstadt), NuSTAR (NUclear STructure, Astro-physics and Reactions). The start version of FAIR consitute of SIS100 synchrotron which will deliver primary beams of protons with kinetic energy upto 29 GeV, gold ions with up to 11 AGeV and light nuclei with Z/A = 0.5 up to 14 AGeV with the intensity of $10^9$

ions/sec. The research program devoted to the exploration of the compressed baryonic matter will start with beams from SIS100. The installation and commissioning of the FAIR experiments is planned to be completed by 2025 and FAIR is scheduled to deliver the first beams for experiments in 2026 [65].

## 2.2 Physics motivation of CBM

The CBM experiment will run protons and of different ions including that of gold of energies from 2 - 11 AGeV in the SIS-100 setup. According to the transport models [66–70] and hydro-dynamical calculations simulating high energy heavy-ion collisions, the nuclear fireball will be compressed to more than six times that of the normal nuclear matter density $\rho_0$ at a beam energy of 5 AGeV in central Au+Au collisions and will spend within the phase coexistence region comparatively for a longer time. The density even reaches $8\rho_0$ at the beam energy of 10 AGeV [71] (See Fig. 2.2). The calculations illustrate that the FAIR energy range is very suitable to produce baryonic matter

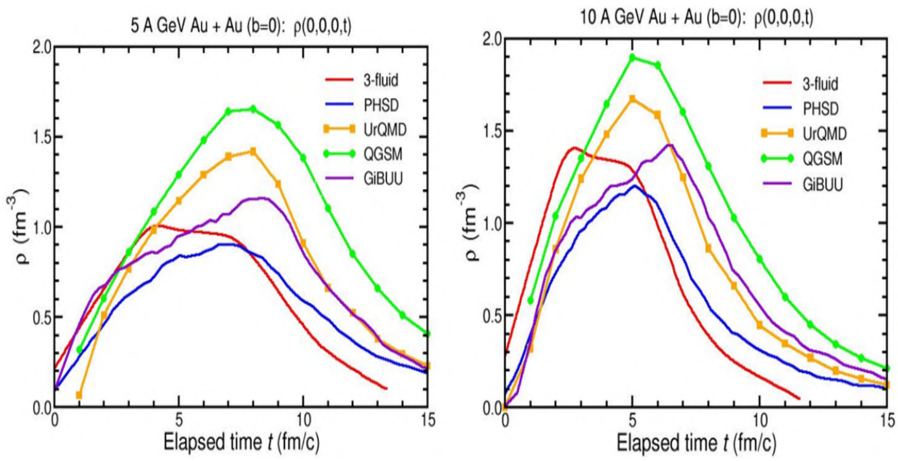


Figure 2.2: Evolution of the net baryon density as a function of elapsed time for central Au+Au collisions at $E_{lab}$ = 5 AGeV (left panel) and 10 AGeV (right panel) according to various transport model calculations and 3-fluid hydrodynamics calculations [72]. A net baryon density of $\rho = 1$ fm$^{-3}$ corresponds to about seven times the density of an atomic nucleus.

at neutron star core densities. The CBM research program which aims to study the QCD phase diagram of baryonic matter is focused on,

- the study of the equation-of-state of nuclear matter at neutron star densities
- the search for the transition from confined hadronic matter phase to the Quark Gluon Plasma

(QGP) phase at high net baryon densities,

- the search for the critical end point (CEP) in the phase diagram of the strongly interacting matter
- the search for modifications of in-medium hadronic properties in the dense baryonic matter and indications for chiral symmetry restoration
- the search for single and double hypernuclei, heavy multi-strange objects
- the existence of exotic QCD phases at high net baryon densities

The CBM experiment will be able to detect a large number of bulk and rare probes which are yet to be measured in heavy-ion collisions in the FAIR energy range. The experimental observables which will address the above-mentioned physics goals of CBM are,

- Yields, collective flow, correlations, event by event fluctuations of hadrons
- Production of (multi-)strange mesons/baryons (K, $\Lambda$, $\Sigma$, $\Xi$, $\Omega$) at (sub)threshold energies
- In-medium modifications of light vector mesons $\rho$, $\omega$, $\phi \rightarrow e^+ + e^-$ ($\mu^+ + \mu^-$) via dilepton measurements
- Yields and lifetimes of hypernuclei
- Production and propagation of charm at threshold energies
- Excitation functions of charmed objects in p+A collisions (J/$\psi$, $D^0$ , $D^\pm$)
- Charmonium suppression in cold nuclear matter.

## 2.3 CBM Detector System

The challenge of the CBM experiment is the measurement of both bulk observables and rare diagnostic probes in nucleus-nucleus collision and in proton-nucleus interactions as reference systems with high precision and high statistics at different beam energies. On the other hand, highly granular detectors are required to cope up with the high particle track multiplicity environment in nucleus-nucleus collisions at FAIR energies. A novel concept of charged particle tracking and vertexing is required due to the complex collision environment of the CBM experiment. For example, D-mesons are reconstructed by their hadronic decay channel $D_0 \rightarrow K^- \pi^+$ ( $c\tau \approx 124\ \mu$m ) and $D^\pm \rightarrow K^\mp \pi^\pm \pi^\pm$ ( $c\tau \approx 317\ \mu$m ). To suppress the combinatorial background of prompt kaons and pions, the displaced vertices need to be measured with an accuracy of about 50 $\mu$m along the beam axis. Moreover, a modular setup of detectors and different running conditions are necessary to study different CBM observables. For instance, to measure $J/\psi$ via their electron-positron decay channel, three conditions are to be dealt with, (a) an interaction rate of $10^7$/s for compensation of the low production cross-section at the threshold energy, (b) an on-line event selection for reduction of the data flow down to an archiving rate of 25 kHz and, (c) an electron identification detector system with a pion suppression factor of the order of $10^5$. Further more, the combinatorial background of electron/positron from $\pi^0$ Dalitz decays and gamma conversions needs to be reduced by rejecting the close pairs to measure low-mass vector mesons. Similar challenges are encountered for dimuon measurements by CBM. Therefore, the CBM detector has to fulfill the following detector requirements [73],

(i) identification of electrons with a pion suppression factor of $10^5$,

(ii) identification of muons,

(iii) determination of the primary and secondary vertices (accuracy of 50 $\mu$m),

(iv) identification of hadrons with large acceptance,

(v) detectors with very short dead time, high granularity, radiation-hard and fast response , (vi) fast radiation-hard trigger and data acquisition & electronics.

The CBM detector therefore consists of both electron and muon identification systems as two setups are not compatible to each other due to the requirement of efficient particle absorbers for muon measurements which would not allow for electron measurements. The core of the CBM experimental setup consist of a Micro-Vertex Detector (MVD) consisting of pixels modules and a Silicon Tracking System (STS) consisting of micro-strips modules installed inside a superconducting dipole magnet. For electron identification and pion separation, two detector systems are placed downstream the magnet, the Ring Imaging Cherenkov detector (RICH) and the Transition Radiation Detector (TRD). The Time-of-Flight (TOF) wall and the Projectile Spectator Detector (PSD) are placed further downstream in the CBM setup. The TOF wall serves as hadron identifications, whereas event plane characterization and the determination of the collision centrality will be performed by the PSD. In the muon setup, RICH detector will be replaced by a set of segmented hadron absorbers and Muon Chamber (MuCh) detector system which will identify vector mesons in their di-muon decay channel. Fig.2.3 present the CBM detector setup with RICH in the beamline and MuCh in the parking position. The different subsystem of CBM detector has been explained further.

### 2.3.1 Dipole Magnet

A H-type superconducting dipole magnet with a magnetic field integral of 1 T-m bends the trajectories of all charged particles created in the collision and hence serves to determine the exact particle momenta. The magnet has a large aperture with polar angle acceptance of ±25° and horizontal acceptance of ±30°.

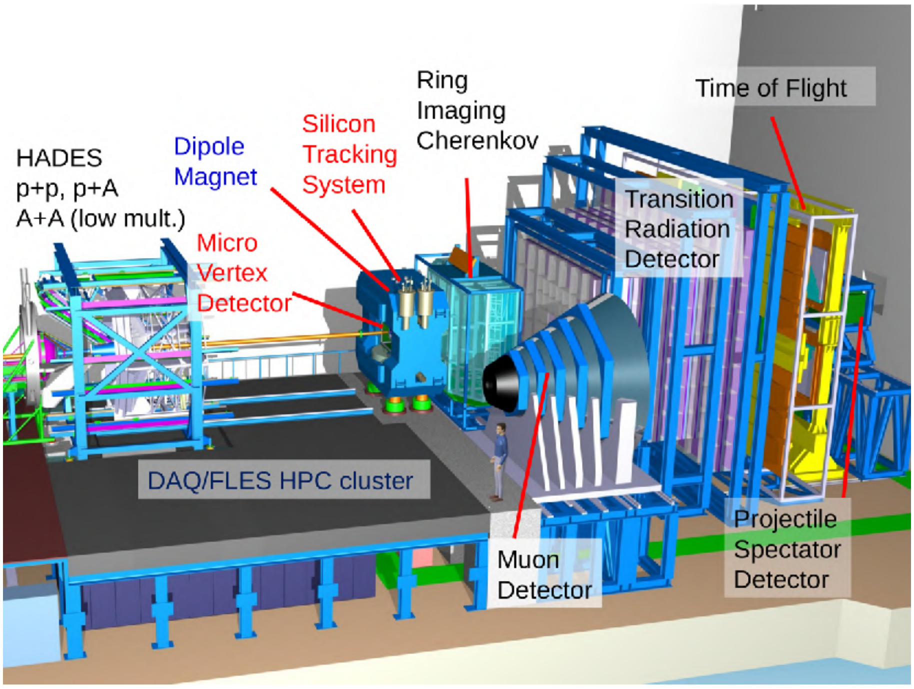


Figure 2.3: The CBM experimental setup in the electron configuration with Muon detector in the parking position

### 2.3.2 Micro-Vertex Detector (MVD)

Four MVD stations placed at z = 5-20 cm downstream the target in the target vacuum are the first detectors behind the collision vertex [74]. A detector with excellent spatial resolution, very low material budget to reduce multiple scattering and radiation hardness due to close proximity of the collision zone is required for the determination of the secondary vertices of open charm particles (D mesons). A silicon pixel detector based on the new generation CMOS Monolithic Active Pixel Sensors (MAPS) named MIMOSIS [74] serves as the Micro-Vertex Detector (MVD) for CBM. It will provide a hit position resolution of $\sim 5$ $\mu$m with a pixel size of $26.88 \times 30.24$ $\mu m^2$ resulting in a secondary vertex resolution of 50 $\mu$m along the beam axis in combination with a material budget of 0.3%–0.5% $X_0$ ($X_0$ being the radiation length of silicon) for a full detector station. The MVD detector stations are equipped to handle particle rate of upto 70 MHz/cm$^2$ with a 5 $\mu$s time resolution of the sensors [74]. The sensors need to be cooled due to their operation in the target chamber vacuum. A highly heat conductive support is made which propels the heat from the sensors to the liquid cooled heat sinks. Poly-crystalline CVD diamond carriers are used as a raw material for constructing these cooling supports for first two stations and sheets of Thermal Pyrolytic Graphite are used for last two stations [74]. The sinks are located outside of the acceptance of the fixed target geometry. The estimated radiation tolerance of MVD detectors needs to be $10^{13}$ $n_{eq}$ /cm$^2$ (non-ionizing), and 3 Mrad (ionizing) per year of operation in the CBM environment (up to 28 GeV p-A collisions) [75].

### 2.3.3 Silicon Tracking System (STS)

The reconstruction of trajectories for charged particles with high efficiency > 95 % for p > 1 GeV/c and the determination of the momenta of those particles with high resolution $\Delta p/p = 1$ % for p > 1 GeV/c will be performed by the Silicon Tracking System (STS) [76]. STS consists of 8 tracking stations placed at z=30-100 cm with a gap of 10 cm behind the target inside the dipole magnet. It cover polar angles from 2.5° to 25°. An extensive view of the STS together with the MVD detector assembled in the magnet is shown in Fig. 2.4. STS comprises of double-sided silicon microstrip sensors. Each sensor is of thickness of about 300 $\mu$m, 20 $\mu$m strip size, 58 $\mu$m strip pitch and 7.5° stereo angle of the p-strips with respect to the n-strips. They come with different sizes $22 \times 62$ mm$^2$, $42 \times 62$ mm$^2$, $62 \times 62$ mm$^2$ and $124 \times 62$ mm$^2$ depending upon their positions [78]. The sensors provide a hit resolution of about 25 $\mu$m. A ultra-low material budget (1% $X_0$) is necessary to achieve the required momentum resolution since it is affected by multiple scattering [79]. To achieve this goal, the sensors are mounted on the lightweight carbon fiber carrying ladders and

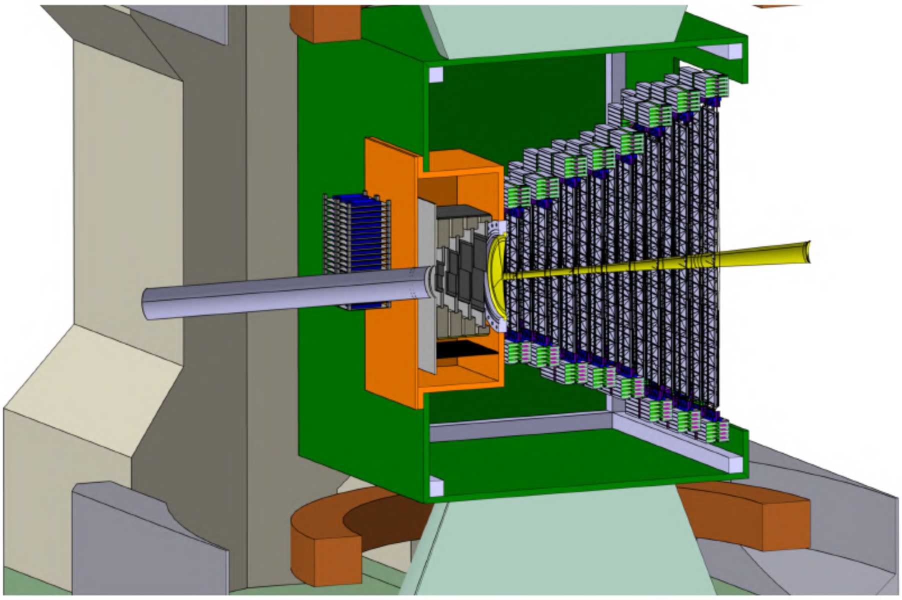

Figure 2.4: Detailed view of the STS together with MVD integrated in the magnet [77].

they are connected via ultralight micro cables to the front-end electronics which in turn are placed outside the active area of STS acceptance. A high level of radiation is expected to impact on the sensors. The neutron equivalent fluences in the sensors are expected to be lower than $1 \times 10^{13}$ $n_{eq}$ $cm^{-2}$ and $1 \times 10^{14}$ $n_{eq}$ $cm^{-2}$ for the harshest running scenarios of the experiment at SIS-100 and SIS-300 respectively [80]. The STS will be operated in a thermal enclosure at about -5° C to reduce radiation damage induced by leakage currents.

### 2.3.4 Ring Imaging Cherenkov detector (RICH)

In the electron-hadron configuration of the CBM detector setup, Ring Imaging Cherenkov detector (RICH) is designed to contribute in electron identification and pion suppression in the momentum range below 8 GeV/c to 10 GeV/c [82]. The RICH detector is positioned outside the magnetic field around 1.6 m downstream of the target and behind the STS detector. The RICH detector comprises of a 1.7 m long gaseous $CO_2$ radiator, two arrays of spherical mirrors with a curvature radius of 3 m made of an reflective aluminium-coated glass substrate with a protective $MgF_2$ coating and a photon detection camera of multianode photomultipliers (MAPMTs). Cherenkov radiation emitted by the charged particles passing the radiator will be reflected by mirrors built from 72 mirror tiles and the cherenkov rings will be projected on the photon-detectors. The particle

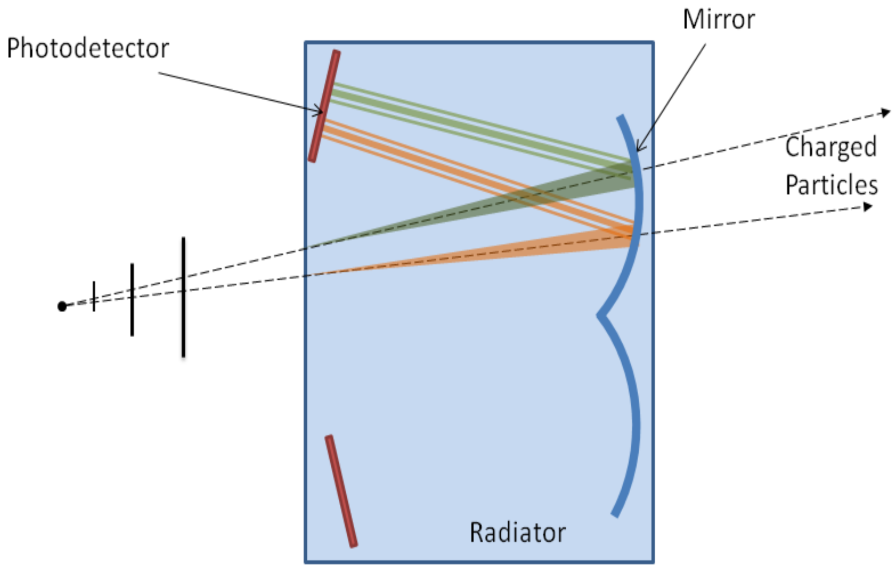


Figure 2.5: Layout of di-electron identification approach in RICH of CBM [81].

speed will be calculated by reconstructing the cherenkov rings. The process has been depicted in Fig. 2.5. The refractive index of the radiator has been adjusted beyond the pion threshold for Cherenkov which is 4.65 GeV/c. The magnet yokes will shield the photo-detector planes from the magnetic field.

### 2.3.5 Muon Chamber (MuCh)

In the muon configuration setup of CBM, the Muon Chamber (MuCh) detector system will identify muons of a range of momenta stations from the low momentum muons from the decay channel of low-mass vector mesons (LMVM) in a high particle density environment at FAIR energies. The detailed description of MuCh can be found in the next chapter.

### 2.3.6 Transition Radiation Detector (TRD)

The Transition Radiation Detector is a detector meant for electron and positron identification with an electron efficiency of 90 %. The detector is capable of identification above momenta of 1 GeV/c with a pion suppression factor 10 - 20. The TRD is used for tracking of particles between the RICH and the TOF detector. The performance of TRD is driven by the requirement of a high quality measurement of dielectrons in the mass range from below the LMVM mass ($\rho$, $\omega$, $\phi$) to beyond the

J/$\psi$ mass. The particle identification by the TRD detector is based on the principle of emission of an electromagnetic radiation (known as transition radiation) when ultra-relativistic charged particles traverse the interface of two media with different dielectric constants. The intensity of radiation is proportional to the particle's Lorentz factor $\gamma = E/mc^2$ [83]. This enables the TRD detector to distinguish between electrons with a high Lorentz factor and pions with a low Lorentz factor. The detector is also involved in the measurements of fragments and hypernuclei due to its ability to identify charged particles via specific energy loss. The TRD detector consists of a irregular foam-radiator where the transition radiation will be produced and a Xe/$CO_2$ filled gaseous detector, Multi-wire proportional counter (MWPC) where the charged particle and the electromagnetic radiation will be measured [84]. Fig. 2.6 (right) shows a schematic of a transition

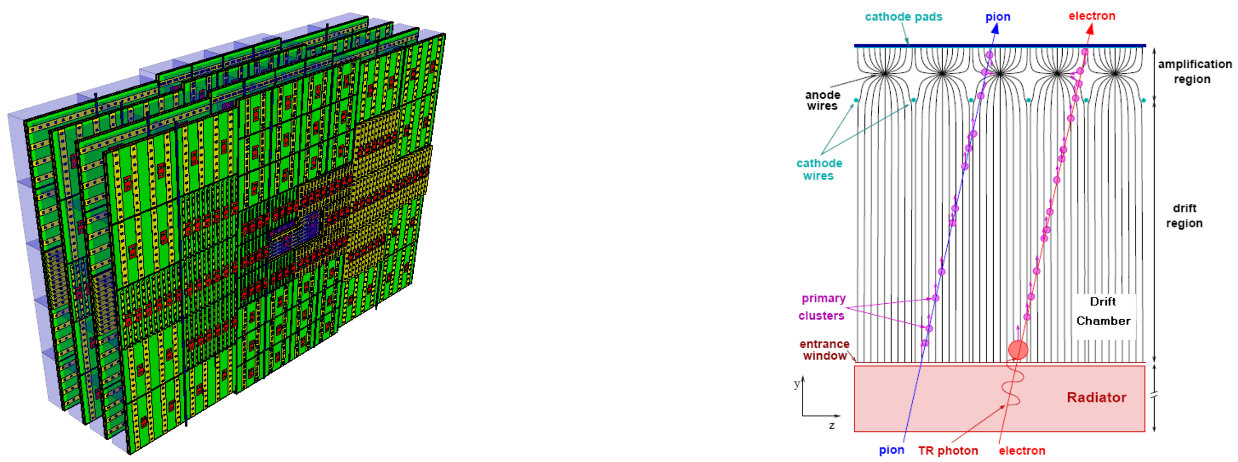


Figure 2.6: Left: Engineering rear view of the transition radiation detector for the CBM experiment [85]. Right: Schematic of a TRD detector comprising of a radiator and a drift chamber. In the module, the schematic signals produced by a pion and an electron are shown. The geometric proportions and the field lines in the drift chamber are accurate [86].

radiation detector consisting a radiator and a drift chamber. In SIS100 configuration, four detector layers grouped into one TRD station are positioned at approximately 4.1 m to 5.9 m downstream of the target (Fig. 2.6 left) [85]. They cover a total active area of 114 $m^2$ (SIS100). The TRD readout will be registered in rectangular pads with a position resolution of $\sim 300$ $\mu$m across and 3 - 30 mm along the pad [85]. Every second transition radiation layer is rotated by 90° to achieve equal position resolution in both dimensions. The TRD is also used as the $4^{th}$ tracking station of MuCh in the muon configuration of CBM.

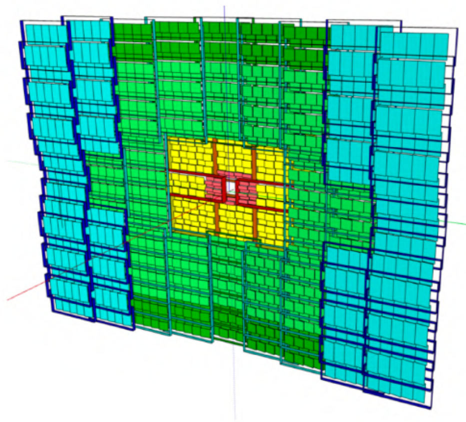

Figure 2.7: Schematic view of the Time Of Flight detector (TOF) used in the CBM experiment, where different colours represent different configurations of MRPC modules [87].

### 2.3.7 Time of Flight (TOF) detector

Time of Flight (TOF) detector wall of the CBM experiment will provide identification for charged hadrons (p, K, $\pi$) upto a particle momentum of about 4 GeV/c [87]. The TOF wall (Fig. 2.7) is located at a distance of about 6 m downstream of the target for SIS-100 setup. It covers a total active area of 120 m$^2$. The detectors for the TOF wall have to fulfill the requirement of a system time resolution below 80 ps and an overall efficiency above 90 %. The most challenging requirement for the TOF detector is a rate capability of about 30 kHz/cm$^2$ which is the estimated rate at the innermost region of the TOF wall from polar angle 2.5° for minimum bias Au+Au collisions with an interaction rate of 10 MHz [88]. The detectors should have an occupancy less

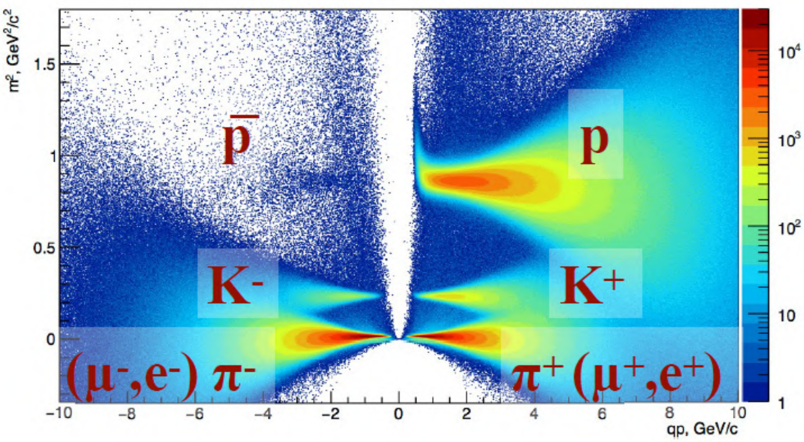


Figure 2.8: Squared mass as a function of the momentum times charge of the reconstructed hadrons by TOF in combination with STS in central Au+Au collisions at a beam energy of 10 AGeV/c [89].

than 5%, and they should work under free streaming data acquisition mode. An array of Multi-gap Resistive Plate Chambers (MRPCs) will serve as active detectors for the CBM-TOF wall. Thus, the mass of a charged hadron can be calculated from the information of particle momentum from STS and the information of time from the TOF, which in turn gives the velocity information. Prototype MRPCs were designed and tested for both the inner TOF wall built with low-resistive glass electrodes and outer TOF wall built with standard float-glass electrodes according to the rate requirement. According to simulation results, TOF provides efficient separation of Kaons and pions in the momentum range upto 3.5 GeV/c, and protons upto 7 GeV/c [90]. Fig. 2.8 shows the realistic simulations results of the separation ability of TOF for protons, kaons and pions.

### 2.3.8 The Projectile Spectator Detector (PSD)

The Projectile Spectator Detector (PSD) is a forward hadron calorimeter located as the most downstream detector at a distance of 8 m from the target [91]. The analysis of event-event fluctuations of conserved quantities needs an accurate determination of the collision centrality and the reaction plane in nucleus-nucleus collisions which is carried out by the PSD detector. A precise determination of the reaction plane, which is done by measuring the particles not participating in the collision, the so-called spectators, is necessary for the study of collective flow. The energy

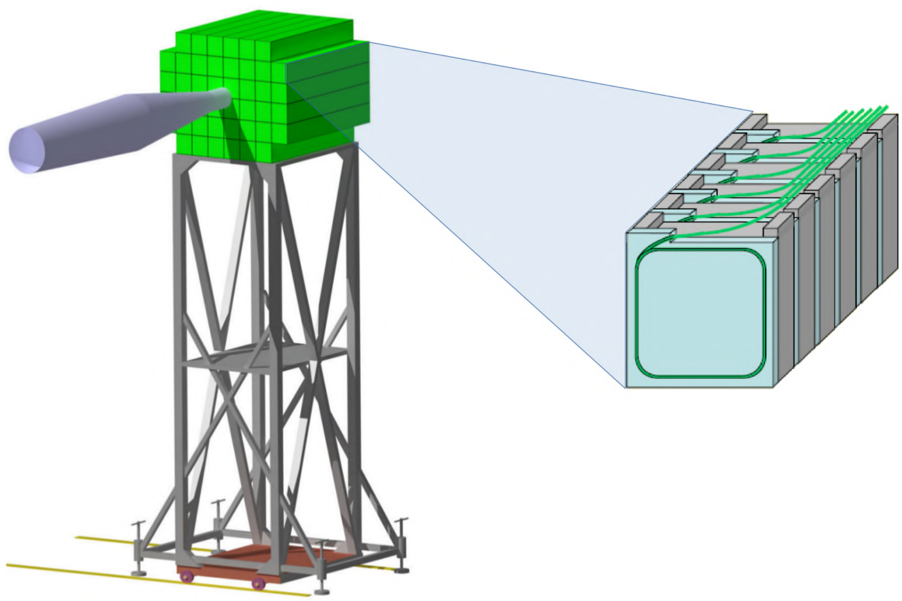

Figure 2.9: Schematic view of the Projectile Spectator Detector (PSD), used in the CBM experiment [91].

distribution of the spectators and the forward going particles formed close to the beam rapidity are measured by the PSD detector. The PSD detector is able to measure . PSD is a full compensating modular calorimeter, consisting of lead plates as absorbers and plastic scintillator plates for the energy measurement deposited by hadronic showers. The detector has a very precise and uniform energy resolution ($\sigma_E$/E $= 50\%/\sqrt{E}(GeV)$). The PSD detector consists of 44 individual modules, each module is composed of 60 lead/scintillator layers with a front surface of 20 $\times$ 20 $cm^2$ (see Fig. 2.9). The total length of the detector is about 120 cm. Multi-Avalanche Photo-Diodes (MAPDs) with an active area of 3 $\times$ 3 $mm^2$ and a pixel density of $10^4$ per $mm^2$ are used as a read-out for the scintillating light via wavelength shifting (WLS) fibres.

### 2.3.9 Online event selection and data acquisition

The physics of the CBM experiment focuses on the measurement of rare probes such as dileptons, or multi-strange particles ($\Xi$, $\Omega$, D, J/$\psi$) at the SIS100 energies. These particles have very low production cross sections. In order to measure rare probes with high statistics, CBM detectors need to be operated at a very high interaction rate and as a result with unprecedented high particle density. The data acquisition system (DAQ) in CBM is designed to operate at extremely high reaction rates up to 10 MHz, which corresponds to a beam intensity of $10^9$ ions/s and 1% target generating $10^7$ collisions per second. In such a scenario, an event volume of 10 kByte for the full setup and minimum bias Au+Au collisions correspond to an input data rate in the order of 100 GByte/s. Considering the highest recording speed of the modern storage media about 1 GByte/s, this input data rate is extremely high and it is not possible to store the data completely in a realistic scenario. Therefore, an online data event selection mechanism is required to perform measurements at 10 MHz interaction rate in CBM that rejects the background events containing uninteresting event signatures to reduce the data rate by a factor of 100 or more. This selection will be based on a fast on-line event reconstruction running on a high performance computer farm equipped with many-core CPUs and graphics cards located a few hundred meters away from the CBM cave in the GSI GreenIT Cube (See Fig. 2.10). This process is named as First Level Event Section (FLES). In the early stages of the hardware read-out chain, there is no hierarchical trigger mechanism which is regarded due to the complex nature of event topologies and resulting signal signatures of interesting events. Instead the system of CBM is a combination of a front-end electronics which is self-triggered, a fast data transport which is free-streaming, an online event reconstruction and event selection mechanism. The front-end electronics (FEE) generate asynchronous data messages autonomously after it gets activated by a particle. Therefore, the FEE will operate in self-triggered mode, where any signal by a particle crossing a previously set threshold gets digitized and provided with a time-stamp against a common clock. The asynchronously time-stamped data messages is then pushed from the FEE to a readout buffer via fast optical links into a high-throughput event building network. The decision to keep the data and push them through the network or throw them out is made by each layer of the readout component itself. Full track reconstruction is necessary involving some sub-detector systems of CBM since many probes have displaced decay vertices from few mm (D-mesons) upto few cm (hyperons) away from the primary collision vertex. The Cellular Automaton [73] and Kalman Filter [92,93] methods have been implemented on the parallel track finding and fitting algorithms for track reconstruction which is the most time consuming combinatorial stage of the event reconstruction.

Figure 2.10: Decicated computer farm Green ITCube at GSI, used for online event reconstruction during the operation of the CBM experiment [94].

# Chapter 3

# The Muon Detection System of the CBM Experiment

The CBM experiment at FAIR is designed to study the properties of the QCD matter at very high net-baryon densities created in high energy heavy-ion collisions with beam energies between 2 and 11 A GeV. Electrons and muons born in the hot and dense fireball of a heavy-ion collision do not suffer strong interaction effects, and carry undisturbed information to the detector system.

### 3.0.1 Conceptual layout of the CBM muon detection system

Identification of low momentum muon pairs arising from the di-muon decay channel of the low-mass vector mesons (LMVM) in a very high particle density environment is one of the major experimental challenges in the CBM experiment at FAIR. The conventional technique to measure muons in high energy physics experiments is placing a thick hadron absorber with high Z material before the sensitive muon detectors. The muons will pass through the absorber due to their low interaction probability with matter. Instead of incorporating a single thick hadron absorber like other HEP experiments, a segmented absorber system will be used as a special feature in the CBM experiment. The muon detectors are positioned in between the segmented layers of absorbers. This novel idea is embraced to facilitate momentum dependent track identification. The detection of low momentum muons is feasible with this approach. Otherwise they would have been stopped by a single thick absorber. An optimization of parameters is necessary to develop the MuCh system layout, like, the number, thickness and material of the segmented absorber, the number and granularity of the tracking detectors. This optimization is done by simulating the response of the Au+Au collisions in a wide energy range in the simulated CBM set up. This is a very challenging case because of the high track density up to 700 charged particle per event. The hadronic background along with the muons from weak pion and kaon decays is calculated with the UrQMD [95, 96] event generator. The embedded dimuon signal from the vector mesons are generated with the PLUTO generator [97]. The particle multiplicities are taken from the

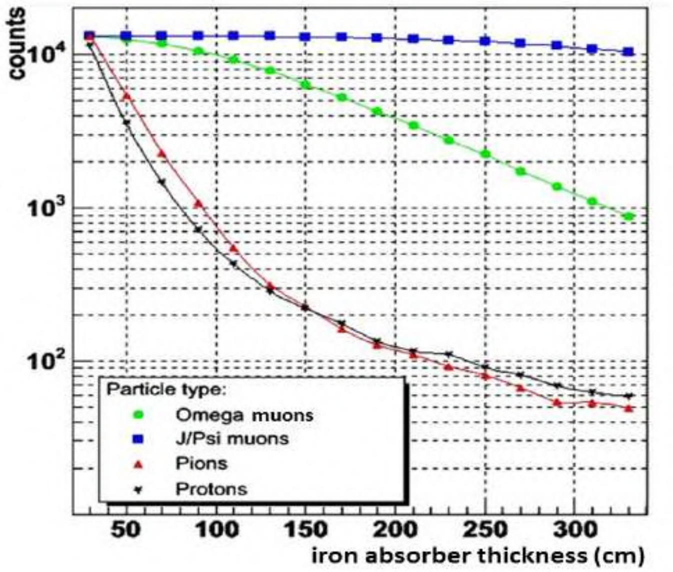


Figure 3.1: Total number of particles as a function of the traversed length in iron. The particle momenta have been taken from the simulation of central Au+Au collisions at 25 AGeV, their numbers have been normalized [98].

PHSD microscopic off-shell transport code [67]. The propagation of particles through the realistic geometry of absorbers and detector stations was carried out by the GEANT3 transport engine [99]. The hadron interaction length ($\lambda_I$) of the material is the key parameter to determine the choice of the material and the thickness of material to be used as an absorber. $\lambda_I$ has been calculated empirically as, $\lambda_I \sim 35\ \mathrm{A}^{1/3}\ \mathrm{gm/cm}^2$ and it depends upon the density of the material as well as the total inelastic cross-section for hadron-nucleus interaction. Small-angle multiple scattering is also an important criterion for the optimization of the hadron absorber. Multiple scattering increases with the absorber thickness and as a result, there is a decrease in the matching efficiency between the incoming and the outgoing tracks. Therefore, a large number of falsely reconstructed background track appears due to track mismatch. An optimization of interaction length and radiation length ($X_0 \propto A/Z^2$) is necessary to choose a hadron absorber. $\lambda_I$ should be as small as possible, whereas to reduce the multiple scattering $X_0$ should be as large as possible. Iron is chosen as the principal component of the hadron absorber. Fig. 3.1 shows the absorption of various particles as a function of the iron absorber thickness. The required thickness of the hadron absorbers for the detection of LMVMs and charmonia can be evaluated from the Fig. 3.1. Muons originated from $J/\psi$ can cover a distance up to 250 cm in iron absorber without significant suppression, while a reduction by a factor of 10 occurs in such a thick absorber for the number of muons decayed from $\omega$ mesons. The absorption of muons from $\omega$ mesons happens by the same amount as protons and pions beyond an iron absorber thickness of 1.5 m. This implies that no further improvemnt of the signal-to-background ratio (S/B) will take place beyond a 1.5 m thick iron absorber. It can be concluded that the thickness of the iron absorber should not exceed 1.5 m for the efficienct measurement of LMVMs. An additional iron absorber layer of about 1 m thick together with a number of detector layers can be included to measure the muons from the $J/\psi$ decay. The thickness of the individual layers of the iron absorber needs to be optimized along with the total absorber thickness. A compromise between the hadron absorption and the multiple scattering is necessary before concluding the thickness and material of the first absorber especially. The first absorber should be sufficiently thick to reduce the hadron multiplicity to a desired level for the tracking chambers to operate smoothly. But a thick absorber intensify multiple scattering, which also increases with Z of the material for a given absorber thickness. As a result, there is a decrease in the matching efficiency between incoming and outgoing tracks. Therefore, a large number of falsely reconstructed background track appears due to track mismatch. Fig. 3.2 shows the variation of particle multiplicity as a function of the first absorber thickness with two absorber materials, iron (left) and carbon (right), for central Au+Au collisions at beam energy 10 AGeV. The simulation results show that the yield of secondary electrons dominates the particle multiplicity which intially increases and then reduces with increasing material thickness for both the absorber materials. An optimum choice for the first absorber is a 20-30 cm iron or equivalently 60 cm thick carbon based on hit multiplicity and background tracks. Since the first absorber in the recent design of CBM will be placed inside the high magnetic field of the CBM dipole magnet, a 60 cm carbon absorber is preferred over iron. Since pure carbon is not available in market, the

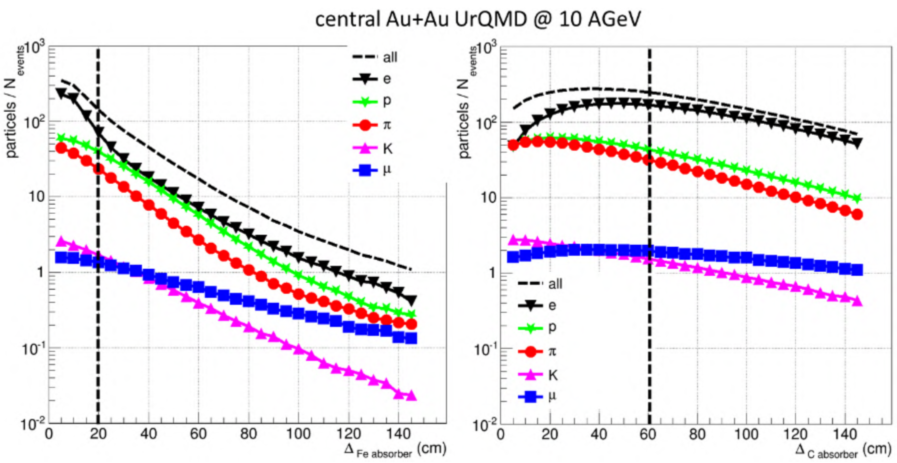

Figure 3.2: Variation of event-by-event particle multiplicity (primary + secondary) with thickness of iron absorber (left) and carbon absorber (right) for central Au+Au collisions at 10 AGeV beam energy [98].

first absorber is made of two different slices of materials, first part is low density (LD) graphite and second part is concrete. An absorber slice made of 28 cm thick LD graphite is placed inside the magnet and a concrete slice of 30 cm thickness is positioned outside the magnet. The rest of the absorbers are made of stainless steel which is non-magnetic in nature instead of soft-iron to avoid any residual magnetic field. They are placed outside the dipole magnet.

### 3.0.2 MuCh Configuration

The Muon chamber (MuCh) of CBM consists of a segmented absorber with detector triplet stations positioned in between the absorber segments. The parameters of the absorber, i.e, material, thickness etc. have been optimized by performing simulations in a CBMROOT environment. The schematic of the MuCh configuration for heavy-ion collision at SIS-100 beam energy is shown in Fig. 3.3. The first version of the SIS100 setup (SIS100B) consists of 4 absorbers and 4 detector tracking stations. Each detector tracking station comprises three detector layers between the air-gap of two successive absorbers which is optimized to be 30 cm. Along with the detector profile, electronics, cooling arrangements and mechanical structures are placed in the air-gap. There are total 12 detector layers present in the SIS100B setup. For the $J/\psi$ measurement in the next version of SIS-100 setup (SIS-100C), an additional iron absorber slice of 100 cm is placed behind the last tracking stations. Therefore, the total thickness of absorber for SIS-100C setup becomes $\sim$ 228 cm ((28 cm LD graphite + 30 cm concrete) + 20 cm Fe + 20 cm Fe + 30 cm Fe + 100 cm Fe). The

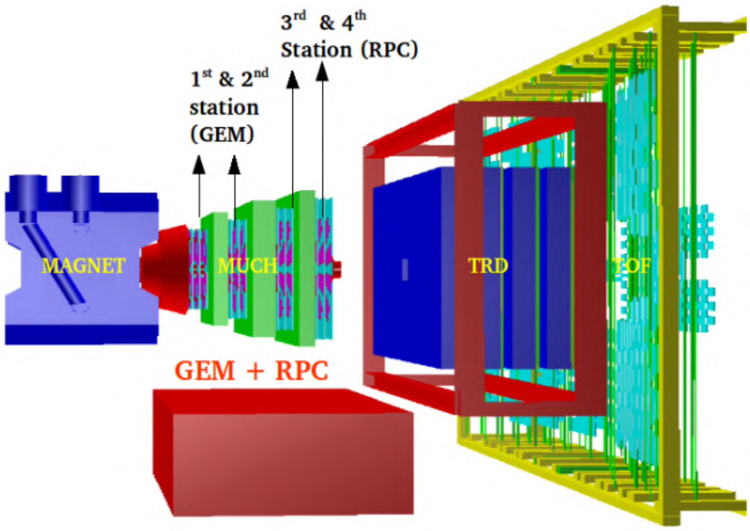


Figure 3.3: Schematic layout of the MuCh geometry SIS100B configuration within CBMROOT software.

specification of the absorbers and detector stations are given in table 3.1 and in table 3.2. The detectors cover an angular acceptance region from ± 5° to ± 25°.

Table 3.1: Table for the specification of absorbers and detector layers for SIS100 setup to measure low mass vector mesons. LD stands for Low Density

| Station Number | Absorber material | Absorber Thickness (cm) | Number of detector layers | Number of modules per layer |
|---|---|---|---|---|
| 1 | LD Graphite+Concrete | (28+30 = 58) | 3 | 16 |
| 2 | Fe | 20 | 3 | 18 |
| 3 | Fe | 20 | 3 | 20 |
| 4 | Fe | 30 | 3 | 22 |

The particle rate distributions have been simulated using FLUKA for Au+Au collisions at 10 AGeV beam energy shown in Fig. 3.4. The particle rate decreases as we go away from the target. Table 3.3 summarises the maximum particle rate for each stations of MuCh. The expected radiation dose level is a neutron equivalent fluence of $10^{12}$ $n_{eq}/cm^2$ and a gamma dose of about 30 krad corresponding to ten years of operation in CBM which is simulated in FLUKA. In the current design, the first two stations are based upon the Gas Electron Multiplier (GEM) detector to cope up with the high particle rate. The Resistive Plate Chamber is proposed as an active detector element for the $3^{rd}$ and $4^{th}$ stations. The detailed discussions about the optimization

Table 3.2: Table for the specification of absorbers and detector layers for SIS100 setup to measure J/$\psi$. LD stands for Low Density

| Station Number | Absorber material | Absorber Thickness (cm) | Number of detector layers | Number of modules per layer |
|---|---|---|---|---|
| 1 | LD Graphite+Concrete | (28+30 = 58) | 3 | 16 |
| 2 | Fe | 20 | 3 | 18 |
| 3 | Fe | 20 | 3 | 20 |
| 4 | Fe | 30 | 3 | 22 |
| 5 | Fe | 100 | TRD | TRD |

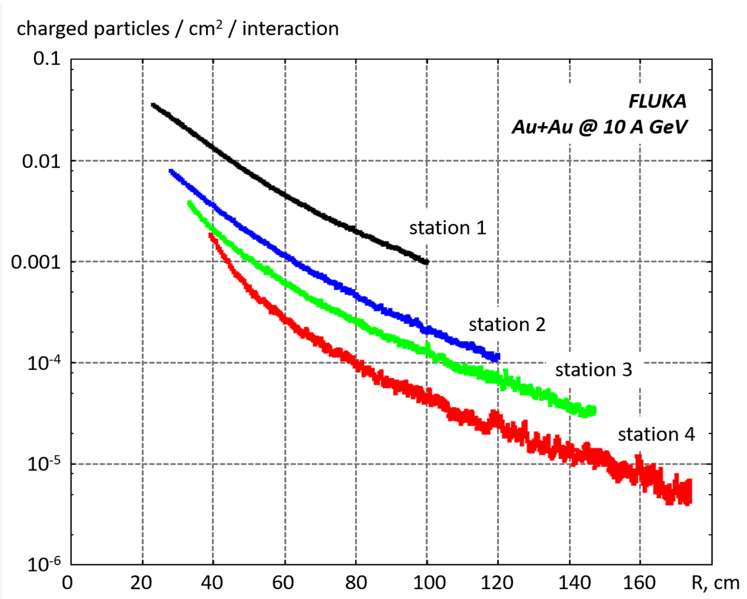


Figure 3.4: Particle rate on the four detector stations of MuCh for Au+Au collision at 10 AGeV beam energy using FLUKA simulation [98].

Table 3.3: Particle rates on the detector stations for Au+Au collision at 10 AGeV beam energy using FLUKA [100].

| Station Number | Max. Particle Rate (kHz) |
|---|---|
| 1 | $\sim$380 |
| 2 | $\sim$80 |
| 3 | $\sim$36 |
| 4 | $\sim$18 |

of the absorbers and detectors of muon detector system in CBM can be found in the Technical Design Report (TDR) of MuCh [98] and in the Muon Chamber (MuCh) section of the annual CBM progress reports [101–105]. The technology options chosen for MuCh detector system are gaseous muon tracking detectors matching the hit density and rate. Gas Electron Multiplier (GEM) detectors will be installed behind the first and the second hadron absorber, where the particle density reaches up to 380 kHz/cm$^2$ for SIS-100 energies. Further downstream at the third and the fourth stations, single gap Resistive Plate Chamber (RPC) detectors made of low resistive bakelite electrodes have been proposed as the technology option due to the reduced peak hit density about 36 kHz/cm$^2$ and 18 KHz/cm$^2$ respectively. The covered active area of each layer has been subdivided into trapezoidal sector-shaped modules. Each GEM module is filled with an Ar-$CO_2$ gas mixture as the active medium of 3 mm. A trapezoidal-shaped aluminum plate with a thickness of 1.2 cm is installed on one side of each GEM module to support it. The aluminum plate also helps to keep the MuCh electronics cool. The RPC module is filled with 2 mm gas between 2 mm thick glass plates. Like in the GEM module, on one side of each RPC module, a trapezoidal-shaped aluminum plate with a thickness of 2 mm is used to provide support and cooling for DAQ systems. A distance of 10 cm between the detector layers and a space of 5 cm between the end of absorber to the nearest detector layer have been provided in the simulation. Realistic sector-shaped geometries consisting of trapezoidal shaped detector modules along with corresponding PCBs have been implemented in the simulation. Detailed simulation using RPCs are still ongoing.

## 3.1 Methodology for MuCh simulation and Analysis

The studies for the simulation of MuCh are performed using the CBMRoot framework, which is a part of FairRoot framework. The CBMRoot framework is established on "Root C++ object-oriented programming" and libraries developed at the European Organization for Nuclear Research (CERN). UrQMD, PLUTO, HSD, GEANT3, GEANT4, FLUKA are some of the event generators and transport engines which are included in the framework for the feasibility studies and optimization of detectors. The basic steps of performance simulation using the UrQMD event generator and GEANT3 transport engine is shown in the flow chart 3.5. The simulation chain is proceeded

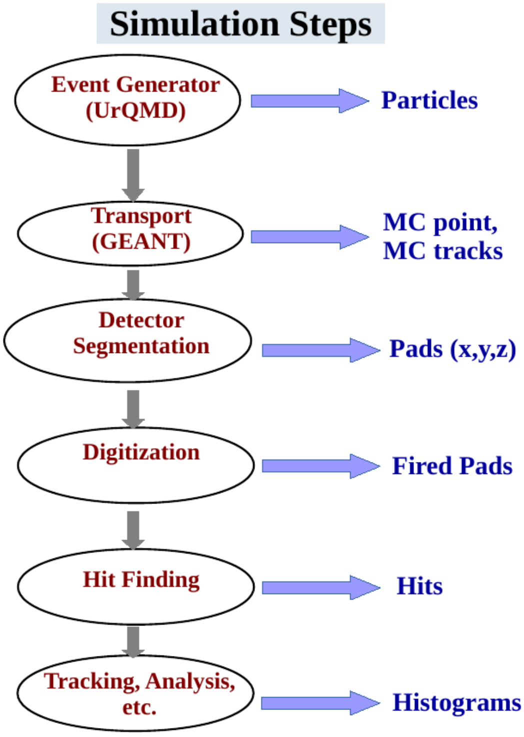


Figure 3.5: Schematic layout of the simulation chain in MuCh [100].

sequentially in the following way: a) event generation, b) geometry implementation and transport, c) segmentation of readout pads and digitization, d) clustering and local hit reconstruction, e) track reconstruction and propagations, and f) selection of tracks as muon candidate. Finally, the identification of muons is carried out which is a part of the analysis chain.

### 3.1.1 Event Genrators

The initial stage of simulation is the generation of particles which will be projected on the detectors.

- **UrQMD:** It is an event generator based on the theoretical model of microscopic many-body collisions which effectively simulates ultra-relativistic p+p, p+A, and A+A collisions in an extensive energy range from SIS to RHIC. A covariant propagation of constituent quarks, diquarks, color strings, mesonic and baryonic degrees of freedom take place in this model. Particle production is portrayed via fragmentation of color strings of the colliding nuclei. Hadrons are produced in string fragmentation and hard scattering. The inclusion of the formation time of hadrons using the PYTHIA model integrates the sub-hadronic degrees of freedom into UrQMD which became relevant at higher energies. The phase transition from the hadronic state to the QGP state is not included in UrQMD. The generation of background is performed using the module in the MuCh simulation.

- **PLUTO:** Since no rare probes, such as LMVM or charmonia are included into UrQMD, the event generator called PLUTO [97] is used for the generation of signal particles. The PLUTO event generator includes the leptonic and Dalitz-decays of the $\omega$ and $\phi$ vector mesons. The dileptonic decay channel of medium-modified $\rho_0$ and QGP radiation are also incorporated in the Pluto cocktail [34]. One decay from Pluto is embedded into each background event created by UrQMD. Later the results are re-scaled by the branching ratio and mulitplicity appropriately.

### 3.1.2 Geometry implementation and transport

The principal goal of MuCh is the identification of the tracks propagating through the segmented absorbers and detector stations. Therefore, trapezoidal shaped absorbers are implemented in the geometry using GEANT3. The detector stations consisting of 3 layers of tracking chambers and each layer (Fig. 3.6) containing several sector shaped modules arranged in a circular shape are also implemented in the geometry behind each absorber block. There is a thin support structure in each layer and the modules are arranged in a staggered manner on both sides of the support structure to reduce dead-space and maintain an overlapping between modules.

### 3.1.3 Detector segmentation

MuCh will operate in a high irradiation environment (hit density upto 4 MHz/cm2 and event rate upto 10 MHz). The reason for the detector segmentation is developing a realistic and optimistic layout of detectors taking into account the physics measurements. Hit density varies radially from the beam pipe ($\propto$ 1/r). The read-out planes of the modules are segmented into pads of appropriate shapes and sizes to achieve the desired pad occupancy ($\sim$ 5%). The maximum pad size is restricted due to the constraint in spatial resolution apart from the hit-occupancy. In case of sector-shaped modules, the segmentation scheme utilizes projective pads of radially increasing sizes as illustarted in Fig. 3.7 The determination of the angular dimensions and the positions of the pads according to

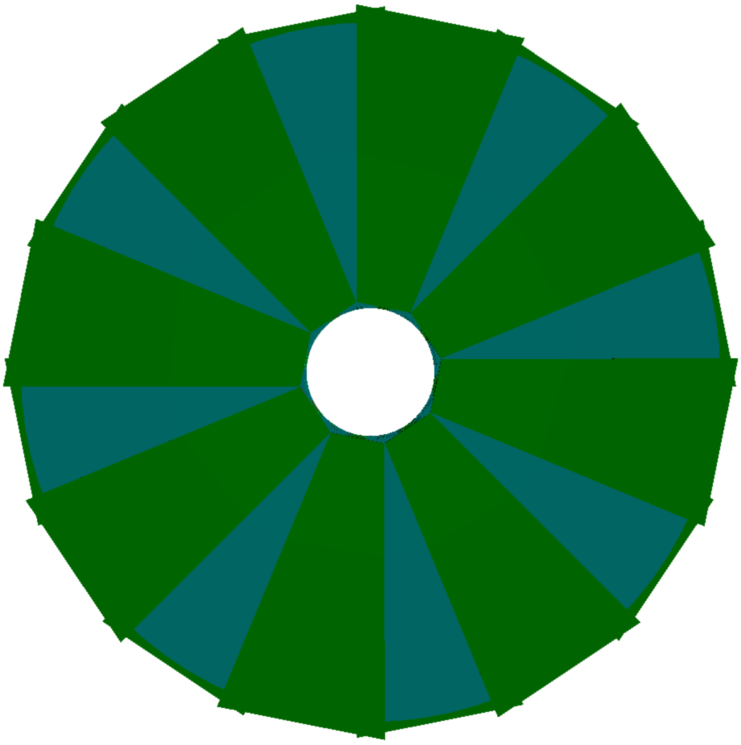

Figure 3.6: Schematic layout of the Muon Chambers (MuCh) with trapezoidal overlapping sectors [100].

the radius are accomplished automatically in the proposed technique of segmentation. At a given radius, the radial dimension of each pad is almost equivalent to the azimuthal dimension ($\Delta$r $\sim$ r$\Delta\phi$). The GEM modules in the $1^{st}$ and $2^{nd}$ stations of MuCh are subjected to 1° azimuthal angle separation. An azimuthal angle separation of 2° is implemented for the pads of RPC detector modules at $3^{rd}$ and $4^{th}$ stations of MuCh.

### 3.1.4 Digitization

The position of the energy deposition (containing coordinates x, y, z) along with the magnitude of deposited energy inside a detector volume due to a traversing particle are called MuCh points. The distribution of the MuCh points to the readout pads is known as digitization, which involves detailed response of energy deposition of particles inside the detector volume. The MuCh points in this scheme are subjected to the generation of primary electron-ions, charge multiplication, and the formation of signal inside the gas gap.

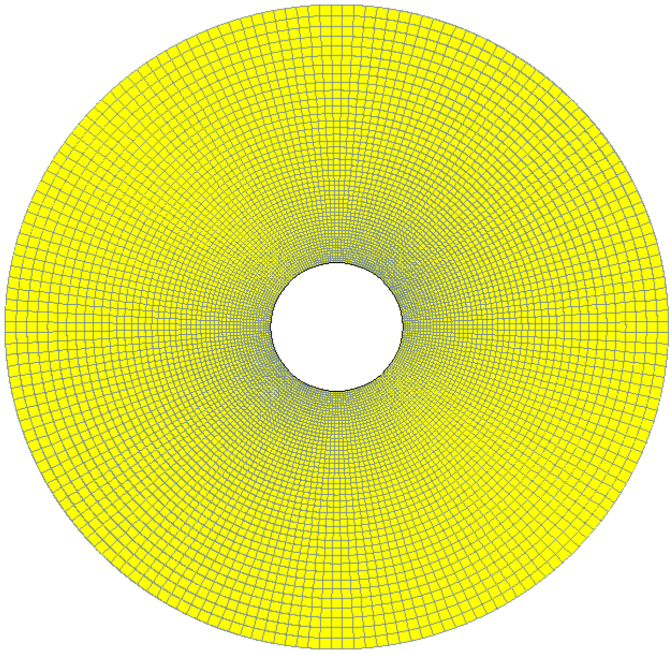

Figure 3.7: Schematic view of a segmented detection layer of the RPC modules. The whole area has been segmented into projective pads of 2-degree angular regions in azimuth.

### 3.1.5 Clustering and hit formation

One or more pads may be affected by a signal formed in a detector due to a traversing particle. The digitized signals from the pads are grouped together to form clusters. The clusters are deconvoluted into multiple sub-clusters that are treated as hits according to an advanced hit finder algorithm or treated as a single hit according to a simple hit finder algorithm based on particle multiplicity and overlapping. The location of a MuCh-hit is allocated to the main cluster in a simple hit finder algorithm or the centroids of the sub-clusters in the advanced hit finder algorithm. The MuCh-hits are considered as candidates for track propagation.

### 3.1.6 Track Reconstruction

The track reconstruction in MuCh is an involved process due to the high track and hit density especially on the first detector planes (see Fig. 3.4) because of huge charged-particle multiplicity created in heavy-ion collisions at CBM energies. The seeds in the track reconstruction algorithm of MuCh is the reconstructed tracks in STS which is based on Cellular Automaton (CA) approach [73].

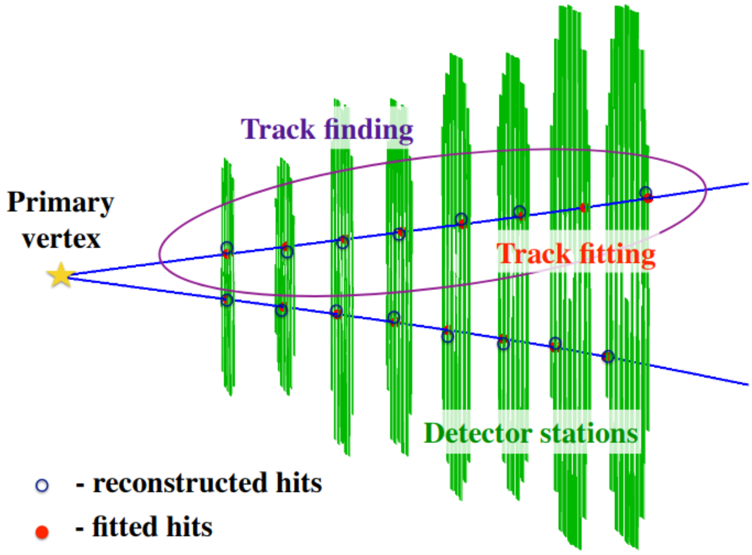


Figure 3.8: Traditional steps of track reconstruction: track finding and track fitting. Track finding groups hit measurements into reconstructed tracks. Track fitting fits reconstructed tracks in order to acquire track parameters afterwards [106].

The track parameters of STS are taken as the onset for successive track prolongation. Tracklets i.e. small track segments are created on adjacent detector planes with this approach and they are combined to form tracks. The track and vertex fitting procedures are formulated on the Kalman Filter (KF) technique [92,93]. The track reconstruction process involves the following steps: track propagation, track finding, track fitting and ultimately a selection of the true tracks.

**Track Propagation :** The track propagation algorithms evaluates the trajectory and related errors in a covariance matrix. Energy loss, multiple scattering, and the effect of magnetic field are the three prime physical processes which are included in the track propagation algorithm. The effect of the material on track momentum is considered during the calculation of average energy loss due to ionization and bremsstrahlung. A Gaussian approximation method based on the Highland formula [107] is used for estimating the average scattering angle. According to the equation of motion of the charged particle in a magnetic field, the propagation of reconstructed trajectory takes place and the $4^{th}$ order Runge-Kutta method [108] is applied for solving the equation.

**Track Finding :** There are two track finding techniques, one is the nearest-neighbor technique where the nearest hit gets associated with the propagated track at each detector station and another is the branching technique where all hits within a specific environment are taken into consideration. Only a single track is propagated further in the nearest-neighbor technique, but multiple track branches are being followed in the branching technique, one for each associated hit. At each detector station, the task of the assignment of new hits is done step-wise. The possibles hits are attached after the track propagates to the next station, and the KF updates the track parameters.

**MuCh Reconstruction :** The track selection is finished after discarding the clone tracks (consists of similar set of hits) and ghost tracks (consists of a random collection of hits) and retaining the correctly identified tracks with high efficiency. The tracks are sorted according to their qualities, such as track length and $\chi^2$. All the hits associated with the tracks are being checked and if a track shares more than 15% of the hits with another track, it gets rejected. The Monte Carlo input also provides information about the performance of the algorithms. The track is considered appropriately found if it composed of more than 70% of hits from a single Monte-Carlo track, otherwise, it is called a ghost track. The associated STS track determines the primary vertex during the track reconstruction in MuCh. The track reconstruction efficiency is defined as;

$$\varepsilon_{track} = \frac{N_{reconstructed}}{N_{accepted}}$$

$N_{accepted}$ is the number of reconstructable tracks in the MuCh acceptance, whereas $N_{reconstructed}$ is the number of befitting tracks after reconstruction.

### 3.1.7 Muon identification and analysis

A set of cuts are applied on the global reconstructed tracks to select muon tracks that are possible to be originated from signals (LMVM, J/$\psi$, etc). The backgrounds generated by non-muonic tracks and muons from weak decays (pions and kaons) need to be rejected. On reconstructed tracks, the following cuts are used to identify muon candidates:

- $\chi^2$ of vertex.
- **STS:** The number of hits in STS and $\chi^2$ of the STS segment of the track.

- **MuCh:** The number of much detection layers and $\chi^2$ of the MuCh segment of the track.

- **TRD:** The number of hits in TRD.

- **TOF:** By applying a $2\sigma/3\sigma$ cut to the reconstructed track mass on the Time of Flight (TOF) wall, the contribution of non-muonic tracks is further reduced.

The muon tracks which satisfy the above set of cuts after reconstruction are considered for the analysis di-muon invariant mass. Each selected muon track is represented by a 4-momentum vector:

$$P_\mu = (E_\mu, p_\mu) \tag{3.1}$$

According to the energy-momentum conservation law, the invariant mass ($m_{inv}$) of the di-muon pair can be written as,

$$m_{inv}^2 = P_{\mu_1\mu_2}^2 = 2m_\mu^2 + 2(E_{\mu_1}E_{\mu_2} - \vec{p_{\mu_1}} \cdot \vec{p_{\mu_2}}) \tag{3.2}$$

Where $m_\mu$ denotes the rest mass of muon, i.e., 105 MeV. The mass $m_{inv}$ is invariant under Lorentz transformation. The other di-muon kinematic variables pair $p_T$, pair rapidity (Y), and the opening/decay angle $\theta_{\mu_1\mu_2}$ defined as the angle between $\vec{p_{\mu_1}}$ and $\vec{p_{\mu_2}}$. Neglecting the mass of muon, the invariant mass can be represented as,

$$m_{inv} \simeq \sqrt{2p_1p_2[1 - cos\theta_1 cos\theta_2 - sin\theta_1 sin\theta_2 cos(\phi_1 - \phi_2)} \tag{3.3}$$

Where $p_i$ is the 3-momentum magnitude, and $\theta_i$ and $\phi_i$ are the polar and azimuthal angles of the single muon tracks, respectively.

The pair $p_T$ from the 4-momentum conservation can be written as,

$$p_{T,\mu_1\mu_2} = \sqrt{p_{x,\mu_1\mu_2}^2 + p_{y,\mu_1\mu_2}^2} \tag{3.4}$$

Where $p_{i,\mu_1\mu_2} = p_{i,\mu_1} + p_{i,\mu_2}$; i, represents the coordinate x,y and z.

The pair rapidity of a particle in the lab frame can be represented by,

$$Y_L = \frac{1}{2} ln(\left(\frac{E + p_z}{E - p_z}\right)) \tag{3.5}$$

where, E and $p_z$ represent the pair energy and longitudinal momentum in the lab frame.

$$Y_L = Y^* + Y_{cm} \tag{3.6}$$

where $Y_{CM}$ is the pair rapidity of the particle in the centre of mass (CM) frame and can be expressed as,

$$Y_{CM} = \frac{1}{2} ln(\left(\frac{1 + \beta_c}{1 - \beta_c}\right) \tag{3.7}$$

where $\beta_c$ is the velocity of the particle at the center of mass of the collision system in the laboratory and can be calculated as

$$\beta_c = \frac{|\vec{P_{lab}}|}{E_{lab}} = \frac{|\vec{P_{beam}}|}{E_{lab} + m_{target}} \tag{3.8}$$

Where $\vec{p_{beam}}$ and $E_{beam}$ represent projectile momentum and energy, respectively, and $m_{target}$ represents the target mass.

### 3.1.8 Kinematics Resolution:

In general, three factors govern the kinematic resolutions of di-muon experiments:

- Muon multiple scattering in the target and hadron absorber,
- muon energy loss in the hadron absorber.
- The proper error of the measurement in the tracking chambers.

The last one is insignificant in comparison to the first two. In contrast to past and existing experiments, the CBM experiment will perform full tracking in the STS detection system upstream to the absorber. As a result, the multiple scattering and energy loss effects inside the absorber will not influence the momentum measurements. In addition, compared to existing measurements, the target thickness of CBM is significantly less, which helps to reduce multiple scattering improving momentum resolution. Only the magnetic field will significantly impact the momentum resolution in such circumstances. It is worth noting that, with a dipole magnetic field of strength B and length L, the momentum resolution of a track with momentum p can be expressed as;

$$\frac{\Delta p}{p} \propto \frac{p}{BL^2} \tag{3.9}$$

The momentum resolution of muon tracks is $\Delta$p/p $\sim$ 1% with the existing dipole magnet designed for tracking. In terms of di-muon mass resolution, recall that we may write by ignoring the muon mass in Eq. 3.3.

$$m_{inv}^2 = 2p_{\mu_1}p_{\mu_2}(1 - cos(\theta_{\mu_1\mu_2})) \tag{3.10}$$

Because the average single momentum rises with mass, multiple scattering, which contributes to angular resolution ($\Delta\theta_{\mu_1\mu_2}$), is more relevant at low masses and does not influence high masses (e.g., J/$\psi$, $\psi'$). On the other hand, as earlier mentioned, energy loss of single muons has a larger impact, which in our scenario is also not extremely significant. We can estimate the expected mass resolution by ignoring the angular resolution:

$$\frac{\Delta m_{inv}}{m_{inv}} = \frac{\Delta p_\mu}{\sqrt{2p_\mu}} \tag{3.11}$$

## 3.2 MuCh Mechanical Integration

The tracking stations of MuCh is subdivided vertically in two half-stations located between two absorbers. Three layers constitute each half-station and each layer is composed of several tracking chambers. There is a provision to move each layer individually in x-direction between the operation position in the gap between the absorbers and a easily accessible service position.

The RICH detector system in the electron setup will replace MuCh in the muon setup with a typical time between configuration changes of several months. Therefore, the mechanical construction of the MuCh system requires a rail system for the ease of transport-ability [109]. The MuCh detector system has two geometry configurations, the compact configuration and the service configuration, due to sharing the same location with RICH [109]. The available space for MuCh gets constrained when RICH detector is taking data or in it's nominal parking position. An installation space of 6400 mm wide is dedicated for the MuCh system [109]. The Superstructure is attached to transverse beam extensions with rails which enables to shift the layers and halves of absorber 1 for maintenance in service configuration outside the absorbers.

The short platform with hydraulic push-pull drive which moves along rails using Hillman rollers is selected as the baseline variant of the MuCh platform [109]. Four first absorbers and the detection elements are supported by the short platform, while the standalone fifth absorber is placed on the separate foundation and is dismantled before MuCh detector is displaced to the parking position. The total movable weight is slightly more than 100 ton [109]. The operation and parking positions of the platform are represented as the stable position. The operation position is denoted by the position of the stations and the absorber 1 around the beam. The service position is denoted by the detection layers and the halves of the absorber 1 positioned outside the external outline of MuCh.

Non-magnetic stainless steel is used for making the basic structural elements such as the platform, brackets, rollers, adjustments and fixing elements. The material used for the wheel rim and guide is Steel 40X GOST 4543-71, or similar [109].

### 3.2.1 Design of the absorbers

The absorbers are designed following these conditions [109],

- A specified tolerance limit of ± 1 mm along X, Y and, Z axis during the assembling and positioning of the absorbers.
- The absorber 4 can be installed or dismantled without disassembling the tracking stations 1 and 2.
- the deviation on the envelope of the surface of each absorber ( due to surface non-planarity and misalignment during installation) should not exceed 5 mm in the plane perpendicular in the beam direction, so that the tracking layers can be moved freely from the operational position to the servicing position.

Absorber 1, made of 28 cm of graphite (density 1.78 g/cm$^3$) and 30 cm of concrete (density 2.3 g/cm$^3$), has a shape of a rectangular parallelepiped with a trapezoidal protrusion which matches

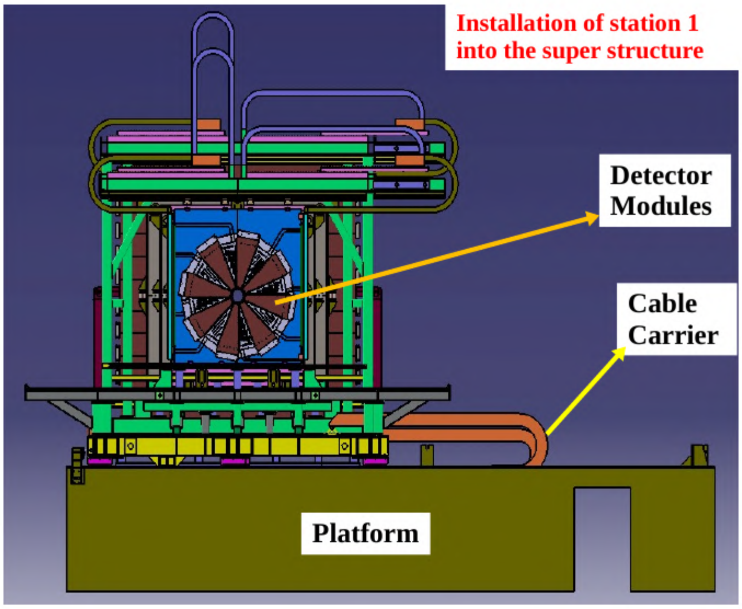


Figure 3.9: The layout of mechanical structure of MuCh setup [100]. Superstructure will hold the detector stations as shown. To handle the cables, cable carriers are installed.

the notch in the yoke of the dipole magnet. It is located at the beam axis in the range of 1250 < Z < 1830 mm. The absorber 1 consists of two mirror-symmetrical halves. A step of 25 mm high at the contact surface of the two halves prevent the direct passage of the particles through the gap between the halves. A conical-shaped aluminum-lead insert works as a shield in the central part of the absorber 1 (around the beam pipe) [109]. It ensures the passage of the beam pipe which has a conical shape with an opening angle of $\theta < 2.5°$) and wall thickness of 1 mm. The spatial and angular tolerances of the position of absorber 1 should be ± 1 mm and ± 0.1° respectively. The vertical position of the absorber 1 can be adjusted coarsely by spacers and finely by a screw-nut threaded pair. The design of an absorber half is a 4-mm thick aluminium case filled with concrete and graphite blocks.

The absorber 5 is a rectangular parallelepiped shaped cast iron block located on the beam axis at position 3770 < Z < 4770 mm sitting on a welded support [109].

The entire MuCh system like detector layers, absorbers, cable carriers etc is shown in Fig. 3.9. The detailed discussion about the assembly of the tracking chambers can be found in [100].

# Chapter 4

# Detector Physics of Resistive Plate Chambers

## 4.1 Historical Development

Gaseous particle detectors have played a crucial role from the early stages in particle detection for High Energy Physics (HEP) experiments. The main principle behind the operation of a gas detector is the physical process of gas ionization. The passage of a charged particle produces ion-electron pairs while traversing through the gas gap. These charge carriers are accelerated by the electric field applied across the electrodes and produce secondary ionizations provided they have enough energy. The charge multiplication causes an avalanche of charge carriers inside the detector. Although the main principle behind each gas detector is nearly the same, the process of charge multiplication and charge collection differ significantly from one gas detector to another. The first gas detector invented in 1908 by Rutherford and Geiger [110] was based on a cylindrical geometry to detect alpha particle. In 1928, the early Geiger counter was improved to detect $\beta$ and $\gamma$ along with $\alpha$ particle by Geiger and Muller and it is known as Geiger-Muller counter [111]. Primary electrons created due to the traversing charged particle are collected at a central anode wire on a cylindrical shaped geometry and the avalanche process occurs in a region immediately surrounding the central wire. This is due to the fact that cylindrical geometry leads to a inversely proportional electric field to the distance from the wire, $E \propto 1/r$. Depending upon the position of the primary ionization, the primary electrons need to drift for a variable time before reaching the multiplication region surrounding the wire to be able to form a detectable signal after avalanche. The time resolution of a wire detector is limited due to the fluctuations in the drift time of the primary electrons [112]. A better time resolution is achievable in a planner geometry with a uniform electric field. The whole detector volume in a planner geometry is available for charge multiplication and the primary electron can start an avalanche immediately after creation without the need to travel to the amplification region. Therefore, the timing fluctuations in a parallel-plate gas detector is much smaller than in a cylindrical gas detector since there is no separate region for drift and multiplication process. The first gas detector based on the planner geometry utilizing the uniform electric field was the spark counter invented by J. W. Keuffel in 1948 [113,114]. The spark counter indeed offered a time resolution around 5 ns which exceeds the time resolution provided by any of the Geiger-Muller counters present at that time ($\sim$ 100 ns) [115]. An enclosed gas volume by two parallel metal electrodes where the high voltage is applied was the general design for Keuffel's spark counters. A Townsand avalanche is triggered immediately due to the intense uniform electric field after a charged particle causes primary ionization in the gas gap. The avalanche transforms into a streamer when the photons created in the recombination process start contributing in the avalanche growth. The streamers form a conducting channel between the two parallel electrodes and a spark is created when the electrodes are discharged via this channel. A fast voltage signal is generated from the rapidly growing anode current via a resistor and the signal marks the arrival time of the charged particle. The large voltage signal in the spark counters omits the further amplification stages of the signal, thereby reducing the electronics time jitter. The spark counter could not work without an external switching-off circuit after the passage of a charged particle to prevent the metal electrodes from being short-circuited. The fact that the spark counters had to be switched off for a relatively long time after the detection of a charged particle introduces a long dead time ($\sim$ 1 s) on the counter which imposes a stringent limit of the maximum flux of particles that it could sustain. Since the surface of the electrodes in a spark counter gets heavily damaged by the large discharge energy from the spark, the area of detector is limited to the order of few cm$^2$. To overcome these problems, a new kind of spark counters with localized discharge has been introduced in 1971 by Pestov's group [116]. The metal electrodes got substituted by resistive electrode materials (glass) for limiting the progress of sparks and a special gas mixture with photon absorption property has been used. The main advantage of the use of resistive electrodes is that there is no need for a High Voltage (HV) switching-off circuit and thereby higher detection rate can be achieved. Pestov's Planar Spark Chamber (PSC) achieved a best possible time resolution of 25 ps with 0.1 mm gas gap and 12 atm gas pressure [117]. However, excellent surface smoothness of the inner side of electrodes are necessary for Pestov's PSC due to the combination of the very thin gas-gap (0.1 mm) and very high values of the electric field (500 kV/cm). The necessity of the operation of Pestov's counters at high pressure to ensure a large density of primary ionization in the thin gap further limits their manufacturing as large area detectors. In the middle of 1970's, Parallel Plate Avalanche Chamber (PPACs) has been developed which is very similar to the spark chamber, but operates in avalanche regime. Streamers and discharges are undesirable side effects in PPAC. The detector is made of two metal/metallized ceramic electrodes and a few mm gas gap defined by the distance between the electrodes is filled with organic gases at low pressure (less than 3 mbar). Due to its operation in the avalanche mode, the PPAC detectors achieved a time resolution of 100 to 250 ps [118–120] quite independently on the detector area and a rate capability up to 10 MHz/cm$^2$ [121]. To detect the minimum ionizing particles, the detectors work with a gas gain of $10^3$ to $10^4$ and the discharge probability is also very low ($10^{-5}$) for these kind of detectors. Due to the very low signal strength $\sim$ 100 fC [118] in PPAC, a very good signal-to-noise ratio and sensitive electronics is necessary to detect the signals in PPAC with good efficiency. But the fast rise time needed for the timing purposes gets compromised due to this very low noise and sensitive electronics.

## 4.2 Resistive Plate Chamber

In 1981, Rinaldo Santonico and Roberto Cardarelli in Rome has developed the first prototype of the modern Resistive Plate Chambers (RPCs) [122] with the intention of overcoming the difficulties inherent to the Pestov's Spark Counter while retaining its more fundamental virtues like the possibility of operation at very high electric fields avoiding the detector breakdown. As the Pestov's Spark Counter and PPAC, RPC is a particle detector with two parallel electrode plates and at least one of the electrode plates is made of a material with high bulk resistivity. The first prototype of RPC (85 $\times$ 13 cm$^2$) employs 2 mm thick high resistive electrode plates made of high pressure laminate (HPL) phenolic resin, namely bakelite, having a bulk resistivity of the order of $10^{10}$ -

$10^{11}$ Ω-cm. The plates enclosed a gas-gap of 1.5 mm filled with a gas mixture of Ar and isobutane in 1: 1 proportion. The main advantage of RPC compared to the Pestov counter is the low requirements of mechanical precision due to the 'wide' gas-gap (1.5 mm vs 0.1 mm) and as a result, the gas circulates at the atmospheric pressure instead of high pressure. A rectangular frame of 1.5 mm thick PVC (polyvinyl chloride) was inserted between the two electrodes plates to keep them separated and parallel to each other and also for gas containment. HV was applied to one of the bakelite plates through a thin foil of conducting paper glued to the bakelite surface. The surface resistivity of the conducing foil was high $\sim 1$ MΩ/□ which made it transparent to the electrical pulses originated inside the gas-gap. In modern day RPCs, the bakelite sheets are generally coated with thin layers of a conductive paint, typically containing graphite, for the purpose of creating a uni-potential surface, characterized by a surface resistivity of 200-300 kΩ/□ range. Moreover, a 0.2–0.3-mm-thick layer of mylar or polyethylene glued on the graphite coated electrode is used to ensure insulation between the electrodes and the readout strips. For the first RPC prototype, the inner surfaces of the bakelite plates were treated with linseed oil for surface-smoothness so that the applied electric field is uniform and noise level is low. The signal was measured with copper pick-up strips, separated from the HV foil through a 3 mm thick PVC plate glued on the conducting paper. According to the present convention, the detector was operated in streamer mode with signal amplitude typically reaching 300 mV over 25 Ω allowing a high simplification of the electronics. The detector achieved an efficiency of 97% in detecting cosmic muons with a time resolution of $\sim 1$ ns at an operating voltage of about 10 kV. RPC detectors need conditioning after switching on for the first time. The preliminary elevated values of current and counting rate gradually decrease almost one or 2 orders of magnitudes by keeping the detector on during a time span ranging from a few days to a couple of weeks. Apart from bakelite, float glass with a resistivity of around $10^{12}$ - $10^{13}$ Ω-cm is also used as electrode material in the construction of a RPC. The schematic diagram of a RPC is shown in Fig. 4.1. The fundamental operational principle of a RPC is well-known. The applied HV to the parallel plate electrodes creates a uniform electric field in the gas-gap. When a charged particle passes through the RPC gas-gap, it ionizes the gas and leaves free charge carriers. The charge carriers are drifted towards the respective electrodes due to the uniform electric field and trigger further ionizations. Therefore, a avalanche of charge carriers originate in the gas-gap. The propagation of the free charges in the gas-gap induces a

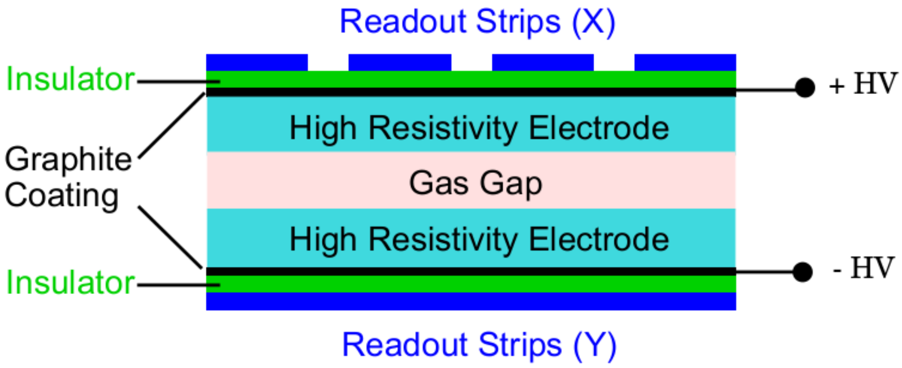


Figure 4.1: The schematic diagram of a RPC geometry [123]

signal on the readout electrode. The high resistivity of the electrodes prevents the avalanche from propagating through the whole gas volume. The electric field is dropped down in a limited area around the point where the avalanche occurred. The detector has a blind spot around this point, but the remaining area of RPC is still sensitive for the detection of charged particles.

## 4.3 Working Principle of RPC

### 4.3.1 Primary Ionization in gas

When a charged particle traverses the RPC gas volume, it transfers part of its energy by going through a series of stochastic interactions with atoms and molecules. The fundamental mechanism underlying the operation of RPC is inelastic diffusion, most specially ionization. If the traversing particle ionize the atom in the gas by the inelastic collision, free electron-ion pairs are created close to the position of the encounter. There remains a possibility that the atom is not ionized by the traversing particle, but brought to an excited state. Then, the excited atom promptly loses the excitation energy, thereby returns to the ground state either by the emission of a photon or an Auger electron or causing ionization through collision (Penning effect). These electrons and photons can further ionize other atoms and so on. This multiplication process ceases after the ionization potential of the atoms in the gas becomes larger than the energy of the emitted particles. The important characteristics of the avalanche and signals in RPC detector depend upon the this initial ionization induced by passage of a charged particle. Free primary electrons can also appear in the RPC gas-gap by emission from the cathode by photoelectric effect upon irradiation by ultraviolet photons.

### 4.3.2 Energy loss by a charged particle

For a heavy charged particle of mass M >> $m_e$, the Bethe-Bloch formula gives the mean energy loss per unit path length by the charged particle traversing a medium through excitation and ionisation processes,

$$-\frac{1}{\rho}\frac{dE}{dx} = K.z^2.\frac{Z}{A}.\frac{1}{\beta^2}\left[\frac{1}{2}\ln\frac{2m_ec^2\beta^2\gamma^2T_{max}}{I^2} - \beta^2 - \frac{\delta(\beta\gamma)}{2}\right] \tag{4.1}$$

where,

$\rho$ - density of the medium, K - a constant defined by, $K = 4\pi N_A r_e^2 m_e c^2$,

$r_e$ - classical electron radius, $r_e = \frac{1}{4\pi\varepsilon_0}\frac{e^2}{m_ec^2}$,

e - the electron elementary charge,

$m_e$ - the electron mass,

$N_A$ - the Avogadro's number,

$z$ - the charge of the incident particle,

$Z$ - the atomic number of the medium,

$A$ - the atomic mass of the medium,

$\epsilon_0$ - the dielectric constant in vacuum,

$\beta$ - the velocity of the particle , $\beta = \frac{v}{c}$,

$c$ - the speed of light,

$\gamma$ - the Lorentz factor, $\gamma = \frac{1}{\sqrt{1-\beta^2}}$,

$T_{max}$ - max. energy transfer in a single collision,

$I$ - the mean excitation potential,

$\delta$ - the density effect correction.

The energy loss of a positive muon on copper due to ionization and excitation is illustrated in Fig. 4.2. The density effect correction becomes important for muon momenta, $p \geq 200$ MeV/c. The maximum energy transfer in a single collision by a particle with momentum $p$ is given by,

$$T_{max} = \frac{2m_ep^2}{M^2 + 2\gamma m_e M + m_e^2} \tag{4.2}$$

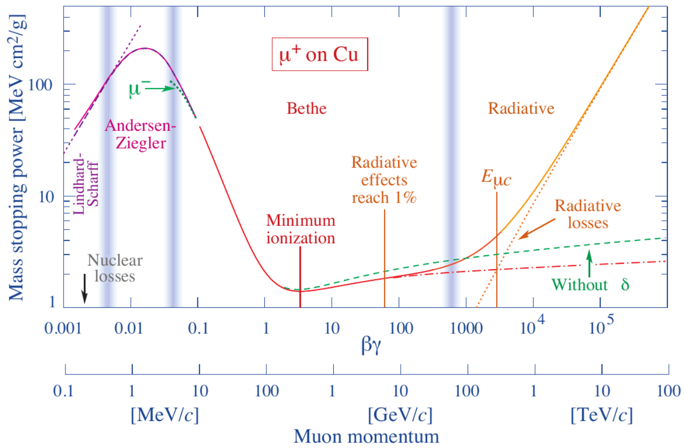


Figure 4.2: The energy loss - $\frac{1}{\rho}\frac{dE}{dx}$ for positive muons in copper as a function of $\beta\gamma = p/mc$ due to ionization and bremsstrahlung. The curves for the energy loss due to ionization and excitation with and without density effect ($\delta$, green-dashed) correction are shown. The critical energy is denoted by $E_{\mu_c}$, at which the energy loss due to bremsstrahlung (orange, dotted) equals the energy loss due to ionization (red, dot-dashed). The total energy loss summing over the two effects are denoted by the solid curve [124, 125].

The Bethe-Bloch equation is particularly valid for heavier particles. The equation needs to be modified for electrons colliding with atomic electrons since the primary and secondary electron are indistinguishable after collision due to their equal mass. Energy loss by electrons via radiative process is known as bremstrahlung which becomes dominant over the ionization process. Fig. 4.3 shows the mean energy loss for different incident particles and different media.

### 4.3.3 Cluster Density Distribution

A cluster is defined as the collective number of primary electron-ion pairs generated by a charged particle while it crosses the RPC gas-gap and any additional electron-ion pairs generated by the energetic primary electrons and photons [126]. If a number of $n_{cl}$ clusters are formed in a single-gap RPC of gap width $g$ due to the ionizing particle, then the average value of the number of clusters per unit length i.e. cluster density is defined as $\lambda = \frac{n_{cl}}{g}$. $n_{cl}$ is a stochastic variable which depends upon the thickness of the gas-gap $g$. For a particle crossing the gas-gap with an azimuthal angle $\phi$ with the normal to the electrode surface, cluster density is defined as $\lambda_{eff} = \frac{\lambda}{cos\phi}$. The cluster densities for several gases have been calculated with the program HEED as shown in Fig.4.4. Since the energy loss in the gas by a relativistic high energy particle is negligible compared to it's initial

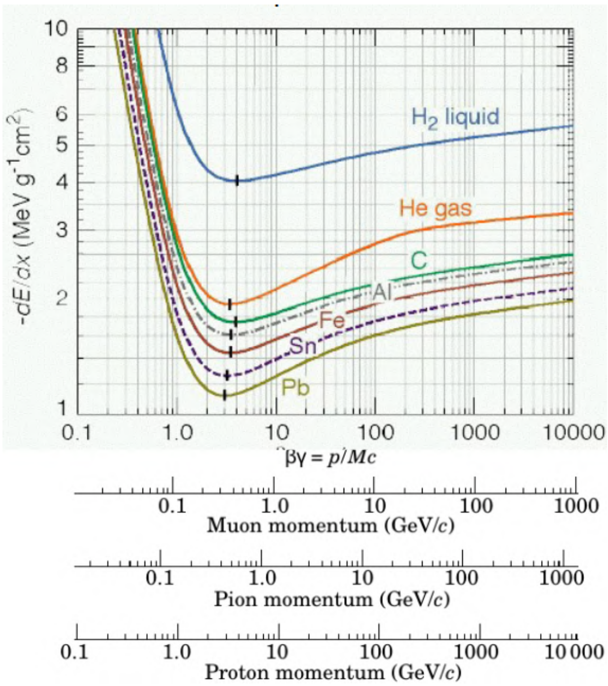


Figure 4.3: The energy loss on account of excitation and ionization in liquid hydrogen, helium gas, carbon, aluminum, iron, tin, and lead [123, 124]

energy, the cluster density is constant throughout the entire gas-gap. On average, a minimum ionising particle produces 7.5 clusters per mm in a typically used RPC mixture. The probability of generating q clusters in the gas gap of thickness g follows a Poisson distribution [127],

$$P_{cl}(n_{cl} = q) = \frac{(g\lambda_{eff})^q}{q!} e^{-g\lambda_{eff}} \tag{4.3}$$

The average value of this probability distribution is $g\lambda_{eff}$ which is simply the cluster density multiplied by the track length. The probability of finding zero cluster in the entire gas-gap is,

$$P_{cl}(n_{cl} = 0) = e^{-g\lambda_{eff}} \tag{4.4}$$

which is the intrinsic inefficiency of RPC. Theoretically, if the gas gain is infinite or a zero value of threshold is applied to the signal, it is possible that all the primary clusters created in the gas gap are detected. Then, the maximum detection efficiency of RPC to be achieved is given by,

$$\epsilon_{max} = 1 - e^{-g\lambda_{eff}} \tag{4.5}$$

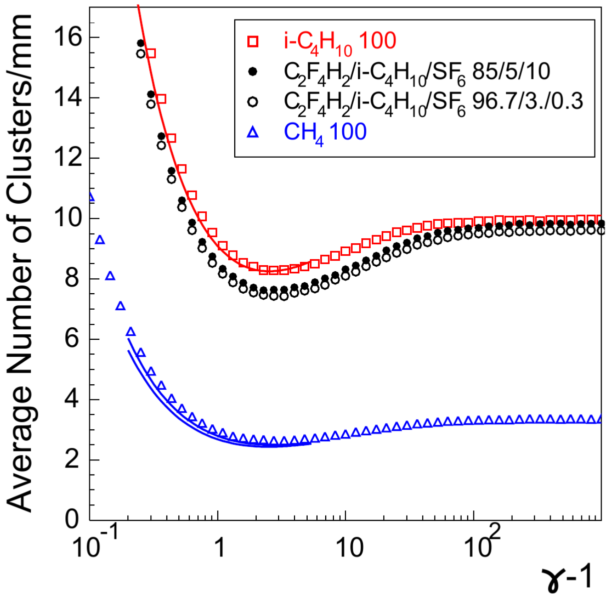


Figure 4.4: Average number of primary clusters per mm as a function of $\gamma$ - 1 predicted by HEED with gas temperature and pressure set to T = 296.15 K and p = 1013 mbar respectively for typical gases used in gaseous detectors. The gas mixture $C_2H_2F_4$:$iC_4H_{10}$:$SF_6$::96.7%:3%:0.3% is generally used for RPC. The solid lines show measurements from [128]. The figure is taken from [129].

Therefore, a narrow gap RPC has lower intrinsic efficiency than a wide gap RPC.

### 4.3.4 Cluster Size Distribution

The probability distribution of the dimensions of the clusters, in terms of the number of electron-ion pairs contained in each cluster is called the cluster size distribution. It depends upon the amount of exchanged energy during the interaction, which can fluctuate considerably. The secondary electrons in a cluster is generally very close in space to the primary electrons. The cluster size can reach upto 100 or more in case of delta rays i.e. very high energetic primary electrons which is a rear phenomenon. The primary clusters are exponentially distributed in the gas gap. Therefore, the probability of finding the first cluster between a position x and x + dx is given by,

$$P_{cl}^{1}(x_0^1) = \lambda_{eff} e^{-x\lambda_{eff}}, 0 < x < g \tag{4.6}$$

The average distance of the first primary cluster from the cathode (assuming the cluster generated closest to the cathode) is $1/\lambda_{eff}$. The position of the second cluster in the gas gap will be according

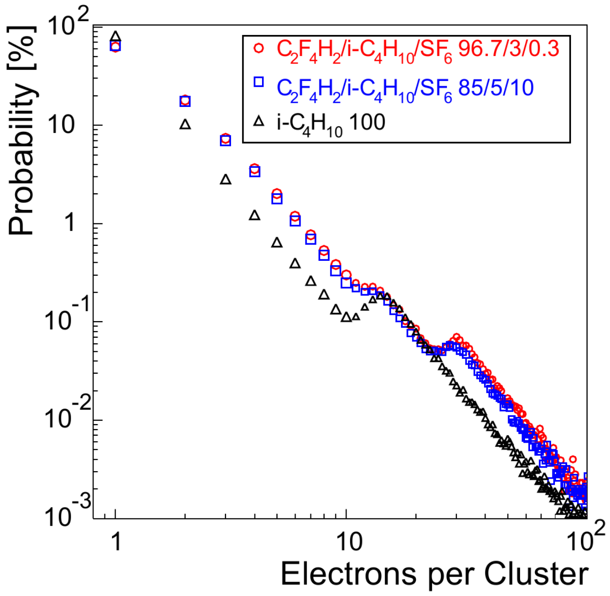


Figure 4.5: Cluster size distribution predicted by HEED [132] for two typical RPC gas mixtures and for pure iso-butane with gas temperature and pressure set to T = 296.15 K and p = 1013 mbar respectively. A 120 GeV muon for the 0.3% $SF_6$ mixture and a 7 GeV pion for iso-butane and for the 10% $SF_6$ mixture were used as incident particle in the simulations. With a cut at 500 electrons, the average cluster sizes are 2.8 for the 0.3% $F_6$ mixture, 2.6 for the 10% $SF_6$ mixture and 1.9 for isobutane. Figure is taken from [123].

to

$$P_{cl}^2(x_0^2) = x\lambda_{eff}^2 e^{-x\lambda_{eff}}, 0 < x < g \tag{4.7}$$

and the average distance from the cathode is $2/\lambda_{eff}$. Similarly, the probability to find the nth cluster between the position x and x + dx, independent of the position of other clusters is given by [130, 131],

$$P_{cl}^n(x_0^n = x) = \frac{x^{n-1}}{(n-1)!}\lambda_{eff}^n e^{-x\lambda_{eff}}, 0 < x < g \tag{4.8}$$

with an average distance from the cathode of $< x_0^n >= n/\lambda_{eff}$.

Therefore, the probability to find a cluster size between $n$ and $n + dn$ is,

$$P(n)dn = \frac{\mu^n}{n!} e^{-\mu} dn \tag{4.9}$$

where, $\mu$ is the average cluster size.

The distribution of the cluster size is shown in Fig. 4.5 and it follows a curve of $\frac{1}{n^2}$. The mean cluster size is about 2.8 electrons for 0.3 % $SF_6$ content RPC gas mixture with a cut of 500 electrons set for the simulation.

### 4.3.5 Diffusion and Drift of Charge Carriers and Avalanche Multiplication

Primary charge carriers in a gas collides randomly with the gas molecules due to the thermal motion and this process is called diffusion. The energy distribution of the charge carriers follows a Maxwell-Boltzmann distribution around the mean $< E > = \frac{3}{2}$kT $\approx$ 40 MeV, where k represents the Boltzmann constant and T denotes the temperature of the gas in Kelvin. The diffusion is isotropic when the gas is not influenced by an electric field and it follows a Gaussian distribution with $\sigma = \sqrt{2\overline{D}t}$ which depends on time. $\overline{D}$ is the Diffusion co-efficient. The narrowness of the gap enable a homogeneous and strong electrical field across the gap due to the voltage applied to the electrodes. Primary electron-ion pairs are subjected to a constant drift motion due to the applied electric field in addition to the thermal diffusion. The diffusion becomes anisotropic due to the presence of electric field and it has two components, longitudinal diffusion and transverse diffusion. The primary electron-ion pairs start drifting towards the respective electrodes (electrons towards anode and ions towards cathode) due to the homogeneous electric field $\vec{E}$ which has a typical value of $|\vec{E}|$ = 50 kV/cm in a single gap RPC. When an electron or an ion passes through a distance of $\delta$z in the electric field $\vec{E}$, they acquire a kinetic energy which is given by [123, 133],

$$T_{el} = e.|\vec{E}|.\delta z \tag{4.10}$$

with e = 1.6022 $\times$ $10^{-19}$ C, the unit charge. The drift speed of the positive ions is about 1000 times smaller than that of the electrons due to the huge difference in mass, the ions are essentially static in the time frame of the electrons. The electrons take of the order of a few nanoseconds to reach the anode for an electric field in the range of 50-100 kV/cm while the positive ions require a few microseconds to reach the cathode. The primary electrons gain enough energy (1 eV) within a distance of about 100 nm to collision-ionize the other gas molecules and they accelerate again until other molecules are getting hit. The process is occurring repeatedly for secondary and tertiary electrons and eventually there is an avalanche of electrons en route the anode. Averaging over a large number of collisions, the electron moves at a constant drift velocity $\vec{v}_D = \mu\vec{E}/$p where p is the gas pressure and $\mu$ is a coefficient called mobility. The drift velocity as a function of the electric

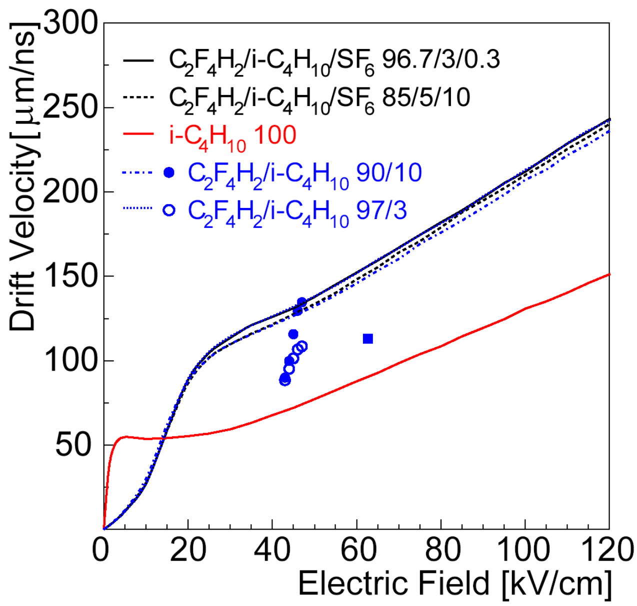


Figure 4.6: Drift velocity versus electric field calculated with MAGBOLTZ for two typical RPC gas mixtures and for pure $iC_4H_{10}$ [123] with gas temperature, T = 296.15 K and gas pressure, p = 1013 mbar. The square shows a measurement from [135] for $C_2H_2F_4/iC_4H_{10}/SF_6$ :: 96.9%/3%/0.1% and the circles show measurements for two different gas mixtures from [136].

field in different gases in shown in Fig. 4.6 calculated with the program MAGBOLTZ [134]. During the drift, each of the primary electron has a certain probability to create an additional electron-ion pairs per unit length which is represented by the Townsand coefficient ($\alpha$) with the basis of the assumption that any scattering event is independent of any previous events. If the initial number of electrons at position $z$ is $n$, then the probability of having $n$+1 electrons at a position $z + dz$ is given by $n\alpha dz$ [129]. At the same time, the capture of electrons per unit length by a gas molecule is represented by the attachment coefficient ($\eta$). The probability of an electron getting attached and thereby forming a negative ion over a distance $z$ is $n\eta dz$. The average number of electrons $\overline{n}$ and positive ions $\overline{p}$ can be calculated from these equations [129, 137, 138],

$$\frac{d\overline{n}}{dz} = (\alpha - \eta)\overline{n}, \quad \frac{d\overline{p}}{dz} = \alpha\overline{n} \tag{4.11}$$

The ionization and attachment rates can be approximated as constants due to the constant drift velocity of electrons and the dependence of the scattering cross-sections on the energies of electrons. The solutions of the previous differential equations with the boundary conditions $\overline{n}(0) = 1$, $\overline{p}(0)$=1 and assuming $\alpha$ and $\eta$ as constants are given by [129,137,138],

$$\overline{n}(z) = e^{(\alpha-\eta)z}, \qquad \overline{p}(z) = \frac{\alpha}{\alpha-\eta}(e^{(\alpha-\eta)z} - 1) \tag{4.12}$$

The average number of electrons follows an exponential growth or decay depending upon the effective Townsend co-efficient $\alpha_{eff}$ = $\alpha$ - $\eta$. For a standard single gap RPC, the value of the effective Townsand co-efficient is around 10/mm at an electric field of 50 kV/cm. It increases linearly with an increase in the electric field. Fig. 4.7 shows the variation of the Townsand co-efficient, attachment co-efficient and the effective Townsand co-efficient in a typical RPC gas mixture with electric field as calculated with the program IMONTE [139]. If an avalanche starts with a single electron, then the probability P(n,z) of having n electrons in the avalanche after a distance z is given by [129,138],

$$P(n,z) = \begin{cases} k\dfrac{\overline{n}(z)-1}{\overline{n}(z)-k} & \text{if n} = 0, \\ \overline{n}(z)\left(\dfrac{1-k}{\overline{n}(z)-k}\right)^2\left(\dfrac{\overline{n}(z)-1}{\overline{n}(z)-k}\right)^{n-1} & \text{if n} > 0 \end{cases} \tag{4.13}$$

with $k = \frac{\eta}{\alpha}$. The variance $\sigma^2(z)$ of the probability distribution is given as,

$$\sigma^2(z) = \left(\frac{1+k}{1-k}\right)\overline{n}(z)(\overline{n}(z)-1) \tag{4.14}$$

Therefore, it is evident that the variance and the distribution itself not only depends on the effective Townsand co-efficient $\alpha_{eff}$, but also on $k = \frac{\eta}{\alpha}$ explicitly. The probability distributions for the same effective Townsand co-efficient but different values of $\alpha$ and $\eta$ are shown in the left plot of Fig. 4.8. The polya distribution can also be used for the determination of the charge spectrum. Although it neglects the contribution from the attachment, it parameterizes the measured curves in a nice way. The simulation of avalanche development is necessary for the calculation of the induced signal instead of using the probability distribution for the final avalanche charge. The avalanche is simulated by dividing a gas-gap into N steps of $\Delta$z. The avalanche multiplication ($\overline{n}(\Delta(z))$) for a single electron starting at one edge of the gas-gap over this $\Delta$z distance is given by $e^{(\alpha-\eta)\Delta z}$. Individual avalanches starting from a single electron is shown in the right side plot

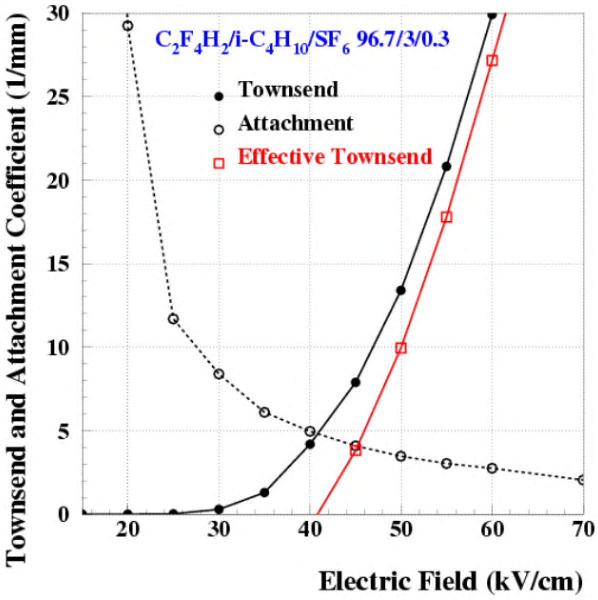


Figure 4.7: Townsend and attachment coefficient as function of the electric field calculated with IMONTE for the gas mixture $C_2H_2F_4/iC_4H_{10}/SF_6$::85%/5%/10% and for pure $iC_4H_{10}$ [123]. The temperature and the pressure of the gas was set to T = 296.15 K and p = 1013 mbar respectively.

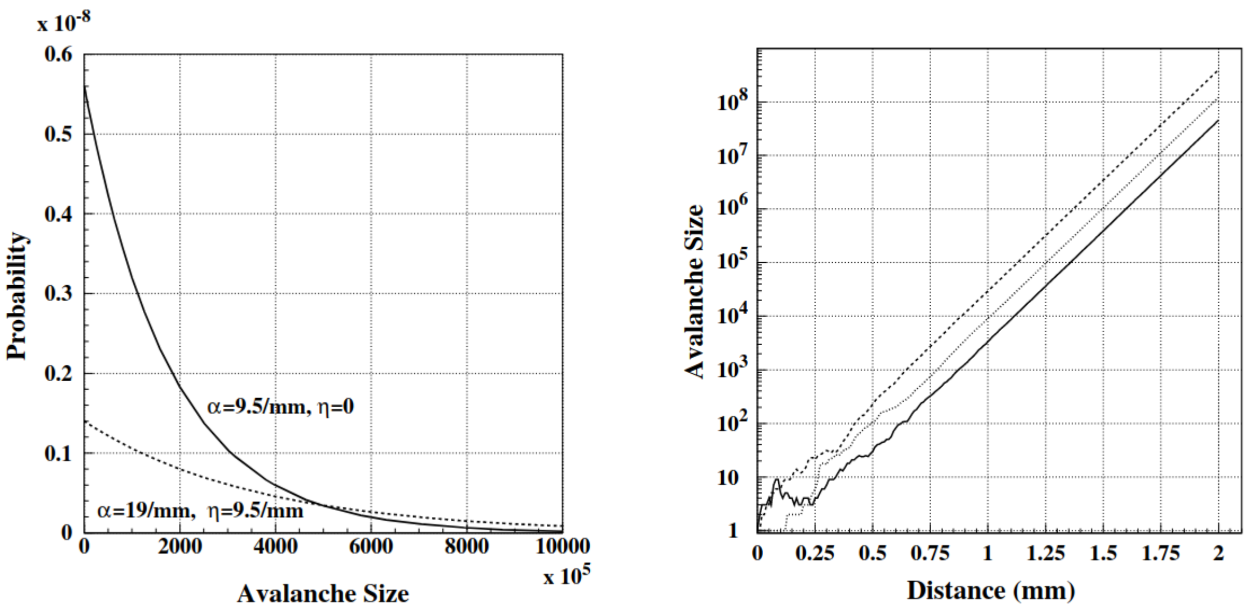


Figure 4.8: (Left) The charge distribution for avalanches which are triggered with a single electron. The effective Townsend coefficient $\alpha_{eff} = \alpha - \eta$ is the same for both curves [129]. (Right) Simulated avalanches starting from a single electron at $z = 0$ for $\alpha = 13$/mm and $\eta = 3.5$/mm [129]. The exponential growth of the avalanche $e^{(\alpha-\eta)z}$ is clearly visible once the avalanche contains about 100 electrons.

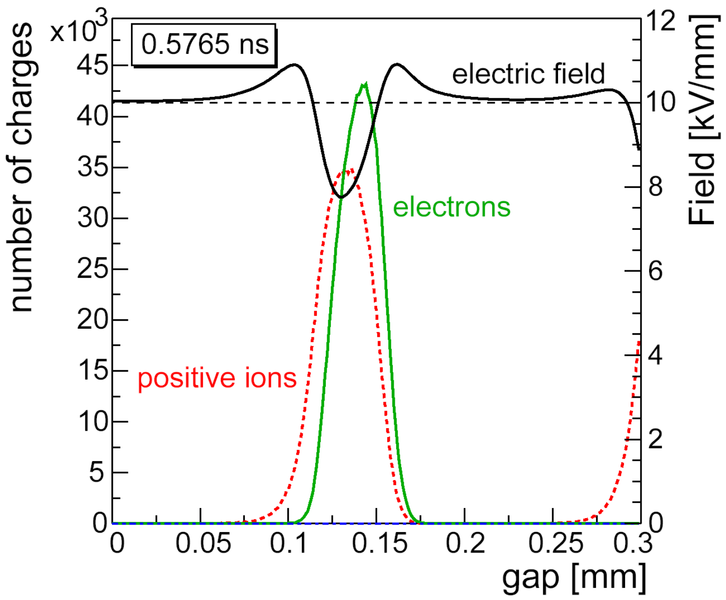


Figure 4.9: A picture of a simulated avalanche is captured after a duration of 0.5765 ns. The electric field (black line) gets modified locally due to the contributions from electrons (green line) and ions (red dashed line) and thereby, the effective Townsend coefficient changes in this region [123].

of Fig. 4.8. The final avalanche size gets decided in the very beginning of the avalanche. The Fig. 4.9 is a snapshot of a simulated avalanche after 0.5765 ns duration. The green line represents the distribution of electrons which are drifting towards the right side. The black line and the dashed red line represent the electric field in the gas-gap and the distribution of positive ions respectively.

The electric field gets diminished due to the cloud of electrons which already arrived on the anode and remains on the surface of the resistive material. As a result, the positive ions in the anode also get depleted. At the tip and tail of the avalanche, the electric field is increased. The electric field is decreased at the center of the avalanche. The effects are shown in Figs 4.9 and 4.10. This is known as the space-charge effect. Due to the lower value of the electric field, the electrons which are mostly residing at the centre of the avalanche go through little multiplication or get attached forming negative ions. Although the value of electric field on the edges of the cluster is very high, almost two times than that of the applied electric field resulting in very large Townsand coefficients, the effect on the avalanche is negligible due to a very low density of electrons in these regions. A dynamical calculation of the electric field that is perceived by the electrons is necessary for the detailed simulation of the avalanche development. Also, the predicted large avalanche statistics get suppressed by the space charge effect. The electron density in a simulated avalanche which is

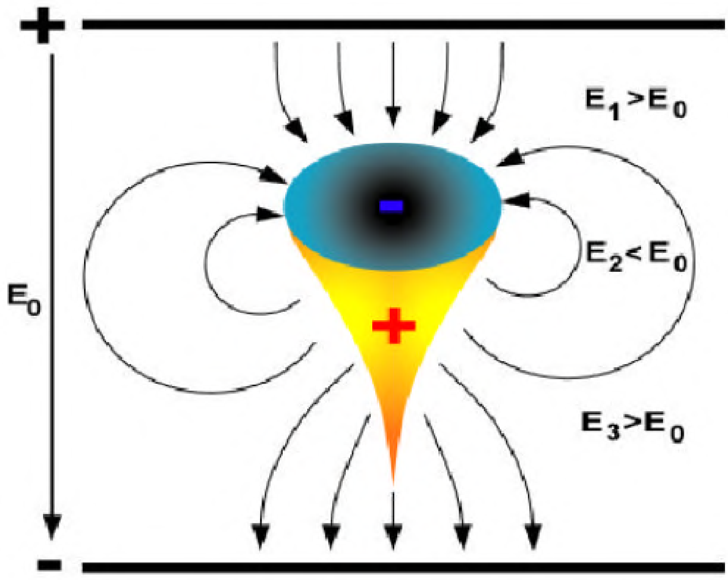


Figure 4.10: A schematic representation of an avalanche and a deformed electric field caused by the charge carriers due to the space-charge effect. The applied electric field $E_0$ is lower than the fields at the tip ($E_1$) and at the tail ($E_3$) of the cluster. $E_0$ is greater than the electric field $E_2$ in the center of the cluster. Therefore, the values of drift velocity, attachment, Townsand and diffusion coefficients are not uniform in the gas-gap.

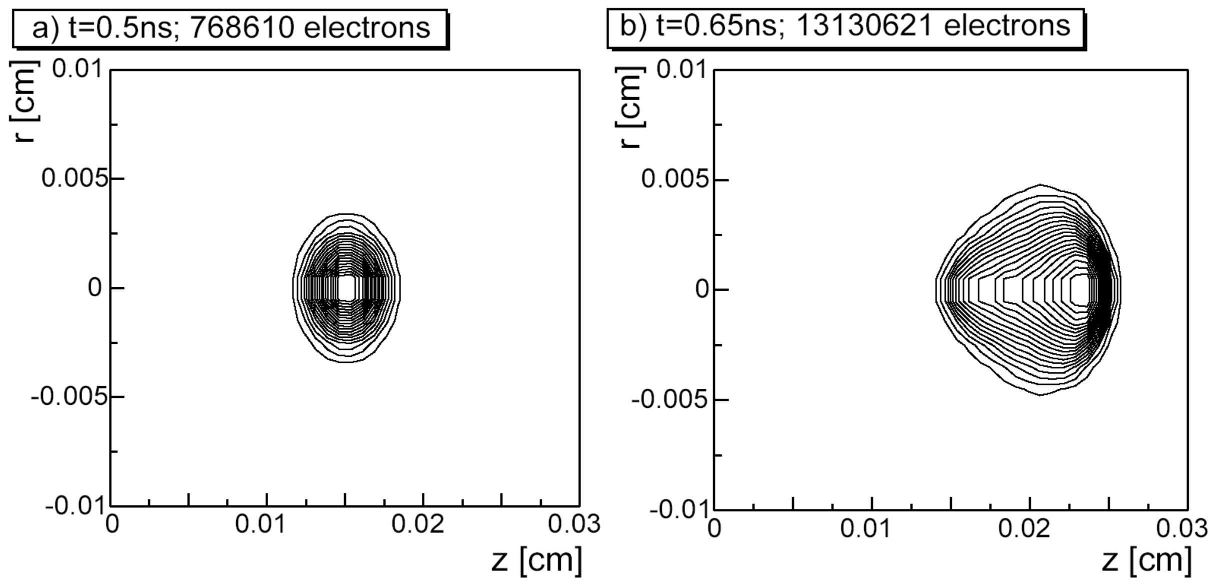


Figure 4.11: Contour plots of electron density in an avalanche captured at t = 0.5 ns and t = 0.65 ns in a 0.3 mm gap Timing RPC operating at 2.8 kV with the standard gas mixture. The avalanche in (a) contains about $8 \times 10^5$ electrons leading to a roughly symmetric distribution. 0.15 ns later (b) the number of electrons increased to about $1.3 \times 10^7$. The density is not symmetric any more due the space charge effect [123].

moving towards the electrode on the right side can be seen in Fig. 4.11.

### 4.3.6 Induced Signal

The primary signal generation mechanism in a RPC is not due to the collection of the avalanche carriers on the electrode plates or readout strips/pads. During the drift,the movement of the charge carriers in the gas-gap induces signal on the pick up electrodes (conductors) outside the active volume and the high voltage electrode plates allow signals to pass through them due to their very high resistivity. The induced signal are calculated from the Shockley–Ramo theorem (Shockley, 1938 and Ramo, 1939). The theorem is based on the principle that instantaneous electric currents in a readout electrode (conductor) induced by charges moving in the vicinity are caused by the instantaneous change of electrostatic flux lines that end on that electrode. Therefore, the current signal induced on the readout electrode by a charge q moving with drift velocity $\vec{v}_D(t) = \dot{\vec{x}}(t)$ is given by [123, 140],

$$i_{ind}(t) = \vec{E}_w(\vec{x}(t)).\vec{v}_D(t).q(t) \tag{4.15}$$

where, $\vec{E}_w$ is the weighting field in the units of $[L^{-1}]$ which is defined as the electric field when the signal electrode is kept at a weighting potential $V_w = 1$ (no units) and all the other electrodes are kept at potential 0. The weighting field $\vec{E}_w$ is uniform and perpendicular to the electric field if the strip/pad dimensions ($\sim$ cm) are much larger than the gas-gap thickness ($\sim$ mm). The module of the weighting field can be expressed as,

$$E_w = \frac{\epsilon_r}{\epsilon_r g + 2d} = \frac{1}{g + 2d/\epsilon_r} \tag{4.16}$$

and correspondingly the potential drop $\Delta V_w$ across cathode and anode can be expressed as,

$$\Delta V_w = \frac{\epsilon_r g}{\epsilon_r g + 2d} = \frac{g}{g + 2d/\epsilon_r} \tag{4.17}$$

where, d is the electrode plate thickness and $\epsilon_r$ is the relative permittivity of the electrode material. The negative and positive ions due to their small drift velocities induce a current signal which is much smaller than that of the electrons. Therefore, the fast signals in RPC is the contribution from electrons only. The signal induction time (from the electron component) is around 10 ns.

Therefore, the resistive plates behave as perfect dielectric because the time constant of the RC circuit formed by the resistive plates, around 10 ms, is much larger than the signal induction time. The electrons drift parallel to the applied electric field in the z direction in a RPC. The above equation for the induced current signal can be simplified to,

$$i_{ind}(t) = \frac{E_w}{V_w} v_D(t) e_0 n(t) \tag{4.18}$$

where $e_0$ is the unit charge and $n(t)$ is the number of electrons in an avalanche at time t. The current signal induced by all of the clusters ($n_{cl}$) in the RPC gas-gap is given by,

$$i_{ind}(t) = \sum_{j=1}^{n_{cl}} \vec{E}_w(x_j(t)).\vec{v}_{D_j}(t) e_0 n_j(t) \tag{4.19}$$

The total induced charge can be calculated as,

$$Q_{ind}(t) = \int_0^T dt \sum_{j=1}^{n_{cl}} \vec{E}_w(x_j(t)).\vec{v}_{D_j}(t) e_0 n_j(t) \tag{4.20}$$

where T is the total signal time.

## 4.4 Mode of Operation of RPC : Avalanche and Streamer

The RPC can run in two different operating modes, defined by the number of electrons generated during the ionization mechanism. One of them is known as the avalanche mode. In the avalanche mode, primary electron-ion pairs are released due to the passage of a charged particle through the gas-gap of RPC. Thereafter, the primary electron-ion pairs start propagating due to the affect of the electric field and get multiplied corresponding to a Townsend avalanche shown schematically in Fig. 4.12. Streamer mode is another type of operational mode for RPC in which the multiplication mechanism is driven by a large number of non linear effects. When an avalanche reaches a size of about $10^8$ electrons known as the Raether limit i.e the gas gain becomes high enough, the avalanche develops into a streamer. Then the electric field generated by the space-charge effects becomes comparable to the external applied electric field [141]. The propagation velocity of streamers far exceeds the drift velocity of the normal avalanche [123, 133, 137]. The streamer at a later

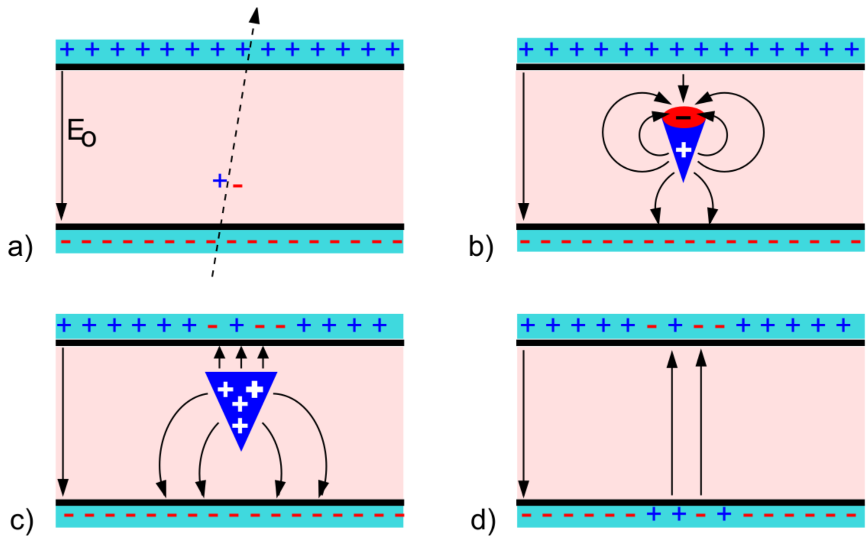


Figure 4.12: The development stages of an avalanche in an RPC are shown schematically. At large gain, the applied electric field gets deformed because of the avalanche charge carriers. $E_0$ is the applied electric field. a) Gas ionization takes place due to the passage of a charge particle b) An avalanche formed and the electric field in the gas gap gets influenced when the avalanche size is sufficiently large. c) Due to the variation in drift velocity, the electrons reach the anode, but the ions are still drifting slowly in the gas-gap, d) The ions reach the cathode. The electric field gets reduced in a small area around the position where the avalanche developed due to the charges in the resistive layers [123].

stage can further evolve into a glow discharge, a luminous filament between the electrodes and a spark. However, the high resistivity of the RPC electrodes suppresses the strong current required to flow in the gap for the later discharge stages to occur. The UV-photons created during the recombination and de-excitation of atoms start to contribute to the multiplication and propagation of an avalanche [142–144]. These photons can ionize the gas at the tip and tail of the avalanche where the external electric field is strongly enhanced and thus generate new avalanches especially at the ion tails. These photons can also knock out electrons from the cathode surface up which will produce succeeding avalanches that may merge into a streamer. Also a streamer formation can be provoked by a very high number of primaries (inducing a high rate of cluster production) without the need of an avalanche precursor. Fig. 4.13 shows schematic images of the streamer development in the gas gap. A streamer mechanism is rather slow due to a certain number of avalanches contributing to it's creation process. Experimentally, the large current pulse of a streamer are preceded by a smaller pulse generated by the original avalanche (the precursor signal) as shown in Fig. 4.14. A variation of 10 - 100 ns on the delay of the streamer signal to the precursor

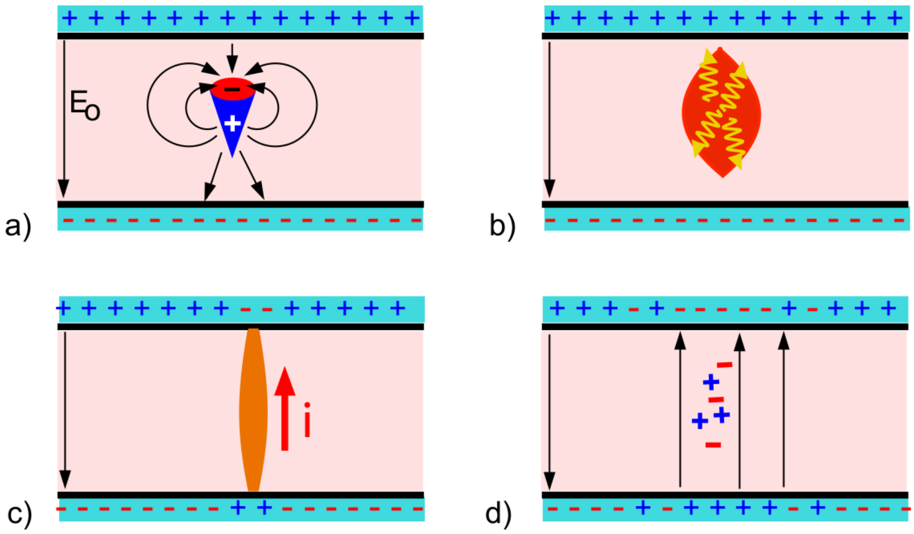


Figure 4.13: The development of a streamer in an RPC is shown schematically. a) An avalanche is developing as in Fig. 4.12. b) Electric field gets largely deteriorated in the gas-gap due to the avalanche charges. Moreover, the avalanche process gets accompanied by the contribution from photons and a rapid spread of the avalanche occurred : A streamer evolves. c) A weak spark may be generated. The local electrode area gets discharged. d) The electric field is strongly reduced around the spot of the avalanche creating a blind spot on the detector for the detection of charged particles [123].

signal is possible. As the voltage increases the time delay of the streamer pulse gets shorter and the two signals merge at a certain voltage. Historically, the first RPC by Santanico and Cardarelli was operated in streamer mode. The signal amplitude in streamer mode RPC is about 100 times larger than an avalanche mode RPC and can be retrieved without the need of an amplifier. This high amount of charge gets deposited in the resistive plates causing a reduced electric field in the gas-gap. The detector develops a temporary inefficiency surrounding the streamer at a particular region due to the high resistivity of electrodes. This blind spot on the detector gets reflected through a reduced rate capability.

The avalanche mode was implemented to operate the RPC at high particle rates. The gas-gain doesn't reach the Raether limit due to the requirement of lower operating voltage in this mode. Therefore, the transition probability of an avalanche into a streamer greatly reduces. A smaller amount of charge gets accumulated in the gas-gap and it's immediate benefit is an increase in the rate capability. This reduced charge induces a small current signal on the pick-up electrodes and a sophisticated front-end electronics with large amplification stage is necessary to retrieve the current signal. The basic idea of avalanche mode is transferring a large fraction of the gain factor

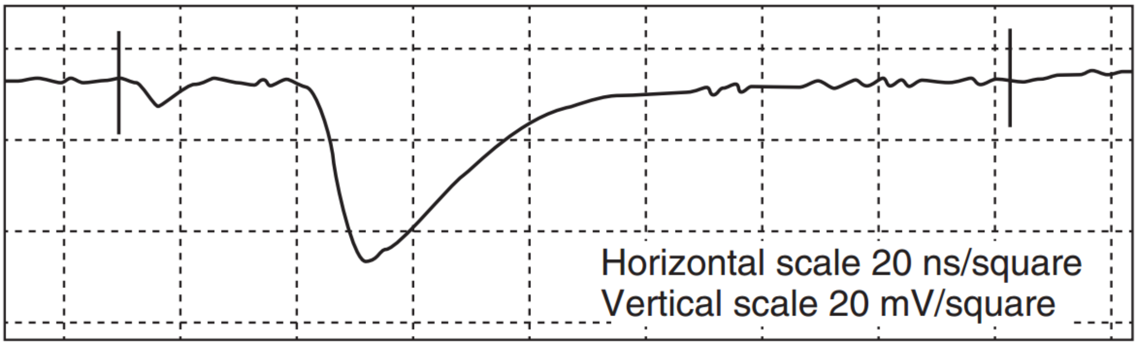


Figure 4.14: Signal from an 2 mm single-gap RPC at 9.4 kV operated with a gas mixture of $Ar : n - C_4H_{10} : C_2H_2F_4 :: 10 : 7 : 83$ showing an avalanche precursor followed by a streamer pulse. [145].

from the gas-gap to the front-end electronics. The use of a electronegative gas such as Freon is beneficial for the avalanche mode of operation in RPC since it can absorb some of the electrons generated in the cluster, and thereby producing slow negative ions. The addition of a small amount of an electron-quencher gas like $SF_6$ make a difference in the total amount of charge in the gas-gap.

## 4.5 The Rate Capability of RPC

In high rate experiments like CBM, the rate capability of the detectors is one of the main challenges. However, a RPC detector by construction is limited in rate capability due to the high resistivity of the electrode plates. The avalanche in a RPC is confined to a small volume, not affecting nearby regions due to the use of high resistive materials as electrodes. As the charges reach the electrodes, the signal also terminates. When a charge $Q_0$ enters the surface of the resistive electrode, it 'decomposes' with time t following an exponential law,

$$Q(t) = Q_0 e^{-t/\tau} \tag{4.21}$$

and the time interval needed for the localized discharge to recharge from the electrode plate (time constant) is given by,

$$\tau = RC = \rho_r \epsilon_0 \epsilon_r \tag{4.22}$$

where, $R = \frac{\rho_r d}{A}$ is the resistance, $C = \epsilon_0 \epsilon_r \frac{A}{d}$ is the capacitance, $\rho_r$ is the bulk resistivity, $d$ is the thickness, $A$ is the surface area and $\epsilon_r$ is the relative permittivity of the resistive electrode plate.

$\epsilon_0$ is the dielectric constant.

The current that can be driven by the high resistivity electrodes is the main limiting factor for the rate capability of RPC. The analytical description of rate effects in RPC is based on a simple DC model,

$$V_d = V_a - V_{gap} = \bar{I}R = \phi\rho_r d\bar{q} \tag{4.23}$$

where, $V_a$ is the applied external voltage, $\phi$ is the incident particle flux, $\bar{q}$ is the average charge per avalanche. The current $\bar{I}$ is proportional to $\bar{q}$. Since $V_a$ is a constant value, the real voltage across the gap is $V_{gap}$. At high particle flux, the voltage drop across the electrodes ($V_d$) should be kept at a minimum value. Therefore, the rate capability of RPC is defined as the incident particle flux per unit voltage drop across the electrodes,

$$\text{Rate Capability} = \frac{1}{\rho_r d\bar{q}} \tag{4.24}$$

There are three parameters to work upon in increasing the rate capability of RPC, reducing the bulk resistivity of electrode material, reducing the thickness of the electrode plates and/or reducing the average charge per each avalanche signal. The resistive electrodes are made of bakelite ($10^9$ - $10^{12}$ Ω-cm) or float glass ($10^{11}$ - $10^{12}$ Ω-cm). The resistivity of the bakelite plates can be optimized according to the required rate capability. Therefore, by using a low resistivity material as electrode plates to increase the rate capability of RPC seems a promising choice. But this approach leads to an increase in the operating current and spontaneous detector noise, thereby ageing of the detector and consequently a reduced detector lifetime. These factors need to be recognized while choosing a low resistivity material. Usually a bulk resistivity on the order $10^9$ - $10^{10}$ Ω-cm is feasible for operating a RPC detector at high rate. The surface quality of the electrodes facing the gas-gap is important in reducing spontaneous discharges which might affect the rate capability. The inner surfaces of the bakelite plates are treated with a drying oil named, linseed oil to refine the surface smoothness of electrodes. Now, another approach in increasing the rate capability by the reduction of the average charge per count leads to a reduction of the induced charge on the readout electrodes. A sophisticated front-end electronics is necessary for the detection of the small signals. Due to the low amplitude of the signals, the signal to noise ratio is very small. Therefore, the detector structure needs an optimization as a Faraday cage for suppressing the noise induced inside the detector by the electronics and by external sources.

## 4.6 The Choice of Gas Mixture

Being the core of the gas detector, the choice of the gas mixture is of fundamental importance for the RPC. The following combination of characteristics are necessary for the efficient operation of RPC,

- To ensure a high detection efficiency, high density of primary ion-electron clusters are required which depends upon the particle energy deposition, the average atomic number, density, and specific ionization potential of the gas mixture.
- Being electro-negative to contain the spatial distribution of the discharge in transverse direction and improve it's localization,
- Possibly not toxic or not dangerous for human health
- Relevant quenching properties to reduce the secondary ionizations initiated by photons.
- The chemical process taking place inside the gas gap during electron multiplication should have reasonable limits in the production of corrosive compounds like hydrofluoric acid for electrode surfaces and gas components [146] and also in the production of polymerization materials which may cause deposition of extraneous material on the electrode surface.

The main gas mixture component for the avalanche mode operation of RPC has been chosen as $C_2H_2F_4$ which is an electronegative gas. It possess a high atomic mass and a high value of cluster density, $\lambda$. $C_2H_2F_4$ or rather environment friendly freon, R134a acts as a ionization compound in the avalanche mode of RPC gas mixture. The drift velocity of electrons is higher in a high concentration of R134a gas mixture compared to that in the other gases. The use of polyatomic molecules,like $iC_4H_{10}$, are necessary to act as a photon quencher. Since these molecules have a large number of non-radiative rotational and vibrational excited states, they absorb the UV photons emitted during the recombination of electron-ion pairs and de-excitation of atoms, and dissipate their energies via non-radiative channels. Therefore, the addition of $iC_4H_{10}$ in the gas mixture restrict the production of secondary avalanches by the UV photons. A small percentage of an electronegative gas $SF_6$ is added to the gas mixture to restrict the avalanches to transit into a streamer. $SF_6$ has a strong electron affinity of $(1.05 \pm 0.10)$ eV and the attachment cross-section is strongly decreasing function of the electric field [147]. At the first stage of the avalanche growth, due to the low concentration levels of $SF_6$ in gas, the electron attachment phenomenon is weak. Only the operating voltage is shifted by a few hundred volts. When the avalanche starts to saturate due to the space-charge effects and the electric field gets diminished, the attachment becomes very effective. The restriction in the formation of streamer also reduces the production of hydrofluoric acid. Also, a high flow of gas and filtration system for the used gas before re-circulation are necessary for large scale and high rate experiments to remove the produced pollutants from the gas. Bakelite RPCs require a gas mixture with an amount of water vapour (typically from 30% to 50% of relative humidity) to retain the conductivity of electrode plates stable in time for long term operation [126,148]. A gas mixture of Ar, R134a, $iC_4H_{10}$ and $SF_6$ is usually being used in streamer mode RPCs. Since Ar is a noble gas, it doesn't interact with the other molecules in the gas and it has a ionization energy of 15.8 eV. Being a monoatomic gas, Ar has a higher value of Townsand coefficient than the polyatomic gases. Thus Ar is being used as a ionizing gas in streamer mode RPCs. R134a and $SF_6$ work as electron quencher and $iC_4H_{10}$ as photon quencher.

## 4.7 Multi-Gap Resistive Plate Chamber (MRPC)

MRPC has been invented in the year of 1996 to improve the time resolution of a single-gap RPC. The intrinsic time resolution of a single-gap RPC is,

$$\sigma(t) = \frac{1.28}{(\alpha - \eta)v_d} \tag{4.25}$$

Townsand co-efficient ($\alpha$), attachment co-efficient ($\eta$) and the drift velocity of electrons ($v_d$) are mainly determined by the gas mixture and the working electric field. The effective way to improve the time resolution of a RPC is to decrease the gap width as much as possible so that the electric field can be considerably increased while operating in the avalanche mode. Hence, the electron drift velocity is much faster and the effective Townsand co-efficient is much higher. Since a narrow-gap RPC has lower intrinsic efficiency than a wide-gap RPC, the construction of a MRPC is done by

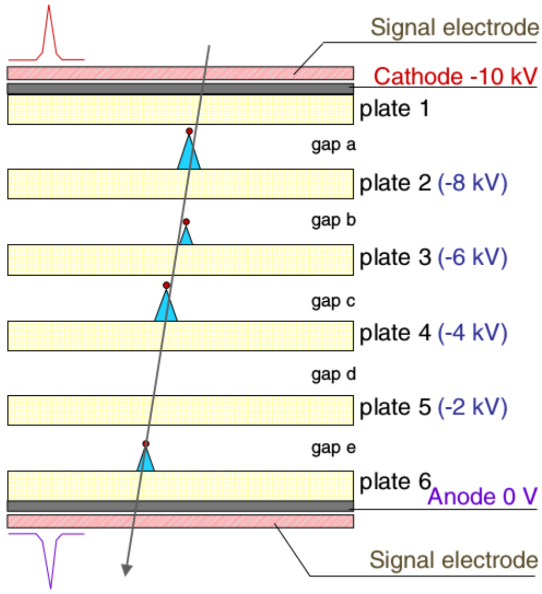


Figure 4.15: Schematic diagram of a Multi-gap RPC. [149].

inserting several equally spaced resistive plates in between a wide-gap RPC to maintain the desired efficiency. The gas volume is divided into a number of individual narrow gaps. The high voltage is applied to the graphite layer coated on the external surfaces of the outer resistive plates. The intermediate resistive plates are electrically floating. They acquire the voltage by electrostatics. The voltage at each of the electrode plates is maintained at such a value that the currents flowing in and out of the electrode plates are equal for the steady-state requirement of a null total current in each electrode plate. This is achieved by the adjustment of the gas gain in the neighbouring gaps. A through-going charged particle ionizes the gas in each of the sub-gaps and produces individual and separate clusters of primary ionisation. The avalanche mechanism starts for each of these primary clusters. The resistive plates are transparent to the fast signal induced on the readout electrodes which are placed on the outer electrode surfaces. The total signal is the analogue sum of the independent avalanches in each of the sub-gaps. The narrow gas-gaps induce less time-jitter to the signal since the fluctuations in the position of the primary ionization significantly reduces compared to a single-gap RPC. The time resolution of a MRPC is $\sigma(t)/\sqrt{n}$, where n is the number of gas-gaps. A schematic diagram of MRPC is shown in Fig. 4.15. A longer efficiency plateau and a larger rate capability can be achieved with the technology of MRPCs. Although this technology has several certain advantages, it possess some serious drawbacks. The requirement of high voltage is much higher for a MRPC detector than a single-gap RPC. The stability of MRPC may be dominated by the dark counting rate for a low ionizing particle flux such.

# Chapter 5

# Development of Resistive Plate Chamber at VECC for the CBM Experiment

An R&D program is ongoing at VECC, Kolkata, India for the development of a Resistive Plate Chamber for the CBM experiment since the year 2016. As has been discussed in the previous chapter, rate capability is one of the main parameters to be achieved in this development study. To achieve the goal, we performed characterization on different types of bakelite RPCs, both single and Multi-Gap configurations. The different stages of development are described in this chapter. First, a single gap bakelite RPC was developed using Indigenous bakelite sheets and it was characterized in an avalanche mode gas mixture in a cosmic ray set up using conventional NIM-based electronics and current sensitive sophisticated FEE NINO. After that, two multi-gap RPC prototypes were developed using the same Indigenous bakelite material and different characteristics of the MRPCs in avalanche mode were extensively measured using cosmic rays and conventional NIM electronics. Subsequently, we started our search for bakelite materials with lower bulk resistivity and developed a few prototypes using Italian bakelite sheets and characterized them. Then, a single gap RPC with bulk resistivity $\sim 4 \times 10^{10}$ was procured from a professional Italian Company, General Technica. Different characteristics of the prototype RPC such as leakage current, current stability, efficiency, noise rate, time resolution, and charge spectrum were measured in avalanche mode in a cosmic ray test setup. Different kinds of electronics were used while performing the characterizations such as conventional NIM-based electronics, current sensitive electronics like NINO and PADI, commercial charge sensitive pre-amplifier 142IH and a charge sensitive FEE MANU.

## 5.1 First Prototype of a Single-Gap bakelite RPC - RPC-P0

A single gap RPC of electrode dimension $\sim$ 30 cm $\times$ 30 cm $\times$ 0.2 cm and of gap size $\sim$ 0.2 cm has been fabricated with P302 grade bakelite plates of 0.3 mm thickness procured from an Indian Company Lamtuf Plastics Ltd. This prototype is called RPC-P0. The gas volume of the chamber was sealed on four sides with long spacers each of length 28 cm and of height 0.2 cm running along the length of the chamber. Four button spacers, each of diameter 1 cm and height 0.2 cm, were glued between the two bakelite plates to maintain a uniform gas-gap and also for gas tightness. Gas was allowed to pass through the chamber via two gas nozzles connected diagonally into the prototype, one for inlet and another for outlet. The long spacers and gas nozzles were made of very high resistivity polycarbonate material. An area of $\sim 28 \times 28$ cm$^2$ on each of the outer surfaces of the bakelite sheets had been painted with a graphite coating with a surface resistivity of $\sim 3 \times 10^{12}$ $\Omega/\square$ for the uniform application of the high voltage. The bakelite plates had a bulk resistivity of

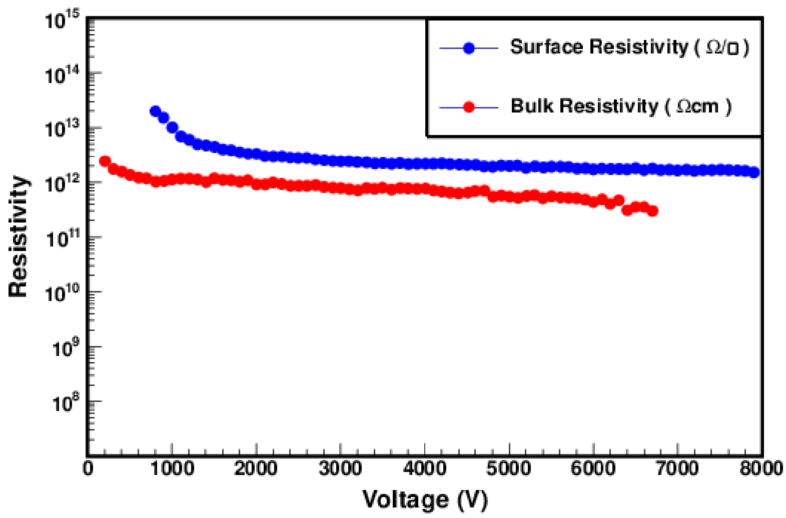


Figure 5.1: The measured surface and bulk resistivity of the P-302 grade bakelite sample [150].

$\sim 9 \times 10^{11}$ $\Omega$-cm. The measured bulk and surface resistivities of the P-302 grade bakelite sample are shown in Fig. 5.1. The surface resistance profiles of the graphite painted electrode surfaces were quite uniform, $\sim$ 1 M$\Omega/\Box$ with some variations around the edges. Fig. 5.2 shows the different stages of the fabrication of the RPC module. More details about the fabrication procedure can be

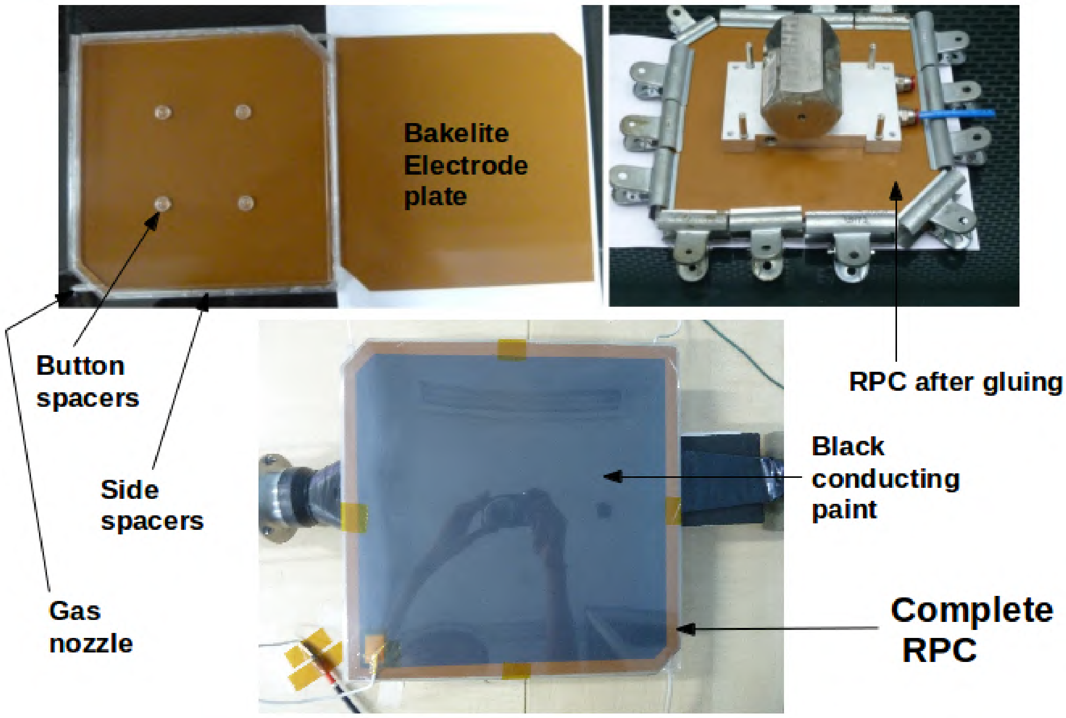


Figure 5.2: Different stages of the development of RPC-P0 [151].

found in [151]. The signal is read out by a pick-up panel consisting of 11 copper strips. A Mylar sheet was placed between the voltage electrodes and the pick-up panels to isolate the high voltage. The upper resistive electrode was connected to a positive high voltage input and the lower electrode was connected to a negative high voltage input. The RPC therefore has one anode pick-up strip plane and one cathode pick-up strip plane. The pick-up panels were made of a FR4 sheet (each of $\sim$ 30 cm $\times$ 30 cm $\times$ 0.15 cm) sandwiched between two copper sheets ($\sim$ 30 cm $\times$ 30 cm $\times$ 0.0035 cm). The copper strips were formed by chemical etching process with anhydrous $FeCl_3$ solution. The width of the pick-up strip is 2.3 cm on a pitch of 2.5 cm. The length of each strip is 28 cm. As our main aim is to develop a RPC for high particle rate, in our study, RPC-P0 was operated using avalanche mode gas mixture. A pre-mixed gas cylinder was used for the continuous flow of gas mixture which is the active medium for ionization. A gas mixture of R134a, $iC_4H_{10}$ and $SF_6$ in proportions of 95.0%, 4.5% and 0.5% respectively are used to operate this RPC in avalanche mode. Gas pipes were connected to respective mass flow controllers for each gas.

### 5.1.1 Experimental setup with conventional NIM-based discrete electronic modules

A trigger signal was formed by the coincidence of three plastic scintillator signals, two "so-called" paddle scintillators (49 cm $\times$ 23.5 cm) and one finger scintillator (27 cm $\times$ 2 cm). The finger scintillator encompassed an overlapping area of 27 cm $\times$ 2 cm, covering part of a single RPC strip and was used to establish when cosmic muons pass through. The scintillators were coupled to the photomultipliers which were connected to a high voltage power supply CAEN N470. The paddle scintillators were provided with 1450 V each and the finger scintillator was given 1050 V. A uniform electric field was generated between the two bakelite plates of RPC-P0 by applying high voltage (HV) from a DC power supply CAEN N471A providing a maximum voltage up to $\pm$ 8 kV individually to the anode and cathode, effectively doubling the total effective voltage. The HV module has a current resolution of 1 nA. The current can be monitored from the display panel of the HV module. The RPC signal has been tapped via a LEMO cable soldered to a pick-up strip. The signal is picked up inductively by a strip on the anode plane and sent to a CAEN N979 10X amplifier for amplification. The amplified RPC signal was discriminted by a CAEN N841 16 channel Leading Edge Discriminator (LED) unit via LEMO cables. The analog signals from the three scintillators were discriminated by a CANBERRA QUAD CFD 454 constant fraction discriminator (CFD). The coincidence signal the logic signals of scintillators was generated by a logic unit CAEN N455 forming the three-fold master trigger. Further coincidence with the RPC logic signal created the 4-fold signal. The logic signal of RPC, the master trigger signal and the 4-fold signal were counted by a CAEN N1145 Quad Scalar and Preset Counter. The master trigger signal, raw RPC signal and amplified RPC signal were connected to an oscilloscope coupled with 1 M$\Omega$ resistances. A photograph of the experimental setup is shown in the Fig. 5.3.

### 5.1.2 Results

#### Leakage Current

The effective potential drop across the gas-gap is determined by an important parameter known as leakage current. The leakage current is monitored via the HV module connected to a RPC as

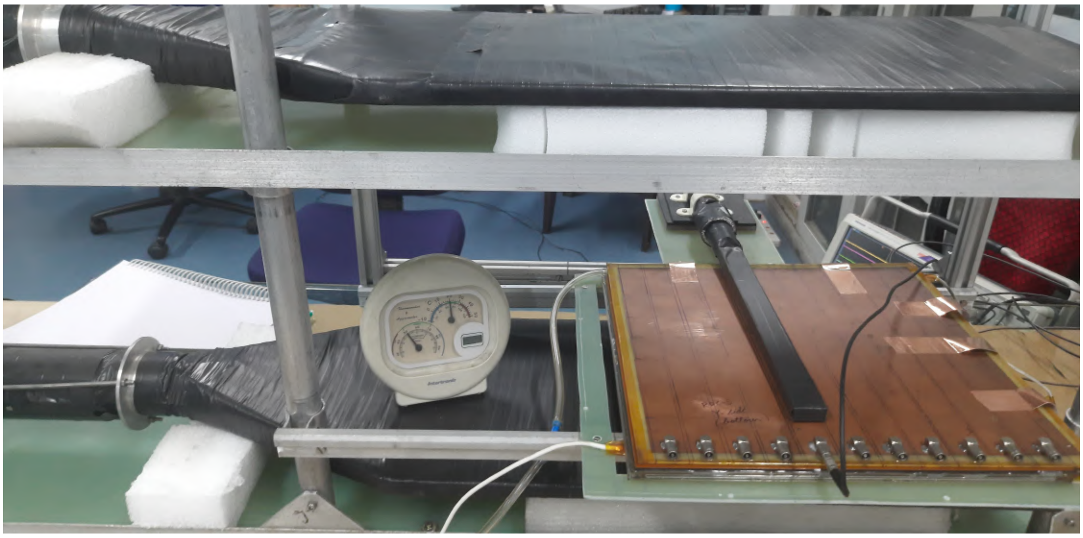

Figure 5.3: Cosmic ray test setup for the characterisation of RPC-P0

the applied voltage between the electrodes is increased in steps. The I-V characteristics of RPC shows a typical two-slope behaviour which can be explained by the electrical representation of the circuit diagram for RPC shown in Fig. 5.4. The gas mixture is represented as a zener diode. At low voltages, the primary electrons are unable to produce an avalanche due to the lower value of electric field between the electrodes. Hence, the gas-gap has infinite resistance and a small leakage current flows through spacers. The behaviour is ohmic.

$$R_{gap} \approx \infty \tag{5.1}$$

$$\frac{dV}{dI} \approx R_{spacer}(R_{spacer} >> R_{Bakelite}) \tag{5.2}$$

As the voltage is increased, the gas becomes slightly conducting indicating the formation of an avalanche providing a low resistance path. This region follows a non-linear increase in current. Then, the electrode resistance determines the current. At a certain point beyond the breakdown voltage of gas, the leakage current drastically increases showing again a linear behaviour of current.

$$R_{gap} \approx 0 \tag{5.3}$$

$$\frac{dV}{dI} \approx R_{Bakelite} \tag{5.4}$$

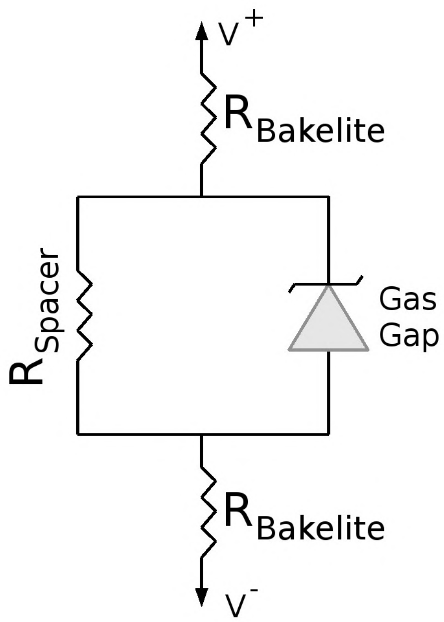


Figure 5.4: Electrical Representation of an RPC gas-gap

The variation in the current through the prototype RPC as a function of the applied voltage was studied which is shown in the Fig. 5.5. Two distinct regions can be shown. The first region shows a linear and ohmic behaviour from 0 to 8000 V. Here, the leakage current is small due to the high resistance put up by the gas. The breakdown voltage at $\sim$ 8500 V indicates the onset of avalanche resulting the generation of measurable signals from the RPC. This voltage is also known as the "knee voltage".

**Efficiency**

The efficiency ($\epsilon$) is defined as the ratio of the number of detected events in the RPC (4-fold RPC coincidence signal) to the number of detected events in the reference scintillators (3-fold master trigger signal),

$$\epsilon = \frac{N_{RPC}}{N_{Ref}} \tag{5.5}$$

The efficiency is measured using the cosmic bench described in the section 5.1.1. The detection efficiency of RPC is the most important characterisation parameter which establishes it's suitability for the targeted experiment. The efficiency is strongly dependent upon the applied voltage across

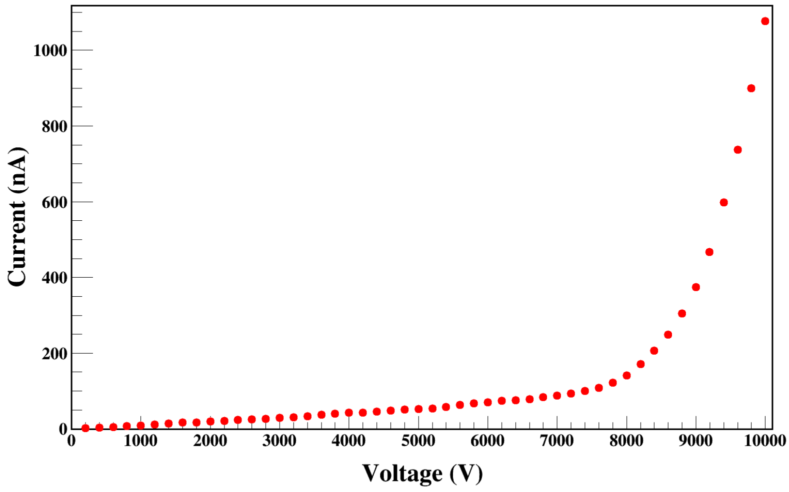


Figure 5.5: IV characteristics of RPC-P0

the gas-gap. As the applied voltage is increased, the primary electrons start to create more and more secondary electron-ion pairs and the attachment process reduces. Therefore, the amplitude of the induced signal on the pick-up strip increases with the applied voltage. Depending upon the signal discrimination threshold, efficiency reaches a plateau region corresponding to an accepted value of efficiency, at $\sim$ 90 %. The error in calculating efficiency was determined by Bernoulli distribution since N$_{RPC}$ and N$_{Ref}$ are correlated. The absolute error of N$_{RPC}$ is as follows [133],

$$\sigma_{N_{RPC}} = \sqrt{N_{Ref}.\epsilon(1-\epsilon)} \tag{5.6}$$

The relative error of N$_{RPC}$ normalized to N$_{Ref}$ gives the error of the efficiency,

$$\sigma_{\epsilon} = \frac{\sigma_{N_{RPC}}}{N_{Ref}} = \sqrt{\frac{\epsilon(1-\epsilon)}{N_{Ref}}} \tag{5.7}$$

Fig. 5.6 shows the trend of the efficiency curve as function of applied high voltage at 250 mV discriminator threshold. The rise of the efficiency with respect to applied voltage in this manner is typical for RPCs. The efficiency reaches a plateau with $\sim$ 88 % efficiency at 11000 V with 250 mV threshold.

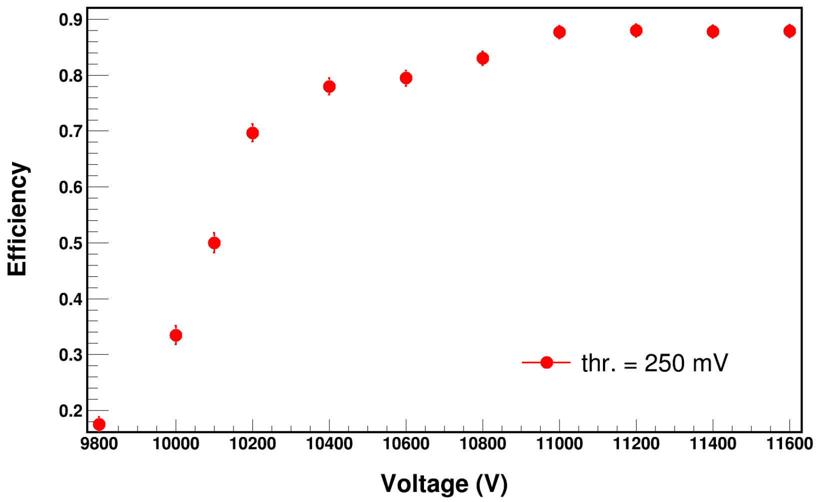


Figure 5.6: Efficiency of RPC-P0 as a function of the applied bias voltage.

### Noise rate

The noise rate of a RPC is defined as the total counting rate of all the signals which cross discriminator threshold. It includes the combined effect of signals from cosmic rays and other background effects as well as spurious discharges or sparks. Non-uniformities on the inner electrode surfaces within the gas-gap may also be a reason of these micro-sparks. Spurious discharges can happen also on the external surfaces of the electrodes, which are in contact with the environment. The nature of genuine RPC pulses due to the passage of cosmic muons closely resemble the properties of the pulses caused by spurious discharges. The fast coincidence between the RPC and the scintillator pulses mostly filters out the spurious events caused by the discharges. However, the noise rate of RPC must be kept as low as possible.

As explained earlier, the noise rate of the RPC was measured from a single strip for one hour duration at each applied voltage. The RPC area covered in this set-up is $\sim$ 28 cm $\times$ 2.3 cm. The variation of noise rate with voltage for a set discriminator threshold value of 250 mV is shown in Fig. 5.7. The threshold of discriminator is applied after the amplification of the signal. The amplification has a gain of approximately 100 (10 $\times$ 10) i.e. a set threshold of 250 mV corresponds to a discrimination value of 2.5 mV on the input signal. A linearly varying behaviour of the noise rate with applied voltage is observed. Also, the noise rate increases with decreasing threshold as expected. The maximum noise rate is found to be $\sim$ 1 Hz/cm$^2$ at 11600 V with 250 mV threshold.

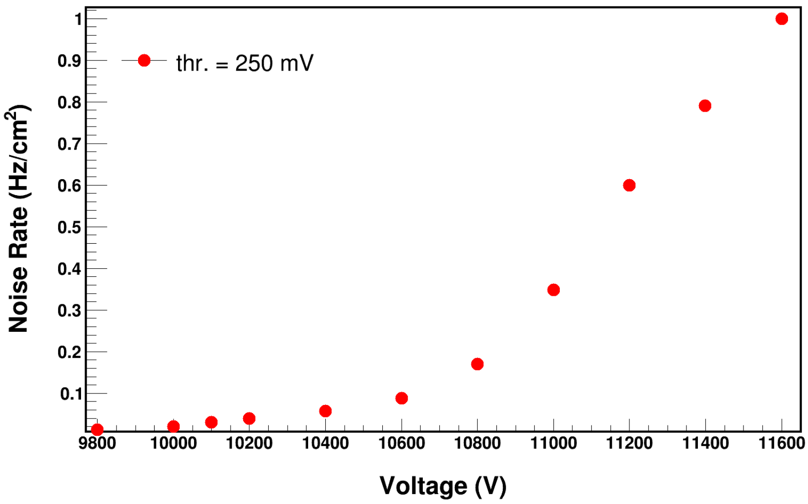


Figure 5.7: Noise rate of RPC-P0 as a function of the applied voltage

### Time Resolution

The accuracy of the time measurements of particle detection is determined by the time resolution of the detector. The time resolution of RPC-P0 was measured by using a Phillips Scientific 7186 Time to Digital Converter (TDC), a single width CAMAC module comprises 16 channels of Time to Amplitude conversion (TAC), followed by a digital processing section and CAMAC interface. The module accepts fast NIM inputs of minimum 10 ns pulse-width at 50 Ohm impedance. The full time scale of the TDC module in our working configuration is 100 ns. The time resolution of the module is about 25 ps and the RMS resolution is $<$ 20 ps. The crosstalk is below 3 LSB between adjacent channels. The 3-fold master trigger signal was fed to the common START channel and a delayed NIM pulse (via a delay module) of the RPC-P0 was given to one of the 16 STOP channels of the TDC module. The time difference between the trigger and the RPC yields a time distribution which can be fitted by a Gaussian function. The Gaussian variance $\sigma$ obtained from the fit gives the time resolution of RPC-P0. Fig. 5.8 shows the time distribution when the RPC-P0 was given a HV of 12000 V. Therefore, the uncorrected time resolution of RPC-P0 was measured to be 2.66 ns at 11000 V. The observed time resolution has the contribution from the three scintillator signals as well. The individual time resolution of each scintillator is estimated by giving a START with one scintillator and providing a STOP by delayed signal of other scintillator. The time resolution of RPC-P0 was obtained by subtracting the contribution from the scintillators

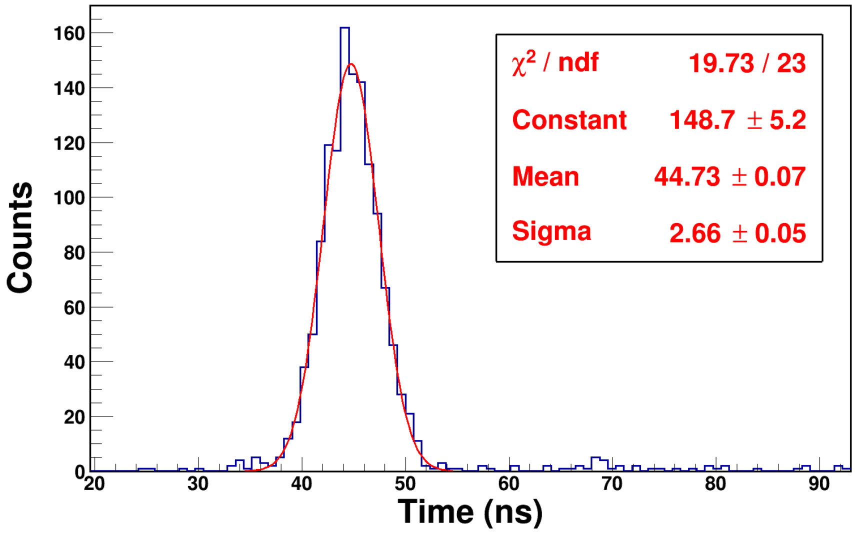


Figure 5.8: Time distribution spectra of trigger and RPC-P0.

using this formula,

$$\sigma^2_{observed} = \sigma^2_{SC1} + \sigma^2_{SC2} + \sigma^2_{SC3} + \sigma^2_{RPC} \tag{5.8}$$

The contributions from the three scintillators using CFD are found to be,

$$\sigma^2_{SC1} + \sigma^2_{SC2} + \sigma^2_{SC3} = 0.512\ ns \tag{5.9}$$

Therefore, the corrected time resolution of RPC-P0 is, $\sigma_{RPC} \sim 2.56$ ns at 12000 V.

### 5.1.3 Characterisation of RPC-P0 with NINO ASIC based electronics

The prototype RPC was tested using a NINO ASIC based front-end board (FEB). NINO is an ultra-fast octa-channel front-end amplifier-discriminator chip, fabricated with 0.25 $\mu$m CMOS technology [152]. The layout of a NINO chip based FEB was first done at CERN to be used in the ALICE Time-of-Flight MRPC detector. The simplified block diagram of the ASIC is shown in Fig. 5.9. NINO is a fully differential ASIC accepting only differential inputs and providing Low Voltage Differential Signal (LVDS) outputs. It features four stages with identical low gain, high bandwidth amplifiers in a cascade with built in hysteresis control. The first stage of the amplifier comes with a peaking time of $\sim$ 1 ns to minimise time-jitter. To stretch the output pulse with a longer width, a pulse stretcher is implemented right before the LVDS output driver. Stretching is

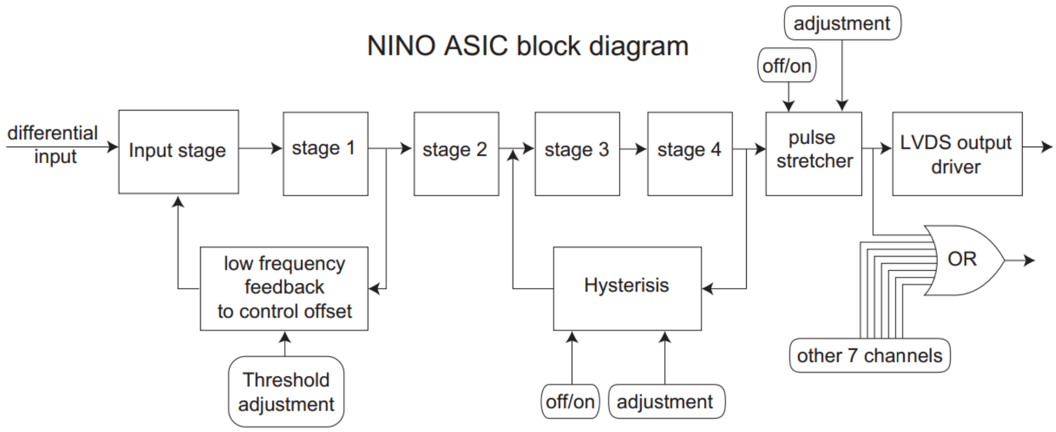


Figure 5.9: Block diagram of the NINO ASIC [152].

needed to process the output pulse via TDC module since the output pulse width before stretcher stage is only 2-7 ns. The generation of output signals compatible with standard LVDS levels is done by an open-drain differential circuit in the final output stage of the NINO chip. The front edge time jitter from the NINO chip is less than 25 ps, giving a good performance for timing measurements.

A six-layer PCB with plated-through holes containing the NINO chip is developed by Tata Institute of Fundamental Research, India inspired from the NINO board developed at CERN [153]. The PCB


Figure 5.10: An image of a NINO front-end board.

has been fabricated to process the single-ended induced signals on the pick-up strips of RPC. The conversion from the single-ended inputs to differential inputs is done by using THS4520, a single channel, wideband (650 MHz) differential amplifier, having low noise and low distortion. Eight differential drivers (unity gain) were used for eight channels of the NINO chip. The dimension of the PCB is 200 mm $\times$ 23 mm. A common threshold adjustment for all the channels can be done by a trimpot mounted on the PCB. The board is operated using $\pm$ 4 V. The power consumption for each channel is measured to be 70 mW. A photograph of the PCB is shown in Fig. 5.10. The efficiency and noise rate of the RPC was measured using the NINO FEB in the cosmic ray test bench with a gas mixture flow of $R134a : iC_4H_{10} : SF_6 :: 95.0 : 4.5 : 0.5$ from a pre-mixed cylinder. The LVDS outputs from the FEB was converted to NIM signal in two steps by a LVDS to Emitter-coupled Logic (ECL) translator and then an ECL to NIM translator. The efficiency and noise rate are shown in Fig. 5.11 and Fig. 5.12. The threshold on the NINO board was kept

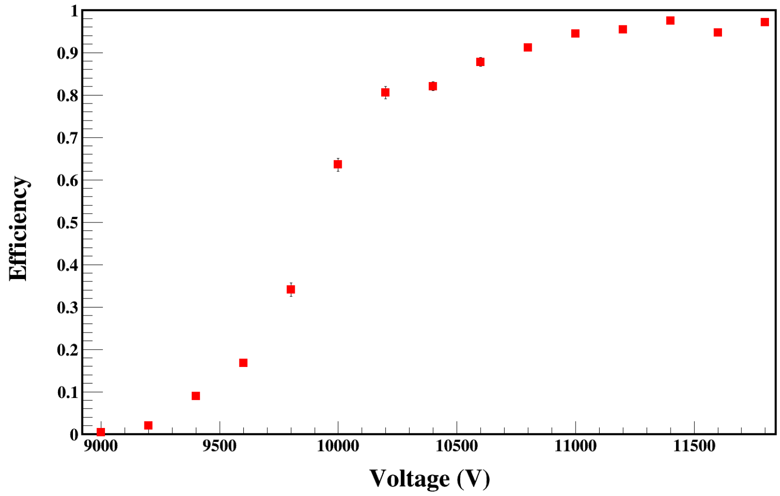


Figure 5.11: Efficiency of RPC-P0 as a function of applied Voltage using the NINO FEB.

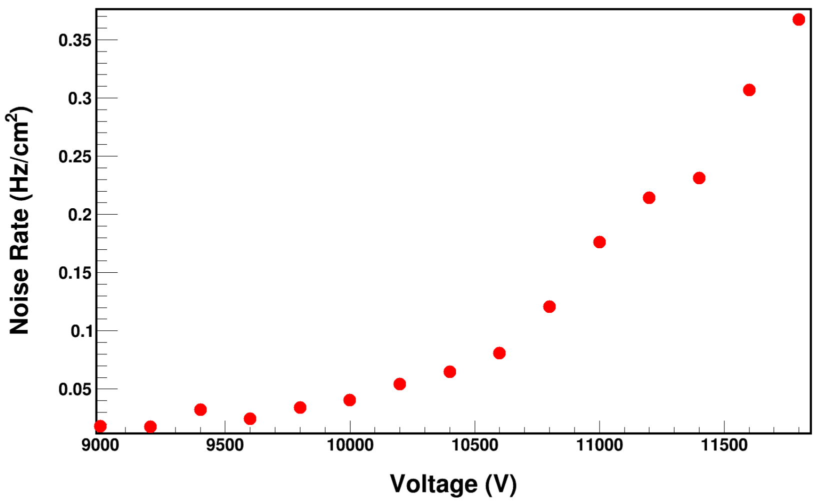


Figure 5.12: Noise Rate of RPC-P0 as a function of applied Voltage using the NINO FEB.

at $\sim$ 370 mV which corresponds to $>$ 2.5 mV input signal. The efficiency reaches $\sim$ 94 % at 11000 V with a noise rate of 0.18 Hz/cm$^2$. The time spectra of RPC-P0 at 11000 V was plotted with respect to the trigger time as shown in the Fig. 5.13. The scintillator corrected time resolution of RPC-P0 using NINO FEB is, $\sigma_{RPC} \sim$ 2.28 ns at 12000 V.

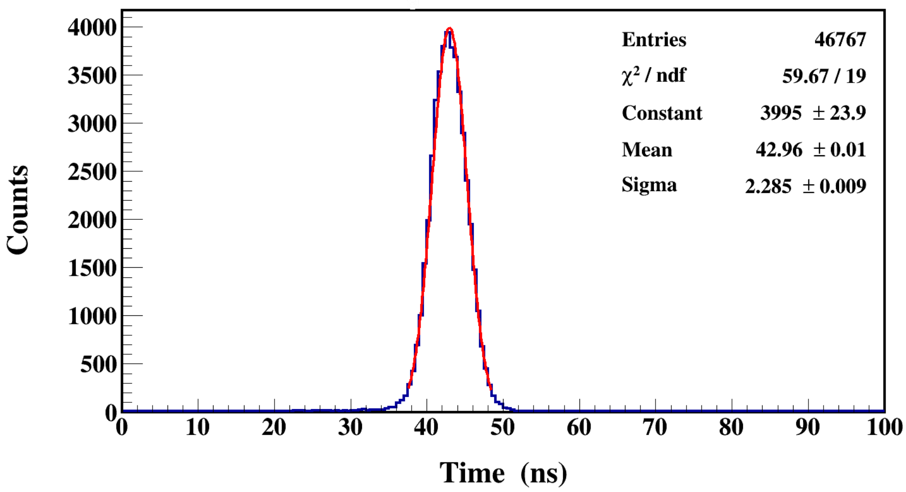


Figure 5.13: Time distribution spectra of trigger and RPC-P0 using the NINO FEB.

## 5.2 Development of Two Prototype Bakelite Multi-Gap Resistive Plate Chambers

Another variant of the RPC chambers called multi-gap RPC (MRPC) which has more than one gap helps in improving the time resolution to tens of pico-secs. A large amount of effort has been dedicated into the R&D of MRPCs for improving the time resolution and detection efficiency since it's emergence in 1996. This detector technology has found widespread applications in modern nuclear and particle physics experiments in the last two decades. Glass is the most commonly used electrode material in the construction of MRPCs due to it's own set of advantages. A parallel effort to develop MRPCs with bakelite electrodes has been carried out in VECC, Kolkata. The major advantages of bakelite over glass are,

1. Due to their mechanical strength, bakelite is favored over glass as they don't break easily. Bakelite MRPCs are more suitable for large area detectors than glass MRPCs. For glass MRPCs, several small modules are assembled to cover a large region which can be avoided if we use bakelite MRPCs.

2. Testing, handling and shifting of bakelite MRPCs are much easier than that of the glass MRPCs.

With the major disadvantages being

1. The surface morphological structure of glass is smoother then bakelite. A common practice is to coat the bakelite sheets with lubricant to smoothen the surfaces. Use of linseed oil for such

application sometimes helps in increase in longevity of the chamber.

2. Glass electrodes do not sag when stacked one over the other in a MRPC.

Keeping in mind the major disadvantages of bakelite over glass, we have developed bakelite MRPCs such that these factors can be taken care of. The developed MRPC is a prototype and of dimension (15 cm $\times$ 15 cm) and placing suitable button spacers at suitable distances solved the sagging problem of the bakelite. After detailed R&D's, we succeeded in getting a suitable bakelite sample which did not require any kind of oil treatment unlike previously developed RPCs using bakelite sheets [154] while developing the detectors, and ensured a better surface morphological structure [150, 155].

### 5.2.1 Construction principle

We have successfully developed two, called as MRPC-1 and MRPC-2 nearly identical 6-gap oil-free bakelite MRPCs each of dimension 15 cm $\times$ 15 cm. The bakelite plates (inner and outer surfaces) have not been treated with any kind of oil. The detector structure consists of 6 gas gaps obtained by stacking seven bakelite plates. High voltage is applied only to the external plates, leaving the intermediate ones floating. The cathode and anode are made of two outermost bakelite plates measuring 15 cm $\times$ 15 cm, with a thickness of 0.3 cm. Like in the case of single-gap RPC, the outer surfaces of the cathode and anode are coated with a mixture of a semi-conducting paint and dry thinner (1 : 1) by spray gun (Fig. 5.14e) for the uniform application of HV, the HV connections are made on the painted surfaces. The total space between cathode and anode is divided into the six 250 $\mu$m spaces, through 5 intermediate bakelite plates each of dimension 14 cm $\times$ 14 cm $\times$ 0.05 cm (Fig. 5.14b). The bakelite plates are P-302 grade glossy finished HPL made by Indian company Lamtuf Plastics Ltd with a bulk resistivity of 9 $\times$ $10^{12}$ $\Omega$-cm. The plates are separated from each other by 5 polished button spacers made of G10 sheets to maintain the thin gas-gaps as shown in Fig. 5.14c. A special frame, as shown in Fig. 5.14a, made of polycarbonate sheets of 0.4 cm thickness and two gas nozzles properly glued on the frame served the purpose of the side spacers. The inner and outer length (breadth) of the frame is 14.5 cm and 15.5 cm respectively. The glue used in the fabrication of MRPCs is a mixture of resin and hardener with 4:1 ratio. The resin is a mixture of Araldite and BC-600 with 1:1 ratio, the hardener is BC-600 hardener. The bulk resistivity of the glue is $10^{14}$ $\Omega$-cm which is 100 times higher than that of the electrode plates.

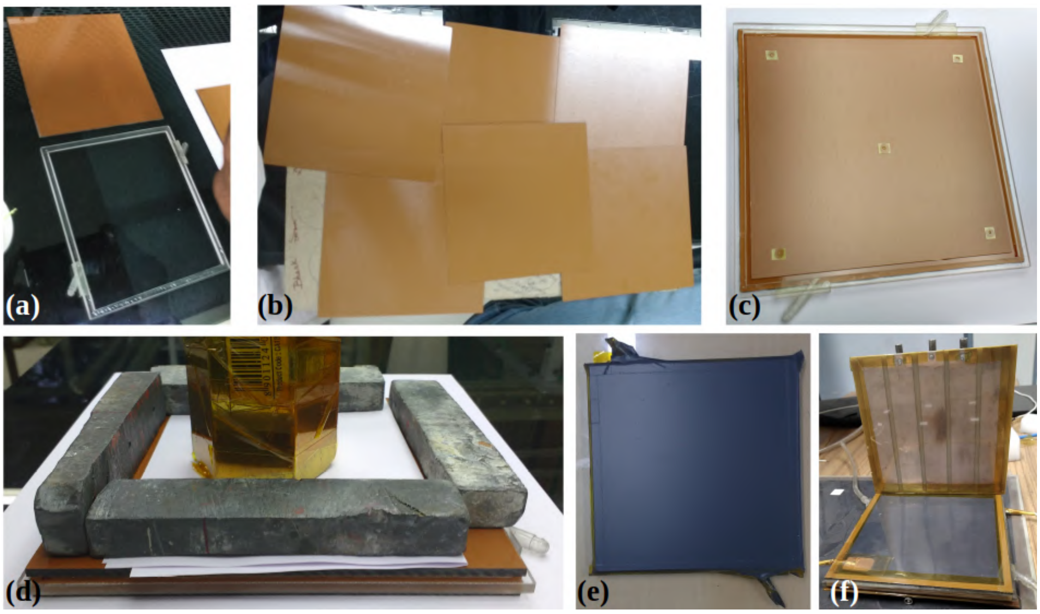


Figure 5.14: Different steps of the development of 6-gap bakelite MRPC [156].

Moreover, a thin insulating layer of Mylar is used to separate the high voltage electrode plates from the readout electrodes plates. The active area of the detector defined by the read-out panel is 14 × 14 $cm^2$. The read-out panel is segmented into five copper strips each of which is 3 cm wide. Chemical etching with the anhydrous iron chloride ($FeCl_3$) solution was carried out to maintain the gap of 0.3 cm between the copper strips in the pick-up panel. The details of the fabricated MRPCs are shown in the Table 5.1. The performance of the detector has been studied measuring the efficiency, noise rate and time resolution with cosmic rays.

### 5.2.2 Experimental test set up with cosmic muons

A cosmic-ray test was conducted to obtain the detection efficiency, noise rate and time resolution of the prototype MRPCs. The chambers were tested separately in the same cosmic ray test setup shown in Fig. 5.15. A reference system was built from three plastic scintillators, two paddle scintillators of dimensions 20 cm × 8.5 cm and one finger scintillator of dimension 7 cm × 1.5 cm, each read out by a photo-multiplier tube (PMT). The overlap area between the scintillators has been used to obtain the cosmic muon detection efficiency. The trigger area covered part of a single strip of the MRPC in width. From a coincidence of all three PMT signals, a master trigger signal is generated using a coincidence unit CAEN N454 and propagated to the next electronics chains.

Table 5.1: Details of the bakelite MRPCs [156].

| | |
|---|---|
| Total area of the MRPC | 15 cm $\times$ 15 cm |
| Active area of the MRPC | 14 cm $\times$ 14 cm |
| Number of outer electrodes | 2 |
| Number of inner electrodes | 5 |
| Dimensions of the outer electrodes | $\sim$ 15 cm $\times$ 15 cm $\times$ 0.30 cm |
| Dimensions of the inner electrodes | $\sim$ 14 cm $\times$ 14 cm $\times$ 0.05 cm |
| Thickness of each button space | $\sim$ 0.024 cm |
| Thickness of the side spacer frame | $\sim$ 0.40 cm |
| Total number of gas nozzles | 2 |
| Total number of gas gaps | 6 |
| Thickness of each gas gap | $\sim$ 0.025 cm |

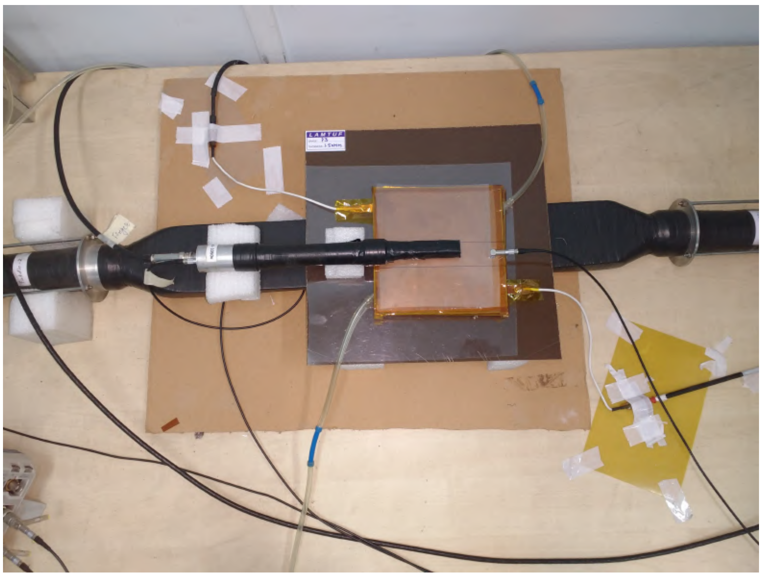

Figure 5.15: Cosmic ray test set up of a single MRPC with three scintillators for trigger setup.

The average master trigger rate was $\sim$ 0.008 Hz/cm$^2$. The high voltage module used for MRPC was CAEN N471A, a 2 Channel 8 kV opposite polarity DC Power Supply for cathode and anode. Hence, there was a limitation in the upper limit of the applied bias voltage of 16 kV ($\pm$ 8 kV). Two-stage voltage amplifiers (CAEN N979) with an overall gain of 100 were used in the front end for amplifying the negative signal from the anode side of the MRPC module. Then the amplified MRPC signal was propagated to a CANBERRA QUAD CFD 454 constant fraction discriminator (CFD) for digitization which was also used for digitizing the analog signals from PMTs. A 4-fold coincidence of the digitized RPC signal and the master trigger signal was generated for obtaining the efficiency. The dark counting rate of the MRPC was measured using the CAEN scalar module N1145. The counting of the master trigger signal and of the 4-fold coincidence signal were done by the same scalar module. For timing measurements, a PHILIPS SCIENTIFIC 7186 TDC module with a common START channel and 16 STOP channels was used. The master trigger signal was given to the START channel and a delayed and digitized MRPC signal was fed to the STOP channel of the TDC module. A CAMAC based data acquisition system has been used in our setup. The MRPC prototypes were operated with a gas mixture of 85 % $R134a$ and 15 % $iC_4H_{10}$ under atmospheric pressure with a gas flow rate of $\sim$ 0.21 ltrs/hr.

### 5.2.3 Results

#### Efficiency

The efficiency of MRPC-1 was measured at two threshold values of CFD, 10 mV and 20 mV (Fig. 5.16). The efficiency gradually increases with HV and reaches a plateau at 15.2 kV for 10 mV threshold and at 15.8 kV for 20 mV threshold. The efficiency reaches $>$ 85 % at the plateau region.

The efficiency of MRPC-2 was measured for two discriminator threshold values, 20 mV and 50 mV. An efficiency of $\sim$ 87 % was achieved at 15.2 kV for 20 mV threshold and at 15.6 kV for 50 mV threshold as shown in Fig. 5.17.

#### Noise Rate

We have also measured the noise rate of the two prototypes at different discriminator thresholds. It is seen from the Fig. 5.18 that the noise rate of MRPC-1 at 10 mV and 20 mV thresholds are

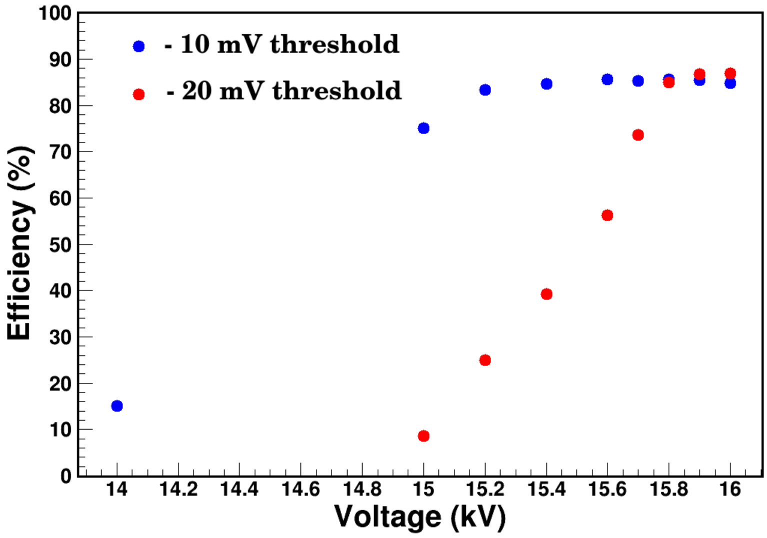


Figure 5.16: Variation of the efficiency of the MRPC-1 as a function of the applied high voltage at - 10 mV and - 20 mV threshold. The error bars are within the marker size [156].

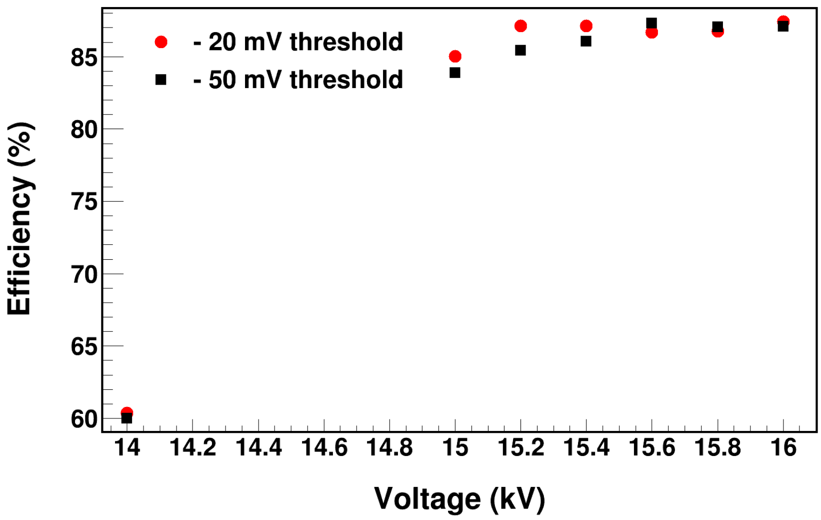


Figure 5.17: Variation of the efficiency of the MRPC-2 as a function of the applied high voltage at - 20 mV and - 50 mV thresholds. The error bars are within the marker size.

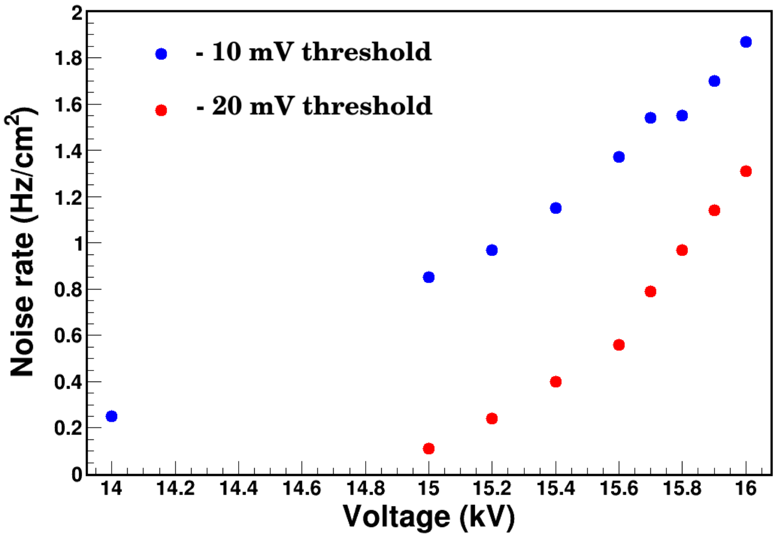


Figure 5.18: Variation of the noise rate of the MRPC-1 as a function of the applied high voltage at - 10 mV and - 20 mV threshold. The error bars are within the marker size [156].

$\sim$ 1.9 Hz/cm$^2$ and $\sim$ 1.3 Hz/cm$^2$ respectively at 16 kV applied voltage. The Fig. 5.19 shows that the noise rate of MRPC-2 at 20 mV and 50 mV thresholds are $\sim$ 2.3 Hz/cm$^2$ and $\sim$ 2.7 Hz/cm$^2$ respectively at 16 kV applied voltage. The noise rate follows nearly a linear behavior for both

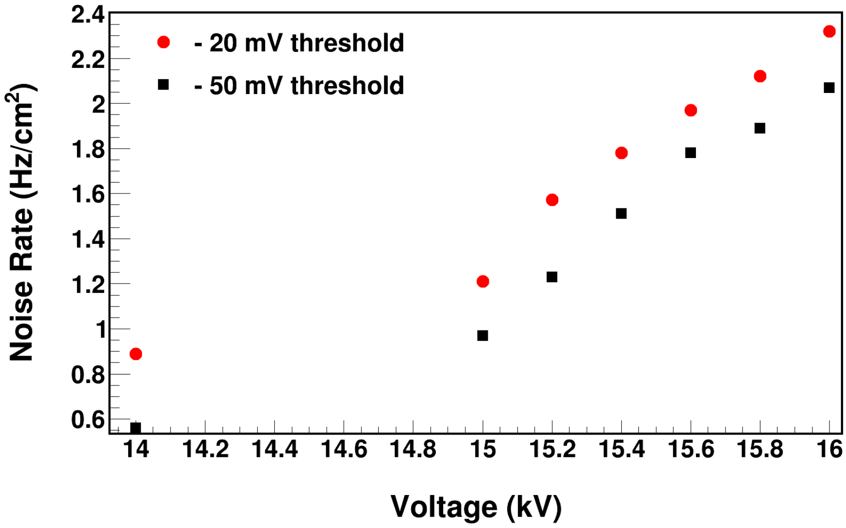


Figure 5.19: Variation of the noise rate of the MRPC-2 as a function of the applied high voltage at - 20 mV and - 50 mV thresholds. The error bars are within the marker size..

the prototypes at different thresholds. Also, the noise rates of the prototypes decrease with an increase in the threshold values at any particular applied voltage.

### 5.2.4 Time Resolution

The time distribution of MRPC-2 is shown in Fig. 5.20. The time resolution of the MRPC-2 was

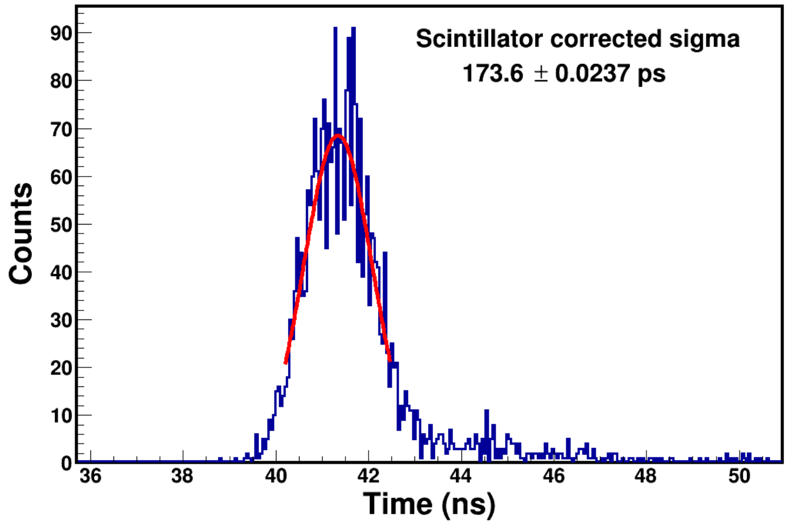


Figure 5.20: The raw time spectra of MRPC-2 at 16 kV [157].

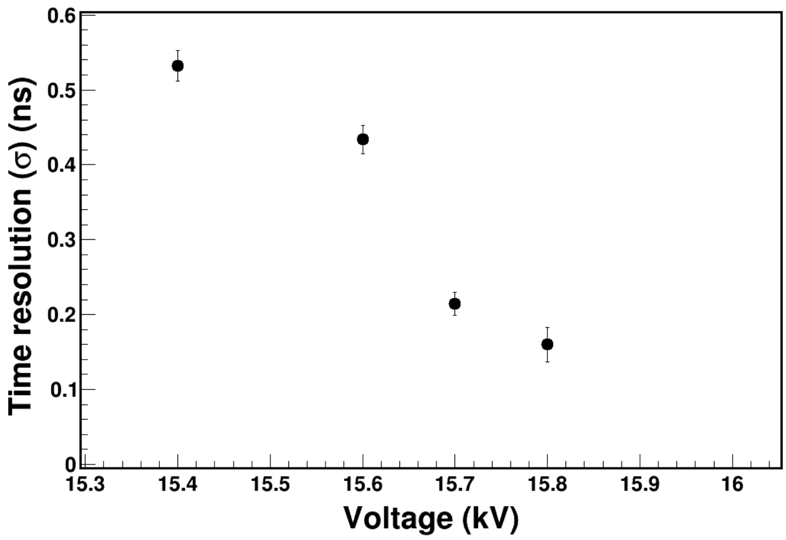


Figure 5.21: The time resolution of the MRPC-1 as a function of the applied high voltage at a discriminating threshold of 10 mV with the scintillator corrections [156].

measured at an overall applied voltage of 16 kV. The TDC spectrum was fitted with a Gaussian function to get the time resolution of the detector. The obtained $\sigma$ from the fit has been corrected for the scintillator contributions as per the reference [10]. The corrected time resolution value was obtained to be 173.6 ps.

The time spectra of the MRPC-1 were recorded from 15.4 kV to 15.8 kV of applied high voltages at

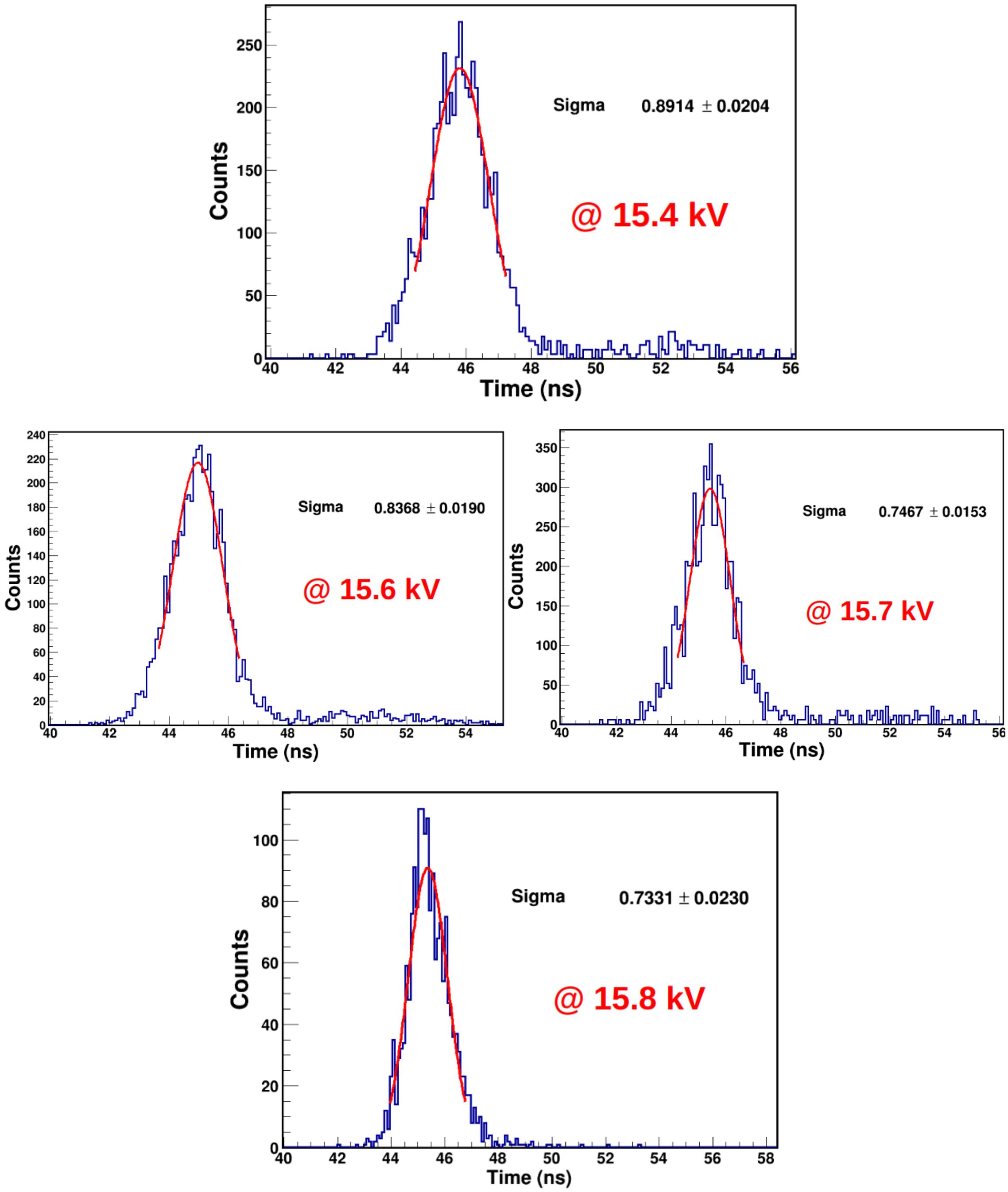


Figure 5.22: Raw time spectra (scintillator uncorrected) of MRPC-1 at different bias voltages for 10 mV discriminator threshold. The red curves show the Gaussian fit.

10 mV CFD threshold as shown in the Fig.5.22. The time spectra were recorded for a reasonable duration of time and then fitted with a Gaussian function. The final MRPC time resolutions ($\sigma$ corrected) were extracted from the Gaussian fit after removing the contribution of the three scintillators [158]. The time resolution of MRPC-1 as function of the applied high voltage is depicted in Fig. 5.21. As seen from the figure, the time resolution gets improved at higher voltages. We have achieved a best time resolution of $\sim$ 160 ps at 15.8 kV.

### 5.2.5 Experimental setup with two bakelite MRPCs

The time resolutions of the two 6-gap bakelite MRPC prototypes were measured simultaneously using cosmic rays in a stack of 5 detectors, two paddle scintillators (49 cm $\times$ 23.5 cm), one finger scintillator (7 cm $\times$ 1.5 cm) and the MRPCs as shown in Fig. 5.23. The master trigger signal

Figure 5.23: Cosmic ray test set up for timing measurements of the MRPCs with three scintillators alongwith PMTs [159].

was defined by the coincidence of three scintillator pulses. The MRPCs were flushed with a gas mixture of $R134a$: $iC_4H_{10}$ :: 85 : 15 (by volume) flowing at a rate of $\sim$ 0.21 l/h. The timing of the MRPCs were measured with the PS 7186 TDC module. The charge spectra were measured with a PS 7167 QDC module. Only a single strip of the each of the MRPCs having a strip-width of 3 cm and strip-length of 14 cm was taken into account. The raw MRPC signals were amplified in two stages (10 $\times$ 10 times) by a CAEN N979 voltage amplifier before proceeding them to the discriminator. The thresholds at the CFD channels were set to 10 mV and 5 mV for MRPC-1 and MRPC-2 respectively. The CFD thresholds of the scintillator pulses were kept at 20 mV. A NIM logic pulse of MRPC-1 served the purpose of the START signal of the TDC module. A delayed NIM logic pulse of MRPC-2 was fed to the STOP channel of the TDC. The master trigger signal was fed to the 'GATE ENABLE' and 'GATE' channels of the QDC module. While analysing the TDC data, the events where cosmic muons got detected by all the 5 detectors (3 scintillators and 2 MRPCs) were considered. The charge spectra was measured for MRPC-2.

### 5.2.6 Results

The dark currents of MRPC-1 and MRPC-2 at 16 kV applied bias voltage were measured to be $\sim$ 1 $\mu$A and $\sim$ 1.5 $\mu$A respectively. The timing of the MRPCs was studied at different applied bias voltages. The TDC spectra were fitted by a Gaussian function to get the Gaussian variance ($\sigma_f$)

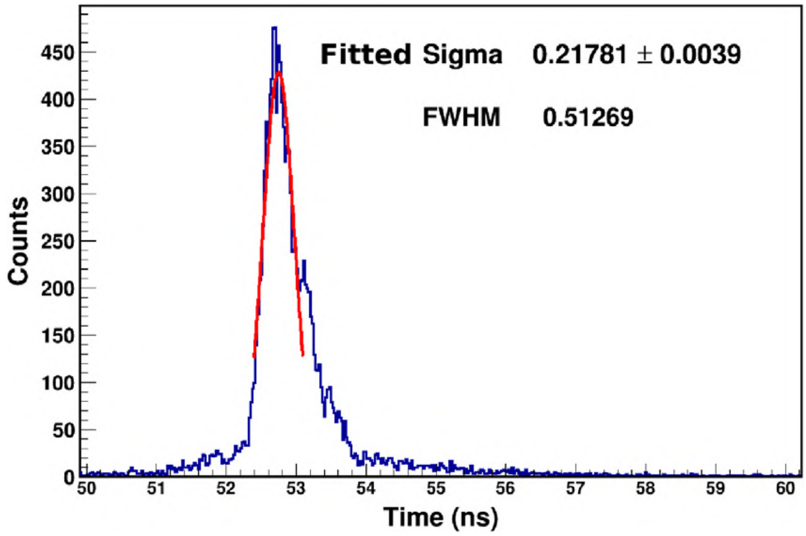


Figure 5.24: TDC spectra of MRPC-2 obtained with respect to MRPC-1 at 16 kV applied voltage [159].

which is the measure of the time resolution of the MRPCs. Fig. 5.24 shows a typical TDC spectrum obtained and fitted with a Gaussian function. The final time resolution ($\sigma$) of the detectors were obtained as follows:

$$\sigma_f = \frac{\sigma}{\sqrt{2}} \tag{5.10}$$

Fig. 5.25 shows the variation of the final time resolution of the detectors as a function of the applied high voltage. The time resolution of the detectors improves with the increase in the applied high voltage. However, we could not operate our detectors beyond 16 kV due to the limitations of the high voltage modules. It has been found out that efficiency saturates at 16 kV. It was assumed that both MRPCs have the same resolution leading to the best time resolution of 154 ps. The charge spectra of MRPC-2 at an operating voltage of 16 kV has been shown in Fig. 5.26.

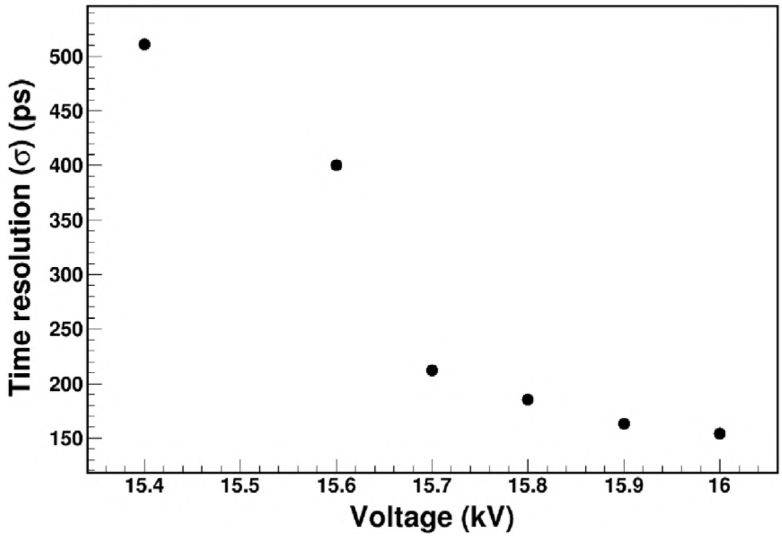


Figure 5.25: Variation of the time resolution of the MRPCs with the applied voltages. The error bars are within the marker size [159].

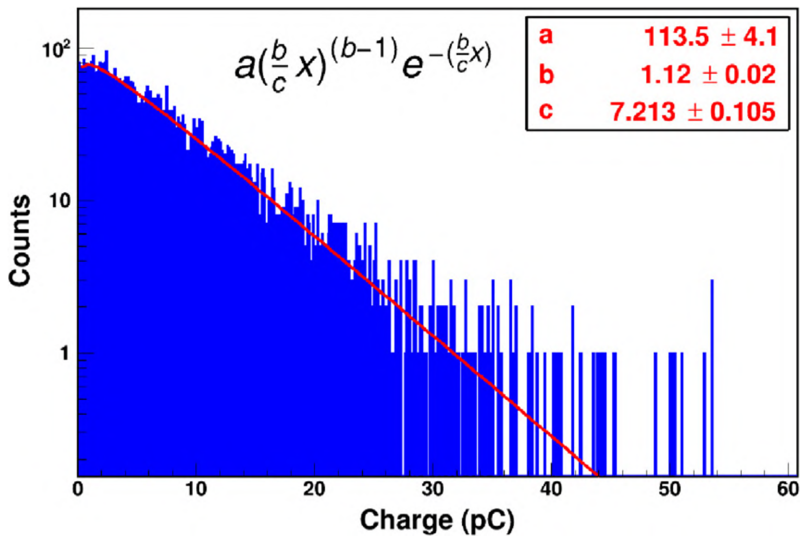


Figure 5.26: Charge spectra of MRPC-2 at 16 kV applied voltage [159].

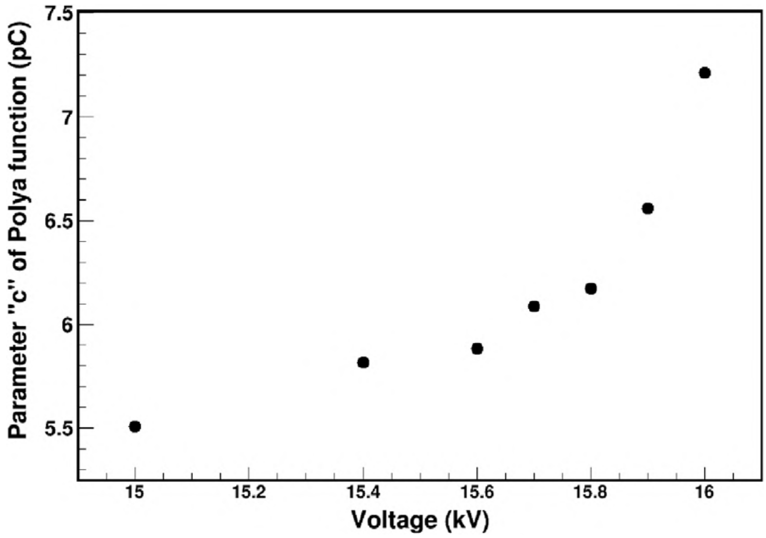


Figure 5.27: Variation of parameter "c" of Polya function as a function of the applied high voltage [159].

The spectrum was fitted with "Polya function" [127] whose functional form has been mentioned inside the Fig. 5.27. The parameter "c" of the "Polya function" has the dimension as that of charge. Hence, we studied the variation of parameter "c" as a function of the applied high voltage, as shown in Fig. 5.27 which clearly shows that value of "c" increases with increase in the applied high voltage to the detector, as expected.

## 5.3 Prototype RPC-P1

### 5.3.1 Search for low-resitivity bakelite samples

The bulk resistivity of the electrode is one of the main parameters which is needed to be optimized to develop a RPC with high rate capability. Therefore, we have started our quest for a low resistivity bakelite sample suitable for the CBM experiment. We have tested three bakelite samples produced by the Indian company Lamtuf Plastics Ltd in search for a low resistivity bakelite sample. We have measured the bulk resistivities of the bakelite plates by measuring the leakage current. We selected bakelite plates each of 30 cm $\times$ 30 cm area as samples. P101, P201 and P301 samples were of 0.3 cm, 0.3 cm and 0.15 cm thickness respectively. Each of the samples was sandwiched between two layers of copper tapes of area 5 cm $\times$ 5 cm. High-tension co-axial cable was soldered on the copper surface, the conducting wire on one side and the grounding wire on another side.

The co-axial cable was then connected to the positive terminal of a high voltage power supply. By varying the applied voltage from the power supply, the change in leakage current was measured. Bulk resistivity is calculated based on the area (A) of the electrodes and the thickness of the sample (t),

$$\rho = (V/I)(A/t) \tag{5.11}$$

As can be shown in the Fig. 5.28, the bulk resistivities of three bakelite samples ($10^{12}$ - $10^{13}$ $\Omega$-cm)

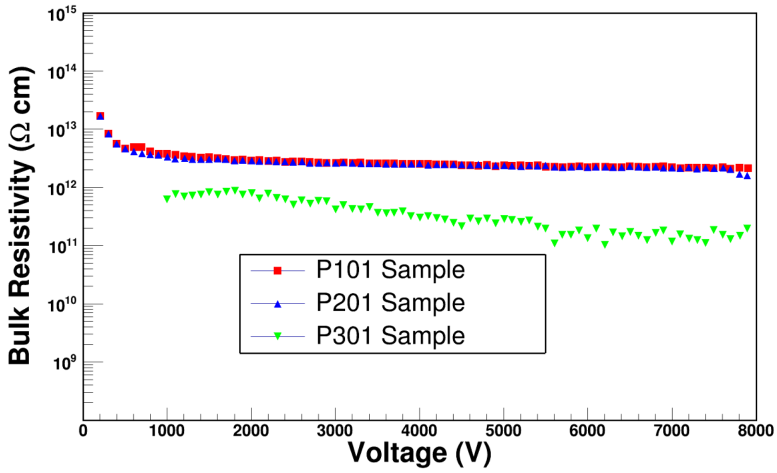


Figure 5.28: Bulk resistivity of the tested samples at different voltages.

do not fulfill our requirement for a low resistivity bakelite sample. Therefore, we procured a bakelite sample of 0.2 cm thickness from an Italian company named General Technica and measured it's bulk resistivity which is shown in Fig. 5.29. The value of volume/bulk resistivity of the Italian bakelite sample is found to be 4 $\times$ $10^{10}$ $\Omega$-cm which fulfills our requirement of low-resistivity bakelite sample. We have therefore used this electrodes for fabrication of the RPC prototype.

### 5.3.2 Characterisation of glue for the fabrication of RPC

The mechanical strength of an RPC is partly controlled by the glue applied on top of the spacers during fabrication. The properties of an RPC is also dependent on the electrical properties of the glue since it has a significant contributing factor in the leakage current of an RPC. The bulk resistivity of the glue should be much higher than that of the electrodes. The bulk resistivities of the glue samples were shown in Fig. 5.30. It can be seen that the resistivity of the glue samples are higher than that of the Italian bakelite sample. Apart from these glue samples, a mixture of

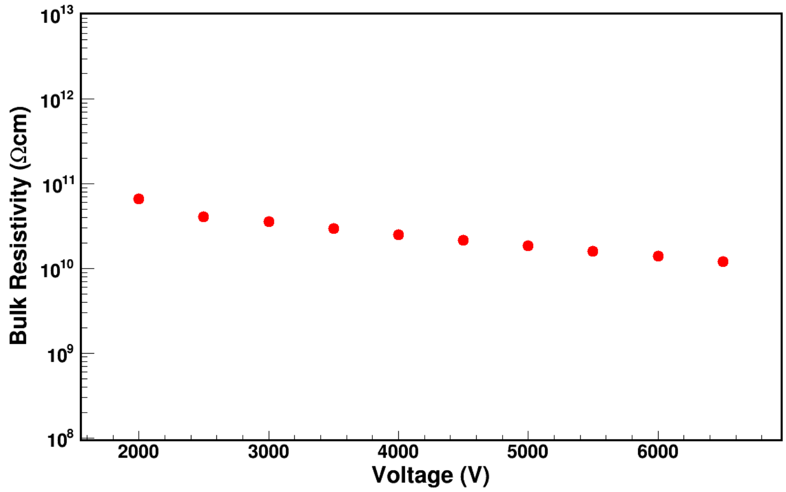


Figure 5.29: Bulk resistivity of the Italian bakelite sample at different voltages.

BC-600 : Araldite [151] resin was found to be feasible for the fabrication of an RPC chamber. A mixture of these glue samples along with BC-600 hardener was used for the fabrication of the prototype RPC chamber made of Italian bakelite sample.

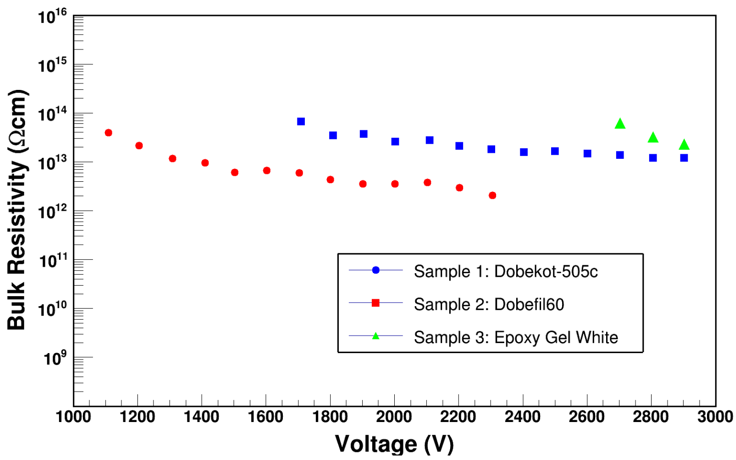


Figure 5.30: Bulk resistivity of the different glue samples as a function of the applied voltage.

### 5.3.3 Construction of RPC-P1

A single gap bakelite RPC of dimension 30 cm $\times$ 30 cm $\times$ 0.2 cm (length $\times$ breadth $\times$ gas-gap) was fabricated with the Italian bakelite plates of thickness 0.2 cm and of bulk resistivity $4 \times 10^{10}$ $\Omega$-cm. This prototype is called RPC-P1. We have followed the same fabrication procedure as of RPC-P0. In this case, we have used a pick-up panel with strip sizes 28 cm $\times$ 1.2 cm.

### 5.3.4 Experimental setup

RPC-P1 was tested with conventional NIM based electronics in the cosmic ray test bench of VECC. The trigger was formed with the coincidence of three scintillator signals, two paddle scintillators (20 cm $\times$ 8.5 cm) and one finger scintillator (7 cm $\times$ 1.5 cm). The photo-multiplier tubes of the scintillators were connected to a DC high voltage power supply CAEN N1470, providing 1450 V to each of the paddle scintillators and 1050 V to the finger scintillator. The scintillator signals processed via a 16 channel LED CAEN N841, followed by a logic unit CAEN N455, forming a three-fold master-trigger signal. RPC-P1 was connected to a HV power supply CAEN N1470A which has a current resolution of 50 nA. We have processed the raw signal from RPC-P1 via a 10X amplifier CAEN N979 before feeding the amplified pulse to a LED channel. The discriminator threshold was kept at 20 mV. Therefore, the discriminator threshold value corresponds to the raw RPC signal is $\sim$ 2 mV.

### 5.3.5 Results

#### Leakage Current

The leakage current of RPC-P1 was measured with increasing bias voltage. The variation of the leakage current with voltage is shown in Fig. 5.31. The breakdown voltage of the gas is found to

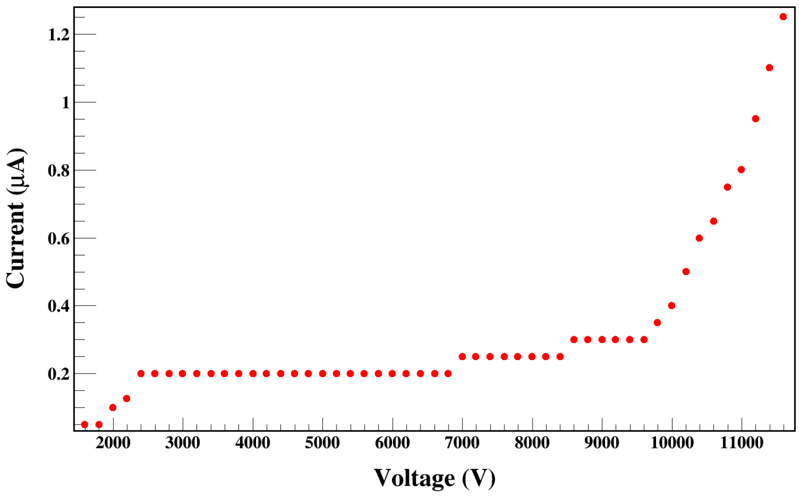


Figure 5.31: IV Characteristics of RPC-P1.

be $\sim$ 9500 V. The steps in the current is attributed to the current resolution of the HV module.

### Efficiency

The efficiency of the detector for the detection of cosmic muons was measured with increase in the bias voltage. The efficiency reaches $\sim$ 90 % at 10000 V with a discrimination threshold of 20 mV which can be seen in Fig. 5.32. The threshold at the input pulse is $\sim$ 2 mV due to amplification of the pulse at the front-end level.

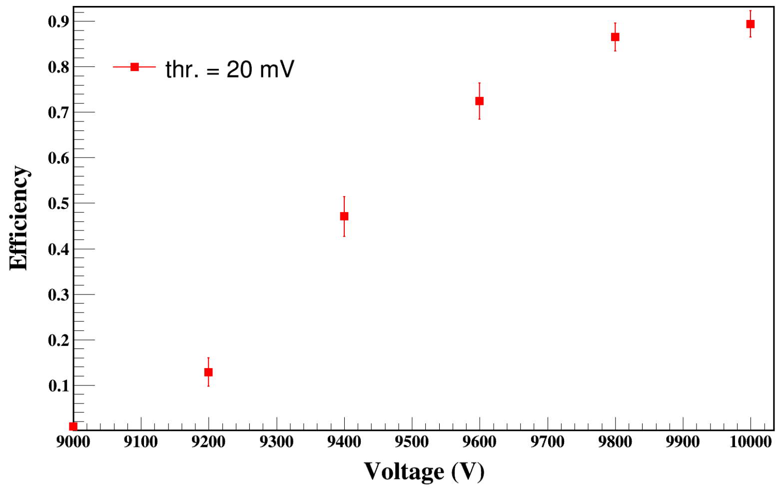


Figure 5.32: Efficiency of RPC-P1 as a function of applied bias voltage.

### Noise Rate

The noise rate is the number of counts per second delivered by the RPC normalized to a detector surface area of 1 $cm^2$. The noise rate of RPC-P1 was measured as a function of the applied bias voltage as shown in Fig. 5.33. At the nominal working voltage (10000 V), a noise rate of 12 $Hz/cm^2$ was measured. The reason for the high noise rate could be attributed to non-uniformity in the surface smoothness of the inner surfaces of bakelite plates since no kind of surface treatment with linseed oil was done during the fabrication of the RPC-P1.

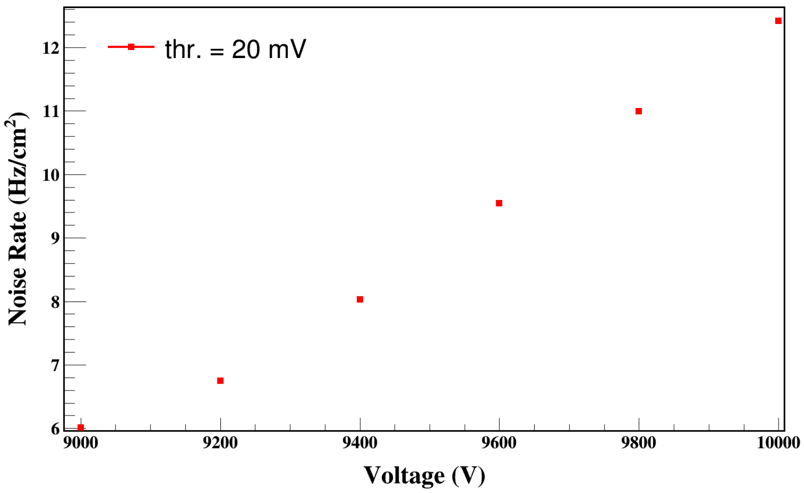


Figure 5.33: Noise Rate of RPC-P1 as a function of applied bias voltage.

## 5.4 Prototype RPC-P2

### 5.4.1 Construction of RPC-P2

In order to achieve a good surface smoothness of the inner bakelite surfaces, a single gap prototype RPC (30 cm × 30 cm × 0.2 cm) named RPC-P2 was fabricated after coating the internal surfaces of Italian bakelite plates with a thin layer of commercially available linseed oil. The chamber was kept under a lamp at 60°C for 1 hour to allow the viscous fluid to fill all the micro-crevices on the surface. Rest of the fabrication procedure was followed like before.

### 5.4.2 Leakage Current

The leakage current through the RPC-P2 was measured as a function of the bias voltage applied by the module CAEN N471A. The IV characteristics of RPC-P2 is shown in Fig. 5.34. The current vs. voltage plot shows a two-slope behaviour with 'knee' region around 9000 V, where the slope changes. The working region of RPC-P2 is beyond the knee voltage. While monitoring the evolution of leakage current with time, the I-V characteristics of the RPC-P2 was performed again with a CAEN SY 1527 crate holding HV modules A1832PE (for positive voltage) and A1832NE (for negative voltage), each providing maximum 6000 V and 20 nA current resolution. The I-V characteristic is shown in Fig. 5.35. Here, we can see that the breakdown voltage for gas was increased from 9000 V to 10000 V and the current values are also on the higher side.

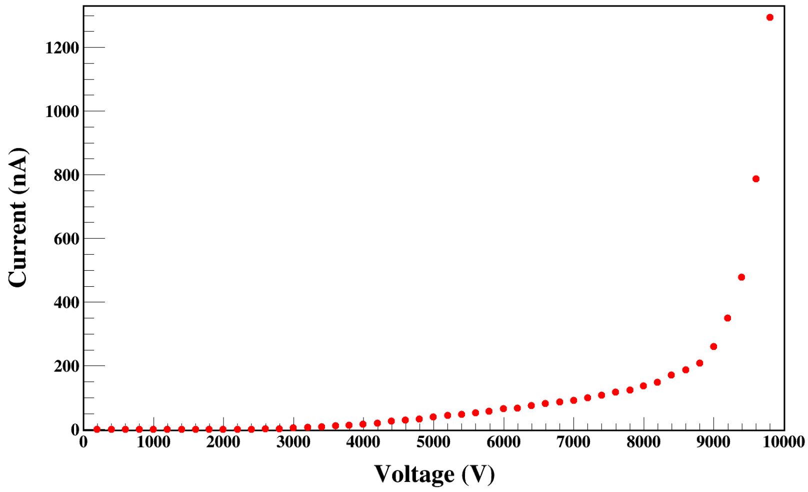


Figure 5.34: IV Characteristics of RPC-P2 with CAEN N471A.

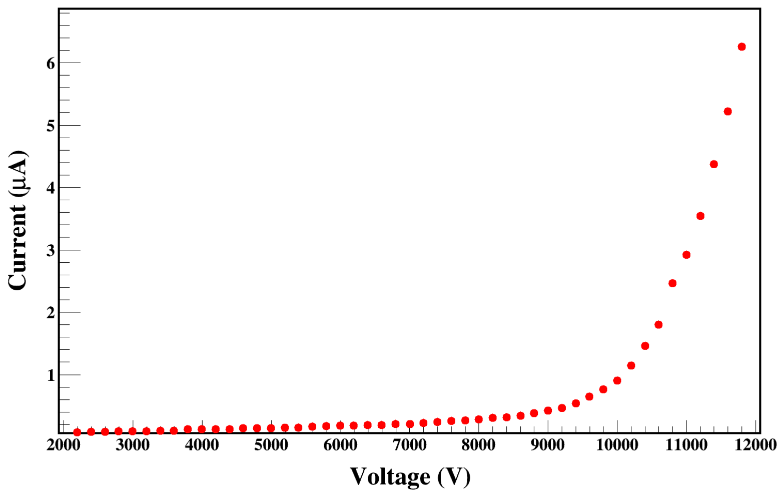


Figure 5.35: IV Characteristics of RPC-P2 with SY 1527 Crate.

### 5.4.3 Current Stability

Due to the increasing current behaviour of RPC-P2, we measured the current at 12000 V for more than 20 hours with SY 1527 crate to make sure that the measured values are stable. The measured values of leakage current is shown in Fig. 5.36. The leakage current kept increasing and never

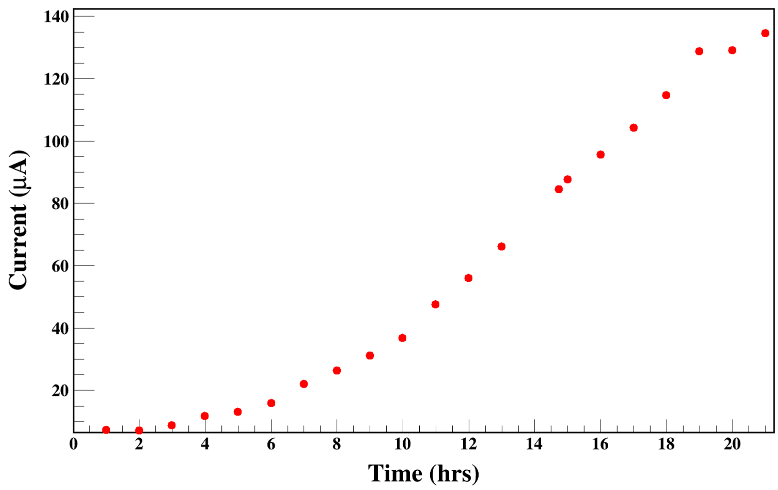


Figure 5.36: Measured leakage current values of RPC-P2 with time using SY 1527 crate.

reached a stable value. We were unable to restore the initial performance of RPC-P2 again. An "autopsy" of the chamber revealed that uncured and sticky linseed oil droplets were spread over the inner surfaces of the Bakelite electrodes. A picture of the inner surfaces of the chamber can be seen in Fig. 5.37. Similar observations were made with the BaBar RPC case and it was seen that non-polymerised linseed oil can form stalagmites or oil droplets under the action of an electric field. The stalagmites can short two electrodes and proviode a physical channel of low resistivity for electric current. The observed high current is due to the flow of ions along these channels. We therefore decided to procure a gap from an industry with a previous record of fabrication of RPCs.

## 5.5 Prototype RPC-P3

A fully fabricated single gap bakelite RPC (RPC-P3) was procured from the Italian company, General Technica. The gas-gap width of the chamber is 0.2 cm which is enclosed by two bakelite sheets each of 30 $\times$ 30 cm$^2$ in size and 0.2 cm thickness. The bulk resistivity of the bakelite sheets are $\sim 4 \times 10^{10}$ $\Omega$-cm. The inner surfaces of the bakelites are coated with double-layered linseed oil

Figure 5.37: . Oil droplets formed inside the bakelite surfaces

in the factory itself. In order to maintain a uniform gas-gap, 9 button spacers are glued equidistant from each other in between two bakelite electrodes. The number of side-spacers used in fabricating the chamber are four which have length and thickness of 28 cm and 0.2 cm each respectively. The material used for the button spacers and side spacers is polycarbonate. There are four gas-nozzles in each corner of the detector, among them two were used for gas-inlet and the other two were used for gas outlet. Signal was picked-up inductively from the anode side by a 30 cm $\times$ 30 cm pick-up panel which comprises strips of length 28 cm. Each of the pick-up strip is 2.3 cm wide and strip-pitch is 2.5 cm.

### 5.5.1 Experimental setup with NINO ASIC

RPC-P3 was characterised in the cosmic bench test set up at VECC. Two paddle scintillators (SC I and SC II) were placed below the RPC and one finger scintillator (SC III) was placed above. All the three scintillators were aligned along the central strip of RPC-P3. The coincidence between SC I (20 cm $\times$ 8.5 cm), SC II (20 cm $\times$ 8.5 cm) and SC III (7 cm $\times$ 1.5 cm) gives the 3-fold trigger as the cosmic muons pass through them which is treated as the Master Trigger. The coincidence between the signal from a single RPC strip and the master trigger was taken as the 4-fold coincidence signal. The high voltage was applied to RPC-P3 on both the electrodes from the DC HV power supply CAEN N471A. The photo-multiplier tubes of scintillators were provided with HV from CAEN N1470. The signals from the scintillators were discriminated by a

CRANBERRA QUAD Constant Fraction Discriminator (CFD) 454 module. A threshold of -20 mV were given to each of the scintillator signal. A single channel of the previously described NINO ASIC was used to amplify/discriminate the signal from a pick-up strip of RPC-P3 attached to the anode side. The threshold at the NINO board was kept at $\sim$ 500 mV which corresponds to a raw input signal of $>$ 3.5 mV. The LVDS signal from the NINO board was converted to NIM signal in two stages by two translator modules, LVDS to ECL translator and ECL to NIM translator. The coincidence between the signals was done by the logic module CAEN N455. A Quad Scalar and Preset Counter Timer module, CAEN N1145 was used for counting 3-fold, 4-fold and digitized RPC signals. Fig. 5.38 shows the schematic of the experimental set-up of RPC-P3. The gas

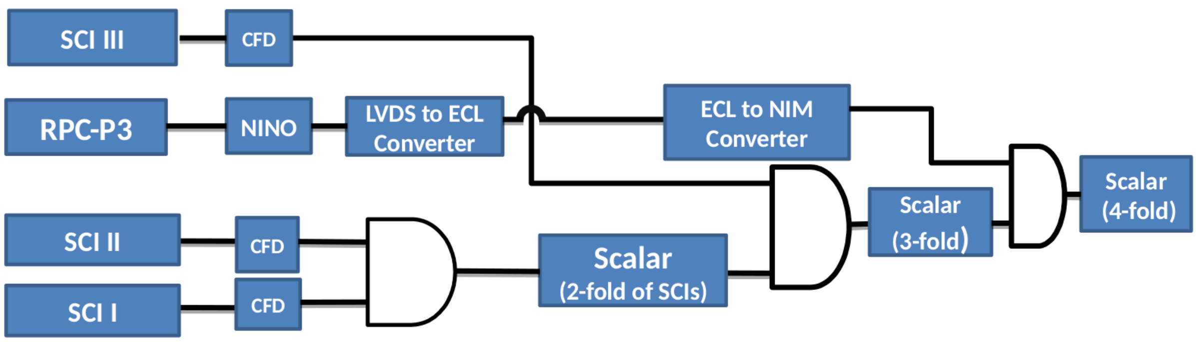


Figure 5.38: The schematic of cosmic muon set up of RPC-P3.

mixture used during the characterisation of RPC-P3 was $R134a/iC_4H_{10}/SF_6$, 94.2%/4.7%/1.1%. An example of the recorded RPC signal on an oscilloscope with 50 $\Omega$ termination is shown in Fig. 5.39 while triggering it with the master trigger signal. The signal has an amplitude of $\sim$ 5 mV which is a characteristic of an avalanche mode signal. Fig. 5.40 shows the LVDS output pulse of RPC-P3 from NINO ASIC recorded on an oscilloscope while triggering with the 3-fold master trigger signal.

### 5.5.2 Results

#### Leakage Current

The leakage currents drawn by RPC-P3 were recorded while voltage was brought up from 0 V up to 10000 V. The I-V characteristics of RPC-P3 is shown in Fig. 5.41. The current vs. voltage plot shows a two-slope behaviour with 'knee' region around 8000 V - 9000 V, where the slope changes.

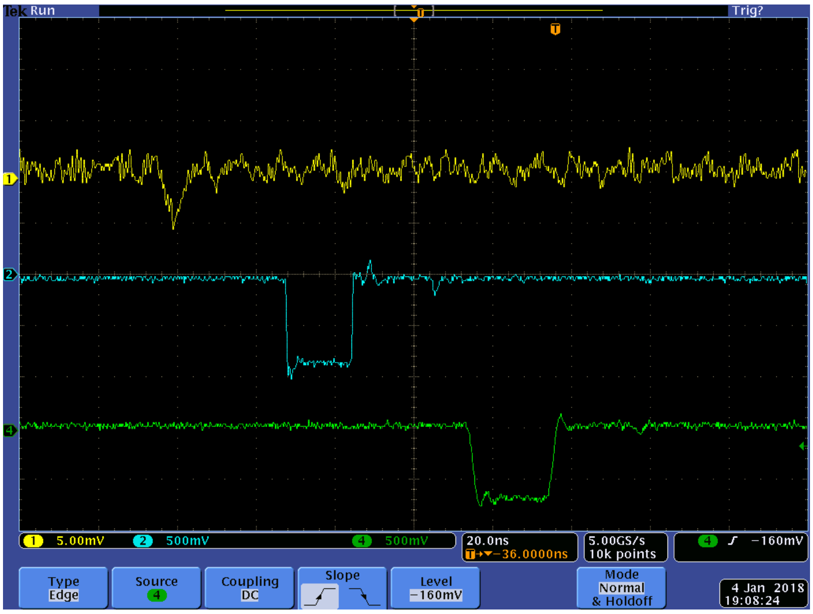


Figure 5.39: An analog signal (yellow) from RPC-P3 with respect to the master trigger signal (green) in oscilloscope. Blue logic signal is the 2-fold of two scintillator paddles. The scale in x-axis is 20 ns and in y-axis is 5 mV for RPC signal. The signal duration is ∼ 12 ns and the signal amplitude is ∼ 5 mV.

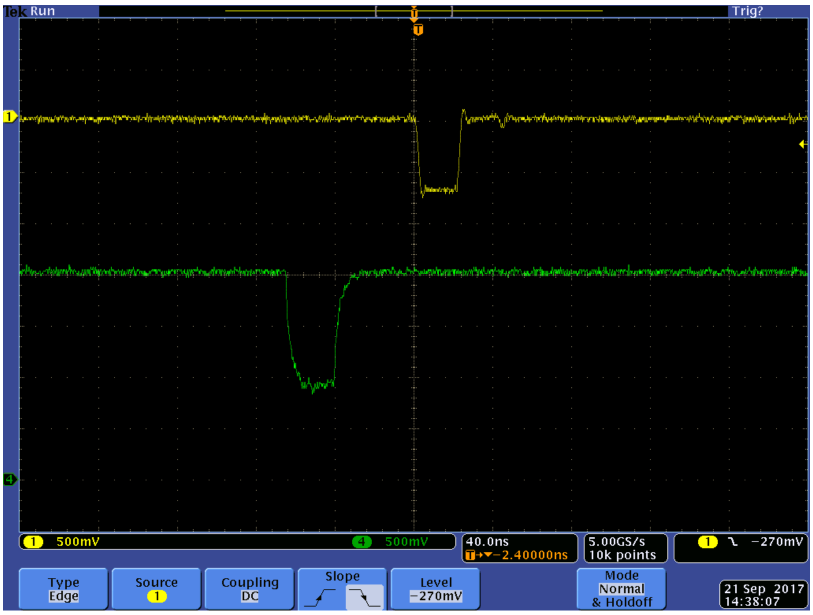


Figure 5.40: A digital output pulse (LVDS) (green) from RPC-P3 with respect to the master trigger signal (yellow) in oscilloscope. The LVDS pulse has an amplitude of 1.2 V and a duration of ∼ 30 ns.

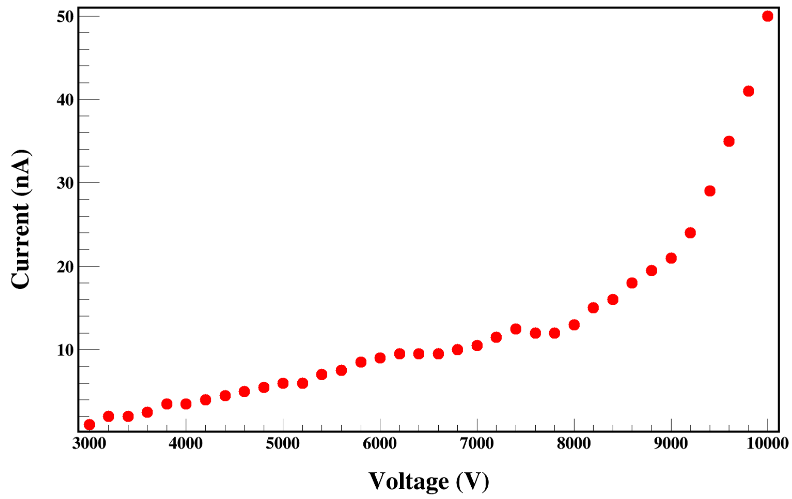


Figure 5.41: Leakage current drawn by RPC-P3 as a function of the applied voltage.

The working point of RPC-P3 will be beyond the knee region.

### Current Stability

The detector was kept for conditioning at 10200 V for 36 hours and the leakage current of the detector was measured for the time interval to check for stability in current. The leakage current is

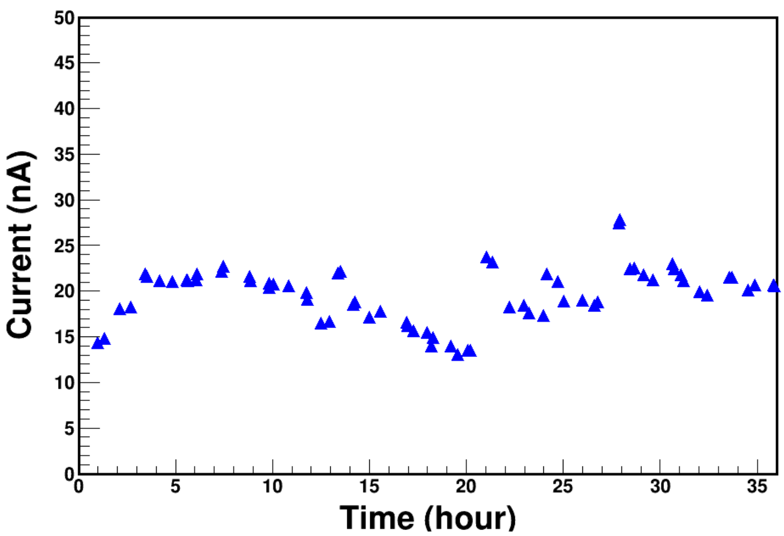


Figure 5.42: Current stability measurement of RPC-P3.

fluctuating between 10 nA to 30 nA over the entire 36 hours and it was observed that the changes in the environmental parameters like humidity and temperature were the primary reason behind this current fluctuation. Also, the fluctuation of humidity in the gas was also causing these small fluctuations in current. Nevertheless, the current stability plot shown in Fig. 5.42 shows that the detector current is almost stable for 1.5 days. We have therefore decided to carry out other investigations using the module.

### Efficiency

The efficiency of RPC-P3 was measured with respect to the coincidence signal of three scintillators. The efficiency plot as a function of applied bias voltage is shown in Fig. 5.43. Each efficiency data at a certain voltage was collected for 1 hour duration. The efficiency of RPC-P3 reaches 93 % at

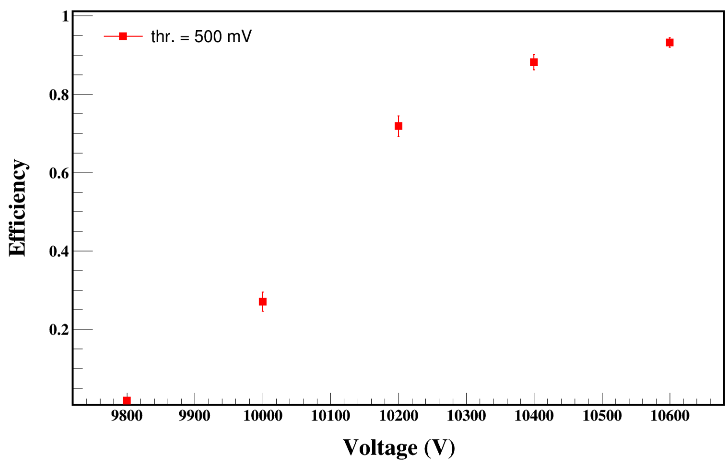


Figure 5.43: Efficiency of cosmic muon detection of RPC-P3 as a function of the applied bias voltage.

10600 V. The temperature of the lab during the efficiency measurements was kept between 20°C - 23°C. The humidity of the lab during the experiment was kept between 44% to 45%.

### Noise Rate

The noise rate of the RPC-P3 was shown in Fig. 5.44 as the applied voltage to the electrodes increases. At 10600 V, the noise rate is $\sim$ 0.52 Hz/cm$^2$ which leads to a noise rate of 468 Hz for the full chamber.

### Time Resolution

The time resolution of RPC-P3 was measured by using the Phillips Scientific 7186 Time to Digital Converter (TDC) module. The 3-fold master trigger signal was acted as the START signal and a

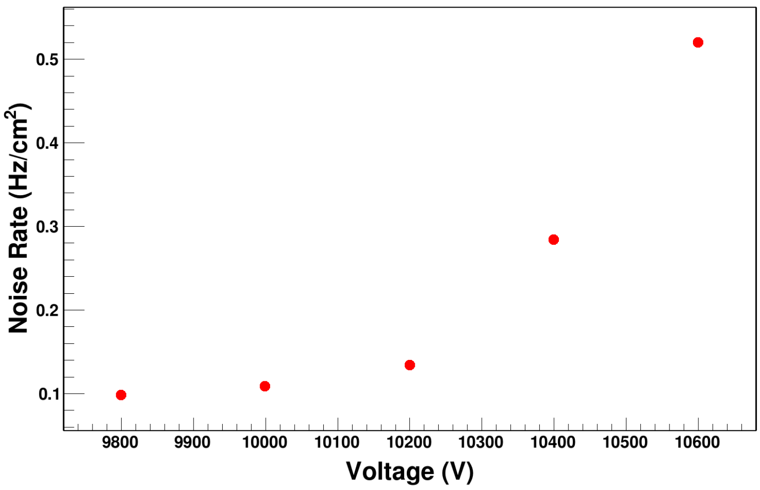


Figure 5.44: Noise Rate of RPC-P3 as a function of the applied bias voltage.

delayed NIM pulse (via a delay module) of the RPC-P3 was used as a STOP signal for the time measurement. Fig. 5.45 shows the time distribution of RPC-P3 at 10600 V. After omitting the

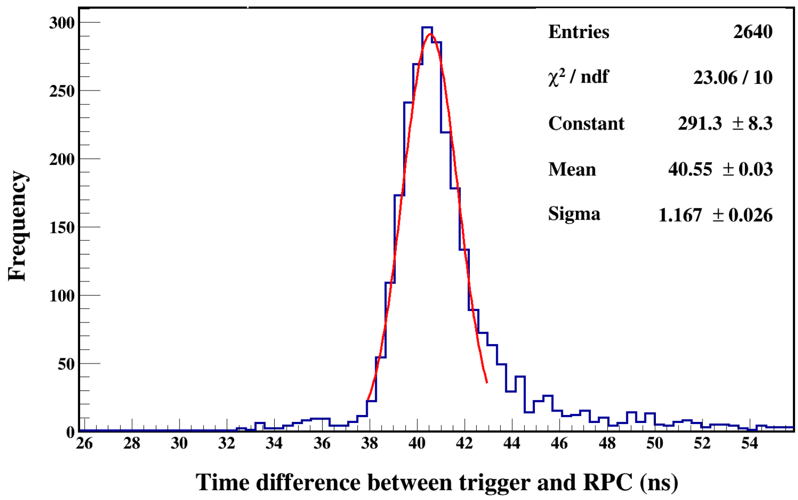


Figure 5.45: Time difference spectra between the master trigger signal and the RPC-P3. A Gaussian fit delivers a time resolution of 1.167 ns for RPC-P3.

contribution of scintillators from the time resolution, the corrected time resolution of RPC-P3 is measured to be 1.05 ns at 10600 V.

### 5.5.3 Experimental setup of RPC-P3 with PADI-6 ASIC

The MRPCs in CBM-TOF [160] system will be read-out by a PreAmplifier-DIscriminator (PADI) ASIC specifically designed to be used as a FEE for the CBM experiment in order to optimize the price and power consumption. The PADI chip has several prototypes, from PADI-1 to PADI-8, consecutively built as per the requirements. It is configured on 0.18 $\mu$m CMOS technology. Among them, we have tested our RPC-P3 prototype with PADI-6 version for comparison with the results obtained by using NINO ASIC. PADI-6 has the following key parameters: fully differential design, LVDS output, four channels per chip, 50 $\Omega$ input impedance, pre-amplifier (PA) voltage gain $\sim$ 244, PA conversion gain $\sim$ 35 mV/fC, PA bandwidth $\sim$ 416 MHz, signal peaking time $< 1$ ns, noise related to input $< 25$ $\mu V_{RMS}$, power consumption 17 mW/channel, DC feedback loop for offset/threshold stabilization, the threshold range between $\pm$ 500 mV [161, 162]. Since PADI-6 accepts only differential signal and we were working with single-ended signals, we have utilised the differential amplifier THS4520 on the NINO ASIC for the conversion of a single-ended signal to a differential signal before feeding the differential signal to PADI-6 ASIC. The differential amplifier THS4520 was also helpful as a spark protection circuit. The threshold could be changed externally by a potentiometer present on the ASIC. Fig. 5.46 shows the LVDS output signal from PADI while the input was given from a pulse generator. Since PADI-6 ASIC doesn't have a pulse stretcher

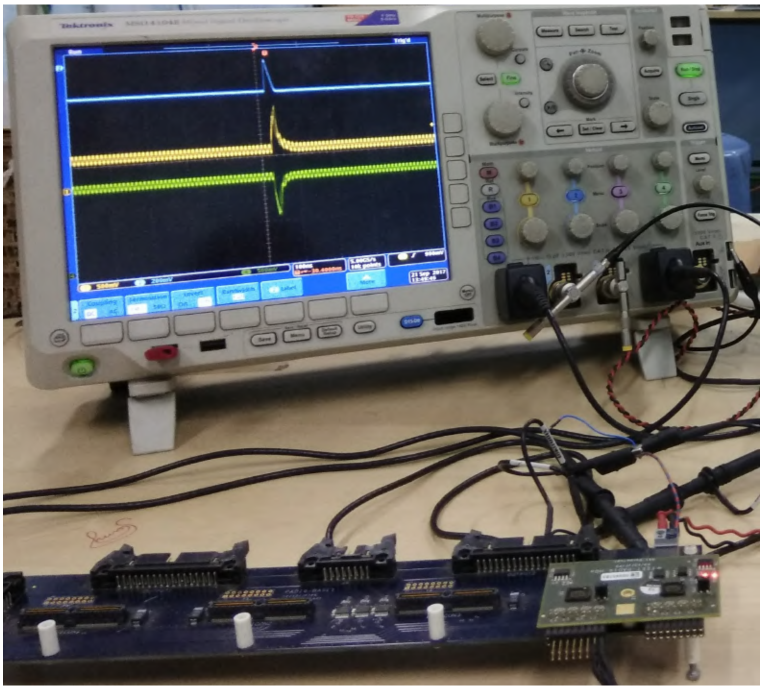

Figure 5.46: The LVDS output pulses (green and yellow) from PADI-6 on oscilloscope providing the input pulse (blue) from a pulse generator. The scale in x axis is 100 ns, while the scale in y-axis is 500 mV for LVDS pulses and 200 mV for the input pulse. This pulse is given to PADI-6 via a 1:10 attenuator.

unlike NINO ASIC at the digital output stage, LVDS to other logic conversion circuits were not responding to low level signals from RPC. GET-4 ASIC designed by the CBM-TOF group has this capability to detect such low signals, but GET-4 ASIC was not avilable at VECC at the time of this integration tests. Therefore, we developed a custom-made PADI specific discriminator to convert the output pulse from LVDS to NIM logic. The LVDS logic pulse from PADI-6 was converted to a NIM logic pulse by our custom-made fast Leading Edge Discriminator with adjustable delay and width and the NIM pulse could be coupled to a conventional NIM electronics to measure efficiency and noise rate of RPC-P3. The discriminator comprises of a fast ECL comparator, two monostables for providing delay and width generation and subsequently gives two NIM outputs and a TTL output. In the heart of the unit, a fast comparator MAX9600 was used. It has a maximum propagation delay of 500 ps, dispersion of 30 ps and also a tracking frequency of 4 Gbps. This IC also has a provision for hysterisis adjustment which is useful for preventing oscillation or multiple transitions due to noise. A voltage reference REF192 was used to provide necessary voltage reference to the fast comparator with ultra low noise and good stability. This reference IC has a temperature coefficient of 5 ppm/°C. The threshold of the comparator can be set from + 50 mV to + 2.5 V which can be adjusted by a multi-turn trimpot. Both the delay and width of the output have a range of 10 ns to 40 $\mu$s adjustable via trimpots R1 and R2 respectively. The block diagram of the discriminator was shown in Fig. 5.47. The threshold kept at PADI-6 was 298 mV and the threshold at the custom-made discriminator was set to 1.407 V during the data taking. The cosmic ray test bench used for characterisation is the same as the NINO board setup. Each of the pick-up strip dimension is 28 cm $\times$ 2.3 cm. The strip-pitch is 2.5 cm.

### 5.5.4 Results

#### Efficiency

We have measured the efficiency of RPC-P3 with PADI-6 at different voltages. Each efficiency data at a certain voltage was measured for 6 hours. The temperature of the lab was between 18°C -20°C and the humidity was between 38% - 46%. The efficiency scan shown in Fig. 5.48 shows that we reach a plateau with $>$ 91 % efficiency at 10400 V.

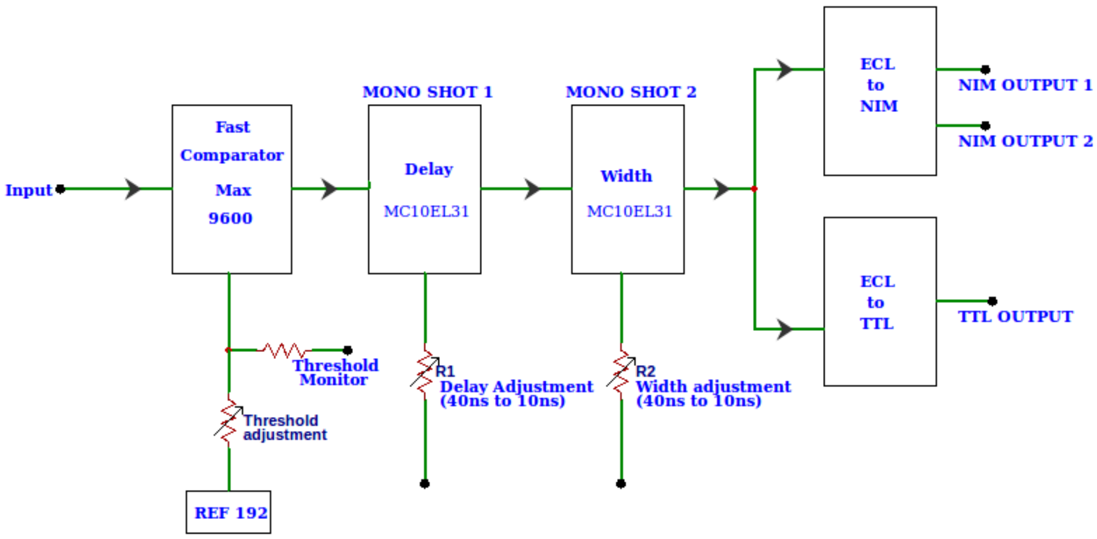


Figure 5.47: Schematic block diagram of the custom made discriminator.

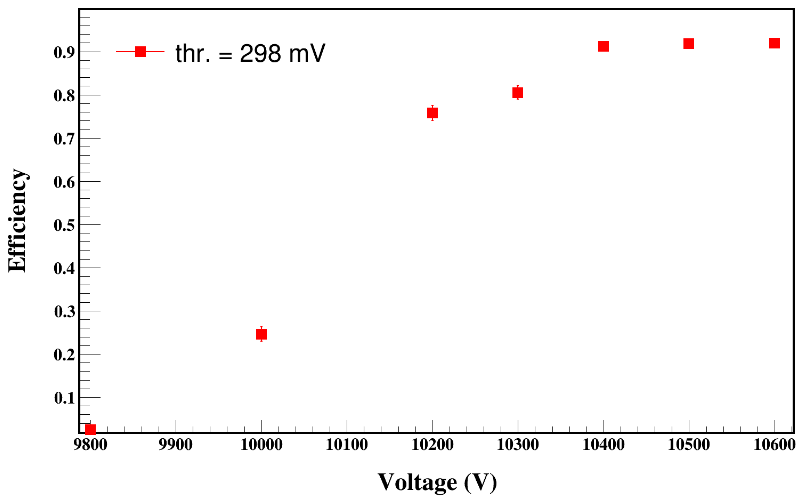


Figure 5.48: Efficiency as a function of the applied voltage of RPC-P3 with PADI-6.

### Noise Rate

Measurements of single counting rate/noise rate are performed at different HV for the previously mentioned front-end thresholds. The noise is plotted as a function of applied HV shown in Fig. 5.49. The noise rate at the start voltage of efficiency plateau, i.e., at 10400 V is 0.73 Hz/cm$^2$. It

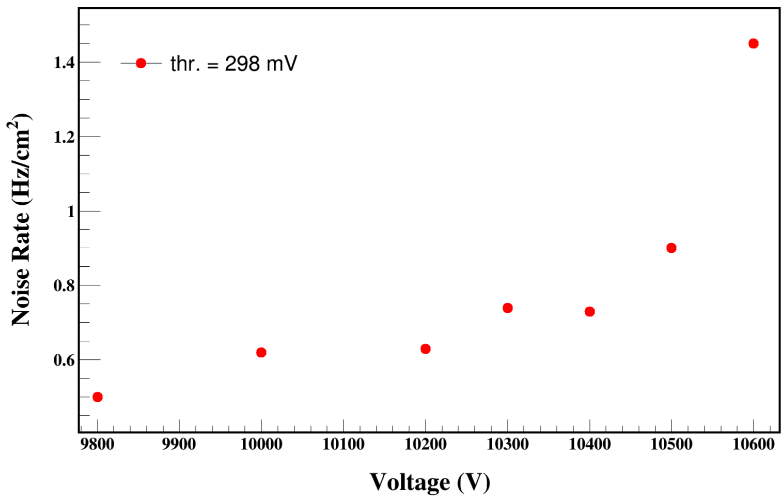


Figure 5.49: Noise rate as a function of the applied voltage of RPC-P3 with PADI-6.

increases with HV and reaches 1.45 Hz/cm$^2$ at 10600 V.

## 5.5.5 Experimental setup with commercial CSA and conventional NIM electronics

MuCh-XYTER ASIC is a self-triggered electronics, to be used as FEE for the Gas Electron Multiplier (GEM) detectors at the 1$^{st}$ and 2$^{nd}$ stations of CBM-MuCh. A planning was made to use a common chip for the entire CBM-MuCh stations to avoid the non-uniformity and complexity involved in using different readout systems. MuCh-XYTER is a charge sensitive pre-amplifier based front-end readout board. Therefore, we have tested our prototype RPC-P3 first with a commercial charge sensitive pre-amplifier (CSP), ORTEC 142IH. The schematic diagram of the test set up is shown in Fig. 5.50. Signals from three plastic scintillators (20 cm $\times$ 8.5 cm, 20 cm $\times$ 8.5 cm and 7 cm $\times$ 1.5 cm) were digitized by a LED module, CAEN N841. A 3-fold master trigger signal was formed with these three scintillator signals using a coincidence unit CAEN N454. The signal from RPC-P3 was given to CSP 142IH via a lemo cable. The output signal of the CSP was amplified 10

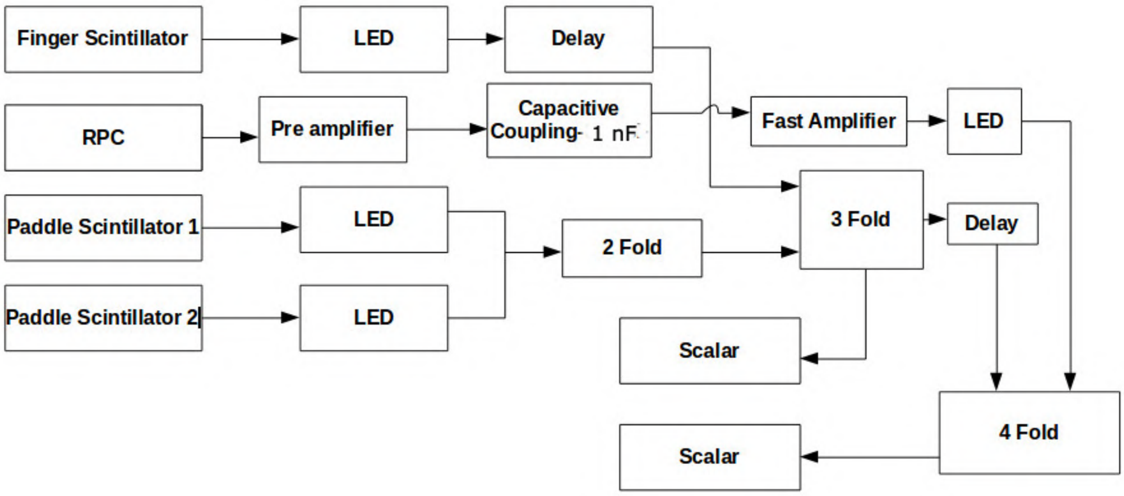


Figure 5.50: Schematic diagram of the cosmic ray test set up of RPC-P3 with CSP 142IH.

times by a fast amplifier CAEN N979 via a capacitive coupling (capacitor value 1 nF). Since the output signal of the CSP is +Ve and the LED module accepts only negative signal, we have used a Linear FIFO module to change the polarity of the signal. Then the negative polarity signal was digitized by the LED module. The threshold at the LED for the RPC signal was set to - 40 mV. Then, a coincidence of the digitized RPC signal and the 3-fold master trigger signal was formed, the "so called" 4-fold signal. These signals were counted using a scalar module, CAEN N1145.

### 5.5.6 Results

#### Efficiency

The efficiency and its statistical error are calculated according to 5.5 and 5.7 respectively. As reference, the coincidence of the three plastic scintillators forming the 3-fold trigger was used. The efficiency as function of the applied high voltage is shown in Fig. 5.51. The detector reaches a plateau in detecting cosmic muons with > 90 % efficiency at 9700 V. The working voltage is lower than what we achieve with NINO and PADI electronics, i.e., current-sensitive electronics. So, we are able to work in a low-gain region of RPC with charge sensitive preamplifier based electronics.

#### Noise Rate

The noise rate of RPC-P3 was measured and plotted with different voltages shown in Fig. 5.52. The ionisations created by the lower energy particles got amplified enough to be detected as the

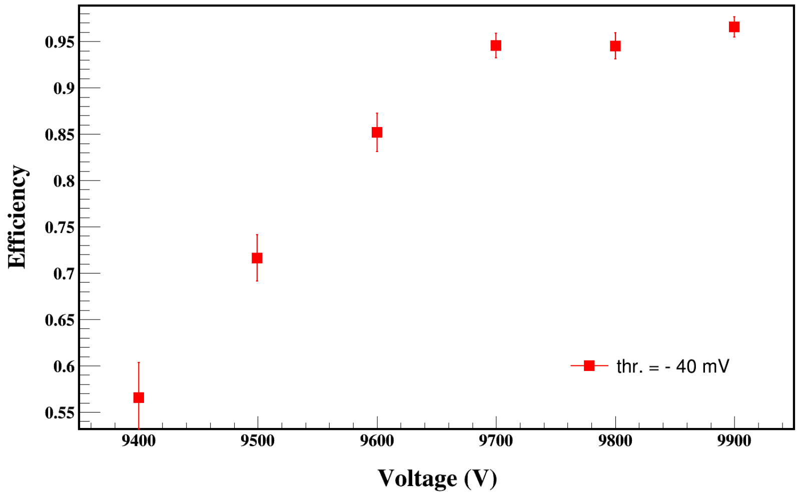


Figure 5.51: Efficiency as a function of the applied voltage of RPC-P3 with CSP 142IH.

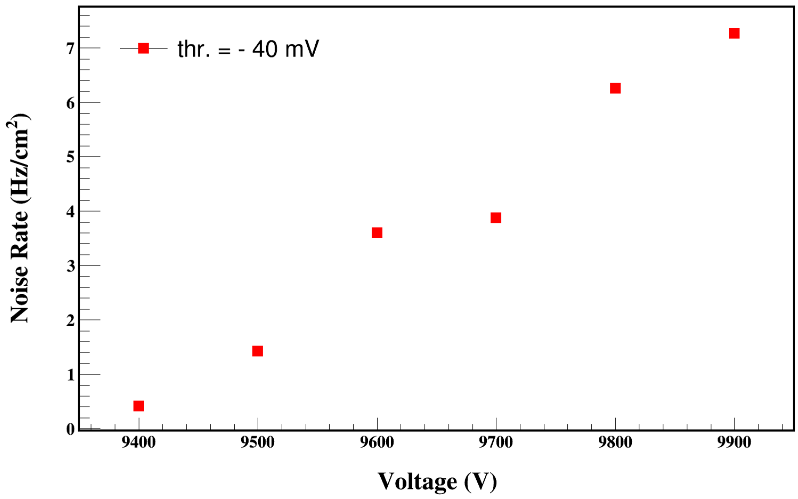


Figure 5.52: Noise rate as a function of the applied voltage of RPC-P3 with CSP 142IH.

voltage, thereby, electric field is increased which results in increased noise rate.

#### Time Resolution

The time resolution of RPC-P3 was measured by using a Phillips Scientific 7186 Time to Digital Converter (TDC) in the configuration where the total time scale range is 400 ns. The time resolution of the module in this mode is about 98 ps. We have prepared the setup with 3-fold master trigger being a START and delayed digital RPC signal being a STOP for the TDC module. The time difference between trigger and RPC yields a time distribution which can be fitted by a Gaussian function. Fig. 5.53 shows the time distribution when the RPC-P3 was given a HV of 9800 V. Therefore, the uncorrected time resolution of RPC-P3 is measured to be 5.291 ns at 9800

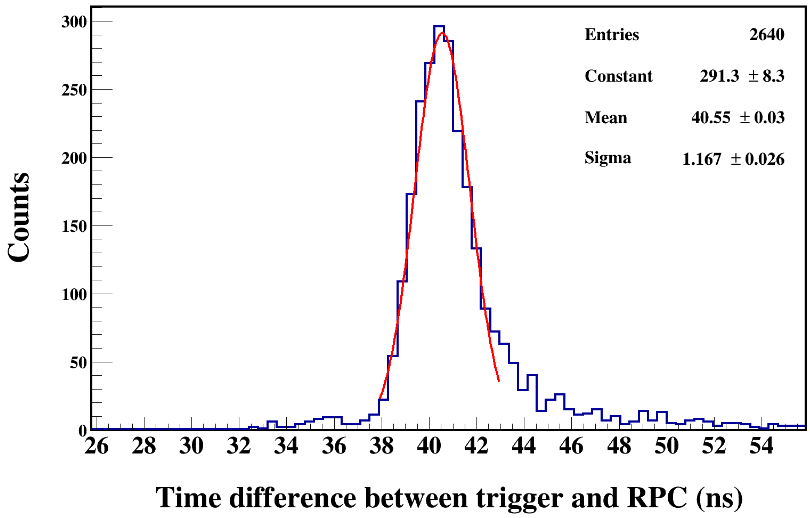


Figure 5.53: Time distribution spectra of trigger and RPC-P3.

V. The contributions from the three scintillators using LED are found to be,

$$\sigma_{SC1}^2 + \sigma_{SC2}^2 + \sigma_{SC3}^2 = 1.378ns \tag{5.12}$$

Therefore, the corrected time resolution of RPC-P3 is, $\sigma_{RPC} \sim 5.16$ ns at 9800 V.

### 5.5.7 Measurement of charge spectra with MANU Board

The charge characteristics of RPC-P3 was measured with the readout chain used for ALICE Photo Multiplicity Detector (PMD) and Dimuon Forward Spectrometer (DFS). The FEE of ALICE PMD and DFS is based on MAnas NUmaric module (MANU card, see Fig. 5.54) mounted on electronic

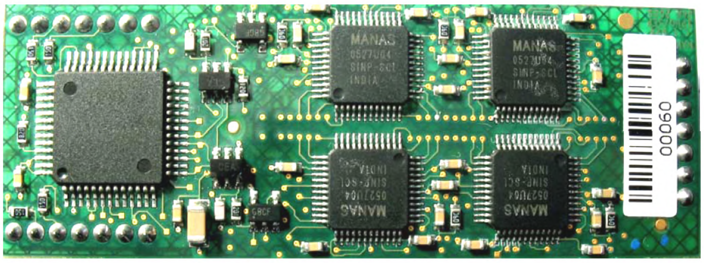

Figure 5.54: The MANU Card.

readout PCB (64 analog input channels), equipped with four 16-channel chips called MANAS (Multiplexed ANALogic Signal processor for charge pre-amplification, deconvolution, gaussian shaping, amplitude memorization and analog multiplexing for 16 channels), two 12 bits Analog to Digital Converters (ADC 7476) and a custom built digital controller chip called MARC (Muon Arm Readout Controller for coding, pedestal subtraction, zero suppression and communication with the readout). The noise level of the full electronics chain is around one thousand electrons. MANAS, designed by Semiconductor Complex Limited (SCL Chandigarh, India), is a custom IC using 1.2 $\mu$m CMOS technology, while the digital front-end MARC chip was designed by INFN Cagliari team in the 0.6 $\mu$m AMS CMOS technology. MANAS chip has a dynamic range of up to - 250 fC for negative signals, pre-amplifier gain of 3.3 mV/fC, shaper with 1.2 $\mu$s peaking time and power dissipation of 9 mW/channel. In the MANU board, a precision voltage reference of + 2.5 V was used, which gives a resolution of 0.61 mV per ADC channel. The final readout was done through a Cluster Readout Concentrator Unit System (CROCUS). The power requirement of MANU board is $\pm$ 2.5 V, + 3.3 V. A delayed 3F master trigger signal from the three plastic scintillator like the last cosmic ray experimental set up was given to the board as trigger. The NIM pulse was converted to a TTL logic pulse before providing it to the FEE board. The analog signal from RPC-P3 was directly fed into the MANU board. The detector was operated at 9800 V. The charge spectrum was fitted with a “polya function” with a 10 fC cut as shown in Fig. 5.55. The mean charge of a signal is represented by the parameter “c” which is found to be $\sim$ 77 fC. Some of the signals are getting saturated due to the maximum dynamic range of the FEE.

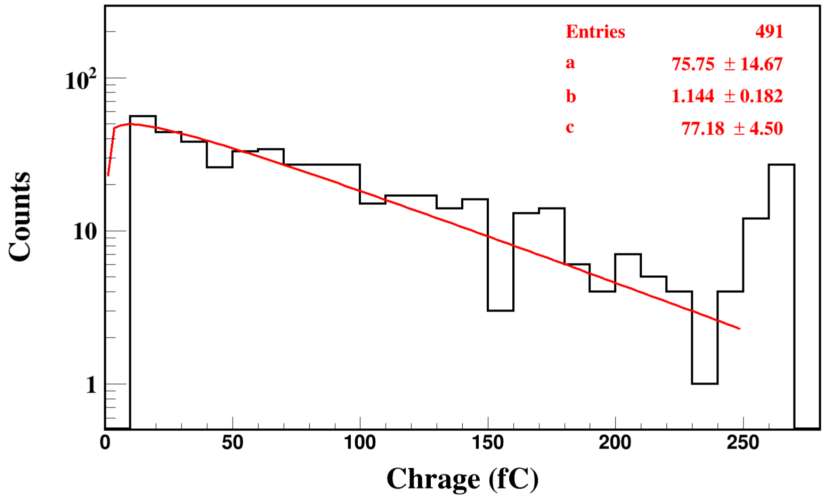


Figure 5.55: The charge spectra of RPC-P3 at 9800 V using MANU board.

## 5.6 Discussions

As per the requirements for CBM, we have developed and tested a few prototypes of single-gap and Multi-gap RPCs in avalanche mode gas mixtures. A single-gap bakelite RPC prototype made of ingenious material (P302 OLTC grade bakelite) with bulk resistivity $\sim 9 \times 10^{11}$ Ω-cm could detect cosmic muons with an efficiency of $\sim$ 88 % and a time resolution of $\sim$ 2.56 ns using conventional NIM based electronics. While testing with the sophisticated current sensitive FEE NINO, detection efficiency of $\sim$ 94 % for cosmic muons was achieved by the prototype with a time resolution of $\sim$ 2.3 ns. The noise rate of RPC-P0 was $< 1$ Hz/cm$^2$ with both kinds of electronics. Two bakelite MRPC prototypes fabricated using the same grade of bakelite as RPC-P0 and each having 6 gas-gaps showed cosmic muon detection efficiencies of $\sim$ 88 %, time resolutions of $\sim$ 154 ps at 16 kV. We have searched for a lower resistivity bakelite sample with an aim to increase the rate capability of RPC for the CBM experiment. We have performed a few R&Ds in developing RPC prototypes using lower resistivity bakelite material than the previous P302 OLTC grade bakelite sample. A prototype single-gap bakelite RPC prototype (RPC-P3) made of bakelite sheets with bulk resistivity $\sim 4 \times 10^{10}$ Ω-cm was capable of detecting cosmic muons with an efficiency $> 90$ %, noise rate $< 1.5$ Hz/cm$^2$, time resolution $\sim$ 1.05 ns at 10.6 kV using current sensitive electronics like NINO and PADI. The prototype was also operated with charge-sensitive electronics (142IH) and showed an efficiency of $\sim$ 94 % at a lower voltage (9.7 kV) compared to current-sensitive electronics. The time resolution of RPC-P3 was degraded using charge-sensitive electronics and found to be $\sim$ 5.2 ns. The charge spectrum of RPC-P3 was measured at 9.8 kV using MANAS electronics and the average charge of RPC-P3 is found to be $\sim$ 77 fC. Few events got saturated due to the maximum dynamic range (275 fC) of the ASIC.

# Chapter 6

# Testing of a prototype and a real Size RPC module with self-triggered MuCh-XYTER electronics

This chapter illustrates the studies on the performance of RPC-P3 described in the previous chapter at the Gamma Irradiation Facility (GIF++) located at CERN SPS North Area, Geneva, Switzerland using the MuCh-XYTER ASIC. The facility provides irradiation by gamma emission through a $^{137}Cs$ source and a muon beam from the H4 North Area line. The aim of the measurement is to test the prototype RPC along with the CBM electronics and DAQ with high intensity muon beam under high particle irradiation flux. Thereafter, the study on RPC-P3 with MuCh-XYTER ASIC was continued at VECC using cosmic muons. Also, the detailed characteristics study of a real size RPC module for the CBM experiment with MuCh-XYTER electronics was carried out cosmic muons.

## 6.1 Testing of prototype RPC-P3 at GIF++

### 6.1.1 GIF++ Facility

GIF+ is a unique test beam facility focussed on the characterization and understanding of the long-term behavior of large area detectors under a high photon flux along with a particle beam.

The facility is located at the secondary SPS beam line H4 in EHN1 where high-energy muon beam (100 GeV/c) are combined with a 13.9 TBq $^{137}$Cs source. The GIF++ area incorporates the actual irradiation area, a preparation zone and a two-floor area to host the gas systems and the electronic devices. The GIF++ bunker is about 5 m high and 100 m$^2$ in area. The bunker is delimited by concrete blocks of 1.6 m thickness and therefore, a shielded area is created which is accessible from two sides. The roof of the bunker is also made of movable concrete blocks for the purpose of the installation of very large area setups. A schematic image of the GIF++ facility is shown in the Fig. 6.1.

GIF++ has two independent irradiation zones named as upstream and downstream, referring

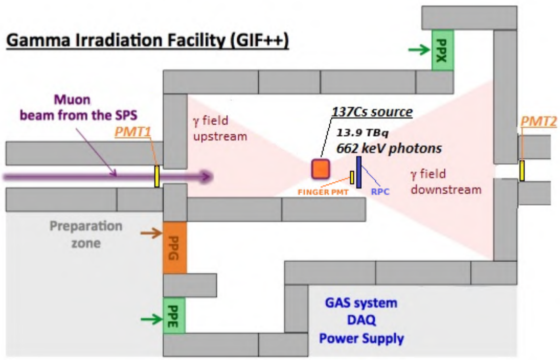


Figure 6.1: A schematic diagram of the GIF++ facility.

to their position with respect to the gamma source. $^{137}$Cs isotope was chosen as gamma source instead of $^{60}$Co due to its long half lifetime of 30.08 years, which can provide a more uniform photon rate over the expected lifetime of this facility (10 years). The energy spectrum of $^{137}$Cs isotope is composed of primary 662 keV photons and scattered photons with lower energy. The $^{137}$Cs source is embedded between two Tungsten blocks and can be moved vertically inside a support tube. When the source is at the bottom of the support tube (garage position), there is no irradiation inside the bunker area, i.e., source OFF condition. At the top of the tube, the source is in ON condition and two $\pm$ 37° panoramic collimators allow to irradiate a large fraction of the upstream and downstream zones inside the bunker. Both openings of the irradiator are equipped with a lens shaped angular correction filter that ensures a uniform photon distribution over a plane rather than a point like source which shows a $\frac{1}{r^2}$ dependence of the photon flux. The photon flux now changes only in z axis, i.e., distance from the source rather than depending upon x, y and z co-ordinates. Large area detectors are mainly benefited due to this arrangement, which would otherwise be subjected to a non-uniform photon flux. For each irradiation zone, a system of two independent 3 × 3 arrays of lead absorption filters (ABS) are used to attenuate the gamma flux. The ABS are mounted on a remotely movable aluminum support plates and positioned inside steel frames like the collimators. There are three planes of filters (A, B, C) and each plane consists of three filters. The nominal attenuation factors of the filters are 1 (A1, B1, C1), 1.5 (B2), 2.2 (C2), 4.6 (C3), 10 (A2) and 100 (A3, B3). There can be 24 nominal attenuation factors according to 27 possible combinations of filters. The ABS can be arranged to fine tune the photon flux with nominal attenuation factors between 1 and 46415. The values are nearly equidistant steps on a logarithmic scale. It is worthwhile to mention that the flux of 662 keV photons are attenuated according to the nominal attenuation factors, whereas the lower energy photons are attenuated by a larger value from the nominal one. The simulated current/flux of 662 keV photons in the yz plane is shown in Fig. 6.2 when the attenuation factor was 1.

The high energy muon beam is a secondary beam generated from the primary SPS proton beam

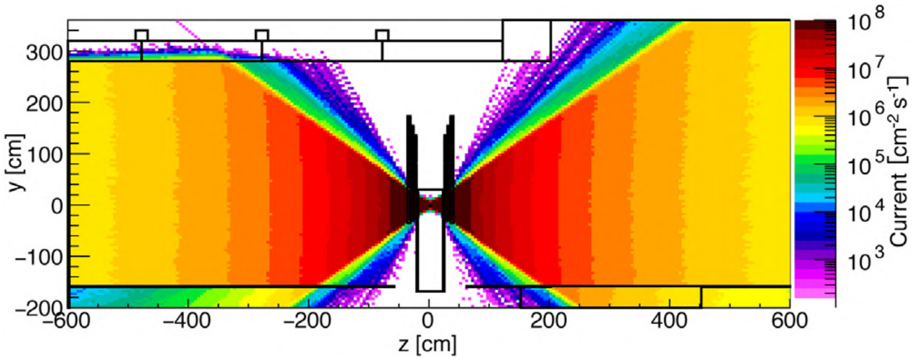


Figure 6.2: Photon current at different distances from the source; attenuation factor 1

on a production target. Muons are generated by the decay of pions and a collimator is used as dump to avoid pion contamination in the beam. The primary SPS proton beam has a spill of 4.8 s with a close to flat distribution and the secondary muon beam follows the same spill structure. One spill arrives about 30 s on average depending upon SPS. The spatial distribution of the muon beam consists of a core covering a surface of 10 cm × 10 cm, containing half of the muon beam and a beam halo spreading over a footprint of about 1 m$^2$ .

The GIF++ facility is equipped with several gas systems in order to provide the gas supply for different gas-based detectors and ensure their smooth operation. Primary supply panels consist of commonly used gases for high energy gas detectors such as R134a, $iC_4H_{10}$, $SF_6$, Ar, $CO_2$, $nC_5H_{12}$, $CF_4$. Gas racks are installed in the service area (Fig. 6.3) so that gas mixtures can be prepared for different detectors. Each gas line is connected to a Mass Flow Controller (MFC) which regulates the output flow, thereby ensuring the ratio of the created gas mixture. A PC is connected to the MFCs for controlling their remote operation via dedicated software. Oxygen level, humidity and flammability level of the gas mixtures are monitored by a gas analysis system. There are gas mixing volumes for different gases subjected to different gas detectors. A dedicated system is made to control and modify the humidity in the gas mixtures. Each gas line is split into two lines after the mixing volume. One of the line is connected to a tank where the gas mixture is forced to flow through water before it reunites with the $2^{nd}$ line containing the original gas mixture. These two gas lines are referred to as wet and dry lines respectively. Two MFCs again regulate the flow of these two lines, thereby controlling the relative amount of dry and wet gas in the final mixture. The final gas mixture lines go to the input of the detectors and there are return gas lines from the detectors which terminate into bubblers. These bubblers allow to visually check whether gas is flushing through the detector. A gas recirculation system is used with an automated gas purification module containing cartridges of larger capacity. This is necessary to keep a check on the green house gas emission. There is also provision for fresh gas mixture injection.


Figure 6.3: Gas panels installed in the gas service room

### 6.1.2 Experimental setup at GIF++

The prototype RPC-P3 (Fig. 6.4) are installed in the GIF++ area, along the beam line on October, 2018. The chamber was positioned vertically on an aluminium structure perpendicular to the muon

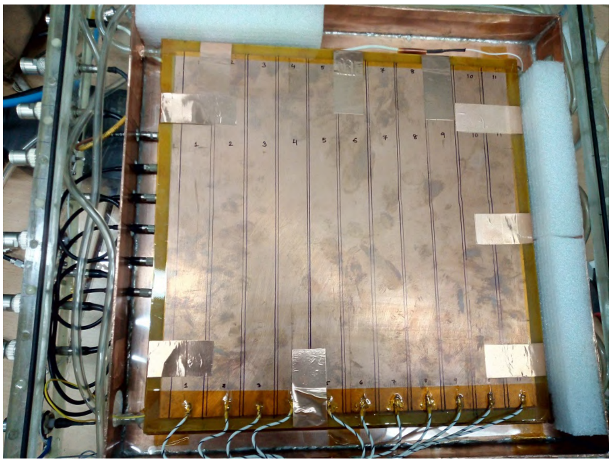

Figure 6.4: The prototype RPC-P3 kept inside the copper and perspex box.

beam line at a distance of ∼ 167 cm from the source position. The chamber was operated with a gas mixture that is constituted by $R134a$, $iC_4H_{10}$, $SF_6$ in fraction respectively of 95.2 %, 4.5 %, 0.3 %. In order to maintain the resistivity of Bakelite sheets, up to 60 % water vapours are being mixed with the gaseous mixture. The chamber was placed inside a copper box for controlling the noise due to electromagnetic interference (EMI) from the other setups in GIF++. Then again, for mechanical stability and controlling the environmental parameters, the copper box was put into a larger size perspex box. The readout FEE board was attached to the outer perspex box. The readout chain of the chamber was a self-triggered electronics setup explained later. The online trigger was composed of the coincidence signal of three plastic scintillators, two paddle scintillators placed outside the bunker and one finger scintillator placed inside the bunker, each equipped with a photo-multiplier. The front and rear plastic scintillators had an area of 40 cm × 40 cm each and the finger scintillator had an area of 11 cm × 3 cm. The width of the finger was in parallel with the width of strips of the chamber. Two prototypes of Transition Radiation Detector (TRD) were present between the chamber and the finger scintillator. The three scintillators were aligned along the beam line in the beam test. A coincidence system was made by using NIM quad scalar, dual timer and coincidence unit modules. A schematic of the experimental Setup at GIF++ with the chamber is shown in Fig. 6.5. When only the muon beam was present, a CAEN HV module

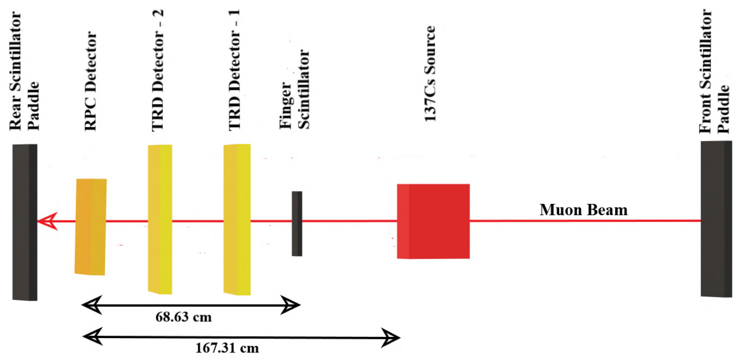


Figure 6.5: The schematic experimental Setup at GIF++ with RPC-P3, scintillators, gamma source and TRD prototypes (Not to scale).

N471A with a maximum current limit of 8 $\mu$A and a current resolution of 1 nA was used to ramp up the RPC as this particular module was suitable to handle very low chamber current in the source OFF condition. During the source ON condition, another CAEN HV module N1470A, with a current resolution of 50 nA and a maximum current limit of 3 mA was used.

### 6.1.3 Readout Chain at GIF++

A block diagram of the readout chain of the tested RPC as planned to be installed in the CBM experiment is shown in Fig. 6.6. It consists of three main blocks. These are : the Front End

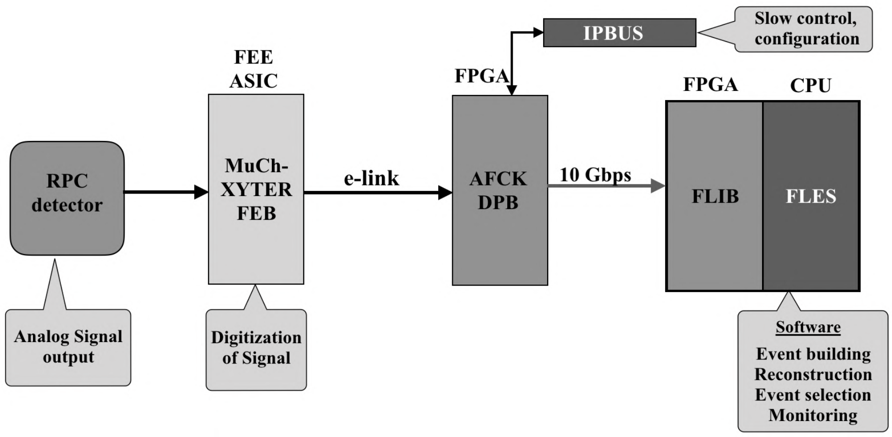


Figure 6.6: Data acquisition chain of the prototype RPC at GIF++.

Board (FEB), connected directly to the chamber and consists of a self-triggered ASIC called MuCh-XYTER v2.0 [163] for processing and digitization of the RPC signals; an FPGA-based data processing board (DPB) implemented on AMC FMC Carrier Kintex (AFCK) boards ; the First

Level Event Selector (FLES), with its interface board FLIB [164] and a workstation.

### MuCh-XYTER FEB

MuCh-XYTER (Muon Chamber – X – Y – Time – Energy Read-out) is a self-triggered ASIC containing 128 charge processing channels fabricated in UMC 180 nm CMOS technology. MuCh-XYTER digitized all detector signals above a pre-defined threshold. Some of the main features [165, 166] of the ASIC are listed below.

(i) a self-triggering feature,

(ii) two paths for time and amplitude measurement,

(iii) an average rate 250 khit/s/channel,

(iv) low-noise Charge Sensitive Amplifier (CSA),

(v) low power consumption (10 mW/ch),

(vi) dynamic range up to 100 fC in MuCh mode,

(vii) a time resolution of $3.125/\sqrt{12}$ ns and,

(viii) radiation-hardened design.

The ASIC enables time and amplitude measurement in each of the 128 channels. Each channel of the ASIC consists of a charge sensitive amplifier (CSA), a polarity selection circuit and two parallel signal processing paths defined by two pulse shaping amplifiers. A block diagram of the chip is shown in Fig. 6.7. The Charge Sensitive Amplifier (CSA) integrates the charge signal induced on

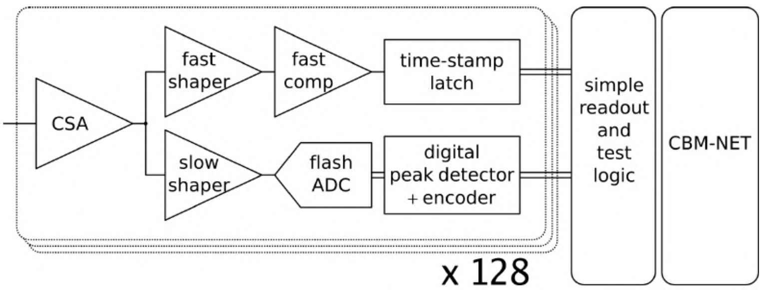


Figure 6.7: Block scheme of the MuCh-XYTER chip.

the PCB. The CSA circuit contains: feedback resistance $R_F$, feedback capacitance $C_F$ and reset circuit which is triggered by the pulse stretcher output signal for improving maximum hit rate of the circuit. The CSA simulated gain in MuCh mode is equal to 1.6 mV/fC. The output signal from CSA is fed to the next stage of the ASIC, the PSC which can process only one pulse polarity in the proceeding stages. If positive charges are integrated by the CSA, the pulse is directly fed to the shapers and if negative input charges are coming from the detector PCB, they are inverted by the differential amplifier before proceeding to the shapers. The PSC output signal is then split into two parallel signal paths. The first path is dedicated to the timing measurement of the incoming pulse. It consists of a fast shaper with high gain and smaller time constant of 30 ns and, a comparator, whose output latches the output of a 12-bit counter driven by the free running internal clock. The second path measures the amplitude of the input pulse using a slow shaper and a 5-bit flash ADC [167]. The time constant of the slow shaper is longer and it can be set in the range of 80–240 ns. Since MuCh-XYTER is a self-triggered ASIC, the trigger to readout a channel is decided by the threshold of the lowest ADC comparator. The Output of the slow shaper is propagated to the 5-bit flash ADC. Whenever any channel crosses the lowest ADC comparator threshold, then the timing output from the counter and the charge output from the ADC are stored in a buffer for further readout from the digital back-end electronics through high-speed LVDS links. It is a very crucial step to properly set the threshold of both the first comparator as well as the fast shaper of any MuCh-XYTER channel. We may acquire more noise data compared to the real signal due to the threshold being too low. On the other hand, we might cut more real signal leading us to lose the overall efficiency of the detector if we put too high threshold. Hence, in order to collect more relevant information of the real signal without losing much of the efficiency, the first threshold needs to be carefully optimized.

In the beam test, The time constant of the fast and slow shapers were set to 30 ns and 280 ns respectively. When a particle goes through the detector, the relevant channels in the MuCh-XYTER ASIC provided the timestamp value and ADC value corresponding to the deposited charge.

To use MuCh-XYTER as FEE is a challenging task for the operation of RPCs since the detectors need to be operated at low gain to match the available dynamic range of the ASIC. The ASIC was calibrated from 50-150 fC for the beam test. A threshold of 50 fC was set to prohibit the consumption of the usable bandwidth due to frequent threshold crossing. Therefore, the data rate was kept within the acceptable limit. Twelve channels of the ASIC were used for data taking in the beam test, eleven of them for negative polarity RPC signals coming from the eleven strips and one channel for the coincidence signal from the scintillators. We have processed 3-fold coincidence signal of the scintillators to use it as an input to the ASIC according to the available dynamic range. The 3-fold signal was first sent to a pulse generator and then a desired pulse shape was fed into one channel of the ASIC via a 1 pF capacitor for the necessary conversion of voltage signal to charge signal. The timestamp of the signal was used as a reference for the event, thereby it acts as an online trigger.

#### Digital Back-end Electronics

The digital interface of this ASIC consists of 3 types of differential electrical links (e-links): clock, 1 downlink and up to 5 uplinks. MUCH-XYTER e-links can work in one of the three speed modes. Accepted clock e-link frequency can be 40, 80 or 160 MHz, respectively, the downlink speed can be 40, 80, or 160 Mbit/s and uplink speed can be 80, 160, or 320 Mbit/s. Uplink e-links use double data rate (DDR) signaling. E-links are designed for synchronous communication, but clock/data phase aligner circuits are required for proper data transmission. ASIC is designed to be interfaced with radaition hard GBTx [7] chip, but interface with FPGA is also possible. In this test-bench, AMC FMC Carrier Kintex (AFCK) [8, 9] board with Kintex 7 FPGA was used. The communication between the back-end of MuCh-XYTER FEE board to the front-end of AFCK board is done by a twisted pair flat ribbon cable. The FPGA firmware of AFCK board emulates GBTx E-link (electrical links) interface and later performs initial data preprocessing. It implements single E-Link as downlink, operated at 160 Mbps to send configuration commands to the FEE, and eight E-Links as uplinks, each operated at 320 Mbps for data readout and control responses of a single FEB. The DPB was configured on AFCK boards. Even though AFCK board has been designed as an AMC board, it can be used in the standalone configuration which is an important feature of the board. For standalone operation, it needs to be connected to a 12 V power supply, JTAG programmer and other required communication links. Two AFCK boards were used in the standalone configuration, one AFCK was gDPB FMC for the data acquisition from the FEB and an additional AFCK was tDPB FMC for time synchronization. IPbus, a simple and fast communication protocol for FPGAs based on Gigabit Ethernet (GbE) was used for the communication between the DAQ PC and the AFCK board using 10 Gbps Ethernet link. The IPbus control connection is provided by the self-made SATA-SFP cable connected to the TP-Link MC220L media converter and further to the Ethernet network. An optical cable was used from the back-end of the AFCK to the FLIB board which was mounted on DAQ PC. Python scripts are used for executing the commands. The data acquisition and data analysis are done with the FLESnet and CBMROOT package.

### 6.1.4 Beam test results

In this section, the results for the detection of muons with and without the presence of a photon flux at GIF++ are presented.

#### Current

In the absence of muon beam or photon source, the current which is monitored on the HV power supply after applying the bias voltage is known as the dark current. The dark current per surface

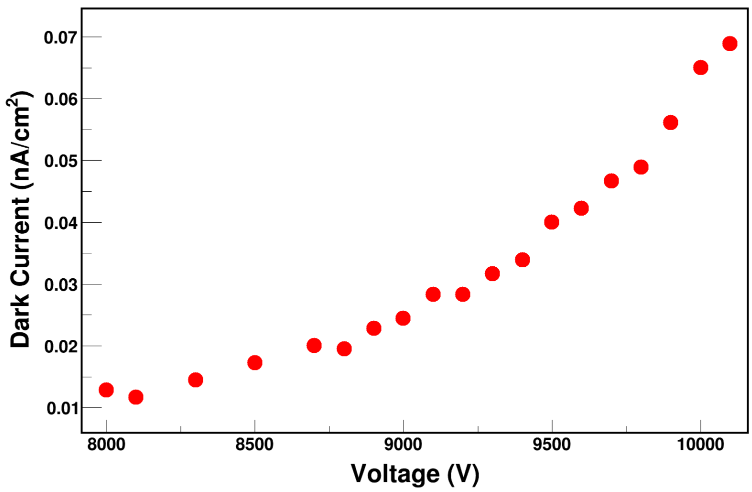


Figure 6.8: Dark Current per surface unit of the RPC, measured as a function of HV.

unit with incraesing HV is shown in Fig. 6.8. The dark current of the chamber per unit area is measured to be 0.07 nA/cm$^2$ at 10000 V. The noise rate came down to 0.5 Mbps due to the threshold setting of 50 fC which corresponds to 77 Hz/cm$^2$ at 10000 V. RPC-P3 is identical to the ALICE single-gap RPCs used for the Muon Spectrometer and a literature survey revealed an average dark current of 0.05-0.07 nA/cm$^2$ [168, 169] for a ALICE RPC prototype operated with a highly saturated avalanche mode gas mixture. The maximum chamber current was measured to be 2.2 nA/cm$^2$ at 10100 V in the presence of muon beam. The current reached 16.7 nA/cm$^2$ at 9900 V when the chamber was exposed to a photon flux of $\sim$ 403 kHz/cm$^2$.

### RPC time resolution and efficiency with muon beam

The efficiency and time resolution of the chamber tested with the muon beam ($10^5$ particles per spill) are discussed here. The spill structure detected in RPC in real time scenario is shown in Fig. 6.9. The flux of the muon beam obtained from the finger scintillator count and the beam profile

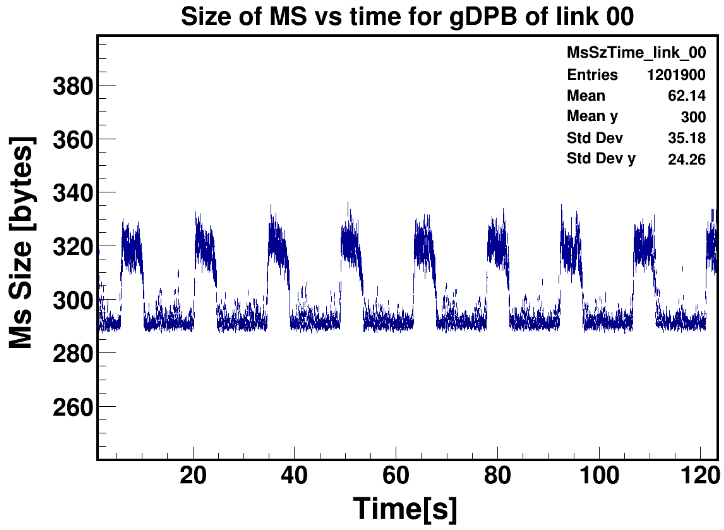


Figure 6.9: Detected beam spill structure in RPC.

is about 60 Hz/cm$^2$. The analysis was carried out in the CBMROOT environment. The time

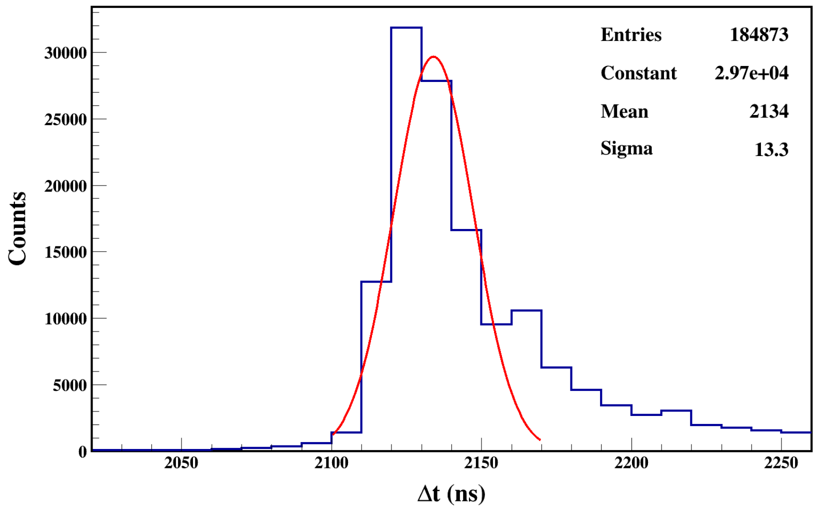


Figure 6.10: Time distribution $\Delta$t of the difference between RPC signals and trigger signal. The blue histogram is the measured data and a Gaussian fit (red curve) to the data delivers a time resolution of 13.3 ns.

difference of RPC signals with respect to a reference time measured by the 3-fold trigger yields a time distribution Δt which can be fitted by a Gaussian function (Fig. 6.10). The manual delay introduced between the RPC signal and the trigger signal is represented by the the peak position of the Gaussian fit, whereas the time resolution of the RPC folded with that of the scintillators is given by the Gaussian variance $\sigma$ obtained from the fit. The time resolution of RPC from the fit is estimated to be $\sim$ 13 ns. The time resolution appears higher than that of a standard single gap ($\sim$ 2 mm) RPC. Possible reasons for such a result are (a) operation of the chamber at relatively lower gain which results in higher time resolution. This could be corrected by walk correction, (b) use of a CSA in the MuCh-XYTER which has a large value of time constant, leading to a larger time-walk, (c) use of a high threshold value of 50 fC to keep the bandwidth under control due to the high system noise, which in turn leads to relatively large time-walk effects. Since the GEM chambers of the $1^{st}$ two MuCh stations have a similar value of time resolution ($\sim$ 13.7 ns) [170], the measured time resolution of the prototype RPC-P3 is acceptable for the CBM experiment. Late events and the streamer contamination in the signals contributed to the tail of the time distribution.

A hit in the RPC-P3 was taken into account for efficiency calculation if the measured time difference lies within ± 25 ns of the peak of the Gaussian distribution, which corresponds to fall within the $2\sigma$ range (Fig. 6.10). The efficiency ($\eta$) was calculated as

$$\eta = \frac{Trigger\ Count\ with\ associated\ to\ RPC\ hit\ within\ time\ window}{Trigger\ count} \tag{6.1}$$

Fig. 6.11 shows the muon detection efficiency of RPC-P3 with an increasing high voltage. The efficiency curve reaches a plateau at 9000 V with $\sim$ 95 %. The efficiency plateau starts at 9000 V, which is substantially lower when compared to similar RPCs with the same configuration, for instance, ATLAS RPCs operated at 9600 V with 96% efficiency using a similar avalanche mode gas mixture ratio of R134a: $iC_4H_{10}$ : $SF_6$ :: 95.0% : 4.7% : 0.3% [171]. We are successful in operating the chamber at a lower gain in comparison to other RPC setups.

#### Cluster size

The cluster size is defined as the number of RPC strips which are getting hit in a single event. The measured average value for strips of 2.3 cm is around 3.8 for 96% efficiency. In presence of

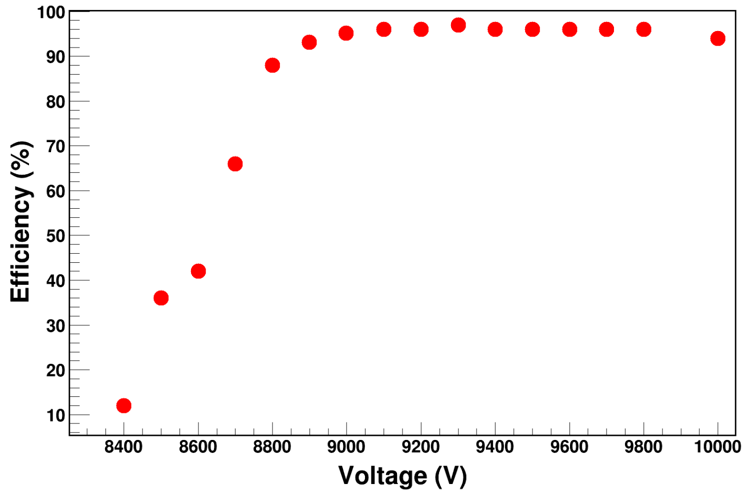


Figure 6.11: Muon detection efficiency of the RPC with respect to HV when exposed to the muon beam.

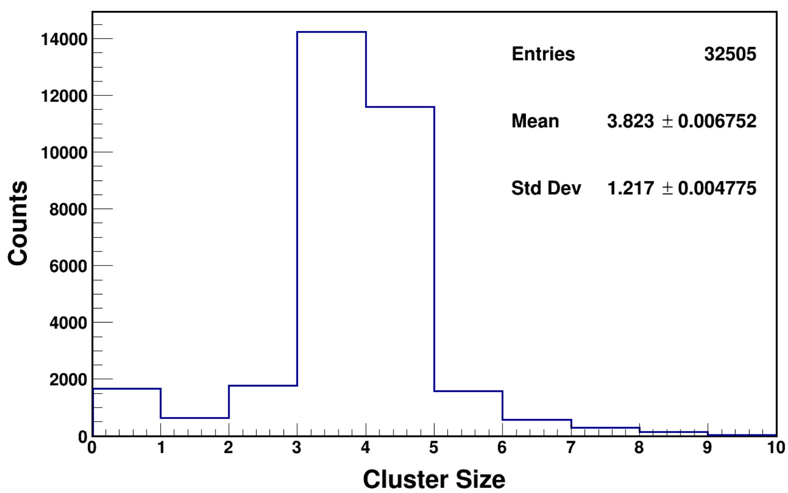


Figure 6.12: Cluster size of muons for RPC at 9200 V

the muon beam, the cluster size distribution for the signals correlated to the trigger signal at 9200 V is shown in Fig. 6.12.

### Rate capability

The Rate capability study was carried out by measuring the detection efficiency of the chamber for muons when the chamber was irradiated with an increasing photon flux. The calculated photon flux impinging on the chamber was $\sim 40$ MHz/cm$^2$ when the ABS = 1. The detection efficiency for

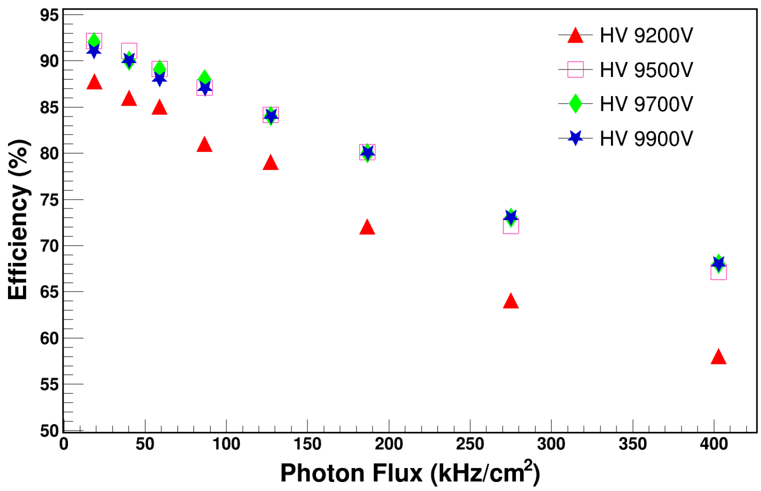


Figure 6.13: Muon detection efficiency as a function of the photon flux for a range of high voltages.

muons of the chamber as a function of the photon fluxes is shown in Fig. 6.13 at various HVs. The efficiency decreases from 92% to 67% at 9500 V when the photon flux increases from 18 kHz/cm$^2$ to 403 kHz/cm$^2$. A detailed knowledge about the interactions of photons with the materials present between the photon source and the chamber is necessary for the conversion from the incident photon flux to the charged particle rate inside the RPC gas-gap. Therefore, an approach based on the strip hit rate was adopted, which may work as a proxy for the actual charged particle rate to compare with the expected rates in CBM. The average number of hits per second per unit surface area of the chamber is termed as the strip hit rate. Fig. 6.14 shows a decrease of the muon detection efficiency with an increase in the strip hit rate at 9500 V. At photon-induced strip hit rates of $\sim 6$ kHz/cm$^2$ and $\sim 10$ kHz/cm$^2$, the achieved muon detection efficiencies reached $\sim 92\%$ and $\sim 83\%$ respectively.

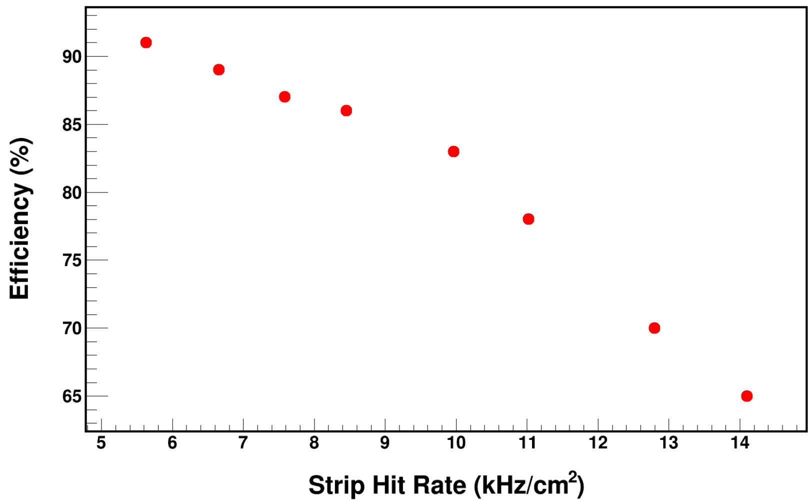


Figure 6.14: Muon detection efficiency as a function of the strip hit rate at 9500 V.

## 6.2 Cosmic Ray testing of a real size RPC module for the $3^{rd}$ station of the CBM muon chamber with MuCh-XYTER electronics

A real size trapezoidal shaped RPC module for the $3^{rd}$ station of CBM-MuCh was procured from the Italian company General Technica. The core of the module is a $\sim$ 2 mm gas-gap between two high-pressure phenolic laminate (bakelite) plates. The bakelite electrodes dimensions of the module are 100.26 $\times$ 509.8 $\times$ 1179.21 mm (height $\times$ short-base $\times$ long-base). Modifications were done on the thickness of the electrode plates, which are $\sim$ 1.2 mm, while the electrode-thickness of RPC-P3 was $\sim$ 2 mm. The bulk resistivity of the bakelite is $\sim 3 \times 10^9$ - $1 \times 10^{10}$ $\Omega$-cm, which is lower by at least a factor of 3.8 from that of the prototype RPC-P3. The inner surfaces of the bakelite plates are double-layer linseed oil coated for surface smoothness. There were four gas nozzles glued near the edges of the two bases of the trapezoid. As we have already discussed in the $4^{th}$ chapter, the rate capability of RPC increases if we reduce the electrode-resistivity and plate thickness. The characteristics of the real size module fulfills both this criteria compared to the prototype RPC-P3. An image of the module is shown in Fig. 6.15, the white circles denoted the positions of the button spacers of $\sim$ 2 mm thickness. The module was tested with different gas mixture components and ratios with an aim of testing this module in the GIF++ and mCBM

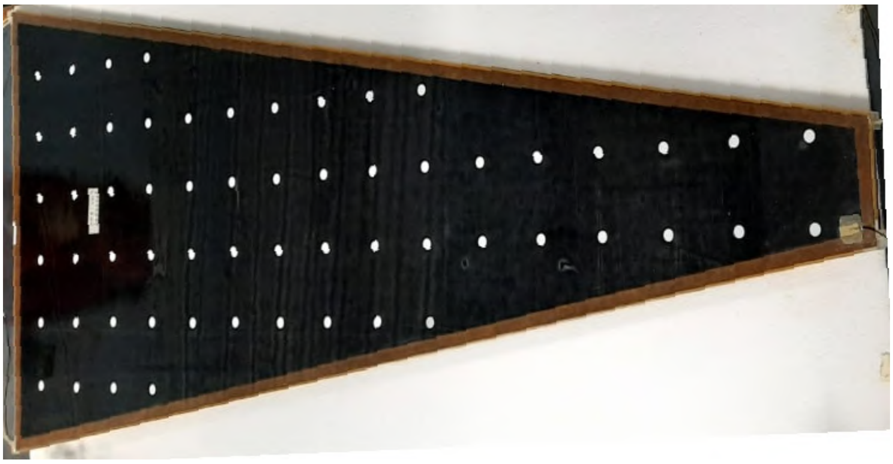

Figure 6.15: The picture of the Real Size Trapezoidal shaped RPC Module for the $3^{rd}$ station of CBM-MuCh.

test beams.

### 6.2.1 Experimental setup with cosmic muons

The reference system consists of two plastic scintillators with the dimensions 4.6 cm $\times$ 4.6 cm and 20 cm $\times$ 8.5 cm placed above and below of the RPC chamber. Each scintillator was read out by a PMT. The coincidence of the PMT signals used as the online trigger signal. A PCB of dimension 30 cm $\times$ 30 cm containing 100 pads of 2.8 cm $\times$ 2.8 cm was used as the readout electrode. The assembled chamber along with the PCB was kept inside a trapezoidal shaped copper box which acted as a Faraday cage. The copper box also served the purpose of the ground plane for the PCB. There were several cut-outs which were custom made for the HV connections, gas pipe lines and FEE. Two MuCh-XYTER v2.1 boards were used in the setup. An image of the experimental setup is shown in the Fig. 6.16. The connection between the connector of PCB and the front-end board (FEB) was done by flexible kapton cables. One single channel in one of the MuCh-XYTER boards was used for the processing of the coincident scintillator signal, the coincidence was done using normal NIM based electronics and then the NIM logic pulse was converted to a Transistor-Transtor Logic (TTL) pulse by a NIM to TTL converter. The 2nd MuCh-XYTER board was used for processing the RPC signals as well as the coincident scintillator signal. A waveform generator was operated in external triggered mode, which was triggered by TTL pulse. Then, a voltage pulse was generated which resembles a RPC pulse. We have tuned the width of the pulse in the waveform

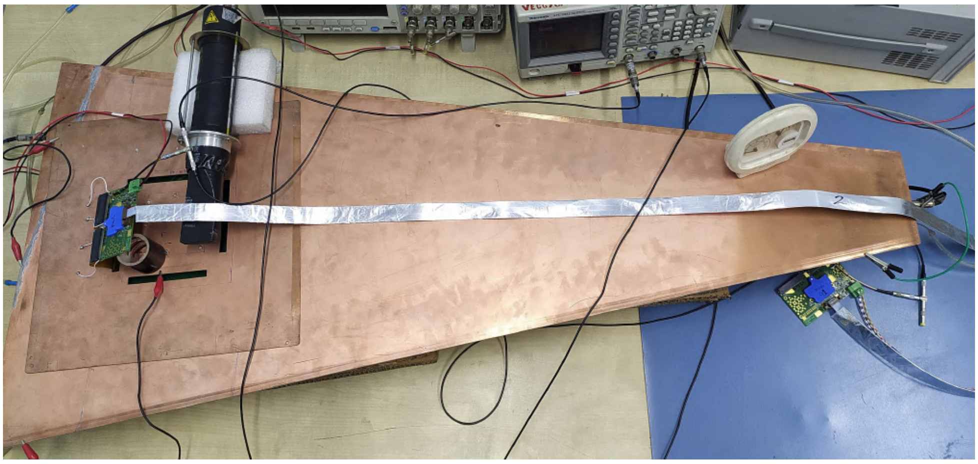

Figure 6.16: The cosmic ray test setup of the real size RPC module for the $3^{rd}$ MuCh station enclosed in the copper box.

generator. The amplitude of the output pulse after the waveform generator is further reduced by a 1:10 attenuator to match the dynamic range of MuCh-XYTER and then sent the pulse to the FEBs after bifurcating the pulse by a T connector and 50 Ω termination resistances. The voltage pulse was converted to charge pulse via 1 pF capacitor before injecting the charge to MuCh-XYTER. While analysing the data, the trigger was counted if there is a coincidence of the same trigger signal on the two FEBs to avoid the time-shift of the different FEE boards. Several ground connections were introduced to minimize the data rate. Four ground pins of the FEB connected to the RPC were soldered with the copper box via short cables. The connections between the HV connectors of RPC and the copper box were done by short length two-way crocodile clips. The back-end digital electronics was the same as the GIF++ setup.

### 6.2.2 Results

#### Gas Mixture I

First results with the real size module were obtained with a gas mixture of $R134a : iC_4H_{10} : SF_6$ :: $90 : 5 : 5$. The choice of this mixture was based upon the fact that the gas system in the mCBM beam test for RPC will be the same as the TOF-MRPC gas mixture. Therefore, we wanted to test our detector in this gas mixture before taking data at mCBM best test. The I-V characteristics was obtained for the real size module using the DC power supply CAEN 1N471H as shown in the Fig. 6.17. As per the plot, the working voltage of this module is beyond 10000 V with this gas

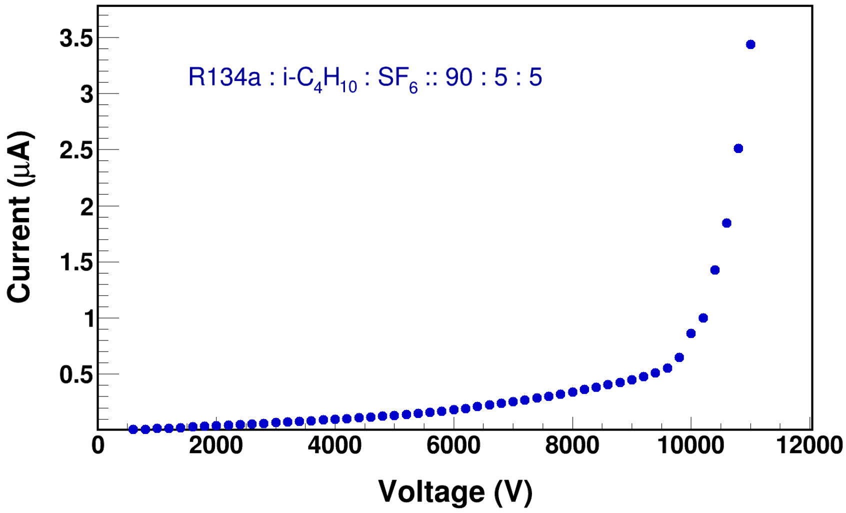


Figure 6.17: Currents drawn by the real size RPC module as a function of high voltage.

mixture.

The data was taken in self-triggered mode, thus all hits are stored along with their timestamps.

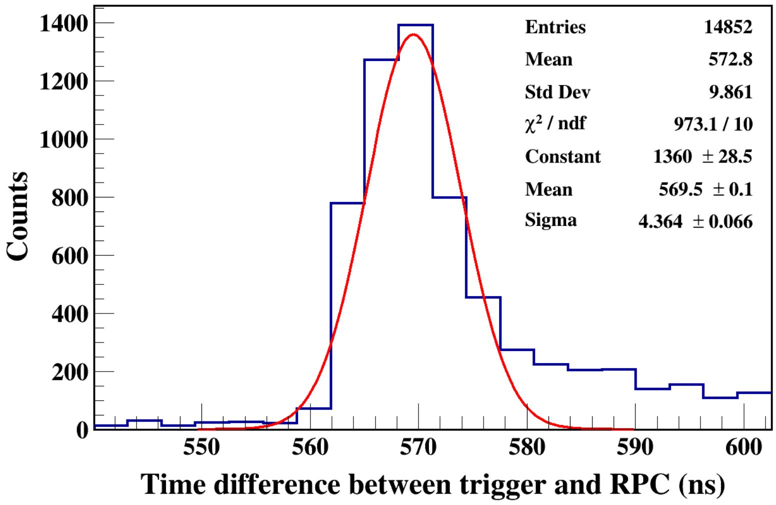


Figure 6.18: Time correlation spectrum between the trigger hits and the RPC hits at 11200 V at 17 fC threshold. The blue histogram is the measured data and a Gaussian fit (red curve) to the data delivers a time resolution of 4.4 ns.

As a first step of analysis, we have identified the hits in RPC which are correlated in time with the scintillator trigger timestamp. The distribution of the time difference between the coincidence trigger signal from the scintillators and those of the RPC hits is shown in Fig. 6.18 at 11200 V. The spectrum was fitted with a Gaussian function and the variance gives the measure of time resolution of the module coupled with that of the scintillators. The time resolution of the module is $\sigma_{uncorrected}$ $\sim$ 4.36 ns. Note that this time resolution value contains the jitter of the whole electronics chain. The dark current of the module at 11200 V was $\sim$ 3 $\mu$A and the data rate was 4.8 - 5 Mbps. The humidity and temperature of the lab was kept at 45 % - 49 % and 20° respectively. The efficiency of the chamber was calculated using the two-fold and three-fold coincidence method as described in the beam test section. The efficiency of the chamber as a function of the HV for three different

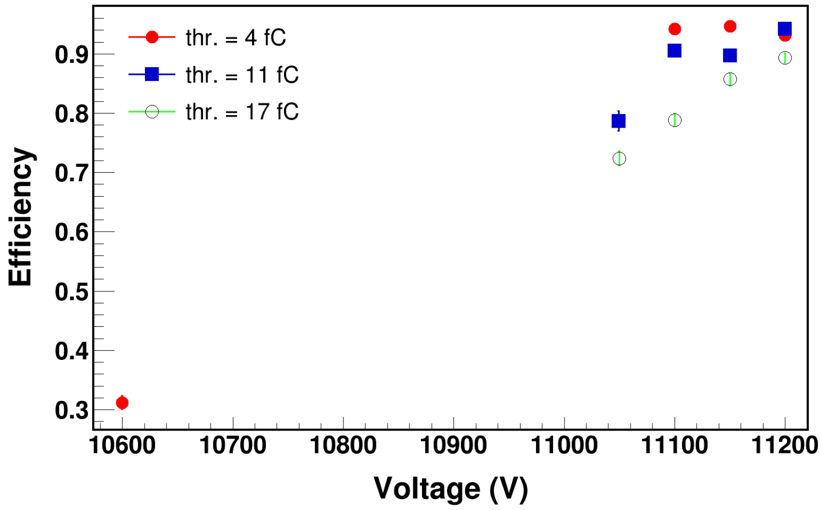


Figure 6.19: Efficiency as a function of HV for three different threshold values.

threshold settings of the FEB is shown in Fig. 6.19. The efficiency reaches $\geq$ 90 % at 11100 V for 4 fC and 11 fC thresholds and at 11200 V for 17 fC threshold. The error is calculated according to Eq 5.7 and represents the statistical error. The distribution of the hits of the detected clusters on the PCB is shown in Fig. 6.20. These measurements were performed at an applied high voltage of 11200 V. The threshold at the MuCh-XYTER was 17 fC. The yellow region corresponds to the triggered area covered by the plastic scintillators. The cluster size distribution was calculated along row-wise and column-wise of the PCB as shown in Fig. 6.21. A distribution was made with the number of pads which are getting hit along row-wise for cosmic ray events. Similarly, the same thing was done for column-wise cluster size distribution.

### Gas Mixture II

The real size module was tested with another TOF-MRPC gas mixture consisting of $R134a : SF_6$ :: 97.5 : 2.5. Few changes was also done in the experimental setup. The waveform generator

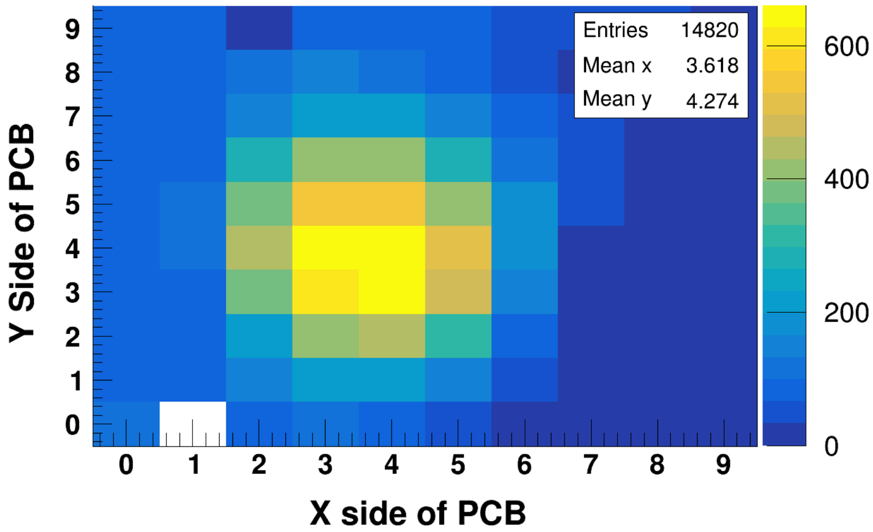


Figure 6.20: Spatial cluster distribution on the RPC surface. The binnings of the x-axis and y-axis are given in units of the Pad Number. The PCB has a configuration of 10 × 10 matrix (row × column).

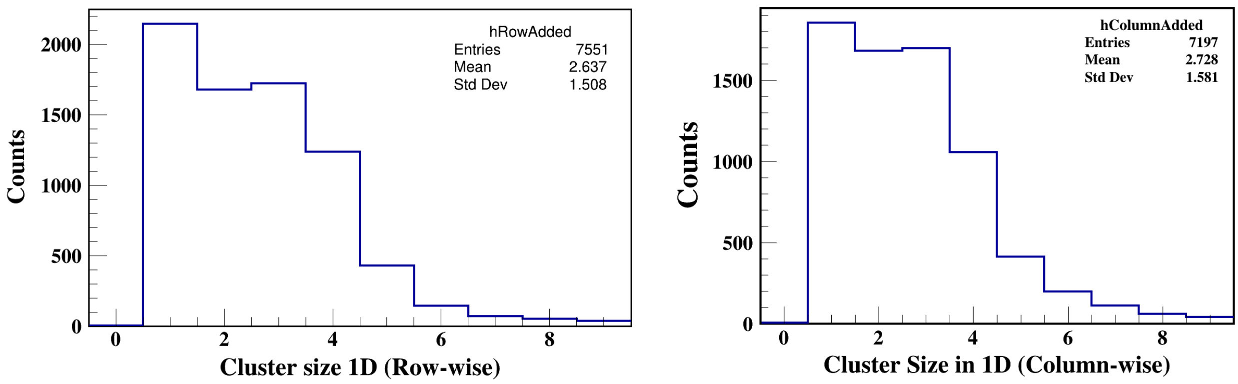


Figure 6.21: Cluster size distribution of the real size RPC module. The applied high voltage is 11200 V. The threshold at MuCh-XYTER is 17 fC.

was removed from the electronics chain. The NIM logic pulse of the coincidence of the two scintillators was directly fed to the FEBs via 1 pF capacitors. The FEBs were calibrated from 5 fC to 144.5 fC with a bin size of 4.5 fC. During the integration of RPC detector with the MuCh-XYTER electronics, we have faced the issue of dead electronics channels with time due to the micro discharges or sparks created in the detector. The communication between the electronics channels and DAQ were destroyed. Several iterations were done to tackle the issue. Initially a series protection resistance (510 k$\Omega$) was introduced on the PCB before the MuCh-XYTER FEE. The data rate became 14-16 Mbps. Although, these series resistances stabilized the electronics channels to some extent, the time resolution of the chamber degraded and the signal to noise (SNR) was still poor. The bandwidth of the ASIC was getting occupied with the noise. Instead of a series resistance, a series capacitor (10 nF) was chosen to overcome the issue. The data rate came down to $\sim$ 5 Mbps. Although the series capacitor deteriorated both the signal as well as the noise, the detector SNR got drastically improved due to an increased gain. Basic studies on the characteristics of the chamber were done using cosmic rays. The I-V characteristics of the module

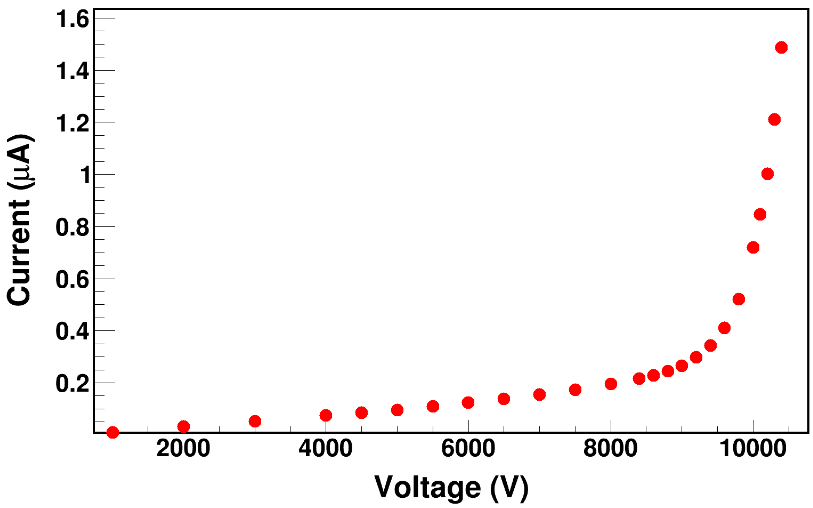


Figure 6.22: Currents drawn by the real size RPC module as a function of high voltage.

with the new gas mixture is shown in Fig. 6.22. The knee region of the plot lies between 9000 V to 9500 V. The working voltage of the chamber is beyond 9500 V. Due to lower percentage of $SF_6$, the breakdown voltage was reduced.

The time correlation spectra is shown is Fig. 6.23. The Gaussian fit delivers a $\sigma_{uncorrected} \sim 5$ ns. The distribution of hits on PCB at 10400 V is shown in Fig. 6.24. The efficiency of the chamber

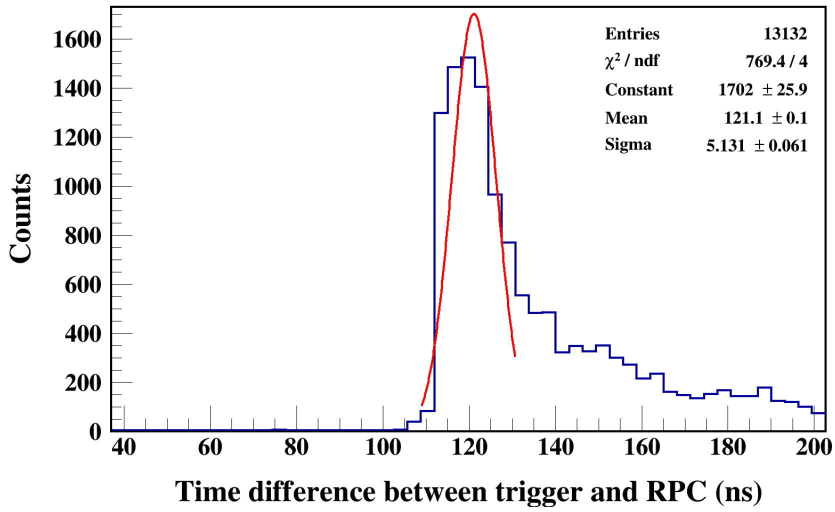


Figure 6.23: [Colour online] Time correlation spectrum between the trigger hits and the RPC hits at 10400 V at 5 fC threshold. The blue histogram is the measured data and a Gaussian fit (red curve) to the data delivers a time resolution of $\sim$ 5 ns.

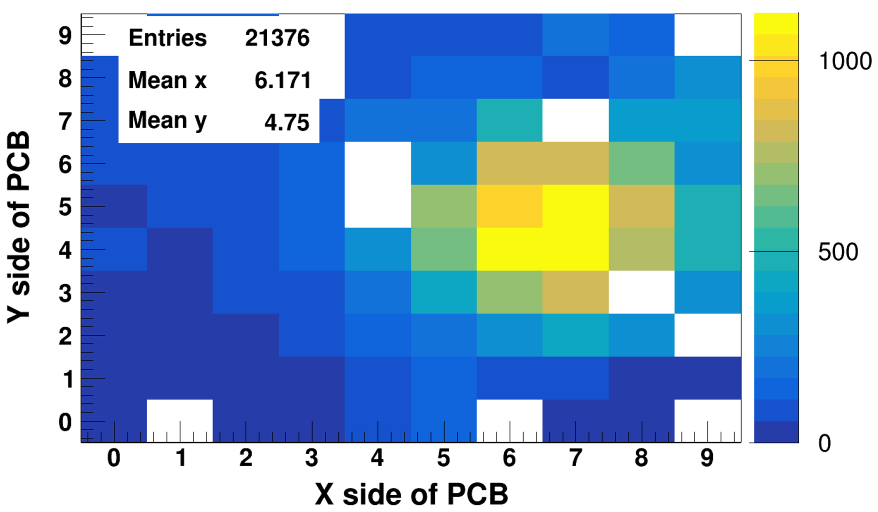


Figure 6.24: Hit distributions of the detected clusters on the RPC surface at 11200 V for 17 fC threshold at MuCh-XYTER. The binnings of the x-axis and y-axis are given in units of the Pad Number. The PCB has a configuration of 10 $\times$ 10 matrix (row $\times$ column). White regions correspond to dead MuCh-XYTER channels connected to that pad.

was measured with increasing high voltage as shown in Fig. 6.25. The efficiency of the chamber reaches a plateau with $\sim$ 91 % at 10300 V.

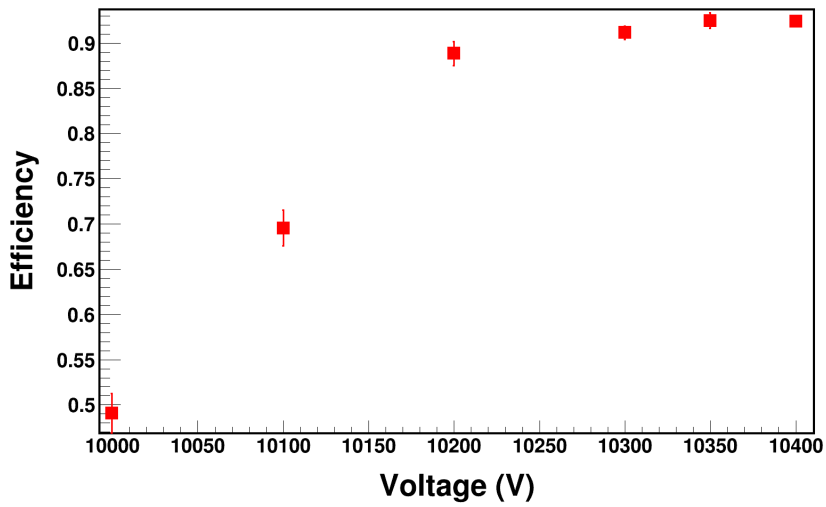


Figure 6.25: Efficiency of the real size RPC module as a function of high voltage.

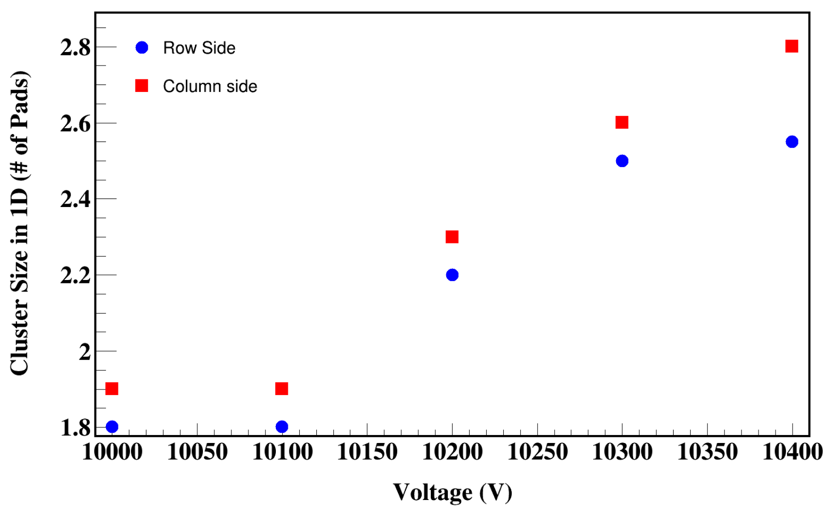


Figure 6.26: Cluster size of the real size RPC module as a function of HV.

The cluster size (# of pads) was also measured as a function of voltage as shown in Fig. 6.26. Spatially, on an average, a single cluster is distributed in a region of $\sim$ 7 cm $\times$ 7 cm.

### Gas Mixture III

The last gas mixture ratio at which the real size module was operated is $R134a : iC_4H_{10} : SF_6$ :: 95.2 : 4.5 : 0.3. The ratio is identical to the gas mixture used in GIF++ beam test. The

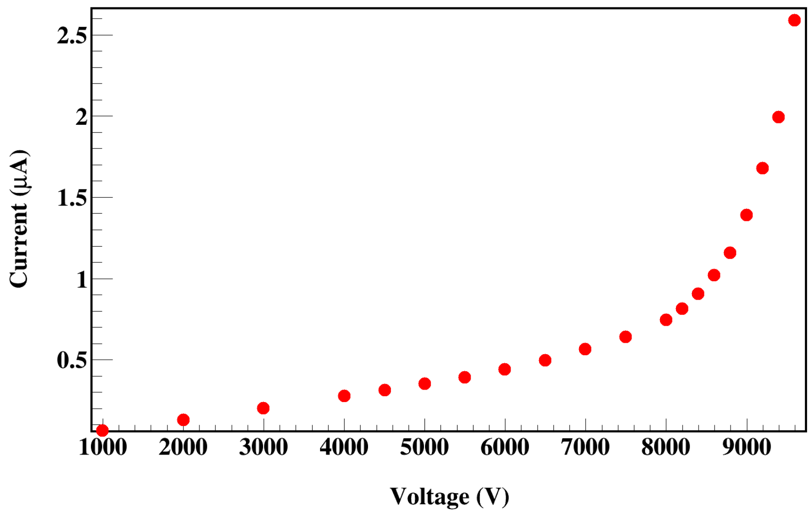


Figure 6.27: Currents drawn by the real size RPC module as a function of high voltage.

performance of the real size module is planned to get tested at GIF++ before installing it in the mCBM setup. So the module was tested with the same gas mixture in the cosmic ray setup with 5 fC threshold in FEB. The results are given below. The leakage current of the module was measured with high voltage as shown in Fig. 6.27. The breakdown voltage is around $\sim$ 8000 V.

Fig. 6.28 shows the distribution of time difference between the coincidence scintillator hits and RPC hits. The spectrum was fitted with a Gaussian function which delivers a uncorrected time resolution of $\sigma_{uncorrected} \sim$ 6.4 ns. The cluster size (# of pads) distributions at 9000 V in 1D along row-wise and column-wise are shown in Fig. 6.29. Spatially, a single cluster is distributed in a region of $\sim$ 7 cm $\times$ 7 cm. The distribution of hits on the PCB at 9000 V is shown in Fig. 6.30.

## 6.3 Discussions

The prototype RPC-P3 was operated in an avalanche mode gas mixture using self-triggered MuCh-XYTER electronics in the GIF++ beam test in the presence of a high-intensity muon beam and photon source. The efficiency of the chamber reached $\sim$ 95 % at 9 kV with a threshold of 50 fC

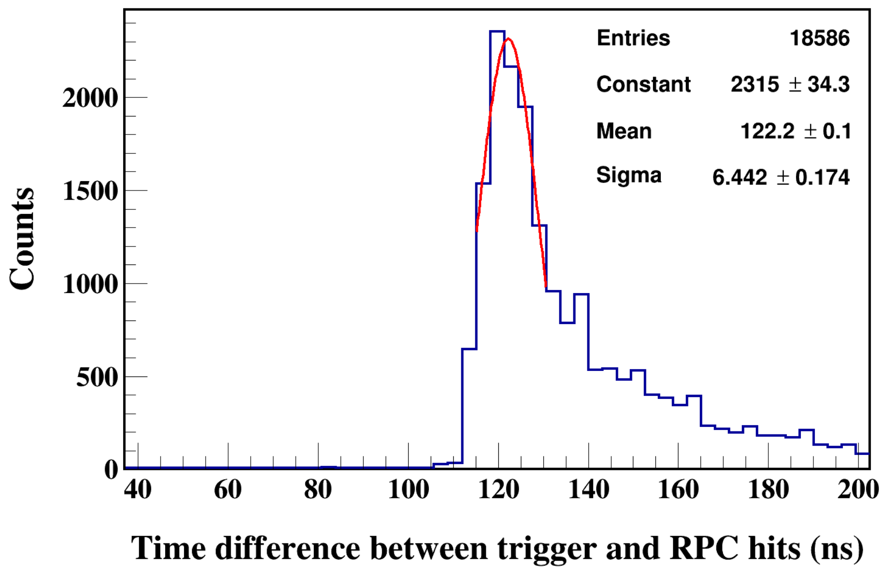


Figure 6.28: Time correlation spectrum between the trigger hits and the RPC hits at 9000 V at 5 fC threshold. The blue histogram is the measured data and a Gaussian fit (red curve) to the data delivers a time resolution of $\sim$ 6.4 ns.

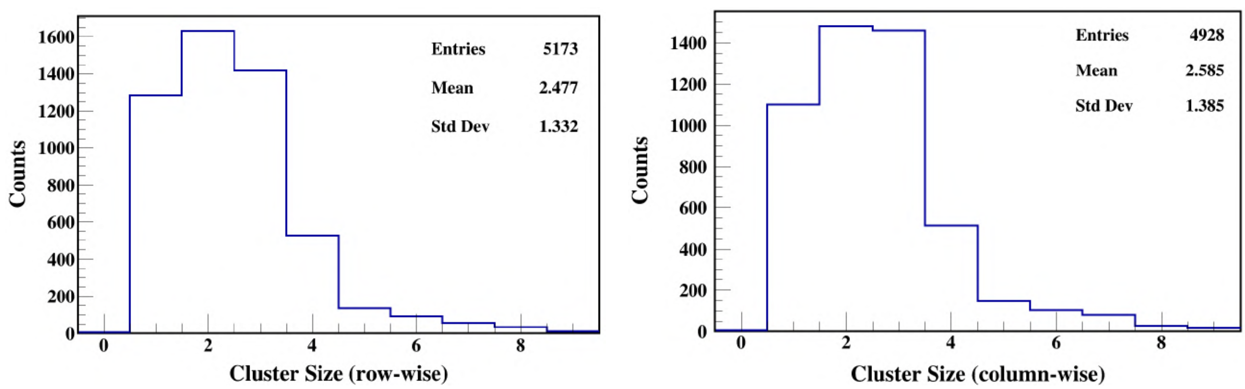


Figure 6.29: Cluster size distributions of the real size RPC module. The applied high voltage is 9000 V.

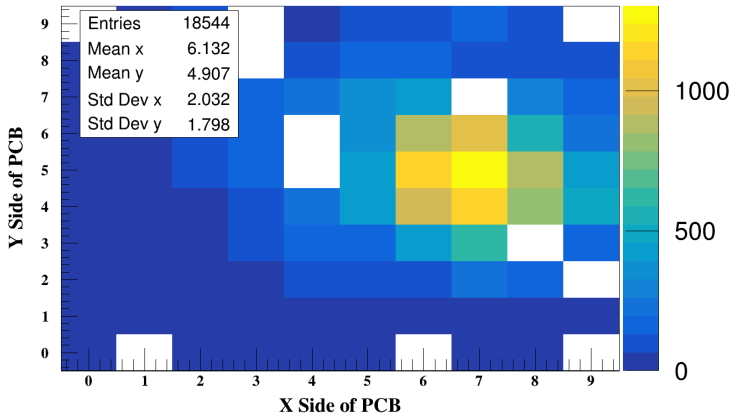


Figure 6.30: Hit distributions of the detected clusters on the RPC surface at 9000 V. The binnings of the x-axis and y-axis are given in units of the Pad Number. The PCB has a configuration of 10 $\times$ 10 matrix (row $\times$ column).

and a time resolution of $\sim$ 13 ns in the detection of the muon beam. While the chamber was exposed to the photon source also, the muon detection efficiency of the chamber was $\sim$ 90 % at a hit rate of $\sim$ 6 kHz/cm$^2$ at 9.5 kV. The efficiency at 9.5 kV dropped down to $\sim$ 83 % at a hit rate of $\sim$ 10 kHz/cm$^2$. To make use of the full bandwidth of the MuCh-XYTER ASIC, the system noise and thereby the threshold of the ASIC can be reduced to operate the chamber with high efficiency at a lower gain. A real size RPC module for the $3^{rd}$ CBM-MuCh station equipped with the self-triggered MuCh-XYTER FEE was tested at VECC in a cosmic ray test setup. The chamber was operated with different ratios of avalanche mode gas mixtures. Reduction of the electrode thickness may further increase the rate capability of the chamber. Applying a proper grounding scheme, we were able to reduce the system noise and operated the real size chamber with a threshold value as low as 5 fC. The chamber has shown muon detection efficiency of $>$ 90 %, time resolution of 4 - 6 ns, cluster size (1D) of $\sim$ 2.5 at different HV points according to the concerned gas mixtures.

# Chapter 7

# Summary & Conclusions

The Compressed Baryonic Matter (CBM) experiment will be one of the major experiments at the future Facility for Antiproton and Ion Research (FAIR) center investigating heavy-ion collisions and reactions at an interaction rate of up to 10 MHz with a fixed target setup and with beam energies ranging from 2 AGeV to 11 AGeV. The experimental setup will consist of a superconducting magnet, multiple detectors, and high-performance computing for online event reconstruction and selection. Muon Chamber (MuCh) is an important part of the CBM detector system for tracking and identifying muon pairs formed via the decay of produced particles like charmonium ($J/\psi$) and low mass vector mesons (LMVM) [172]. The rate of incident particles per unit area on the detector surface decreases radially and as we go away from the target in the Z direction. The CBM MuCh system comprises two subsystems of detectors: one of them is based on Gas Electron Multiplier (GEM) detectors for the $1^{st}$ and $2^{nd}$ stations [173], the other on fast planar detectors, the Resistive Plate Chambers (RPCs) for the $3^{rd}$ and $4^{th}$ stations. Simulation results indicate the hit rates on the $3^{rd}$ and $4^{th}$ stations of MuCh reach a maximum of 36 kHz/cm$^2$ and 18 kHz/cm$^2$ respectively for minimum-bias Au-Au collisions at a beam energy of 10 AGeV. The RPCs in CBM, therefore, should be capable of handling these high rates for muon detection with high efficiency ($\sim$ 90 %). RPCs are classified into two groups, (i) trigger RPCs, and (ii) timing RPCs depending upon their application in an experiment. The application of trigger RPCs in an experiment is mainly for tracking and triggering purposes. The timing RPCs are required to provide a better time resolution in an experiment than that of the trigger RPCs due to their usage as a Time-of-Flight (TOF) detector. Cosmic ray experiments like Cover Plastex [174] in UK, Pierre Auger Cosmic Ray Observatory [175] in Argentina, neutrino physics experiments like Daya Bay Reactor in China [176] and INO-ICAL in India [177], high energy physics experiments like CMS, ALICE [178], ATLAS at LHC [179], STAR at BNL [180], BaBar at PEPII [181] and BELLE at KEKB [182] are using or planning to use RPCs and MRPCs for muon detection and as TOF detectors at various particle rates. These detectors are preferred for muon detection due to several reasons,

(a) good time resolution,

(b) fast response time,

(c) high detection efficiency,

(d) simple and less expensive construction compared to other gaseous detectors like GEM or Micromegas, and

(e) the possibility to build them in large areas and different shapes [122].

The main goal of this thesis was the design and development of an RPC prototype for the muon detector system of the CBM experiment and the evaluation of its detector characteristics such as leakage current, efficiency, noise rate, time resolution, charge spectra, and mean cluster size at different working conditions. We have taken the approach towards the reduction of average charge $\langle$ Q $\rangle$ and the reduction in the bulk resistivity of electrodes to achieve the required rate capability. Several detector prototypes have been built and tested.

Our R&D started with the development of a single gap ($\sim$ 0.2 cm) RPC with Indian OLTC grade bakelite sheets of bulk resistivity ($\sim 9 \times 10^{11}$ $\Omega$cm). The performance of the fabricated RPC-P0 was evaluated in a cosmic ray test set up at VECC with plastic scintillators while operating it in avalanche mode first equipped with NIM-based electronics and then with a current-sensitive FEB NINO. The prototype RPC-P0 showed promising results in detecting cosmic muons with efficiency $\sim$ 90 %, noise rate $<$ 1 Hz/cm$^2$, and time resolution $\sim$ 2 ns at an operating voltage of 11kV.

After that, we fabricated two 6-gap bakelite MRPC prototypes with the same OLTC grade bakelite sheets. The prototype MRPCs have shown muon detection efficiency of $>$ 85 %, noise rate of $\sim$ 2 Hz/cm$^2$, time resolution of $\sim$ 154 ps, an average charge of $\sim$ 7.2 pC at 16 kV operating voltage in the avalanche mode.

Next, we started our quest for a low resistivity bakelite material and fabricated some prototypes, and tested them in a cosmic ray setup. Although, the prototype RPC-P1 fabricated with an Italian bakelite sample of bulk resistivity $\sim 4 \times 10^{10}$ $\Omega$-cm showed a detection efficiency of $\sim$ 90 % at

10 kV operating voltage, the leakage current ($\sim \mu$A) and noise rate ($\sim$ 12 Hz/cm$^2$ of RPC-P1 at the operating region was quite high. The lack of surface smoothness of the bakelite electrodes may be one of the reasons for such a behavior of the prototype. Therefore, a single-gap ($\sim$ 0.2 cm) prototype RPC-P2 was fabricated with the same Italian bakelite sheets. The inner surfaces of the electrodes were coated with a thin layer of commercially available linseed oil to fill all the micro-crevices on the surface. But, the leakage current of RPC-P2 after the application of HV on the bakelite electrode surfaces couldn't reach a stable value, the current kept increasing due to the formation of stalagmites because of non-polymerized linseed oil.

Then, a prototype single-gap bakelite RPC (bulk resistivity $\sim \sim 3 \times 10^{10}$ $\Omega$cm) fabricated at the professional Italian company General Technica was tested for efficiency, noise rate, time resolution, charge spectra with conventional NIM-based electronics as well as current-sensitive electronics like NINO and PADI using an avalanche mode gas mixture ratio of $R134a/iC_4H_{10}/SF_6$, 94.2%/4.7%/1.1%. At the working point of 10.6 kV (lab temperature $\sim 20^{circ}$ and relative humidity $\sim$ 40 %) and at the FE electronics threshold (NINO) of 500 mV, the performance of RPC-P3 can be described by the following average values: detection efficiency $\sim$ 93 %, noise rate $\sim$ 0.52 Hz/cm$^2$, time resolution $\sim$ 1.05 ns and gap current 50 nA. The results were consistent for the tests with PADI electronics. Then the performance of the chamber was evaluated using a charge-sensitive electronics, commercially available CSA, ORTEC 142IH along with standard NIM-based electronics. We could bring down the operating voltage to 9.7 kV which is beneficial for increasing the rate capability of the chamber. The charge spectrum of RPC-P3 was measured using MANAS ASIC, and an average charge of $\sim$ 77 fC was determined for the detection of cosmic muons.

An exhaustive test of RPC-P3 was performed at CERN, utilizing the Gamma Irradiation Facility (GIF++), a very intense photon source along with a high-intensity muon beam replicating the high rate environment foreseen at CBM. The chamber was operated with an avalanche mode gas mixture of $R134a/iC_4H_{10}/SF_6$, 95.2%/4.5%/0.3% containing 60% humidity. A PCB with 2.3 cm strip-width and 2.5 cm strip-pitch was used for signal readout. The chamber was integrated with the real electronics chain for CBM-MuCh, consisting of MuCh-XYTER v2.0 ASIC, AFCK boards, FLES, and FLIB. A high voltage scan showed an efficiency plateau (at 95% efficiency) beyond 9 kV. The time resolution of the chamber with MuCh-XYTER, a self-triggered charge-sensitive electronics, was measured to be 13 ns or less at 9.2 kV, which is in good agreement with the requirements of CBM-MuCh. At a hit rate of $\sim$ 6 kHz/cm$^2$ and $\sim$ 10 kHz/cm$^2$, the efficiencies of the chamber were measured to be 90% and 83% at 9.5 kV. More studies on beam tests are required to have a fully efficient RPC at rates such as those foreseen for the CBM stations.

A real size, trapezoidal-shaped, single-gap bakelite RPC module for the $3^{rd}$ station of CBM-MuCh was tested at the cosmic ray set up with pad readout ($\sim$ 2.8 cm $\times$ 2.8 cm) and the same electronics chain used in GIF++. The bulk resistivity of the bakelite plates of thickness 1.2 mm was $\sim$ 3 $\times$ $10^9$ - 1 $\times$ $10^{10}$ $\Omega$-cm. The rate capability of RPC may be increased if we take into account these two factors of the real size chamber compared to the prototype RPC-P3. The chamber is planned to be tested for rate capability in GIF++ and mCBM beam tests. The performance of the chamber was evaluated using three different gas mixture ratios of avalanche mode as per the requirements of the test beams. Few modifications to the grounding scheme helped in bringing down the noise, thus we could bring down the threshold of MuCh-XYTER from 50 fC (GIF++ beam test) to 4 fC. The chamber has shown muon detection efficiency of $\sim$ 90 %, time resolution of 4.4 - 6.5 ns, single cluster distributed in a region of $\sim$ 7 cm $\times$ 7 cm.

The rate capability of the real size module for the $3^{rd}$ station of CBM-MuCh is planned to be get tested at GIF++ and mCBM beam tests. The data for the test beams are getting analyzed. Another real size module for the $3^{rd}$ station with a smaller gas gap ($\sim$ 1 mm) is planned to be characterized at first in cosmic rays and then in the test beams to determine the basic characteristics and the rate capability of the detector. We will be able to conclude experimentally the effect of reducing the gas gap size or the bulk resistivity of electrodes or the electrode thickness on the rate capability of the detector.

# Bibliography


[1] D. J. Griffiths. *Introduction to Elementary Particles.* WILEY-VCH Verlag GmbH & Co. KGaA, Weinheim, 2 edition, 1995.

[2] F. Halzen and A. D. Martin. *Quarks and Leptons: An Introductory Course in Modern Particle Physics.* Wiley, Newyork, 1984.

[3] M. Tanabashi and et al. *Phys. Rev. D*, 98,(030001), 2018.

[4] L. S. Glashow. *Nuclear Physics*, 22:579–588, 1961.

[5] Peter W. Higgs. *Phys. Rev. Lett.*, 13:508–509, 1964.

[6] S. Chatrchyan and et al (CMS Collaboration). *Phys. Lett. B*, 716(1):30–61, 2012.

[7] G. Aad and et al. *Phys. Lett. B*, 716(1):1–29, 2012.

[8] G. Aad and et al. *Phys. Rev. Lett.*, 114(191803), 2015.

[9] B Friman and et al. *The CBM Physics Book*, volume 814. Springer-Verlag, 2011.

[10] F. Jegerlehner. Quantum chromodynamics and strong interaction physics.

[11] Yoshihito Iwasaki. *A Measurement of Quark and Gluon Jet Differences at the $Z^0$ Resonance.* PhD dissertation, Department of Physics, Tohoku University, Japan, 1994.

[12] M. E. Peskin and D. V. Schroeder. *An Introduction to Quantum Field Theory, Advanced book classics.* Addison-Wesley, 1995.

[13] D. H. Perkins. *Introduction to High Energy Physics*, volume 814. 4 edition, 2000.

[14] Kenji Fukushima and Tetsuo Hatsuda. *Rep. Prog. Phys.*, 74(1):014001, 2010.

[15] Y. Aoki and et al. *Nature*, 443:675–678, 2006.

[16] Z. Fodor and S. D. Katz. *JHEP*, (04):050, 2004.

[17] Larry Mclerran and Robert D. Pisarski. Phases of dense quarks at large nc. *Nucl. Phys. A*, 796:83–100, 2007.

[18] A. Andronic and et al. *Nucl. Phys. A*, 837:65–86, 2010.

[19] B. C. Barrois. *Nucl. Phys. B*, 129(3):390–396, 1977.

[20] Mark G. Alford and et al. *Rev. Mod. Phys.*, 80:1455–1515, 2008.

[21] W. Florkowski and et al. *Phenomenology of Ultra-Relativistic Heavy-Ion Collisions.* 2010.

[22] H. Satz. *Extreme States of Matter in Strong Interaction Physics: An Introduction*, volume 945. Springer International Publishing, 2018.

[23] Sevil Salur. *Investigation of Hadronic Resonances with STAR.* PhD dissertation, Yale University, 2006.

[24] E J Lofgren. 10 1975.

[25] Yu. B. Ivanov and et al. *Phys. Rev. C*, 73:044904, 2006.

[26] M. M. Aggarwal and et al. (STAR Collaboration). *ArXiv e-prints*, 2010.

[27] A. László and et al. *International Journal of Modern Physics E*, 16:2516–2521, 2007.

[28] G. Agakishiev and et al (The HADES Collaboration). *Eur. Phys. J. A*, 40:40–45, 2009.

[29] V. Kekelidze and et al. *EPJ Web of Conferences*, 171(12001), 2018.

[30] A. Sorin and et al. *PoS(CPOD2014)*, 042, 2014.

[31] C. Montag and et al. *PoS(CPOD2014)*, 041, 2014.

[32] J. Michel and et al. *IEEE Trans. Nucl. Sci.*, 58(1745), 2011.

[33] G. Odyniec and et al. *Pos(CPOD2013)*, 043, 2013.

[34] H. Sako and (for the J-PARC heavy-ion collaboration). *JPS Conf. Ser.*, 8(022010), 2015.

[35] A. Dainese. *Frascati Phys. Ser.*, 62(55), 2016.

[36] W. Reisdorf and H. G. Ritter. *Annual Review of Nuclear and Particle Science*, 47(1):663–709, 1997.

[37] Horst Stocker. *PoS*, CPOD07:025, 2007.

[38] Yasushi Nara and et al. *Phys. Lett. B*, 769:543–548, 2017.

[39] D. H. Rischke. *APH N.S. Heavy Ion Phys.*, 1:309–322, 1995.

[40] A. Andronic. *Nucl. Phys. A*, 834:237c–240c, 2010.

[41] P. Braun-Munzinger. *Phys. Lett. B*, 596:61–69, 2004.

[42] P. Chung and et al (E895 Collaboration). *Phys. Rev. Lett.*, 91:202301, 2003.

[43] G. Agakishiev and et al. (HADES Collaboration). *Eur. Phys. J. A*, 52, 2016.

[44] C. Blume. *J. Phys. G: Nucl. Part. Phys.*, 31:S57, 2005.

[45] C. Simon. *PoS*, CPOD2017:014, 2018.

[46] Feng Li and et al. *Phys. Rev. C*, 85:064902, 2012.

[47] G. Graef and el al. *Phys. Rev. C*, 90:064909, 2014.

[48] A. R. Tripolt and et al. *Int. J. Mod. Phys. E*, 26:1740028, 2017.

[49] R. Rapp and H. van Hees. *Phys. Lett. B*, 753:586–590, 2016.

[50] R. Chatterjee and et al. *Phys. Rev. C*, 75:054909, 2007.

[51] P. Mohanty and et al. *Phys. Rev. C*, 85:031903, 2012.

[52] T. Ablyazimov and el al. *Eur. Phys. J. A*, 53(60), 2017.

[53] R. Averbeck. *Prog. Part. Nucl. Phys.*, 70:159–209, 2013.

[54] T. Matsui and H. Satz. *Phys. Lett. B*, 178(4):416–422, 1986.

[55] M. C. Abreu and et al (The NA50 collbaoration). *Phys. Lett. B*, 410:327–336, 1997.

[56] A. Adare and el al (PHENIX Collaboration). *Phys. Rev. Lett.*, 98(232301), 2007.

[57] B. Abelev and el al (ALICE Collaboration). *Phys. Rev. Lett.*, 109:072301, 2012.

[58] M. Doering. and V. Koch. *Acta Phys. Polon. B*, 33:1495–1504, 2002.

[59] V. Koch and et al. *APH N.S., Heavy Ion Physics*, 14:227–237, 2001.

[60] I. Vassiliev. *JPS Conf. Proc.*, 17:092001, 2017.

[61] P. for the CBM Collaboration Senger. *J. Phys.: Conf. Ser.*, 50:357–360, 2006.

[62] J. Eschke. *J. Phys. G.: Nucl. Part. Phys.*, 31:S967, 2005.

[63] H H Gutbrod and et al, 2006.

[64] W. Erni and et al (The PANDA Collaboration). 2012.

[65] N. Herrmann and for The CBM Collaboration. *EPJ Web of Conferences*, 259(09001), 2022.

[66] Yu. B. Ivanov and et al. *Phys. Rev. C*, 74:044904, 2006.

[67] P. V. Konchakovski and et al. *Phys. Rev. C*, 90:014903, 2014.

[68] A. S. Bass. *Prog. Part. Nucl. Phys.*, 41:255, 1998.

[69] G. Burau and et al. *Phys. Rev. C*, 71:054905, 2005.

[70] M. Wagner. *Phys. Rev. C*, 71:034910, 2005.

[71] P. Senger and N. Hermann. *Nucl. Phys. News.*, 28(2), 2018.

[72] I. C. Arsene and et al. *Phys. Rev. C*, 75:034902, 2007.

[73] I. Kiesel. *Nucl. Inst. Meth. A*, 566:85–88, 2006.

[74] M. Deveaux and et al. *Nucl. Inst. Meth. A*, 958:162653, 2020.

[75] P. Klaus and et al. *Nucl. Inst. Meth. A*, 936:705–706, 2019.

[76] P. Larionov and for The CBM Collaboration. *J. Phys.: Conf. Ser.*, 599(012025), 2015.

[77] U. Frankenfeld and et al. *CBM Progress Report*, page 22, 2012.

[78] H. R. Schmidt and for the CBM Collaboration. *Nucl. Inst. Meth. A*, 936:630–633, 2019.

[79] J. Heuser et al., editors. *Technical Design Report for the CBM Silicon Tracking System (STS)*. GSI, Darmstadt, 2013.

[80] M. Teklishyn and on behalf of the CBM Collaboration. *EPJ Web of Conferences*, 171(21003), 2018.

[81] Alhussain Abuhoza. PhD thesis, Goethe University, Frankfurt am Main, Germany, 2015.

[82] C. Höhne. *Technical Design Report for the CBM Ring Imaging Cherenkov Detector*. 2013.

[83] F. Roether and for the CBM Collaboration. *J. Phys.: Conf. Ser.*, 1024(012040), 2018.

[84] P. Kähler, F. Roether, and for the CBM Collaboration. *Nucl. Inst. Meth. A*, 958(162727), 2020.

[85] C. Blume, C. Bergmann, and D. Emschermann. *Technical Design Report for the CBM Transition Radiation Detector (TRD)*. Darmstadt, 2018.

[86] Yvonne Pachmayer and For the ALICE Collaboration1. *Nucl. Inst. Meth. A*, 706:6–11, 2013.

[87] N. Herrmann. *Technical Design Report for the CBM Time-of-Flight System (TOF)*. GSI, Darmstadt, 2014.

[88] I. Deppner, N. Herrmann, and for the CBM Collaboration. *JINST*, 14(C09020), 2019.

[89] P. Senger. *Int. J. Mod. Phys. E*, 29:2030001, 2020.

[90] D. Kresan and C. Höhne. *CBM Progress Report*, page 63, 2008.

[91] F. Guber and I. Selyuzhenkov. *Technical Design Report for the CBM Projectile Spectator Detector (PSD)*. GSI, Darmstadt, 2015.

[92] S. Gorbunov and et al. *Comp. Phys. Comm.*, 178:374–383, 2008.

[93] R. Frühwirth. *Nucl. Inst. Meth. A*, 262:444–450, 1987.

[94] The Green IT Cube. https://ttsp-hwp.de/projects/green-it-cube/.

[95] A. Basavov and et al. *Phys. Rev. D.*, 85(054503), 2012.

[96] S. A. Bass and et al. *Prog. Part. Nucl. Phys.*, 41:255, 1998.

[97] I. Fröhlich and et al. *PoS ACAT*, 050:076, 2007.

[98] S. Chattopadhyay and et al. GSI, 2015.

[99] R. Brun. *CERN Program Library Long Writeup W5013*, 1993.

[100] Ajit Kumar. *Development and performance studies of GEM based tracking detectors for the Compressed Baryonic Matter (CBM) experiment at FAIR.* PhD dissertation, Homi Bhabha National Institute, 2021.

[101] P. Senger and V. Friese. CBM Progress Report 2020. Technical Report 2021-00421, 2021.

[102] CBM Progress Report 2019. Technical Report CBM-PR-2019, 2020.

[103] CBM Progress Report 2018. Technical Report CBM Progress Report 2018, 2019.

[104] CBM Progress Report 2017. Technical Report CBM Progress Report 2017, 2018.

[105] I. Selyuzhenkov and A. Toia, editors. *CBM Progress Report 2016.* GSI, 2017.

[106] Valentina Akishina. *Four-dimensional event reconstruction in the CBM experiment.* PhD dissertation, Goethe-Universitat, 2016.

[107] C. Amsler. *Phys. Lett. B*, 667:1–6, 2000.

[108] R. Frühwirth and et al, editors. *Data Analysis Techniques for High-Energy Physics.* Cambridge University Press, 2000.

[109] V. Nikulin and et al. Report on development of the conceptual design of mechanical structures for the much detector of the cbm experiment. MuCh Mechanics CDR, 2020.

[110] E. Rutherford and H. Geiger. In *Proceedings of the Royal Society of London. Series A*, volume 81, pages 174–177, 1908.

[111] H. Geiger and W. Müller. In *Naturwissenschaften*, volume 16, pages 617–618, 1928.

[112] Satyanarayana Bheesette. *Design and Characterisation Studies of Resistive Plate Chambers.* PhD dissertation, Indian Institute of Technology, Bombay, India, 2009.

[113] J. Keuffel. *Phys. Rev.*, 73:531, 1948.

[114] J. Keuffel. *The Review of Scientific Instruments*, 20:202–208, 1949.

[115] P. Galison. *Image and Logic, A material culture of microphysics*, volume 20. The University of Chicago Press, 1997.

[116] V. V. Parkhomchuck. *Phys. Rev.*, 93:269, 1971.

[117] G. V. Fedotovich and et al. In *Proceedings of the international conference on instrumentation for colliding beam physics, Standford, CA, USA*, pages 127–131, 1982.

[118] *ALICE Time-Of-Flight system (TOF): Technical Design Report.* CERN, Geneva, 2000.

[119] G. Charpak. *Nucl. Inst. Meth. Phys. Res. A*, 307:63–68, 1991.

[120] A. Arefiev and et al. *Nucl. Inst. Meth. Phys. Res. A*, 348:318–323, 1994.

[121] A. Akinov. *Nucl. Inst. Meth. Phys. Res. A*, 344:120–124, 1994.

[122] R. Santonico and R. Cardarelli. *Nucl. Inst. Meth. A*, 187:377–380, 1981.

[123] Christian Lippman. *Detector Physics of Resistive Plate Chambers.* PhD dissertation, Johann Wolfgang Goethe Universität, 2003.

[124] K. Hagiwara and et al. *Phys. Rev. D.*, 66, 2002.

[125] Filip Thyssen. *Commissioning, Operation and Performance of the CMS Resistive Plate Chamber System.* PhD dissertation, University Ghent, Belgium, 2014.

[126] M. Abbrescia and et al. *Resistive Gaseous Detectors: Designs, Performance, Perspectives.* 2018.

[127] M. Abbrescia and et al. *Nucl. Inst. Meth. Phys. Res. A*, 431:413–427, 1999.

[128] F. F. Rieke and W. Prepejchal. *Phys. Rev. A*, 6:1507–1519, 1972.

[129] W. Reigler and et al. *Nucl. Inst. Meth. Phys. Res. A*, 500:144–162, 2003.

[130] F. Sauli. *Yellow Report.* CERN 77-09, 1977.

[131] M. Abbrescia and et al. *Nucl. Inst. Meth. Phys. Res. A*, 398:173–179, 1997.

[132] I. Smirnov. *Heed, program to compute energy loss of fast particles in gases, Version 1.0.* CERN.

[133] Ingo Martin Deppner. *Development of a fully differential Multi-gap Resistive Plate Chamber for the CBM Experiment.* PhD dissertation, Ruperto-Carola-University of Heidelberg, Germany, 2013.

[134] S. Biagi. *Magboltz, program to compute gas transport parameters, Version 2.2.* CERN.

[135] V. Golovatyuk and et al. *Nucl. Inst. Meth. Phys. Res. A*, 508:29–33, 2003.

[136] A. Colucci and et al. Technical report, CERN, Geneva, Nov 1998.

[137] H. Rather. *Electron Avalanches and Breakdown in Gases.* Butterworth & Co., London, 1964.

[138] W. Legler. *Zeitschrift für Naturforschung A*, 16:253–261, 1961.

[139] S. Biagi. *Imonte, program to compute gas properties, Version 4.5.*

[140] S. Ramo. *Proc. IRE*, 27:584–585, 1939.

[141] Diego González Díaz. *Research and developments on timing RPC's. Application to the ESTRELA detector of the HADES experiment at GSI.* PhD dissertation, University of Santiago de Compostela, Spain, 2006.

[142] P. Rice-Evans. *Spark, Streamer, Proportional and Drift Chambers.* Ri helieu Press, London, 1974.

[143] E. D. Lozanskii. *Sov. Phys. Usp.*, 18:83, 1975.

[144] P. Fonte. *IEEE Trans. Nucl. Sci.*, 43:2135–2140, 1996.

[145] R. Cardarelli and et al. *Nucl. Inst. Meth. Phys. Res. A*, 382:370–374, 1996.

[146] M. Abbrescia and et al. *Nucl. Phys. B. (Proc. Suppl.)*, 158:30–34, 2006.

[147] P. Camarri and et al. *Nucl. Inst. Meth. Phys. Res. A*, 414:317–324, 1998.

[148] G. Carboni and et al. *Nucl. Inst. Meth. Phys. Res. A*, 533:107–111, 2004.

[149] M. C. S. Williams. *J. Phys. G: Nucl. Part. Phys.*, 39:123001, 2012.

[150] R. Ganai and et al. *JINST*, 11:P04026, 2016.

[151] Rajesh Ganai. *Probing the Earth Matter Density Through INO-ICAL and Related Detector Development.* PhD dissertation, Homi Bhabha National Institute, 2017.

[152] F. Anghinolfi. *Nucl. Inst. Meth. Phys. Res. A*, 533:183–187, 2004.

[153] Md. Naimuddin (ed.). Proceedings, XXII DAE High Energy Physics Symposium: Delhi, India, December 12 -16, 2016. volume 203, pages 174–177. Springer, 2018.

[154] M. Abbrescia and et al. *Nucl. Inst. Meth. Phys. Res. A*, 394:13–20, 1997.

[155] R. Ganai and et al. *JINST*, 11(C01090), 2016.

[156] R. Ganai and et al. *JINST*, 13(P07022), 2018.

[157] R. Ganai and et al. *JINST*, 14(C06010), 2019.

[158] P. Fonte and et al. *Nucl. Inst. Meth. Phys. Res. A*, 449:295–301, 2000.

[159] R. Ganai and et al. *Nucl. Inst. Meth. Phys. Res. A*, 936:505–506, 2019.

[160] Yi Wang and et al. volume 26, page 024006, 2019.

[161] V Friese and C. Sturm, editors. *CBM Progress Report 2012.* GSI, 2013.

[162] M. Ciobanu. *IEEE Nucl. Sci. Symp.*, 61:1015–1023, 2014.

[163] Rafal Kleczek. *JINST*, 12(C01053), 2017.

[164] P. A. Loizeau and et al. *Proc. of SPIE*, 9662(96622X), 2015.

[165] K. Kasinski and et al. *IEEE Nucl. Sci. Symp. Med. Imag. Conf. Rec. (NSS/MIC)*, pages 1–6, 2014.

[166] Rafal Kleczek. *JINST*, 12(C01053), 2017.

[167] R. Kleczek and et al. *IEEE Nucl. Sci. Symp. Med. Imag. Conf. Rec. (NSS/MIC)*, pages 1–4, 2013.

[168] M. Gagliardi. *Nucl. Instrum. Meth. A*, 661:S45–S49, 2012.

[169] A. Ferretti and on behalf of the ALICE Collaboration. *JINST*, 14(C06011), 2019.

[170] R. P. Adak and et al. *Nucl. Instrum. Meth. A*, 846:29–35, 2017.

[171] G. Cattani and on behalf of the RPC Group. *Journal of Physics: Conference Series*, 280(012001), 2011.

[172] T. Balog. *J. Phys.: Conf. Ser.*, 503:012019, 2014.

[173] A. K. Dubey. *Nucl. Instrum. Meth. A*, 718:418–420, 2013.

[174] G. A. Agnetta and et al. *Nucl. Instrum. Meth. A*, 381:64–72, 1996.

[175] L. Lopes and et al. *JINST*, 9(C10023), 2014.

[176] F. P An and et al. *Nucl. Instrum. Meth. A*, 811:133–161, 2016.

[177] A Kumar and et al. *JINST*, 11(C03034), 2016.

[178] A. Akindinov and et al. *Nucl. Instrum. Meth. A*, 456:16–22, 2000.

[179] Y Haddad and et al. *Nucl. Instrum. Meth. A*, 718:424–426, 2013.

[180] B. Bonner and et al. *Nucl. Instrum. Meth. A*, 478:176–179, 2002.

[181] D. Piccolo and et al. *Nucl. Instrum. Meth. A*, 477:435–439, 2002.

[182] M. Yamaga and et al. *Nucl. Instrum. Meth.*, 456:109–112, 2000.

# List of Figures

# List of Tables